



Influence of Composition and Processing on the Oxidation Behavior of MCrAlY-Coatings for TBC Applications

Juan Toscano

Forschungszentrum Jülich GmbH
Institut für Energieforschung (IEF)
Werkstoffstruktur und Eigenschaften (IEF-2)

Influence of Composition and Processing on the Oxidation Behavior of MCrAlY-Coatings for TBC Applications

Juan Toscano

Schriften des Forschungszentrums Jülich
Reihe Energie & Umwelt / Energy & Environment

Band / Volume 28

ISSN 1866-1793

ISBN 978-3-89336-556-2

Bibliographic information published by the Deutsche Nationalbibliothek.
The Deutsche Nationalbibliothek lists this publication in the Deutsche
Nationalbibliografie; detailed bibliographic data are available in the
Internet at <http://dnb.d-nb.de>.

Publisher
and Distributor: Forschungszentrum Jülich GmbH
Zentralbibliothek, Verlag
D-52425 Jülich
phone: +49 2461 61-5368 · fax: +49 2461 61-6103
e-mail: zb-publikation@fz-juelich.de
Internet: <http://www.fz-juelich.de/zb>

Cover Design: Grafische Medien, Forschungszentrum Jülich GmbH

Printer: Grafische Medien, Forschungszentrum Jülich GmbH

Copyright: Forschungszentrum Jülich 2009

Schriften des Forschungszentrums Jülich
Reihe Energie & Umwelt / Energy & Environment Band / Volume 28

ISSN 1866-1793
ISBN 978-3-89336-556-2

D 82 (Diss., RWTH Aachen, 2008)

The complete volume is freely available on the Internet on the Jülicher Open Access Server
(JUWEL) at <http://www.fz-juelich.de/zb/juwel>

Neither this book nor any part may be reproduced or transmitted in any form or by any means,
electronic or mechanical, including photocopying, microfilming, and recording, or by any
information storage and retrieval system, without permission in writing from the publisher.

Summary

The adherence of the thermally grown oxide (TGO) to the bond coat is recognized to be crucial for the lifetime of thermal barrier coatings (TBC) in aircraft engine and gas turbine blades. The stability of the system has to be guaranteed over extended service times (around 25000h) at high operation temperatures. With this aim, it is necessary that the TGO is slow-growing and adherent.

This work studies the influence of different parameters in the oxidation behavior and scale adherence on MCrAlY-bond coats. For this purpose, three MCrAlY-coatings were selected and subjected to oxidation tests at high temperature in the form of TBC systems, overlay coatings and free-standing coatings. The first part of the work treats the influence of the chemical composition on the oxidation behavior of the bond coat. The second part investigates the influence of non material-dependent parameters: starting with geometrical parameters (surface roughness and coating thickness) and followed by pre-treatment/processing parameters (surface processing sequence, heat treatment parameters and amount of O-impurities). Finally, the work deals with the possibility of defining a critical TGO thickness to failure in EB-PVD TBC systems.

The results demonstrate that not only the chemical composition of a MCrAlY-coating but also those geometrical and processing parameters selected can have an influence on its oxidation behavior and scale adherence. The studied Co-base coating exhibited better resistance to scale spallation despite faster oxidation kinetics, apparently favored by phase stability over a wide temperature range. Furthermore, it is shown that for a specific material, the oxidation behavior can be considerably influenced by the geometrical and processing parameters mentioned above. In general this influence was achieved due to a variation of the yttrium reservoir, mobility and/or distribution, which in turn determined to which extent this element can act at the surface during oxidation. Only by varying the oxygen partial pressure of the atmosphere could be obtained scales with different oxidation kinetics but identical in morphology and composition. After assessment of these scales it seemed to be that a critical TGO thickness to failure in EB-PVD TBC systems exists.

Zusammenfassung

Es ist bekannt, dass die Haftung des thermisch gewachsenen Oxids (TGO) zur Haftvermittlerschicht (Bond Coat) von entscheidender Bedeutung für die Lebensdauer von Wärmedämmschichten (TBC) in Schaufeln von Flugzeugtriebwerken und Gasturbinen ist. Die Stabilität dieses Schichtverbunds muss über lange Zeiträume (ca. 25000h) bei hohen Temperaturen gewährleistet sein. Daher ist es notwendig, dass das TGO ein langsames Wachstum und eine gute Haftung aufweist.

Diese Arbeit untersucht den Einfluss verschiedener Parameter auf das Oxidationsverhalten und die Haftung des TGO auf MCrAlY Bond Coats. Zu diesem Zweck wurden drei verschiedene MCrAlY Beschichtungen ausgewählt und bei hohen Temperaturen ausgelagert. Dabei wurden TBC Schichtsysteme, freistehende Schichten sowie MCrAlYs auf IN738 (overlays) untersucht. Im ersten Teil der Arbeit wird der Einfluss der chemischen Zusammensetzung des Bond Coats auf das Oxidationsverhalten untersucht. Im weiteren Verlauf wird der Einfluss von nicht materialabhängigen Parametern bestimmt. Dazu gehören geometrische Parameter (Oberflächenrauigkeit und Schichtdicke) sowie Vorbehandlungsparameter (Sequenz der Vorbehandlungsschritte, Wärmebehandlungsparameter und Gehalt von O-Verunreinigungen). Im letzten Teil wurde versucht die kritische TGO Dicke zu bestimmen, bei der es zum Versagen des Schichtverbundes kommt.

Die Ergebnisse zeigen, dass nicht nur die Zusammensetzung der MCrAlY Beschichtungen, sondern auch die besprochenen geometrischen und Prozessparameter einen Einfluss auf das Oxidationsverhalten und die Schichthaftung haben. Im Vergleich zu Ni-Basis Bond Coats zeigt die untersuchte Co-Basis MCrAlY eine bessere Haftung trotz höherer Oxidwachstumsrate. Es wird vermutet dass, dies mit der Stabilität der Mikrostruktur zusammenhängt. Die gewählten Geometrischen- und Vorbehandlungsparameter können einen Einfluss auf die Verteilung, Mobilität und Reservoir von Y haben. Dies wiederum bestimmt den Einfluss dieses Element auf das Oxidationsverhalten.

Die Variation des Sauerstoffpartialdrucks in der Auslagerungsatmosphäre führte zu Oxidschichten, die sich nur in der Dicke, nicht aber in der Morphologie oder Zusammensetzung unterschieden. Diese zeigten einen Zusammenhang zwischen Oxidschichtdicke und Versagen von EB-PVD TBC Systeme.

Index

1	Introduction	1
1.1	Energy demand and contribution of natural gas to the energy mix	1
1.2	Power generation with natural gas	2
1.3	Gas Turbines	3
2	TBC Systems	5
2.1	Turbine blade superalloy (substrate)	6
2.2	Bond Coat	7
2.3	Thermal barrier coating (TBC)	14
3	Oxidation of MCrAlY-coatings	17
3.1	Oxidation Reaction	17
3.2	Formation of the thermally grown oxide (TGO) in TBC systems	20
3.3	Failure mechanisms of coating systems	24
4	Purpose of this investigation	28
5	Experimental Procedure	30
	RESULTS AND DISCUSSION	35
6	Effect of the Bond Coat chemical composition on the oxide growth and adherence	35
6.1	Oxidation studies on TBC systems with MCrAlY-coatings	35
6.1.1	Lifetime of TBC systems	35
6.1.2	TGO stress measurements in TBC systems	36
6.1.3	TGO growth and morphology in TBC systems	37
6.2	Oxidation studies on overlay MCrAlY coatings	39
6.2.1	TGO growth and morphology in overlay coatings with as- sprayed surfaces	39
6.2.2	Exposure of overlay coatings with ground surfaces	40
6.3	Oxidation studies on free-standing MCrAlY-coatings	44
6.3.1	TGO growth and morphology after discontinuous exposure	44
6.3.2	Characterization of Y/Al-oxide compounds	45
6.3.3	Oxidation kinetics of free-standing MCrAlY-coatings during isothermal exposure	49
6.3.4	Oxidation kinetics and scale adherence on MCrAlY-coatings during cyclic exposure	57

6.4 Summary and final comments	59
7 Temperature dependence of phase relationships in different MCrAlY-coatings	61
7.1 General remarks	61
7.2 Modeling of phase equilibria in commercial MCrAlY-coatings	62
7.2.1 Modelling of phase equilibria in NiCoCrAlY(hi-Al)	62
7.2.2 Modelling of phase equilibria in NiCoCrAlY(lo-Al)	63
7.2.3 Modelling of phase equilibria in CoNiCrAlY	63
7.3 Microstructure of annealed MCrAlYs in the temperature range 800-1100°C	64
7.3.1 Microstructure at 1100°C	64
7.3.2 Microstructure at 1000°C	66
7.3.3 Microstructure at 900°C	67
7.3.4 Microstructure at 800°C	68
7.4 Physical CTE measurements on free-standing MCrAlYs	70
7.5 Accuracy of thermodynamic calculations	71
7.5.1 Accuracy of phase composition calculations	71
7.5.2 Accuracy of volume fraction calculations	72
7.6 Correlation of experimental findings with observations in a gas turbine blade after service	74
7.7 Summary	78
8 Geometrical effects on the oxide growth and morphology in MCrAlY-coatings	80
8.1 General Remarks	80
8.2 Effect of coating roughness	81
8.2.1 TGO growth and morphology on rough surfaces	81
8.2.2 Temperature dependence of the effect of roughness	86
8.2.3 Characterization of Y-rich compounds	86
8.2.4 Mechanistic explanation of the effect of roughness	88
8.2.5 Limitations of the effect of roughness	89
8.3 Effect of coating thickness	92
8.3.1 General remarks	92
8.3.2 Effect of coating thickness during discontinuous oxidation	92
8.3.3 Effect of coating thickness during cyclic oxidation	96
8.3.4 Discussion on the effect of Y-reservoir on the TGO growth rate and adherence	101
8.4 Summary on the geometrical effects	102

9	Effect of pre-treatment and processing on the oxidation behavior of MCrAlY-coatings	104
9.1	General remarks	104
9.2	Effect of surface processing sequence (Heat treated vs. heat treated and ground)	105
9.2.1	Modifications of the surface chemical composition by vacuum heat treatment	105
9.2.2	Discontinuous exposure of MCrAlYs with different initial surface Condition	108
9.2.3	Cyclic exposure of MCrAlYs with different initial surface condition (HT vs. HT+G)	116
9.2.4	Mechanism of the effect of the initial surface condition on the MCrAlY oxidation	122
9.3	Effect of heat treatment conditions	126
9.3.1	General remarks	126
9.3.2	Alteration of the surface chemical composition by alternative heat treatments	127
9.3.3	Discontinuous exposure of MCrAlYs subjected to alternative heat treatments	128
9.4	Effect of oxygen impurities on the oxidation behavior of VPS MCrAlY-coatings	134
9.4.1	General remarks	134
9.4.2	Isothermal oxidation of free-standing MCrAlYs with varying O-content	135
9.4.3	Estimation of amount of Y bound in MCrAlYs with varying O-content	140
9.5	Summary on the effect of pre-treatment	142
10	Effect of the TGO growth rate on the lifetime of TBC systems	144
10.1	General Remarks	144
10.2	Lifetime of EB-PVD-coated specimens in air and Ar- 4% H ₂ - 2% H ₂ O environments at 1100°C	145
10.3	Lifetime of APS-coated specimens in Air + 2% H ₂ O and Ar- 4% H ₂ - 2% H ₂ O environments at 1100°C	149
10.4	Summary and final comments	153
11	Summary and Conclusions	154
12	References	158

1. Introduction

1.1 Energy demand and contribution of natural gas to the energy mix

In the near future the energy demand will increase steadily, it is expected to expand by almost 60% until 2030 [IEA] due to both the population increase and to the growth of the world's gross domestic product (GDP), which is the strongest driver of the energy demand. Especially in the emerging markets, this demand will rise considerably in the coming years caused by the rapid industrialization of energy intensive sectors, like steel and cement industries, together with a still moderate efficiency of energy conversion.

Motivated by environmental concerns and aiming to diminish the dependence on the limited traditional fossil fuels, significant efforts are dedicated to diversify the primary energy mix that covers the continuously increasing energy demand. Despite the enduring dominance of oil and coal in the global energy use [IEA], cleaner and more sustainable sources of energy will gain more terrain in the primary fuel mix. Fig. 1 exemplifies how the global increase in required power generation is expected to be covered not only by coal but also by natural gas and renewable energies. According to this source, the use of natural gas in the power generation sector is expected to almost triple from 2002 to 2030.

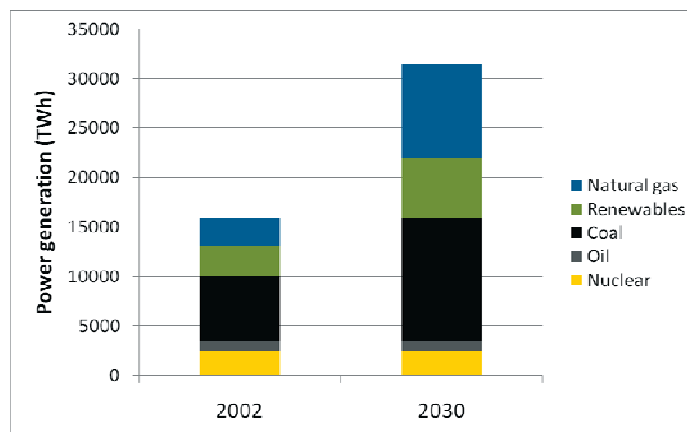


Fig. 1.1 – Expected growth in power generation worldwide with share of respective energy sources [IEA].

1.2 Power generation with natural gas

Natural gas is the most environmentally friendly among the fossil fuels in power generation. In Table 1.1 is presented, as a reference, a comparison of the average CO₂ output per kWh produced in the operating power plants in the United States, depending on the fuel used. Within the two year period 1998-1999, the coal-based power plants emitted in average 59%, and the oil-based power plants in average 49%, more CO₂ per kWh generated than the gas power plants.

Fuel Used	Output Rate (Kg CO ₂ per kWh)
Coal	0,952
Petroleum	0,895
Gas	0,600
Other Fuels (i.e. solid wastes)	0,626

Table 1.1 – Average CO₂ output per kWh produced in the operating power plants in the United States between 1998 and 1999, by fuel used.
Source: U.S Energy Information Administration, Department of Energy.

In a gas-based single cycle power plant, where the exhaust heat is wasted, net efficiencies of 35-36% are achieved. In contrast, in modern combined-cycle power plants (CCPP) thanks to the high exhaust temperature of the gas turbines at $T = 550-600^{\circ}\text{C}$, this waste heat is utilized to drive a steam cycle for further power generation, reaching total net efficiencies of up to 58% [Lechner].

In addition to the high efficiencies, the CCPPs are characterized by comparably low investment costs and short construction times [VGB]. The advantages of this technology promote the more extensive usage of natural gas as a fuel for power generation. For instance, more than 60% of the planned expansion in power generation capacity in the European Union corresponds to gas-based plants (Fig 1.2).

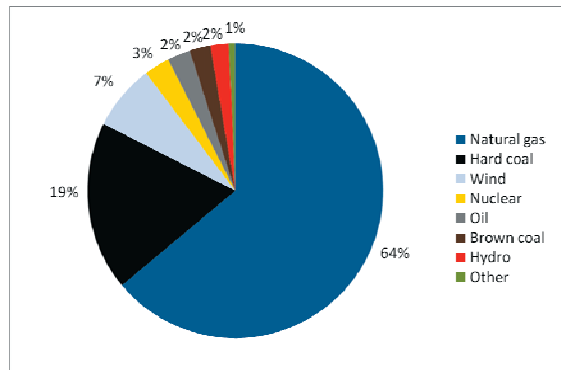


Fig. 1.2 – Upcoming projects of expansion of power generation capacity in the European Union sorted by fuel source [VGB].

1.3 Gas Turbines

One of the main components of a CCPP is the gas turbine (GT), which contributes to around two thirds of the power output of the plant. This turbomachine converts thermo-chemical energy into mechanical energy based on the thermodynamic Joule-Brayton cycle, according to which, the enthalpy difference between a high and a low pressure process is utilized to generate work. In the turbine, the gas stream undergoes three main processes: compression, combustion and expansion (Fig. 1.3). Across a multi-stage compressor, flow rates around 500 kg/s can reach a pressure ratio up to 15 [Lechner]. Following the compression, the combustion takes place releasing exhaust gases at high velocities into the expansion stage which will drive a series of rotating blades. At this point the gas temperature can be between 1200 and 1400°C. The rotation induced in the axle of the gas turbine is used to drive an electrical generator coupled to it.

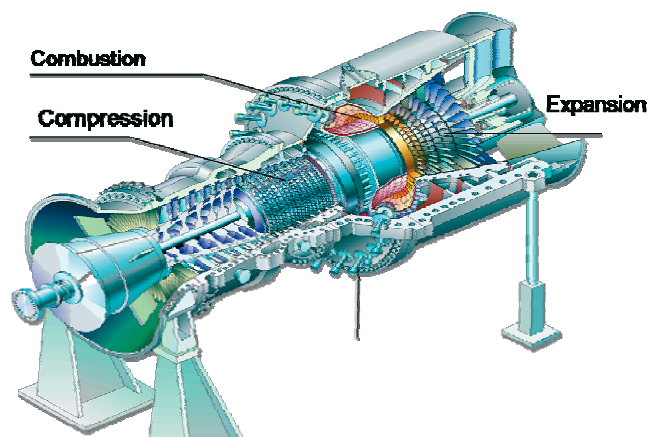


Fig. 1.3 – Gas turbine Vx4.3A (Siemens Power Generation).

Currently, gas turbines in operation offer power outputs over 150 MW and the most powerful nowadays are designed to deliver over 250 MW. Their net efficiency can be improved (i) by increasing the turbine inlet temperature [Nicholls-1] and (ii) by reducing the amount of air bypassed from the compression stage for cooling. An increase in the turbine inlet temperature not only has the benefit of a higher efficiency, but also reduces the CO₂ emissions.

Such a temperature increase directly affects the hottest sections of the turbine: combustion chamber, vanes and blades. The function of the stationary vanes is to deflect and accelerate the gas to an angle so that the flow along the profile of the blades is aerodynamically optimal. The rotating blades and the axle are set in motion by the accelerated gas. Both components withstand thermal stresses, and additionally the vanes are subjected to bending forces during operation, while the blades are subjected to centrifugal forces [Lechner]. The aerodynamic profile of a turbine blade can be observed in Fig. 1.4



Fig. 1.4 – Gas turbine blade, view of the pressure side.
Source: University of Utah.

The superalloys from which these components are made cannot maintain their thermo-mechanical properties, and moreover, suffer degradation due to high temperature oxidation and corrosion if directly exposed to the combustion exhaust gases. In order to possibly minimize this damage without affecting the efficiency of the turbine, oxidation and corrosion protection coatings are applied. In the hottest sections, additional insulating ceramic layers, the thermal barrier coatings (TBC), have been applied to these components along with internal air cooling for over a decade. Since then, big efforts have been dedicated to guarantee the thermo-mechanical stability of this coating for long service times at increasing gas temperatures.

2. TBC SYSTEMS

The thermal barrier coatings are multi-layer systems that provide thermal insulation to the materials that operate in contact with high temperature gases (over 1200°C) (Fig. 2.1); the adoption of this technology has permitted a considerable improvement of the efficiency in gas turbines and aircraft engines. The use of a ceramic coating in the TBC system enables, due to its low heat transfer coefficient (0.8-1.9 W/mK), a temperature drop of up to 150°C within a thickness commonly below 0.8 mm in internally cooled blades.

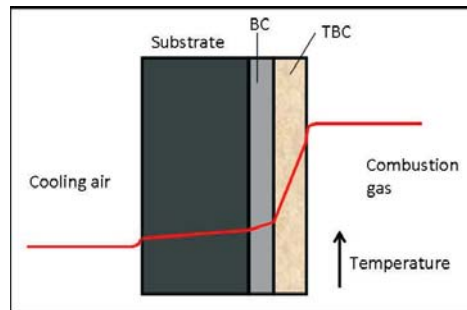


Fig. 2.1 – Thermal insulation achieved by a TBC system.

A TBC system is composed of three different materials, the actual TBC or topcoat, the bond coat (BC) and the substrate, which in this application is the bulk superalloy of the turbine blade. Additionally, during exposure to the gas at high temperature, an oxide scale forms on the BC surface becoming part of the original system [Gell-1]. This thermally grown oxide (TGO), mainly consisting of alumina, builds up between the TBC and the bond coat and is of significant importance since it often represents the starting point for failure which leads to TBC delamination [Quadakkers-1, Tolpygo-1]. The cross section of a typical TBC system during operation is illustrated in Fig. 2.2.

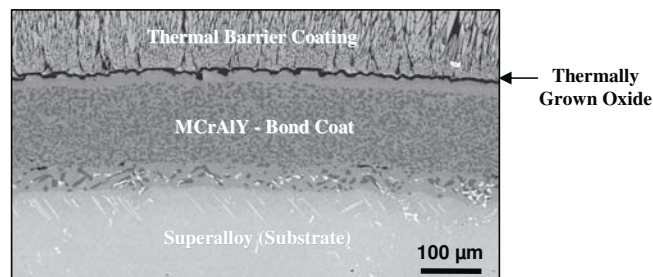


Fig. 2.2 – Cross section of a typical TBC system after 4000h of air exposure at 1000°C.

Due to the different nature and properties of topcoat, BC and substrate, the selection of these materials is also based on the mechanical and chemical stability of the system under the severe operation conditions. The current research on the TBC technology focuses on improving multiple aspects such as oxidation and corrosion protection, adherence, and mechanical compliance in order to guarantee that each component maintains its properties and the system can perform reliably during the desired lifetime, which typically amounts to 25000 operating hours in stationary gas turbines [Czech-1].

2.1 Turbine blade superalloy (substrate)

The development of the superalloys over the past decades has considerably contributed to a better high temperature capability of the components. From the first wrought alloys in the 1940s to the most modern single-crystal alloys nowadays, the gas inlet temperature in these turbo-machines could be increased around 300°C [Lechner].

In the blades of the front rows, directionally solidified (DS) and single-crystal Ni-base superalloys are predominantly employed. The most important properties these materials must possess in this application are resistance to high temperature corrosion, creep and fatigue. The chemical composition of three commercial superalloys used in gas turbine blades is presented in Table 2.1. IN 738 LC (Low Carbon) is a DS alloy, while PWA 1483 and CMSX-4 are single-crystal alloys.

Alloy	Ni	Co	Cr	Al	C	W	Ta	Ti	Mo	Re	Zr	Nb	Y	Hf
IN 738 LC	61,6	8,5	16	3,4	0,15	2,6	1,7	3,4	1,7	-	0,04	0,9	0,1	-
PWA 1483	60,2	9	12	3,6	0,07	3,8	5	4,2	1,9	-	0,03	-	-	-
CMSX-4	61,7	9	6,5	5,6	-	6	6,5	1	0,6	3	-	-	-	0,1

Table 2.1 – Chemical composition of commercial superalloys [Lechner].

The high temperature creep resistance of the modern superalloys is provided by solid solution- and/or precipitation hardening. Ni-base superalloys can contain a volume fraction up to 70% of γ' -Ni₃Al strengthening precipitates within a γ -matrix, guaranteeing creep resistance during 30000h in service, for material temperatures up to 950°C [Lechner].

Regarding corrosion and oxidation resistance, these Ni-base materials are commonly alloyed with Cr and Al, which promote the formation of protective oxide layers or “scales” (Cr_2O_3 and Al_2O_3 , respectively). Minor alloying elements such as Ta, Hf, Ti, Y and Re are added in order to enhance the oxidation resistance and the high-temperature creep strength. The exclusive formation of protective alumina scales on these superalloys is however not achieved at the operation temperatures of the hottest section in a gas turbine. Li et al. [Li-1, Li-2] reported on the heterogeneous oxide scale that can form on a Ni-base superalloy when oxidized in a temperature range from 800-1150°C; besides the protective, slow-growing α - Al_2O_3 , various (Ni,Co)-spinel and complex oxide compounds of Cr, Ta and Ti were found. Seal et al. [Seal] distinguished sub-scales of alumina, chromia and Ni-oxides together with different spinels and TiO_2 after exposing IN738 LC in air between 850-950°C. For a reliable protection of the substrate, an oxidation resistant bond coat is incorporated into the system.

2.2 Bond Coat

Lying between the substrate and the ceramic topcoat, the bond coat fulfills vital functions in the TBC system: oxidation protection, adherence and chemical and mechanical stability between the components of the system.

Due to the high oxygen permeability of the external ceramic topcoat, the oxidation protection of the underlying superalloy is imposed to the bond coat [Gleeson-1]. This metallic coating is engineered to ideally ensure the formation of a slow-growing, uniform and defect-free α - Al_2O_3 scale that acts as an oxygen diffusion barrier [Padture]. Thus, a sufficient aluminum reservoir is a necessary constituent of the coating chemical composition.

The significant contribution of the bond coat to the oxidation protection and adherence in a TBC system is illustrated in Fig. 2.3. A TBC + BC-coated superalloy and a TBC-coated superalloy (without BC) were exposed simultaneously in air at 1100°C for 110h. As can be observed on the cross-section micrographs, on the surface covered by a BC, a thin, protective alumina scale formed and the ceramic coating is still adherent (Fig. 2.3a), whereas, on the surface without a BC, the ceramic topcoat spalled off and severe oxidation of the IN738LC occurred; the TGO in this case is a fast-growing, non-protective mixed oxide (Fig. 2.3b).

Two types of bond coats for TBC systems are commercially employed depending on the application: the diffusion aluminide coatings and the MCrAlY coatings.

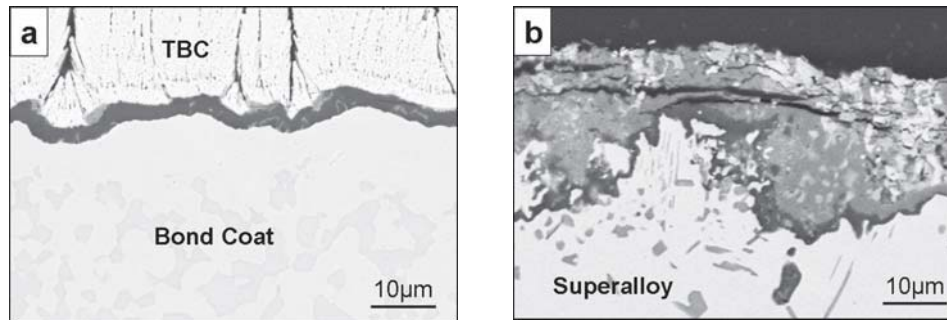


Fig. 2.3 – Effect of exposure in air at 1100°C (110h) on
a) TBC + BC-coated superalloy and on b) TBC-coated superalloy.

2.2.1 Diffusion aluminide Bond Coats

The diffusion aluminides are predominantly used in jet engines. For their production, the substrate surface is enriched with Al generating a protective 30-70µm thick NiAl layer (Fig. 2.4). The most common deposition method of aluminized coatings is the pack cementation; in this technique, the component is immersed in a mixture of powders containing Al, inert filler and an activator. During subsequent annealing, the activator volatilizes and reacts with the aluminum source, producing Al-rich volatile compounds which diffuse to the substrate surface. Here a second reaction takes place causing Al deposition on the alloy surface. Internal diffusion of Al and the substrate elements establish the coating with the desired chemical composition. In an alternative process, the chemical vapor deposition (CVD), the coating gases are generated externally and then fed into an evacuated retort, which contains the substrate. The gaseous compounds eliminate the risk of solid pack material being captured in the coating and can better flow through cooling holes of turbine blades to deposit [Meier].

Seeking after a further improvement in oxidation and hot corrosion resistance, platinum is commonly added to the diffusion aluminides. Although the beneficial effect of Pt on the oxidation resistance has not been completely clarified, various authors have suggested possible mechanisms for it. Gleeson et al. [Gleeson-2] attribute the enhanced high temperature resistance to a reduction of oxygen diffusivity in the presence of Pt, and the selective oxidation of Al. Moreover, other authors [Pint-1, Nesbitt] suggest that the addition of reactive elements like zirconium and hafnium to Ni-Pt-Al can further improve the scale adherence with a simultaneous reduction of the oxide growth rate. They attributed these improvements to the segregation of these reactive elements to the metal-scale interface

and the scale grain boundaries, and a controlled generation of stresses in the scale.

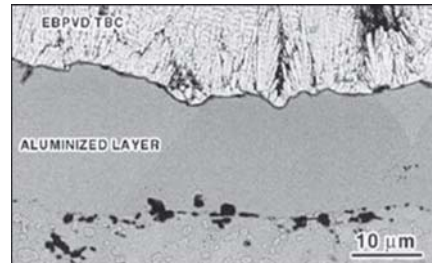


Fig. 2.4 – cross-section of a TBC specimen with a Pt-modified NiAl coating after cyclic exposure in air at 1100°C [Yanar-1]

2.2.2 MCrAlY Bond Coats

The MCrAlY-coatings are mainly employed in the first blade rows of stationary gas turbines. Different to the diffusion aluminides, the final chemical composition of the coating is not obtained through chemical reaction with the substrate. The source material, usually in the form of gas-atomized powder possesses the nominal chemical composition of the coating, allowing incorporation of the elements that are difficult to deposit in diffusion coatings, such as Cr or Y [Meier]. In the denomination, M represents the base element of the coating alloy, which can be Ni, Co or a combination of both. NiCrAlY-coatings are designed for high oxidation resistance, CoCrAlY-coatings for high corrosion resistance and NiCoCrAlY/CoNiCrAlY to obtain an optimum balance of both properties (Fig. 2.5) [Nicholls-2].

Typically, the high temperature microstructure of the MCrAlY-coatings is mainly composed of two phases: γ -Ni, which provides ductility, and β -NiAl which provides the Al-reservoir and thus, the oxidation resistance.

Cobalt is added to MCrAlY-coatings, usually in concentrations between 15-30 wt.-%, to improve the ductility and the corrosion resistance [Singheiser-1, Goward]. The former property is achieved by an increased solubility of Cr in the γ -matrix phase, reducing the tendency to form brittle phases such as γ' and α -Cr. Furthermore, additions of Co reduce the stacking fault energy (SFE, a measure of the mobility of dislocations inside the material) of the γ -phase, since SFE for Ni is 300 mJ/m² and for Co 25 mJ/m², and thus improve the creep resistance of the MCrAlY [Täck].

The exact contents of Cr and Al in the MCrAlY-coating are adjusted to provide a compromise between oxidation and corrosion resistance (Fig. 2.5). The typical concentrations of Cr vary between 15-25 wt.-%, while those of Al vary between 10-15 wt.-% [Gleeson-1]. The presence of chromium in the alloy reduces the necessary amount of Al for the exclusive formation of a protective alumina scale. Since in a TBC coated component the adherence of the oxide scale is crucial for the life of the system, rather than the ability of self-rehealing after oxide scale spallation, higher aluminum contents are not necessarily beneficial for the system [Anton].

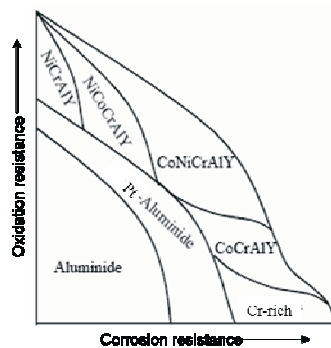


Fig. 2.5 – Relative oxidation and corrosion resistance of high temperature protective coatings [Nicholls-2].

In addition to the major alloying elements, the so-called reactive elements (RE) are added to the coating composition mainly to improve the oxide scale adherence. The most important of these RE in a MCrAlY-coating is yttrium, alloyed in concentrations of 0.1-0.5 wt.-%. The effects of Y on the high-temperature performance of the bond coat are a large topic of discussion in the literature (chapter 3.4). However, there is a general consent that minor additions of Y improve the adherence of the alumina scale by gettering harmful sulfur impurities and changing the scale growth mechanism to inward growth, thus preventing vacancy condensation at the oxide/metal interface [Quadakkers-2].

Rhenium has been incorporated in some commercial MCrAlY-coatings, in concentrations of about 1-3 wt.-%, due to improved oxide scale adherence, thermo-mechanical fatigue resistance and retardation of interdiffusion with the substrate. These improvements were attributed to the presence of additional phases (σ and α -Cr) in the coating microstructure [Beele, Czech-1]. Phillips and Gleeson also observed a reduction of the internal oxidation in Re-alloyed MCrAlYs during cyclic high-

temperature exposure [Phillips]. The risk of excessive formation of brittle phases such as σ and α -Cr is however a drawback of the Re additions.

Also additions of Tantalum to MCrAlY-alloys were observed to have beneficial effects. In some investigations a better oxidation resistance was achieved by Ta, since this element reacted with the upward diffusing carbon and titanium from the substrate, and thus, prevented their inclusion in free form in the oxide scale. Moreover, improved mechanical properties such as creep resistance and yield strength were measured in Ta-containing MCrAlY-coatings compared to baseline MCrAlYs [Fox, Taylor-1]. Monceau and Raffaitin have conducted several experiments with NiCoCrAlYT-Ta-coated specimens which have exhibited promising high-temperature lifetimes [Monceau, Raffaitin]

Though less commonly used, other alloying additions (e.g. Pt [Taylor-1, Quadackers-1], Hf [Goward] and Zr [Smialek]) have been incorporated into MCrAlY-coatings, obtaining some important improvements in high-temperature oxidation protection and in mechanical properties.

2.2.2.1 Microstructure of MCrAlY Bond Coats

At high temperatures above ca. 1000°C, the MCrAlY bond coats are multi-phase systems consistent essentially of a γ -Ni matrix and an Al-rich β -NiAl phase [EvansA-2]. However, depending on its chemical composition and the temperature of exposure, other phases such as γ' -Ni₃Al and α -Cr may form, as observed in the ternary Ni-Cr-Al phase diagram (Fig. 2.6).

Fig. 2.6 shows the sensitivity of the phase composition of MCrAlY-alloys to changes in temperature and chemical composition. By establishing an arbitrary chemical composition “A”, the ternary phase diagram predicts a $\gamma + \beta$ microstructure in equilibrium at 1150°C, see Fig. 2.6b. However, if the Cr and Ni concentrations are increased at the expense of Al, due to Al consumption for scale growth and/or interdiffusion with the substrate, the chemical composition changes from “A” to “B” (Fig. 2.6b), which corresponds to a $\gamma + \beta + \gamma'$ ternary phase field. A further Al loss to the scale or to the substrate could result in the new coating composition “C”, implicating the transformation into a $\gamma + \gamma'$ phase field.

Should the chemical composition remain barely invariable, but the coating temperature vary, as can happen during adjustment from peak to base load operation in a gas turbine, the BC can also acquire a new microstructure. For instance, a coating with the original composition “A”, exhibiting a $\gamma + \beta$ microstructure at 1150°C (Fig. 2.6b), will undergo a phase transformation to $\alpha + \beta + \gamma'$ if the temperature is reduced to 850°C (Fig. 2.6a).

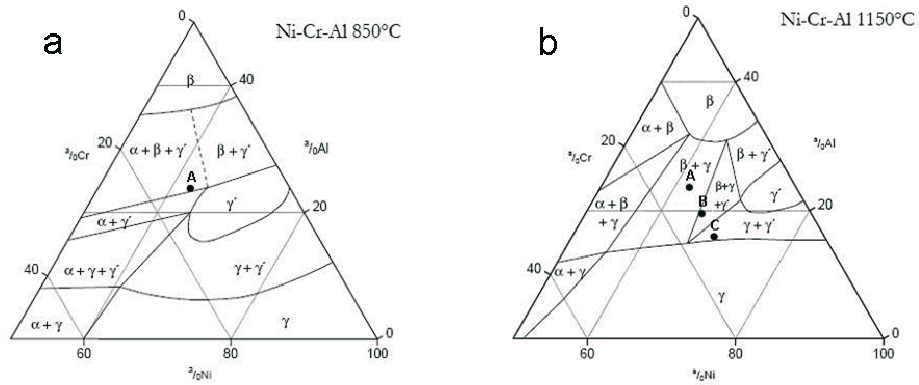


Fig. 2.6 – NiCrAl ternary phase diagram at a) 850°C and b) 1150°C (phases in equilibrium state) [Muñoz-1].

Such possible phase transformations in a MCrAlY have a strong influence on the physical properties and thus, on the mechanical performance of the TBC system. Muñoz and Quadakkers [Muñoz-2] showed how specific phase transformations can dramatically increase the physical coefficient of thermal expansion (CTE) of the coating alloy, and hence, augment the thermal mismatch between BC and TGO. During their investigation they demonstrated that the addition of Co to a NiCrAlY-alloy can mitigate this detrimental effect.

Though not appearing in the ternary phase diagram, σ -(Co,Cr) and Ni-Y intermetallic phases are also often part of the coating microstructure [Achar, Beele]. The α -Cr phase forms if the solubility of Cr in γ -Ni is exceeded; the formation of σ -(Co,Cr) is induced by the presence of Co. An in-depth study on the phase relationships in MCrAlY-coatings as a function of temperature is presented in chapter 7.

2.2.2.2 Deposition methods of MCrAlY Bond Coats

The MCrAlY-coatings are generally deposited by thermal spraying processes: plasma spraying (PS) and high-velocity oxygen fuel (HVOF), and more seldom by electron-beam

physical vapor deposition (EB-PVD). In the plasma spraying process, a pre-alloyed powder is injected into a high-temperature plasma gas stream, and is then accelerated through a nozzle and sprayed at high velocity to the substrate's surface. The molten particles are deformed by the impact with the substrate spreading parallel over its surface where they rapidly solidify forming the coating. To achieve the final coating thickness multiple layers of deposition are necessary. Depending on the environment conditions during the deposition, this technique is classified in air plasma spraying (APS), low-pressure plasma spraying (LPPS) and vacuum plasma spraying (VPS). Best quality results regarding coating adherence, microstructure and impurity content are obtained with the VPS, carried out in vacuum chambers. Advantages such as high deposition rates and allowance for large component sizes have made this technique popular for MCrAlY bond coat deposition. Nevertheless, subsequent finishing operations can be required due to the rough surfaces produced and automated robotic equipment is necessary for complex geometrical surfaces with narrow passages such as turbine blades. This is because the method works with the "line-of-sight" principle; that is, the area of application has to be placed in the direct line of the spraying plume [DeMasi].

The more modern HVOF process allows the material deposition in solid (plastic) state rather than in molten state. Fuel and oxygen are fed into a chamber at high temperature (above 2000°C) in order to induce combustion and generate a hot, high pressure flame that is directed through a nozzle, reaching velocities of 2000 m/s. The material to be deposited is usually fed to the flame in the form of a powder, and transported to the substrate at high velocity by the flame. In contrast to plasma spraying, the powder material is not molten during HVOF-process; the cohesion between the sprayed particles is established due to their high kinetic energy. The final coatings are dense, with porosities around 1-2%, and present less residual stresses than those deposited by PS. The process efficiency can also be superior thanks to higher deposition rates, which can achieve around 60 g/min [Zhao]. One concern of this method is the relatively high amount of oxygen that is also incorporated in the coating, Zhao and Lugscheider found this values to be between 0.3 – 0.7 wt.-% [Zhao]. Taylor et al. reported that such high contents can tie up around 2 wt.-% of the available Al and also tend to oxidize Y [Taylor-2]. However, HVOF has the advantage of lower operation costs since the deposition takes place at atmospheric pressure. The EB-PVD process, more commonly used to deposit the ceramic topcoat is described in the next section.

2.3 Thermal barrier coating (TBC)

The considerable temperature insulation in a TBC system is achieved by a ceramic topcoat, thanks to its very low coefficient of thermal conductivity (CTC). The material currently used for the ceramic topcoat is yttria stabilized zirconia (YSZ). It possesses CTC values between 0.8-1.9 W/mK; thus, more than an order of magnitude below those of Ni-base superalloys, and also below those of many other ceramics [Peters]. Besides, this ceramic meets the important requirement of having a thermal expansion coefficient ($9 - 11.5 \times 10^{-6} \text{ K}^{-1}$; temperature dependent) close to that of the bond coat material ($12 - 20 \times 10^{-6} \text{ K}^{-1}$; temperature dependent), reducing therefore the internal stresses generated during thermal cycling due to the mismatch of the different coefficients of thermal expansion [Echsler-2].

However, pure zirconia is not thermodynamically stable in solid state (Fig. 2.7); with temperature changes, it undergoes dangerous phase transformations which can lead to cracking or physical damage. Particularly critical for the TBC applications, the transformation from the tetragonal phase into the monoclinic phase that occurs at around 1170°C can generate a volume increase of about 5% [Anton].



Fig. 2.7 – Phase transformations of pure zirconia

In order to stabilize zirconia in a wide temperature range suitable oxides can be added, among which yttria, included in concentrations around 6-8 wt.-%, has been found to be optimal for the application in TBC. This doped ceramic is characterized by good strength, fracture toughness and thermal cycling resistance; it also prevents chemical reaction with impurities such as vanadium and sodium sulfate. Additionally, the YSZ has a lower Young's modulus than pure Zirconia, what reduces the stresses induced by a high thermal expansion mismatch between TBC and TGO [Donachie].

Alternative ceramic materials for the next generation ceramic coatings have been sought in numerous investigations. Vassen et al. tested different zirconates as TBC and found lower thermal conductivity than in the YSZ and complying mechanical properties in the $\text{La}_2\text{Zr}_2\text{O}_7$ [Vassen]. Leckie and Levi showed how additions of $\text{GdO}_{1.5}$ to ZrO_2 in concentrations below 30% also offer reduced thermal conductivity and increased sintering resistance without compromising the stability of the system [Leckie]

2.3.1 Deposition methods of TBC

The ceramic topcoat is deposited mainly by APS and EB-PVD. In the EB-PVD process, the ceramic material to be coated is fed as solid rods in an evacuated chamber. Using a high energy electron beam, this material is heated up to temperatures around 5000°C, and evaporated. The vaporized material condenses onto the preheated component to be coated, which is rotating inside the chamber. Preheating the substrate element to temperatures above 600°C reduces the stresses that originate during the deposition [DeMasi]. In addition, the high temperatures guarantee dense coatings and good adhesion to the substrate by removing sulfur contaminants.

This deposition method produces a columnar structure which can be clearly distinguished from that of plasma sprayed coatings (Fig. 2.8). The existence of single columns of 5-15µm diameter, and respectively of inter-columnar gaps, significantly contributes to the strain compliance of the ceramic layer. As can be noted in Fig. 2.8, an important portion of the volume (10-20%) of an APS ceramic coating is composed by pores that reduce the thermal conductivity; in the case of EB-PVD coatings, microscopic porosity inside the columns serve this function [Clarke-1].

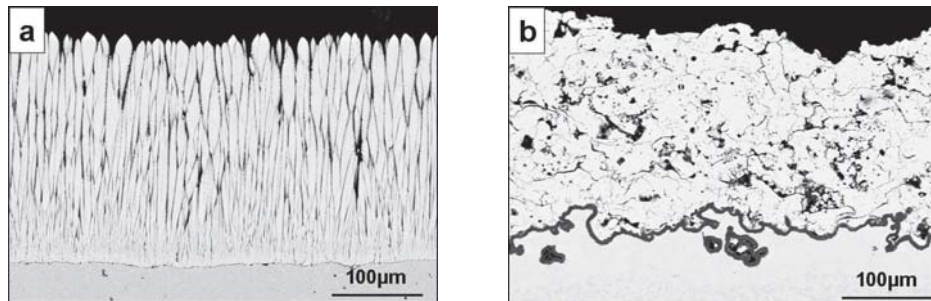


Fig. 2.8 – Overview of ceramic topcoats deposited by: a) EB-PVD, b) APS.

EB-PVD deposited coatings possess higher thermal shock resistance than APS coatings; they also offer smoother surfaces, which increase the resistance to erosion and diminish aerodynamic losses. The adhesive strength of an EB-PVD coating, reported to be around 400MPa, exceeds by far that of an APS coating, which lies between 20-40MPa (values at room temperature) [Nicholls-3]. Another recognized advantage is that the condensing material does not obstruct the cooling air channels during the deposition, contrary to the APS method, where subsequent laser drilling of the cooling ducts is required. Drawbacks of the

EB-PVD technique in comparison with the APS, are higher deposition costs and lower deposition rates [Singheiser-2]. In addition, the thermal conductivity of a vapor deposited topcoat is, with 1.5-1.9 W/mK, higher than that of a plasma spray coating (0.8-1.1 W/mK). Aiming to shorten this difference, Nicholls and Rickerby have proposed the intentional inclusion of atomic defects and thin sublayers with varying density in order to reduce the phonon conduction through the coating [Nicholls-3].

Not only thermal insulation and mechanical compliance are important requirements for the TBC, but also its chemical compatibility with the underlying bond coat and growing oxide. Braue et al. studied the early stages of TGO growth from the TBC deposition and found a mixed zone in which not only the desired protective Al_2O_3 forms, but also ZrO_2 , followed by Y-aluminates and spinels [Braue]

Failure of thermal barrier coatings in service can occur due to a severe physical interaction with solid particles contained in the combustion gases (foreign object damage and erosion), and also due to chemical degradation caused by deposits (e.g. V_2O_5) originally present in alternative or low-quality fuels, like heavy oil. However, for gas turbines operating in clean conditions the growth of the alumina scale at the TBC/BC interface has been shown to a common failure source. This aspect will be considered in detail in the next chapter.

3. Oxidation of MCrAlY-coatings

Due to its relevance for the stability of TBC systems, the oxidation behavior of MCrAlY-coatings has been intensively investigated in the last decades. It is in general considered in terms of the high temperature oxidation theory.

3.1 Oxidation Reaction

The oxidation reaction of a metal with the oxygen in the surrounding atmosphere leading to the formation of an oxide on its surface can be generally described as follows [Kofstad-1]:



The driving force for oxidation is the Gibbs free energy change (ΔG),

$$\Delta G = \Delta G_0 + RT * \ln \left(\frac{a_{M_xO_y}}{a_M^x pO_2^{y/2}} \right), \quad (3.2)$$

where,

ΔG_0 : Standard Gibbs free energy,

R: Gas constant,

T: Temperature,

α : Activity of the species,

pO_2 : Oxygen partial pressure

Under thermodynamic equilibrium $\Delta G = 0$. Thus, it follows from Eq. 3.2 that using the standard Gibbs free energy (ΔG_0), conditions can be determined for the stability of the oxide, depending on temperature and oxygen partial pressure of the atmosphere. These relationships for pure metal elements are visualized in the Ellingham-Richardson diagram (Fig. 3.1). The diagonal lines set out the conditions for the oxidation reaction of an element with its surrounding atmosphere to take place. As it can be observed, under ambient conditions all the elements presented in the diagram oxidize, while, at significantly lower oxygen partial pressures, only a few elements form oxides. For this reason, the latter elements form the most stable oxides; i.e. in the diagram, CaO is the most stable, followed by MgO and Al₂O₃.

However, the only elements which form protective scales are Cr, Al and Si [Meier] since their oxides (Cr_2O_3 , Al_2O_3 and SiO_2 , respectively) are slow-growing, dense, continuous layers, and thus, relevant to various engineering applications. As mentioned before, in TBC coated components the formation of an alumina scale provides the protection.

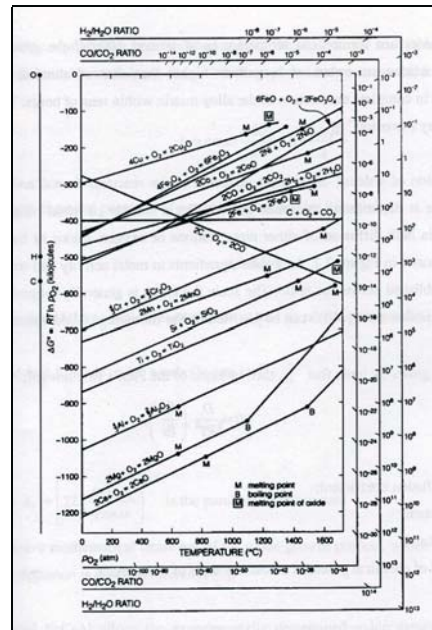


Fig. 3.1 – Ellingham-Richardson diagram showing the standard free energy of formation for selected oxides [Kofstad-1].

Since the MCrAlYs are alloys, their oxidation behavior is not as simple as that of pure elements. Theoretically any of its elements could oxidize if the conditions are favorable; however, the standard Gibbs free energy (ΔG_0) defines the O-affinity of every element (Table 3.1). It is appreciated in table 3.1 that Y has the highest O-affinity, followed by Al. In the case of an eventual depletion (total or local) of these elements, the oxidation of the other elements added in major concentrations can occur.

Y_2O_3	$\alpha\text{-Al}_2\text{O}_3$	Cr_2O_3	CoO	NiO
-1025	-844	-540	-294	-253

Table 3.1 – Standard Gibbs free energies of formation (in kJ per mol O_2) for the oxides formed by the elements added to MCrAlY-coatings calculated at 1100°C and 10^5 Pa [Nijdam-1]

3.1.1 Internal Oxidation

Internal oxidation of an element can occur if oxygen diffuses into the alloy, i.e. if the solubility and diffusivity of oxygen in the base metal(s) are high and the scale cannot prevent the dissolution of oxygen. This form of oxidation takes place if the element has a higher O-affinity than the base metal(s) and its concentration is lower than that required for external oxidation [Meier]. As a result, oxide precipitates will form in the sub-surface area. In the case of MCrAlY-coatings, the element in such low concentrations which can oxidize internally beneath the stable alumina scale due to inward oxygen diffusion is yttrium.

3.1.2 Scale formation

If an element with high O-affinity is present in larger concentrations, and in addition can rapidly diffuse to the surface before being internally oxidized, then external oxidation will take place. This is the case for Al in the MCrAlY-coatings. The growth of a protective α -Al₂O₃ on MCrAlY-coatings follows essentially a parabolic or sub-parabolic law [Anton, Echsler-2]:

$$h = k_p t^n; n \leq 0,5 \quad (3.3)$$

where,

h: scale thickness

t: time

k_p: rate coefficient

Once a continuous oxide layer has formed, the direct metal-gas contact is lost, and the oxidation continues due to diffusion of reactant ions through the oxide. Wagner developed a theory of oxide growth, in terms of diffusion of these species and their driving forces (Fig. 3.2). In his model, thermodynamic equilibrium is assumed to exist at both the gas/oxide and oxide/metal interfaces, generating opposite activity gradients for both the metal and the oxygen that cause in turn, a diffusion of metal cations and oxygen anions in opposite directions. The mobility of these charged ions establishes an electric potential gradient as well, which allows the migration of electrons [Meier]. In real oxide scales, not only the lattice diffusion of reactants but also the grain boundary and short-circuit path diffusion (voids, pores, microchannels) determine the kinetics of oxidation. The following section describes the formation of the oxide scale on an MCrAlY-coating.

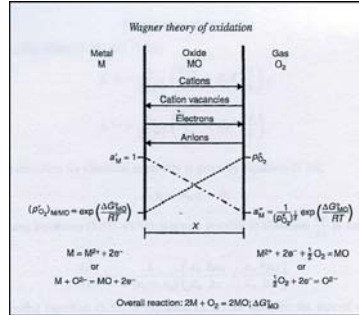


Fig. 3.2 – Wagner theory of oxidation; diffusion of reactant ions.

3.2 Formation of the thermally grown oxide (TGO) in TBC systems

3.2.1 Transient oxidation stages

Prior to the formation of the protective Al₂O₃ scale, other components of the MCrAlY alloy can oxidize even during the pre-treatment and TBC deposition stages, being the starting point of a heterogeneous TGO. Yttrium oxide possesses a lower free energy of formation than aluminum oxide (Table 3.1); hence, if the diffusion of Y to the surface is enabled, yttria is the most stable oxide that can form in a MCrAlY coating. Its formation can take place at the coating surface even during vacuum pre-treatments at very low oxygen partial pressures, as was reported by [Braue] during investigations on NiCoCrAlY-coatings.

Yttrium is commonly added to MCrAlY bond coats in lower concentrations than those required to form an external yttria layer. If at the same time, the alloy and the atmosphere present favorable conditions for fast inward oxygen diffusion (faster than the outward Y diffusion from the bulk), it will oxidize internally below the oxide/metal interface [Douglass, Meier], as explained previously. Nijdam et al. proved this statement after obtaining deeper internal oxidation of yttrium in specimens exposed in an atmosphere with pO₂=100Pa than when exposed in a lower pO₂ atmosphere (pO₂=0.1Pa). They noted however, that the presence of a native oxide that retards the inward flux of oxygen can suppress the internal oxidation [Nijdam-2].

Also the major alloying elements Ni, Co and Cr can oxidize together with Al, especially during the initial stages of high-temperature exposure in air. The reason is, that prior to the formation of a protective scale, the alloy is fully exposed to the atmosphere and all

elements can react with oxygen [Kofstad-1]. As a consequence of these reactions, Ni/Co-oxide rich spinels form and become part of the TGO. The growth of less protective (Ni,Co,Cr)-based oxide compounds was observed by [Braue] and [Levi] even after TBC deposition by EB-PVD, prior to air exposure.

Not only other oxides, but also metastable phases of aluminum oxide can grow during the transient stages of oxidation. The most common of these are γ -Al₂O₃ and θ -Al₂O₃. While the γ metastable phase generally forms below 900-950°C and transforms to α -Al₂O₃ on heating, without the risk of a reverse transformation on cooling [Kofstad-1], the θ phase formation can occur at temperatures above 1000°C. Increase of temperature and time will promote its transformation to the stable α phase, which is generally associated with volume shrinkage and a reduction of growth stresses [Sohn].

The formation of a heterogeneous TGO can also be influenced by the microstructure of the coating. Quadakkers et al. showed that if the phases of the coating prevail as coarse grains, the oxide grown on γ -Ni can differ from that grown on β -NiAl. They reported a large presence of Ni and Cr impurities together with α -Al₂O₃ on γ -Ni and comparably less of such impurities together with θ -Al₂O₃ on β -NiAl upon exposure in air at 1000°C [Quadakkers-2]. Similarly, Nijdam et al. correlated the formation of non-protective oxides on a NiCoCrAlY-coating after 1h of exposure in air at 1100°C to the phase where they are grown at: They detected NiCr₂O₄ and Cr₂O₃ over the Al-poor γ -phase, and NiAl₂O₄ on the Al-rich β -phase [Nijdam-2]. Nevertheless, these authors indicated that when exposed in lower pO₂ atmospheres, the formation of oxide spinels is suppressed due to a reduced oxygen activity at the oxide/metal interface, a lower oxide growth rate and the exclusive formation of the Al-rich β -phase on the alloy surface.

3.2.2 Scale formation on MCrAl-alloys

After the transient oxidation stages, the growth of the protective scale is expected to dominate (α -Al₂O₃ for the MCrAlY-coatings). In the case of undoped alumina-forming FeCrAl, it was shown by using two-stage oxidation experiments in O-isotopes followed by secondary-ion mass spectroscopy (SIMS) depth profiling, that the scale growth mechanism consists on a combined outward-cation and inward-anion transport [Quadakkers-5].

However, the alloys where this scale growth mechanism prevails are known to exhibit poor scale adherence.

3.2.3 Effect of reactive elements on the scale formation on MCrAlY-coatings

In order to improve the oxidation behavior and in particular scale adherence, reactive elements (most commonly yttrium) are added to the alumina-forming materials [Czyrska, Huntz]. Several mechanisms have been proposed to explain this positive effect, as reviewed by Sariouglu and Meier [Sariouglu]:

- Suppression of void formation at the metal/oxide interface
- Segregation to the metal/oxide interface to strengthen the bond
- Change of the scale growth mechanism to inward growth
- Binding of sulfur before it reaches the metal/oxide interface.

The latter two have at the moment the most extensive experimental support. Nevertheless, Quadakkers et al. showed how sensitive the Y-effect can be to Y-concentration: optimum oxidation and improved adherence can be obtained by low concentrations of Y in the coating (around 0.1wt-%), whereas a few tenths of a weight percent more (over 0.5wt-%) can lead to accelerated oxidation and detrimental oxide morphology [Quadakkers-3]. With this cognition it would be expected that only minor amounts of Y are required in the coating. However, such low concentrations can be tied up by the oxygen impurities resulting from the plasma spray deposition, constraining its beneficial effect [Quadakkers-2]. In order to avoid this risk, commercial bond coat alloys contain higher RE-concentrations than the optimal from the standpoint of scale growth rate.

There is sufficient experimental evidence on to which extent little variations of Y-concentration can affect the high temperature performance of the BC. For example, Stecura conducted cyclic oxidation tests with TBC specimens having variations in BC chemical composition; the TBC lifetimes on specimens with BC doped with 0.5%Y (wt-%) were 4 to 5 times higher than similar specimens with 1.5%Y in the BC [Stecura].

One common feature of the oxide morphology in BC with high Y-concentrations is the formation of Y-rich compounds near or at the metal/oxide interface (see Fig. 3.3), which are known in the literature as “pegs”. The coefficient of diffusion of oxygen in Y_2O_3 is with $2.2 \times$

10^{-11} cm²/s considerably higher than in Al₂O₃, where it amounts to 1×10^{-17} cm²/s (data measured at 700°C) [Ryan]. Therefore, the presence of Y-rich oxides in the alumina scale is associated with locally accelerated oxidation along these Y-compounds which appear intruding in the coating alloy. Regarding the mechanical implications of this morphology in the system there is no definite agreement. Zhu and Evans proved, with a series of experiments and a model that the plastic strains that accumulate near a peg are not large enough to overcome the interface toughness and concluded that the presence of pegs rather reinforces the adherence by impeding the propagation of delamination cracks at the mentioned interface [Zhu]. In contrast, Mumm et al. believe these thickness heterogeneities set up, while growing, normal stresses of sufficient magnitude to induce scale separation [Mumm].

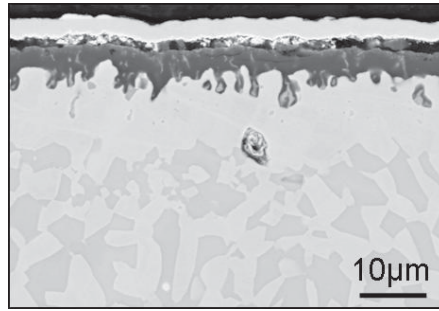


Fig. 3.3 – Oxide scale of a NiCoCrAlY-coating exhibiting Y-pegs after 110h of exposure in air at 1100°C

The above mentioned pegs refer to Y-aluminates resulting from the reaction of Y₂O₃ (formed during early oxidation stages) with Al after its incorporation into the alumina scale. Depending on the amount of Al reacting, yttria transforms to the perovskite phase YAlO₃ (YAP) or to the garnet phase YAl₅O₁₂ (YAG). The monoclinic phase Y₄Al₂O₉ (YAM) is generally not observed in the TGO of MCrAlY bond coats.

3.2.4 Effect of pre-treatment procedures on BC oxidation and TBC lifetime

Some investigations have demonstrated that the formation of the protective oxide scale and of transient oxides can be affected by different pre-treatment procedures. For instance, laser melting of the surface of NiCrAlY-alloys led to the formation, upon high-temperature exposure, of denser, thinner oxide scales with less Y-oxide compounds than those formed on as-annealed alloys without laser melting. In the latter case, the oxide scale contained a porous top layer and numerous Y-rich compounds at the interface oxide-metal [Smeggil].

Nijdam and Sloof attributed such effects in similar experiments using laser surface melting (LSM), to a microstructure refinement with reduced β -phase particle size. On the coatings subjected to LSM, the oxide formed was uniform in thickness and homogeneous in composition while that formed on the original cast coating-alloy exhibited thickness heterogeneities and mixed oxides [Nijdam-2].

Oxide growth rate and adherence are two factors determining the protectiveness of alumina scales. Poor scale adherence is detrimental in overlay coatings, since the scale forming element Al, is consumed faster for scale rehealing. In the case of MCrAlY bond coats poor scale adherence results in earlier failure of the TBC. The scale growth rate is important since the oxide spallation is believed to occur upon reaching a critical thickness [Yanar-1]. In the next section, different factors believed to lead to the loss of adherence of the alumina scale on MCrAlY bond coats will be presented. In addition parameters not related to high temperature oxidation which can also be crucial for TBC lifetime are also considered.

3.3 Failure mechanisms of coating systems

Failure in a TBC system refers to the loss of one or more of its components. The most observed failure case is, by far, the spallation of the ceramic coating, after which the thermal insulation is lost and the bond coat is directly exposed to the high temperature gases.

3.3.1 Failure mechanisms not related to MCrAlY-oxidation

The thermal barrier coating of gas turbine blades is vulnerable to the impact of solid particles coming from the combustion chamber; this phenomenon, known by the turbine manufacturers as foreign object damage (FOD), can lead to erosion and in the worst case to spallation of the TBC. Fig 3.4 shows how the impact produces cracks which can end up in delamination of the ceramic layer. Several studies have dealt with the extent of this damage though no relevant solution has yet been proposed; among them, Wellman and Nicholls modeled the relationship between impact angle and velocity with the erosion rate [Wellman] and Watanabe and Evans described the forces necessary to break or deform the individual columnar structure of EB-PVD coatings [Watanabe].

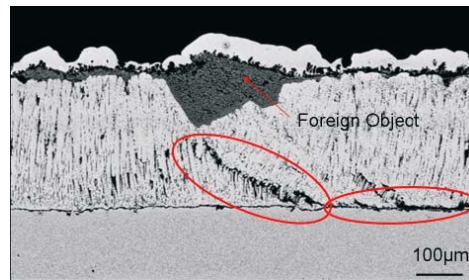


Fig. 3.4 – Illustration of foreign object damage in a gas turbine blade.

During exposure at high temperatures, sintering of the ceramic coating can occur, leading to an increase of its elastic modulus, and thus to an increase of the thermal mismatch with the underlying alloy. The detrimental stresses developed for this reason can lead to coating failure, due to the loss in strain compliance. This densification process also increases the thermal conductivity of the TBC due to the reduction of porosity [Clarke-1].

Serious consequences for the stability of the system can also have the interaction between bond coat and substrate. Anton et al. showed that formation of brittle carbides at the interface bond coat/substrate can occur causing extensive cracking along this interface. In their experiments, exposures in air over 1000h at 900°C actually provoked BC separation from the substrate [Anton]. Not only the formation of new brittle phases at this interface but also pronounced porosity (Kirkendall pores) and considerable loss of Al can be the result of element interdiffusion, driven by the chemical incompatibility of bond coat and substrate. Moreover, Schulz et al. found that the substrate may have a direct influence on the TBC lifetime if the same bond coat is applied [Schulz].

3.3.2 Failure mechanisms related to MCrAlY-oxidation

The end of the protective oxidation is in principle demarked by complete Al depletion of the coating. After the Al reservoir in the alloy is reduced considerably, the conditions are favorable for the oxidation of other major alloying elements, leading to the formation of less protective scales. However, the Al-reservoir of a MCrAlY-coating is large enough and, therefore, the Al supply can be guaranteed for relatively long times at high temperatures. Scale spallation generally takes place before this critical Al depletion is reached [Stott], and this scale separation occurs primarily at the oxide/metal interface in case of EB-PVD TBC [Clarke-1]. Thus, in such a TBC system, where the ceramic coating is adhered to the oxide

scale, this spallation represents already the irreversible failure of the system. Although not yet well understood, several theoretical approaches to the failure modes and conditions have been developed intending to explain how the scale adherence is lost.

It is well established that stresses originated in the oxide (from its growth and the thermal expansion mismatch with the underlying coating) often represent the driving force for failure in TBC systems, since they are relieved by deformation or cracking [Clarke-2]. The magnitudes of the stresses in the TGO depend on multiple parameters like temperature and exposure conditions, cooling rates, BC chemical composition and scale thickness.

It has been suggested in the literature [Kim, Tolpygo-1] that in TBC systems with NiPtAl-bond coats, the TGO will tend to spall when a critical thickness is reached; the determined values fluctuate between 5-7 μm . It was though emphasized that these values are predicted for systems with EB-PVD coatings, where the oxide scales grown are more homogeneous in thickness and remain relatively flat during high temperature exposure. For TBC systems with MCrAlY bond coats precise values have not been reported.

Oxide/metal interfaces, where the spallation usually takes place in systems with EB-PVD coatings, are inherently tough (toughness values over 200 Jm^{-2}) and ductile to resist high stresses if they are free of imperfections and impurities. However, Evans et al. reported that these values can decrease by a factor of 10 in the presence of contaminants, such as sulphur [EvansA-2]. Sergio and Clarke added that the existence of moisture can also weaken this interface and favor crack propagation [Sergo]. Gell and Jordan concluded during lifetime tests that the bond strength between oxide and BC decreases slowly even during early oxidation stages and more rapidly as the failure is approached. This drop in strength was attributed mainly to interdiffusion and oxide degradation [Gell-1]

On a weakened flat interface (systems with EB-PVD coatings), the preferential starting points for the initiation of failure are interfacial imperfections like undulations and scale thickness heterogeneities [Quadackers-2]. The sequence of events leading to TBC failure are divided in: crack nucleation at the TGO imperfections (where the misfit stresses induce a higher strain energy release rate), crack propagation along the weakest pathway and finally, coalescence of cracks reaching a sufficient area for detachment [EvansA-2].

Yanar and Meier showed how failure can also occur at the TBC/TGO interface if the adherence at this point is degraded by the growth of NiCr-rich spinels [Yanar-1]. Such mixed oxides can form in an atmosphere with high oxygen partial pressure before Al has been significantly depleted in the bond coat; for example, in plasma sprayed coatings exhibiting deposition defects such as splat boundaries, which tend to oxidize and thus locally exhaust the Al reservoir [EvansH-2]

Surface pre-treatment procedures applied on the bond coat can also influence the TBC lifetime, as shown by Yanar and Meier [Yanar-2]. They conducted oxidation experiments on systems with diffusion aluminide bond coats and EB-PVD TBC, in which the BC surface was selectively subjected to grit-blasting (heavy: 8grit (2mm) / light: 220 grit (700µm)), surface smoothening or simply kept in its original as-deposited form before ceramic topcoat deposition. It was found out that, despite scattering in lifetimes after high-temperature exposure, the specimens with light grit-blasted surfaces exhibited 1.5 – 2 times longer lifetimes than those with heavy grit-blasted and as-deposited surfaces. A pre-oxidation further improved these times.

4. Purpose of this investigation

Not only economic but also environmental reasons strive for an increase of the operating efficiency of gas turbines in power generation. The allowance for higher combustion and turbine inlet temperatures associated with increased efficiencies has to be provided by the TBC-coated materials of the hot sections (combustion chamber, vanes and blades of the turbine's first row)

Under normal operating conditions the failure of the TBC systems is related to the growth and adherence of the alumina scale (TGO). In this matter, many authors have reported for systems with PtAl bond coats a critical TGO thickness beyond which the adherence to the bond coat is lost. However, for TBC systems with MCrAlY bond coats, no precise estimations have been proposed so far. Nevertheless it is known that generally a thick scale is more prone to spallation than a thin one. If a critical TGO thickness to TBC failure exists for systems with MCrAlY bond coats, and this can be reliably predicted, gas turbine designers and operators can maximize the use of this turbomachine, by establishing adequate times for general inspection and blade refurbishing. However this would presuppose as well that the TGO thickening and adherence is predictable and reproducible.

The first major purpose of this work is to determine the effect of the bond coat composition on the lifetime of EB-PVD TBC systems. For this purpose, three compositions similar to that of commercial MCrAlY bond coats were studied. After lifetime tests on TBC coated specimens containing the bond coats in question, new specimen types (overlay coatings and free-standing coatings) were produced to isolate the influence of the ceramic topcoat and of the substrate and so, better understand the oxidation behavior of the coating alloys under isothermal, discontinuous and cyclic conditions in air at high temperatures.

Subsequently, microstructural studies of the MCrAlY-coatings were conducted over a wide temperature range covering both typical service temperatures in turbines and laboratory testing temperatures. The results of these studies were compared with the observations on analyzed blades after service.

The second major purpose of this work is to determine which parameters have a decisive influence on the oxide adherence in MCrAlY-coatings, independent of its chemical

composition. The parameters considered are separated in geometrical parameters and pre-treatment/processing parameters. More precisely, the former refer to MCrAlY surface roughness and coating thickness; the second category of parameters includes processing sequence, heat treatment conditions and oxygen impurities content. After a variation of these parameters (whereby it is tried to be done separately) follows an insight study of the implications for oxide growth rate, morphology and adherence.

Finally, the investigation deals with the issue of determining a critical TGO thickness to TBC failure in systems with MCrAlY-coatings. In these studies a parameter that would cause a different TGO growth rate, without changing the composition, morphology and mechanical properties of the oxide produced is sought. All other parameters not complying with these conditions have to be excluded.

5. Experimental Procedure

5.1 Materials

The specimens investigated in this study can be divided into three groups according to the materials they are composed of (Fig. 5.1):

- TBC specimens: composed of superalloy substrate, bond coat and thermal barrier coating.
- Overlay coatings: composed of superalloy substrate and bond coat.
- Free-standing coatings: composed of only the bond coat.



Fig 5.1 – Specimen types prepared for the study.

All the TBC specimens and overlay coatings of this study contained the IN738 LC as a substrate; its nominal chemical composition is shown in Table 2.1. The thermal barrier coating employed in all TBC specimens was yttria stabilized zirconia (YSZ: $\text{ZrO}_2 + 7\text{-}8 \text{ wt.-% } \text{Y}_2\text{O}_3$) and was deposited mainly by EB-PVD. Only for comparison purposes APS deposited topcoats are analyzed in chapter 10.

Three different commercial MCrAlY-type bond coats were used in this study, they are identified as: NiCoCrAlY(hi-Al), NiCoCrAlY(lo-Al) and CoNiCrAlY. The NiCoCrAlY(lo-Al) was produced by two different deposition techniques, VPS and HVOF. The chemical compositions determined after chemical analysis by inductively coupled plasma optical emission spectrometry (ICP-OES) are presented in table 5.1.

Bond Coat	Ni	Co	Cr	Al	Y	Re
NiCoCrAlY(hi-Al)	base	< 15	> 20	11	0.38	1.70
NiCoCrAlY(lo-Al) [VPS]	base	> 20	< 20	10	0.27	1.50
NiCoCrAlY(lo-Al) [HVOF]	base	> 20	< 20	10	0.22	1.50
CoNiCrAlY	> 25	base	> 20	10	0.60	-

Table 5.1 – Chemical composition of studied bond coats (in wt.-%).

The minor impurities were detected with infrared spectrometry and thermal conductivity measurements; the values reported for the different materials are shown in table 5.2

Bond Coat	C	S	N	O
NiCoCrAlY(hi-Al)	120	< 5	80	510
NiCoCrAlY(lo-Al) [VPS]	20	< 5	20	440
NiCoCrAlY(lo-Al) [HVOF]	210	< 5	60	2400
CoNiCrAlY	40	< 5	40	730

Table 5.2 – Minor impurities present in studied bond coats (in wt.-ppm).

5.2 Specimen types

The different batches of specimens prepared for this study are described in Table 5.2:

Batch	Specimen Type	Geometry	Dimensions (mm)	BC Thickness	BC Material
KHZ	TBC specimen	cylindrical	25 x Ø10	200 µm	NiCoCrAlY(lo-Al)
KUM	TBC specimen	rectangular	20 x 20 x 4	200 µm	NiCoCrAlY(hi-Al)
KUN	TBC specimen	rectangular	20 x 20 x 4	200 µm	CoNiCrAlY
KUK	Overlay	rectangular	10 x 10 x 4	200 µm	NiCoCrAlY(hi-Al)
KUL	Overlay	rectangular	10 x 10 x 4	200 µm	CoNiCrAlY
LPL	Free-standing	rectangular	10 x 10 x 2	2 mm *	NiCoCrAlY(hi-Al)
LPP	Free-standing	rectangular	10 x 10 x 2	2 mm *	CoNiCrAlY
LPM	Free-standing	rectangular	10 x 10 x 2	2 mm *	NiCoCrAlY(lo-Al)
LZG	Free-standing	rectangular	10 x 10 x 2	2 mm *	NiCoCrAlY(lo-Al)

* 2mm refers to the original specimen thickness, for some experiments this thickness was reduced.

Table 5.3 – Specimens prepared for the various investigations.

The Bond Coats in all batches were produced with vacuum plasma spraying (VPS), with the exception the LZG bond coat, which was deposited with high velocity oxygen fuel spaying (HVOF).

5.3 Specimen preparation

5.3.1 Free-standing coatings

A 3 mm thick MCrAlY layer was deposited (by VPS or HVOF, depending on the batch) on a steel plate, and thereafter removed from the substrate using spark erosion. The eroded plate was cut into 10 x 10 mm specimens which were ground down to 2 mm thickness on the bottom side to remove contamination originated from the erosion process; the surface finish was given with a 1200 grit SiC, so that at the end these specimens had a rough, as sprayed surface on the top and a ground surface on the bottom. On part of the specimens, for thermogravimetric measurements and cyclic oxidation, the rough side was given the same surface finish and a Ø2mm hole was drilled for the sample to be hung. Finally, the specimens were subjected to high temperature heat-treatment in vacuum (10^{-5} mbar) or in an oxidizing atmosphere.

5.3.2 Overlay coatings

3.5 mm thick IN738LC plates were coated by vacuum plasma spraying (VPS) with a 200 µm layer of a MCrAlY-coating and subsequently subjected to a two-stage vacuum annealing according to specifications for IN738 (2h at 1100°C and 24h at 845°C). Finally, 10 x 10 mm specimens were cut from the plate with a low speed saw.

5.3.3 TBC specimens

The initial production steps were identical to those of the overlay coatings. Following the vacuum annealing, the rough bond coat surfaces were smoothened by cut wire peening and subsequently coated with a 300 µm thick YSZ top layer using EB-PVD. Depending on the geometry, 20 x 20 mm or 25 x Ø10 specimens (see Table 5.3) were cut from the coated plate with a low speed saw.

All specimens were ultrasonically cleaned in acetone and ethanol before oxidation.

5.4 Oxidation Experiments

Three different types of oxidation tests were carried out with the above mentioned specimens:

5.4.1 Isothermal and discontinuous oxidation

Performed in laboratory air at temperatures between 700°C and 1100°C. The exposure interruptions in the discontinuous mode had as purpose the specimen observation in order to determine the time to oxide and TBC spallation. In some specimens these interruptions were used to measure the stress in the TGO with fluorescence piezospectroscopy.

5.4.2 Cyclic oxidation

Performed in laboratory air and Ar-4% H_2 -2% H_2O atmospheres at 1100°C. The standard cycling comprises a high temperature stage of 2h and a cooling stage of 15min. In some experiments a longer cycle of 4h at high temperature and 1h cooling was programmed. The TBC specimens used for lifetime tests were inspected every 36h (total testing time) in order to detect ceramic failure. Cycled free-standing specimens were weighed every 18h (total testing time) in order to calculate the evolution of mass change.

5.4.3 Thermogravimetric measurements (TG)

Carried out for 72h in synthetic air at 1000°C, 1050°C and 1100°C using a thermo balance as described in [Grabke]. The oxidation kinetics of the different MCrAlY-coatings was determined by deriving an instantaneous oxide growth rate constant, $k_p(t)$, from the measured data as indicated in [Naumenko-3]. Each $k_p(t)$ point represents a time interval of approximately 14 minutes.

5.5 Measurement of physical CTE on free-standing MCrAlYs

The coefficients of thermal expansion (CTE) were measured by heating rectangular free-standing MCrAlYs with dimensions 10 x 10 x 2 mm in argon from room temperature to 1100°C using a Netzsch DIL402E dilatometer as described in [Muñoz-2].

5.6 Metallographic preparation

For the cross section analysis, the oxidized specimens were cleaned with acetone and ethanol and mounted on an epoxy resin. A series of grinding and polishing steps followed, finishing with a fine polishing of 0.25 μm granulation in a SiO_2 solution. In order to obtain a better contrast between the oxide scale and the epoxy mass and to protect the oxide scale during preparation, a Ni-coating was added electrochemically to the specimens in a NiSO_4 bath previous to the mounting.

5.7 Analysis Techniques

Cross section micrographs of the specimens were obtained with optical microscopy and scanning electron microscopy (SEM). The chemical analysis in SEM was performed mainly with energy dispersive X-ray analysis (EDX) and wavelength dispersive X-ray spectroscopy (WDX). X-ray diffraction (XRD) and transmission electron microscopy (TEM) were used for selected samples when EDX did not allow unequivocal analysis of the various phases. The working principles of these techniques can be found in reference [Rahmel]. Secondary neutrals mass spectrometry (SNMS) was used to measure elemental depth profiles as explained elsewhere [Quadackers-4]. Cathodoluminescence (CL) was utilized to better detect Y-rich compounds, based on their properties described in [D'Silva]. Fluorescence piezospectroscopy was employed to estimate TGO stresses following the procedures presented in [Gell-2], and to detect metastable alumina phases as asserted in other works [Tolpygo-2]. This technique is rather used for local stress measurements: typical laser penetration depths in the TGO are between 1-2 μm , and surface areas covered can vary from 2 μm to 20 μm diameter depending on the optical objective used [Bennett, Selcuk]. The stress values reported using this method refer to hydrostatic loading, hence they are dimensionless. Their calculation is possible by using a piezospectroscopy coefficient tensor:

$$\Delta\nu = \Pi * \sigma \quad (5.1)$$

where,

$\Delta\nu$: wavenumber shift of the luminescence spectrum peak if oxide is under stress

Π : piezospectroscopy coefficient tensor (composed by the sum of uniaxial stress coefficients; found to be equal to 7.61 $\text{cm}^{-1}/\text{GPa}$ by He and Clarke after measurements in polycrystalline $\alpha\text{-Al}_2\text{O}_3$ [HeJ])

σ : stress in the oxide

6. Effect of the Bond Coat chemical composition on the oxide growth and adherence

6.1 Oxidation studies on TBC systems with MCrAlY-coatings

The influence of the bond coat chemical composition on the TGO formation and topcoat adherence was investigated in TBC specimens exposed discontinuously in air at 1100°C. For this experiment, TBC specimens with NiCoCrAlY(hi-Al) and CoNiCrAlY bond coats were selected. Previous to the ceramic deposition, the samples were subjected to a two-stage vacuum heat treatment: 2h at 1100°C and 24h at 845°C. The oxidation was interrupted after regular time intervals to carry out TGO stress measurements; during these interruptions the samples were cooled down by direct exposure in air at room temperature. For TGO assessment, specimens of both batches were analyzed after 16h, 110h and 406h (see Fig. 6.4); other specimens were exposed until macroscopic TBC failure occurred (see Fig. 6.1).

6.1.1 Lifetime of TBC systems

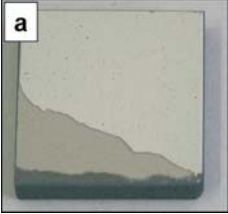
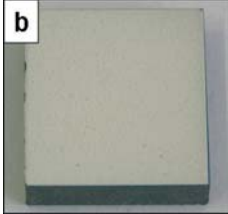
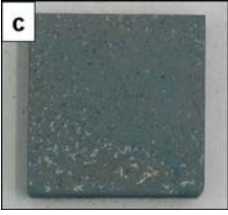
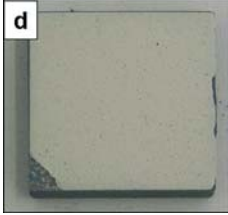

	BC: NiCoCrAlY(hi-Al)	BC: CoNiCrAlY
560h		
950h		
1230h		

Fig 6.1 – Evolution in time of TBC condition on specimens after discontinuous oxidation in air at 1100°C.

As can be observed in Fig. 6.1, the TBC specimen with the CoNiCrAlY-coating exhibited a longer lifetime than that with a NiCoCrAlY(hi-Al)-coating. On the latter, partial TBC spallation was observed after 560h of exposure (Fig. 6.1a) and complete failure after 740h (Fig. 6.1c). On the specimen with the Co-base coating, the TBC remained adherent until 1230h of exposure (Fig. 6.1e). The spallation of only a small portion on a corner of this sample after 950h, observed in Fig 6.1d, was not judged as complete TBC failure.

6.1.2 TGO stress measurements in TBC systems

Fig. 6.2 shows the residual stresses measured with fluorescence spectroscopy in the TGO beneath the TBC on both batches during the discontinuous oxidation tests at 1100°C. In both coating systems high compressive stresses in the TGO were measured, the values are higher in the system with the CoNiCrAlY bond coat. Also the tendency of the stress values to change with time had an apparent difference. In the system with the Co-base BC after 400h the stresses continuously increased with time until an average value of nearly 6GPa was reached. In contrast, in the system with the Ni-base coating the residual stresses were at a constant level, slightly above 3GPa during almost all its lifetime. The measured lower residual stress in the TGO with the NiCoCrAlY-bondcoat apparently indicates a worse TGO-adhesion and can be correlated with the shorter time to TBC-failure.

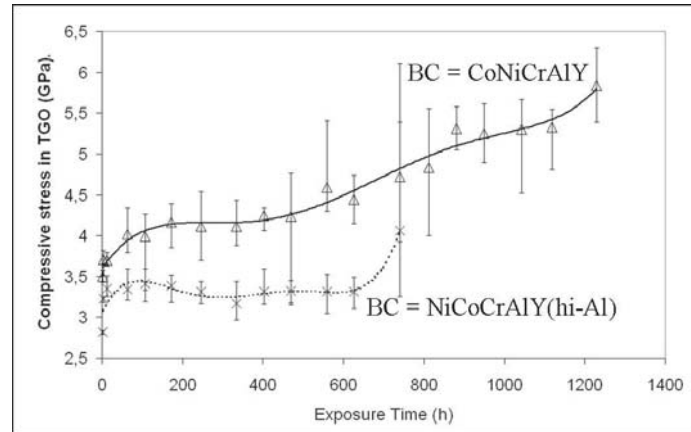


Fig 6.2 – TGO stresses in TBC specimens measured during discontinuous oxidation in air at 1100°C.

This idea is supported by the residual oxide stress measurements in the specimens with partially spalled TBC. These measurements clearly indicate that in many areas beneath

macroscopically intact TBC-ceramic the scale stress was relaxed, presumably through cracking or local delamination. In Fig. 6.3 it can be seen on a partially failed sample, that the stress values in locations very near to the spalled area (in red) are considerably lower than elsewhere (in black). The low values registered in the area of exposed bond coat (in white) indicate an almost total stress relaxation after the spallation.

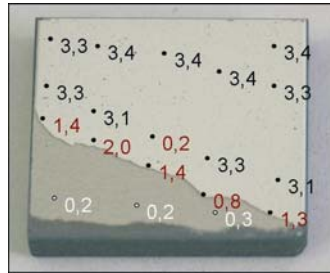


Fig 6.3 – Residual TGO stresses (in GPa) in different locations in the TBC system with NiCoCrAlY(hi-Al) BC after 560h of exposure in air at 1100°C.

6.1.3 TGO growth and morphology in TBC systems

Fig. 6.4 shows the cross-section of the specimens oxidized for different times prior to TBC failure for microstructural studies. The scale growth in both TBC systems did not exhibit significant differences (Fig. 6.4). In the system with the Ni-base bond coat, the average TGO thickness (measured from the SEM images) was 1.4 μ m after 16h and 3.8 μ m after 406h. Similar values were registered in the system with Co-base BC, 1.3 μ m after 16h and 4.1 μ m after 406h.

Despite the similarities in TGO thickness, an interesting observation is, that the oxide on the NiCoCrAlY coating consists of “purer” alumina than that on the Co-base BC; the latter exhibits a minor amount of stringer-like Y/Al-oxide precipitates in the TGO. It is important to note that, after 406h of high-temperature exposure, the oxide scale has detached from the Ni-base bond coat while the scale grown on the Co-base is still adhering. Although this separation occurred during sample preparation due to the forces exerted by the hardening epoxy resin, it is an indication of a weaker interfacial adhesion in the system with the Ni-base bond coat.

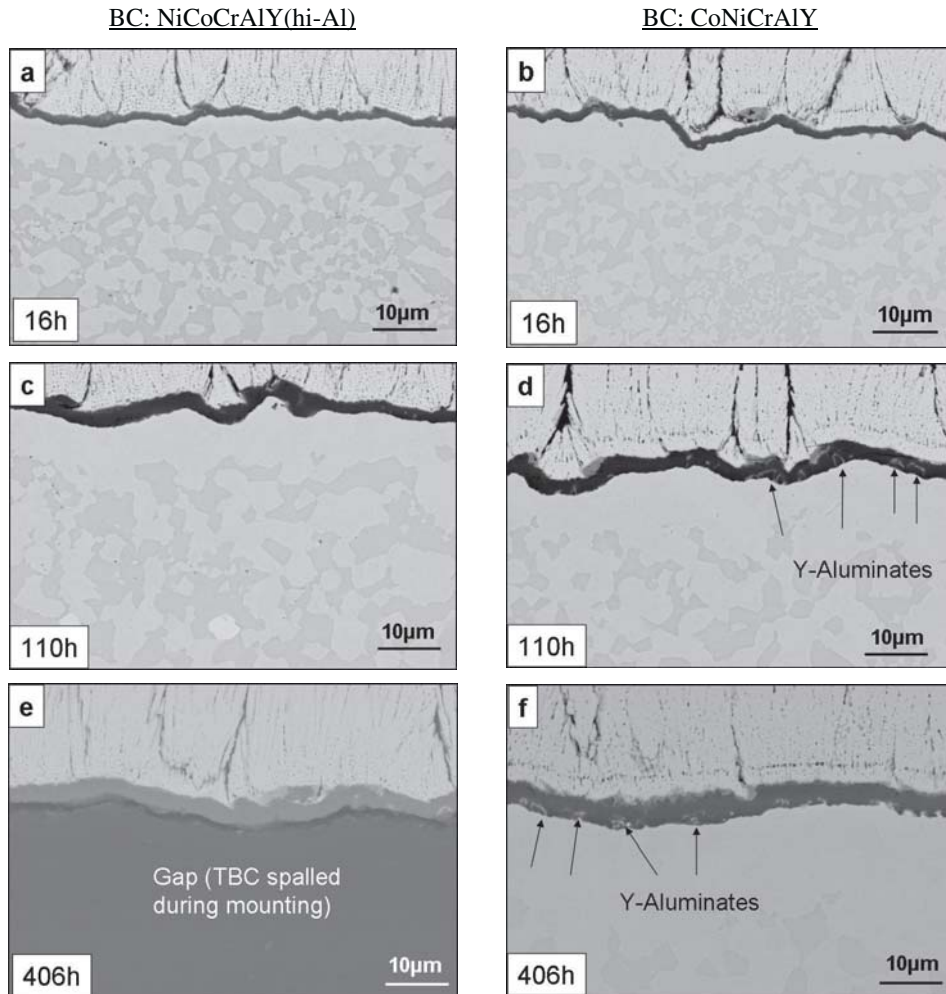


Fig 6.4 – SEM micrographs of TBC specimens containing NiCoCrAlY(hi-Al) BC after a) 16h, c) 110h e) 406h and CoNiCrAlY BC after b) 16h, d) 110h f) 406h of discontinuous oxidation in air at 1100°C.

After these observations a question arose whether the differences in TBC lifetime can be solely attributed to the MCrAlY-oxidation or to a better mechanical and chemical compatibility of the CoNiCrAlY-coating to the properties of the ceramic topcoat and the superalloy. In order to answer this question, similar tests as described above were conducted on overlay- and free-standings coatings. The corresponding results are presented in the following sections 6.2 and 6.3.

6.2 Oxidation studies on overlay MCrAlY-coatings

The overlay coatings were produced to separate the effects of the thermal barrier coating on the oxidation behavior of the MCrAlY-coatings. After VPS-coating, these samples were subjected to the same heat treatment as the TBC samples (2h at 1100°C and 24h at 845°C). The exposure conditions of these specimens were identical to those of the TBC specimens described in the previous section, i.e. discontinuous oxidation in air at 1100°C. Cross-sections of the analyzed samples are presented in Fig. 6.5.

6.2.1 TGO growth and morphology in overlay coatings with as-sprayed surfaces

It can be observed in Fig. 6.5 that compared to the TBC specimens substantial spinel formation took place on the overlay coatings. The tendency to form these (Cr,Co)-rich mixed oxides is, more noticeable on the Co-base coating due to its significantly higher cobalt concentration. Rather than a continuous top layer above the alumina, such spinels seem to grow rapidly only in some parts of the coating surface (see Fig. 6.5f).

By measuring the thickness of the alumina scale (excluding the contribution of the mixed oxides), it is found that with 2.9µm after 16h and 5µm after 406h for the overlay with NiCoCrAlY(hi-Al) and 2.8µm after 16h and 6.5µm after 406h for the overlay with CoNiCrAlY. Therefore, the scale growth is slightly faster on the overlay coatings than on the TBC specimens.

Since local TGO spallation often occurred (Fig. 6.5), especially on the peaks of the rough surfaces, no definitive correlation on oxide adherence could be established with the TBC specimens; it was thus decided to smoothen the as-sprayed MCrAlY-surfaces intending to obtain a more comparable situation to the flat surfaces of the EB-PVD systems. These results follow in the next section.

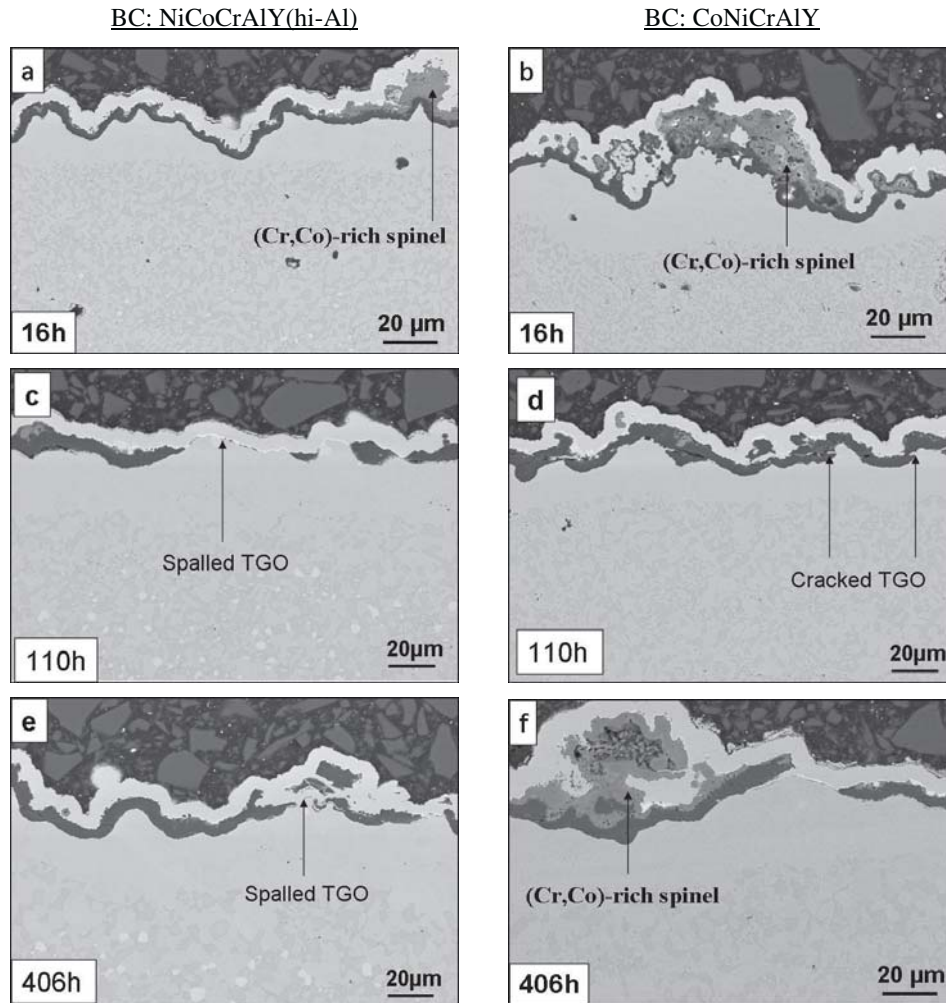


Fig 6.5 – SEM micrographs of overlay coatings containing NiCoCrAlY(hi-Al) BC after a) 16h, c) 110h e) 406h and CoNiCrAlY BC after b) 16h, d) 110h f) 406h of discontinuous oxidation in air at 1100°C.

6.2.2 Exposure of overlay coatings with ground surfaces

6.2.2.1 TGO adherence in overlay coatings with ground surfaces

The as-sprayed surfaces of the heat treated overlay coatings (batches KUK and KUL) were ground with a 1200 grit SiC paper and then subjected to the same exposure in air at 1100°C as the specimens described in section 6.2.1. Differences in the oxidation behavior on the samples with Ni- and Co-base coatings were observed even on macroscopic scale after 1230h of discontinuous exposure (see Fig. 6.6).

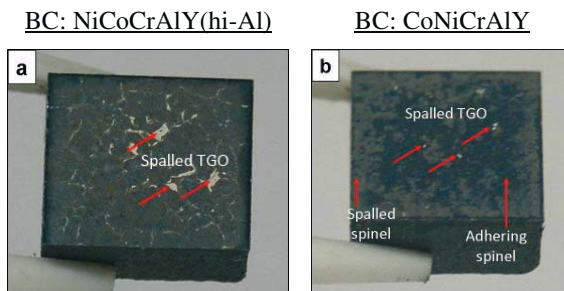


Fig 6.6 – TGO adherence on overlay coatings with a) NiCoCrAlY(hi-Al) bond coat and b) CoNiCrAlY bond coat after 1230h discontinuous oxidation in air at 1100°C. Inclined arrows indicate the areas of oxide spallation.

The NiCoCrAlY(hi-Al) overlays exhibit ridges and larger areas of spalled oxide on its surface than CoNiCrAlY. Additionally, it can be appreciated that more blue-colored Co-rich oxide-spinels formed on the latter, which is in agreement with the results on overlay coatings with rough surfaces (see Fig. 6.5).

6.2.2.2 TGO growth and morphology in overlay coatings with ground surface

Inherently flat oxide scales composed mainly of Al_2O_3 and a top sub-layer of oxide-spinels formed on these specimens. The spinel distribution is more homogeneous across the specimens than it was on the rough surfaces of Fig. 6.5; it was observed however on Fig. 6.6b that these non-protective oxides tended to spall especially in areas near-by the sample's edge.

The alumina scales grown on the Co-base coating were, with an average value of $7\mu\text{m}$ after 406h, thicker than those grown on the Ni-base coating, which accounted for $4.2\mu\text{m}$ (note that the area with oxide intruding into the metal in fig. 6.7e corresponds to a pore set free to the surface after grinding). An interesting observation is that in spite of thicker scales, the TGO grown on the CoNiCrAlY-coating remains intact while the one grown on the NiCoCrAlY-coating exhibits numerous cracks (compare Figs. 6.7e and 6.7f).

A comparison of Figs. 6.4 and 6.7 reveals that the same bond coat, with comparable thickness exposed under identical conditions can present a different TGO morphology when it is TBC-coated than when it is uncoated. On the TBC-coated MCrAlY the spinel formation is substantially suppressed and the inclusion of Y-aluminates in the oxide is promoted (Figs 6.4d and 6.4f). In contrast, the uncoated MCrAlY-overlay presents a TGO of purer alumina underneath a well distinguished Co-rich spinel sub-layer (Figs. 6.7d and 6.7f).

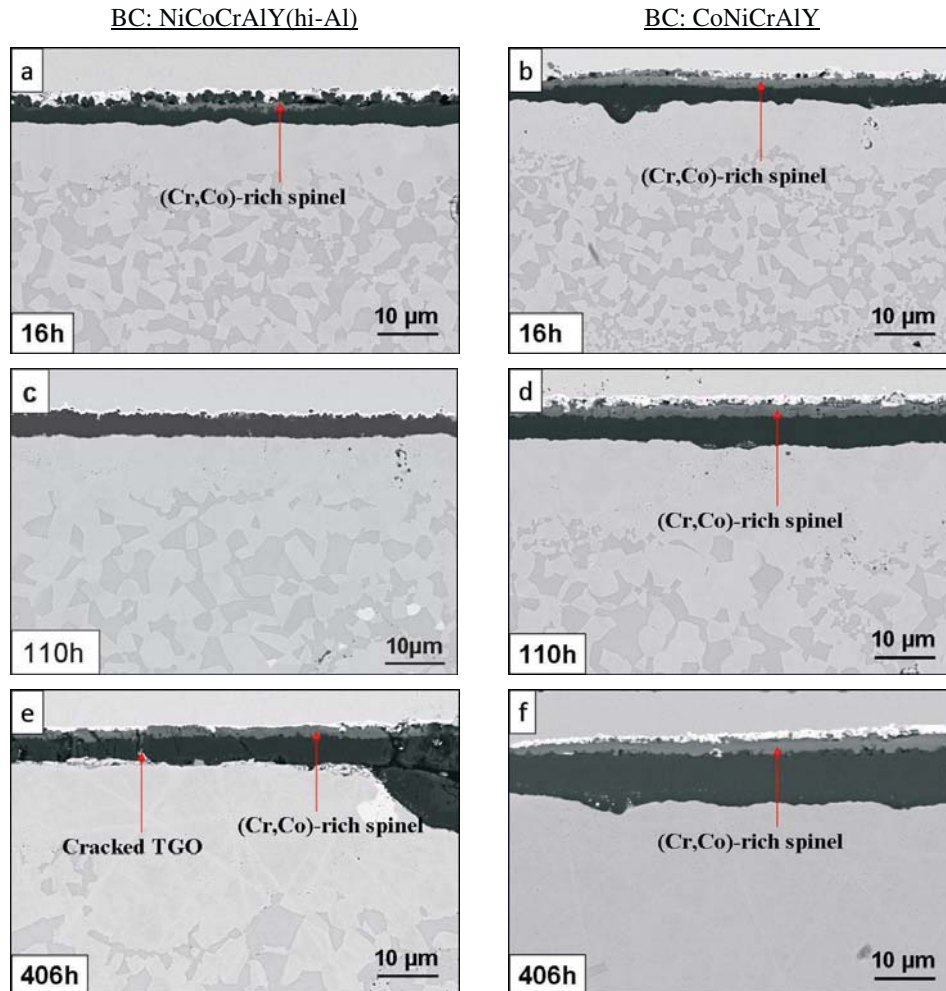


Fig 6.7 – SEM micrographs of overlay coatings on IN738 with ground surface containing NiCoCrAlY(hi-Al) BC after a) 16h, c) 110h e) 406h and CoNiCrAlY BC after b) 16h, d) 110h f) 406h of discontinuous oxidation in air at 1100°C.

This finding illustrates the fact that the bond coat oxidation is not only material-dependant but also processing-dependant. After the VPS deposition over the IN738 and the subsequent vacuum heat treatment, the two specimen types followed different processing steps: the MCrAlY-overlays (Fig. 6.7) were simply ground before oxidation. The MCrAlYs on the TBC specimens (Fig. 6.4) were additionally smoothed with cut wire peening and exposed to high temperatures in high vacuum during the ceramic deposition with EB-PVD. Such differences in processing appear to be enough to alter the surface condition previous to oxidation. This important effect was investigated with separate experiments and is addressed in detail in chapter 9.

6.2.2.3 Bond coat-substrate interaction

The formation of pores at the interface bond coat/substrate is known to be a consequence of strong element interdiffusion between both materials. In the case of the studied coatings, the CoNiCrAlY has a lower chemical compatibility with the Ni-base substrate IN738 compared to NiCoCrAlY(hi-Al). This is apparently related to a higher cobalt content in the former coating. This stronger element gradient explains why a more pronounced interfacial degradation occurred in the CoNiCrAlY overlays, where these two materials were interacting (see Fig. 6.8).

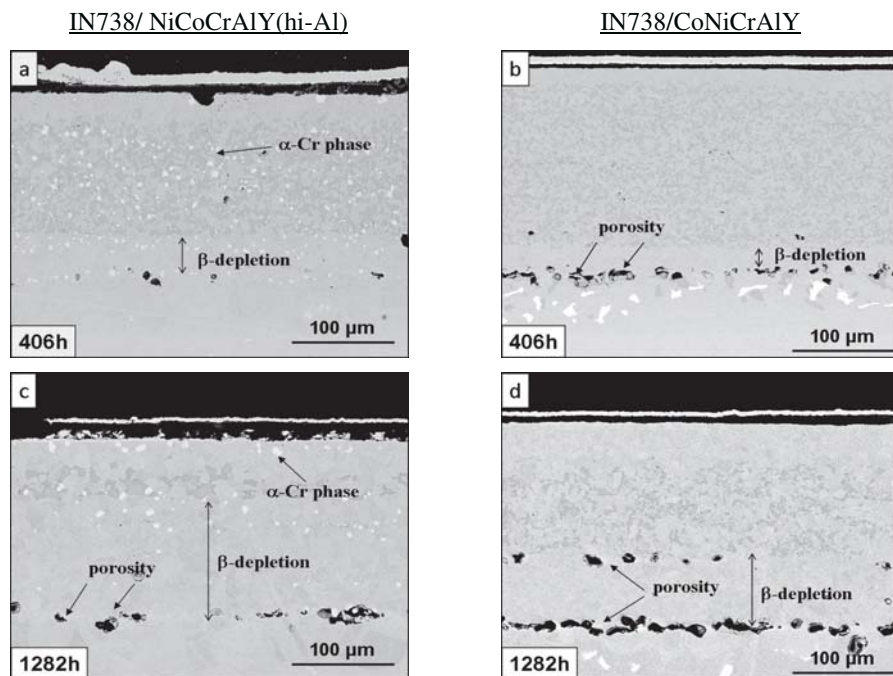


Fig 6.8 – Interfacial degradation due to interdiffusion with the substrate in overlay coatings containing NiCoCrAlY(hi-Al) BC after a) 406h, b) 1282h and CoNiCrAlY BC after b) 406h d) 1282h of discontinuous oxidation in air at 1100°C.

In Fig. 6.8d can be appreciated that after 1282h of exposure pores have not only formed at the interface but also inside the CoNiCrAlY-coating. Three other facts could be established after the cross-section analysis: firstly, the β -depletion occurs faster in the overlay Ni-base coating (compare Figs. 6.8c and 6.8d), perhaps due to its higher Al-content (11 wt.-%) in relation with that of the IN738 (3.4 wt.-%) and also due to the pronounced pore formation that might have limited the diffusion pathways between the Co-base and the

superalloy. Second, the bond coats do not have a similar thickness after plasma spraying, the CoNiCrAlY BC being approximately 40µm thicker than the NiCoCrAlY(hi-Al) BC. The consequences this difference might have for the oxidation behavior are discussed in Chapter 8. Third, the coatings do not present identical microstructures. The α -Cr phase is part of the microstructure of the Ni-base bond coat while it is absent in the Co-base coating. A detailed investigation of the coatings microstructures follows in chapter 7.

As it appeared to be that both TBC and substrate affect the coating oxidation and/or microstructure, it was decided to compare the oxidation behavior of Ni-base and Co-base MCrAlYs in the form of free-standing coatings. The results follow in section 6.3

6.3 Oxidation studies on free-standing MCrAlY-coatings

6.3.1 TGO growth and morphology after discontinuous exposure

The first oxidation experiments were conducted using identical exposure conditions as for the other specimen types described in the preceding sections (discontinuous oxidation in air at 1100°C) in order to have direct comparisons. Cross section images of those exposed for 406h evidence significant differences in the TGOs formed on the free-standing coatings (see Fig. 6.9) compared to the scales observed in overlay and TBC specimens. First, the oxide growth rate at 1100°C was considerably higher on the free-standing specimens; their thickness was between 6 - 8.5µm after 406h whereas the scales grown beneath the TBC reached only 3.5 - 4µm. Second, the thicker scales of the free-standing MCrAlYs are more heterogeneous in composition by containing large amounts of coarse Y/Al-oxides, which partially formed as “pegs” intruding into the metal. In contrast, the thinner oxide scales on the overlays and TBC specimens consist of “purer” alumina. In spite of the fact that the specimen types of the preceding sections were procured from the same powder batches by the same VPS-installation as the free-standing ones, the larger volume to surface ratio of the latter seem to have a significant influence on the oxidation behavior. This important effect is investigated more in detail in chapter 8, section 8.3.

Comparing the oxide scales formed on the three different coating alloys, the lowest growth rate was measured on the NiCoCrAlY(lo-Al), where the TGO thickness reached an average of 6µm after 406h of exposure (Fig. 6.9a). The oxide on the NiCoCrAlY(hi-Al) grew

up to 8 μ m (Fig. 6.9b), and a slightly thicker TGO of 8.5 μ m formed on the CoNiCrAlY (Fig. 6.9c). This tendency is in agreement with that observed in overlay and TBC specimens.

It is interesting to observe that scale cracking and delamination occurred on the two Ni-base coatings studied during cross-section preparation. In contrast, the scale on the Co-base coating remained intact. This might be an indication of a better scale adherence on the latter coating material. A thorough study of the oxidation kinetics and scale adherence in these coating alloys follows in sections 6.3.3 and 6.3.4.

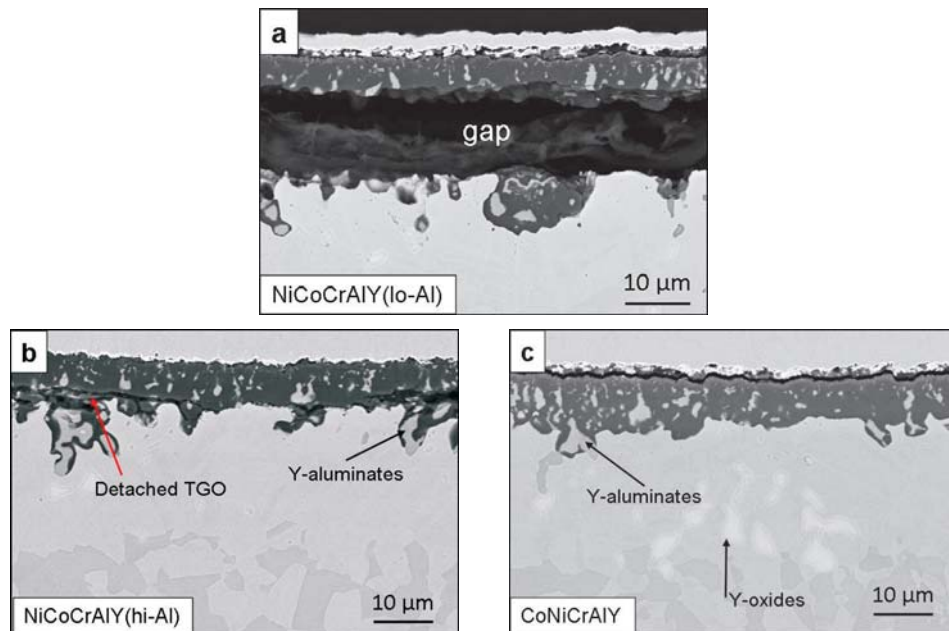


Fig 6.9 – SEM micrographs of 2mm thick free-standing a) NiCoCrAlY (lo-Al), b) NiCoCrAlY (hi-Al), c) CoNiCrAlY coatings with ground surface after 406h oh discontinuous oxidation in air at 1100°C.

6.3.2 Characterization of Y/Al-oxide compounds

An important difference of the oxides scales formed on the free-standing coatings compared to those formed on overlay coatings and in TBC specimens was the significant incorporation of Y/Al-mixed oxides, which explains the high scale growth rate in the former materials. The binary phase diagram yttria-alumina predicts formation of three possible types of aluminates -with increasing concentration of alumina- (see Fig. 6.10): $Y_4Al_2O_9$ (YAM), $YAlO_3$ (YAP) and YAl_5O_{12} (YAG). The monoclinic phase YAM is, however, instable [Abell] and thus, generally not observed in the oxidized MCrAlY bond coats [Braue].

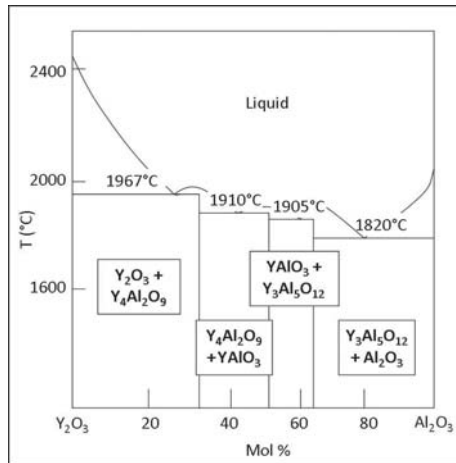


Fig 6.10 – Binary phase diagram yttria-alumina [Roth].

A typical spatial distribution of these compounds at the surface of the studied thick free-standing MCrAlY-coating after high temperature exposure is shown in Fig. 6.11. Under the present test conditions, yttria precipitates could be found in the coating alloy from the oxide/metal interface until depths of 40-50 μm below this interface. All other compounds in the immediate vicinity or in contact with the TGO are Y-aluminates. The EDX measurements indicate that in general, after the established exposure conditions, those particles fully enclosed in the oxide are YAP, whereas those only partially incorporated and those lying beneath the scale are commonly YAG. The usage of monochromatic CL-imaging supports this observation. This method is based on the finding that the luminescence signal of yttria and YAP is in a wavelength range around 360nm while that of YAG is in a wavelength range around 540nm. Hence, by collecting the emitted light of a specific wavelength range by using a monochromator it is possible to distinguish these Y-rich compounds. Fig. 6.12 gives an example of this technique applied on a 2mm thick free-standing CoNiCrAlY after 110h of exposure in air at 1100 $^{\circ}\text{C}$. In Fig. 6.12b is observed the light emitted from yttria and YAP particles (the latter found predominantly in the upper half of the scale), and in Fig. 6.12c the light emitted from YAG particles.

In spite of these observations, it must be noted that YAP is recognized to be a meta-stable phase, and is thus expected to transform into YAG upon longer exposures [Abell]. A reason why this transformation has not been completed for some particles, can be a lower Al-activity inside the scale (in comparison to that in the metal) which slows down the transformation.

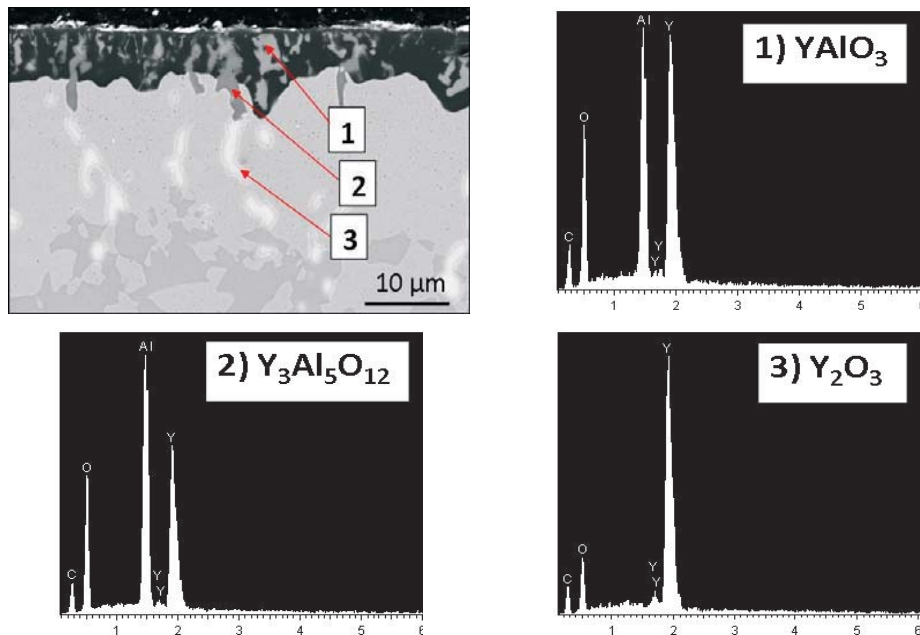


Fig 6.11 – Identification of Y/Al-compounds by EDX measurements on a 2mm thick free-standing CoNiCrAlY coating after 406h of discontinuous oxidation in air at 1100°C. Area 1 identified as YAP; area 2 as YAG; area 3 as Yttria.

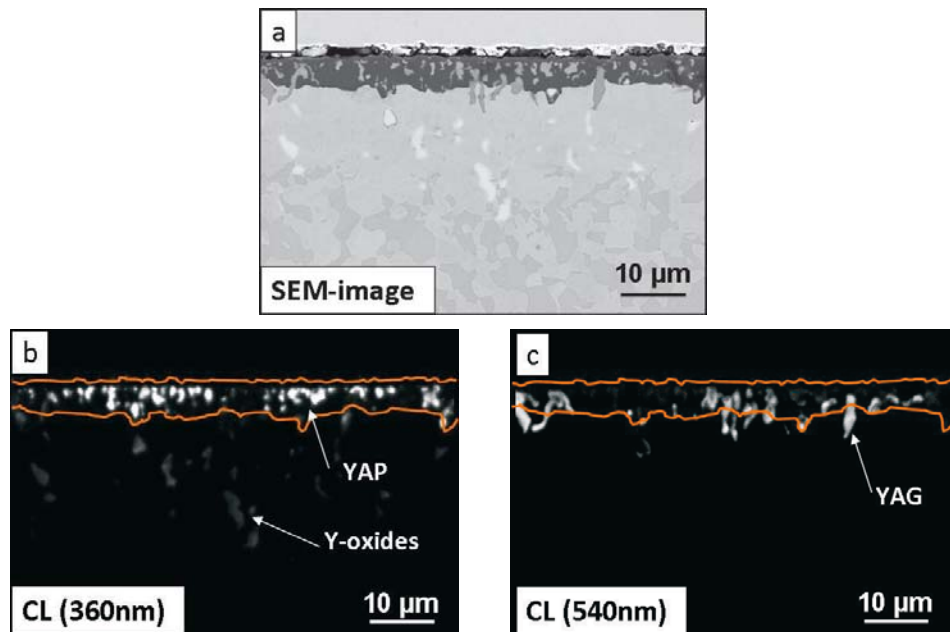


Fig 6.12 – Identification of Y/Al-compounds by monochromatic CL-imaging on a 2mm thick free-standing CoNiCrAlY coating after 110h of discontinuous oxidation in air at 1100°C. a) SEM/BSE-image; b) CL-image (360nm); c) CL-image (540nm). Solid line delimitates oxide scale.

The gradual transformation of Y-rich compounds is depicted in Fig. 6.13. A particle located at the oxide/metal interface is shown, whose chemical composition corresponds in its core to Y-oxide, around this core to YAP and on its external surface to YAG. These three areas in the particle can be even distinguished on the SEM image if the contrast is adequately set. A phase with a higher amount of Al will appear darker on the micrograph while a phase with a higher amount of the heavier element Y will appear lighter. EDX mappings of yttrium and aluminum attached in Fig. 6.13 support this observation. The Y-concentration is clearly higher in the core of the precipitate while the Al-concentration is particularly higher at the external surface, where the transformation to YAG has completed. Therefore, not every precipitate can be characterized as a fully transformed particle.

A mechanistic explanation of the formation and distribution of the different Y/Al-oxides is given schematically in Fig. 6.14. Having yttrium the highest oxygen affinity in the MCrAlY-alloy, yttria is the first oxide to form during early oxidation stages and even during vacuum heat treatment as shown by [Gil] and [Nijdam-1]. Gil et al. proved that the technical vacuum used in practice, commonly in the order of magnitude of 10^{-5} mbar, is enough to originate a strong diffusion of Y to the surface and its subsequent oxidation.

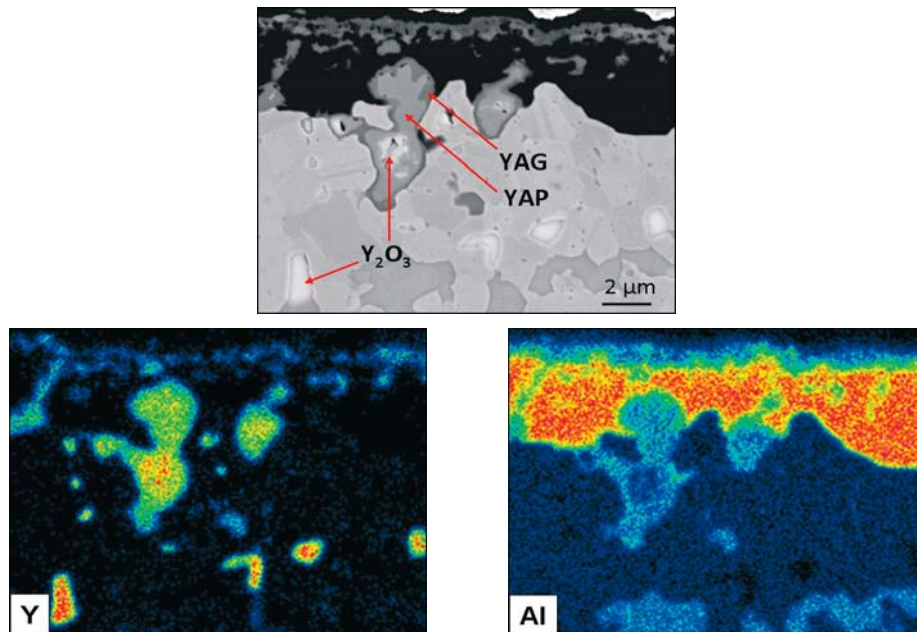


Fig 6.13 – Close-up view of Y/Al-compounds in transformation at the oxide/metal interface with corresponding Y and Al mappings. (2mm thick free-standing CoNiCrAlY after 110h of discontinuous oxidation in air at 1100°C).

In the case of a thick MCrAlY coating, where yttrium is largely available in the bulk and thus not rapidly exhausted, its outward diffusion can continue during later exposure stages after a continuous TGO has formed (see t_1 in Fig. 6.14). If the inward flux of oxygen is larger than the outward flux of yttrium, the latter will oxidize internally in the metal (t_2 in Fig. 6.14). The yttria precipitates located in the vicinity of the TGO/metal interface are in a zone of high O and Al –activities. Therefore these precipitates easily react with Al to form Y-perovskites (t_3 in Fig. 6.14).

With further exposure, the YAP precipitates formed in the near-surface regions are fully incorporated into the TGO (t_3 in Fig. 6.14), where the Al-activity is significantly lower than in the metal. Consequently the reaction of YAP into YAG which is apparently limited by the Al-diffusion through the boundary YAG layer occurs at a relatively slow rate. Contrariwise, those sub-surface YAP precipitates not fully incorporated into the scale are in the zone of high Al-activity and sufficiently high O-activity to enable their transformation to the Al-rich YAG compound. Deeper in the alloy the oxygen activity is rapidly decreased and the bulky internal yttria precipitates are formed which remain stable for relatively long exposure times in spite of a high Al-activity in the coating (t_4 in Fig. 6.14).

6.3.3 Oxidation kinetics of free-standing MCrAlY-coatings during isothermal exposure

The oxidation kinetics at 1000°C, 1050°C and 1100°C of the three MCrAlY-coatings was investigated using thermogravimetry (TG) on 2mm thick free-standing specimens during isothermal exposures of 72h in synthetic air.

The specimens were heat treated (2h at 1120°C + 24h at 845°C) in vacuum and their surfaces were subsequently ground to 1200 grit prior to the exposures in synthetic air.

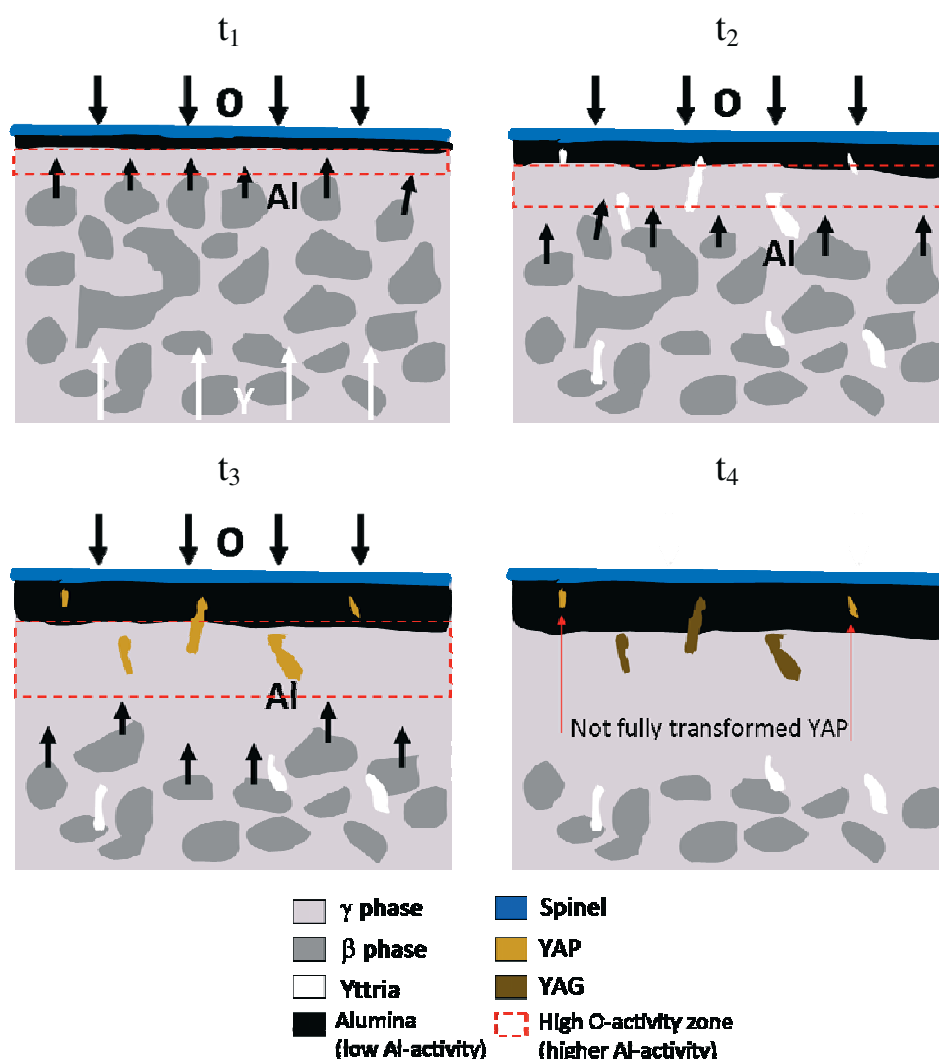


Fig 6.14 – Schematic explanation of the formation of Y-aluminates.

6.3.3.1 Temperature dependence of oxidation kinetics of the NiCoCrAlY (hi-Al)-coating

In Fig. 6.15 the weight change curves are presented for the coating alloy measured during exposure in synthetic air at three different temperatures. The expected temperature dependence, i.e. accelerated kinetics with increasing temperature, could be observed after the TG-measurements. However, according to the measured data, the oxide growth seems to be faster during early stages when the coating alloy was exposed in air at 1000°C. This effect is better appreciated if the instantaneous rate constant, $k_p(t)$, is presented in a semi-log plot (Fig.

6.16). This rate constant is derived by local linear fitting from the weight change data shown above using the parabolic law:

$$k_p(t) = \left(\frac{d(\Delta m)}{dt^{1/2}} \right)^2 \quad (6.1)$$

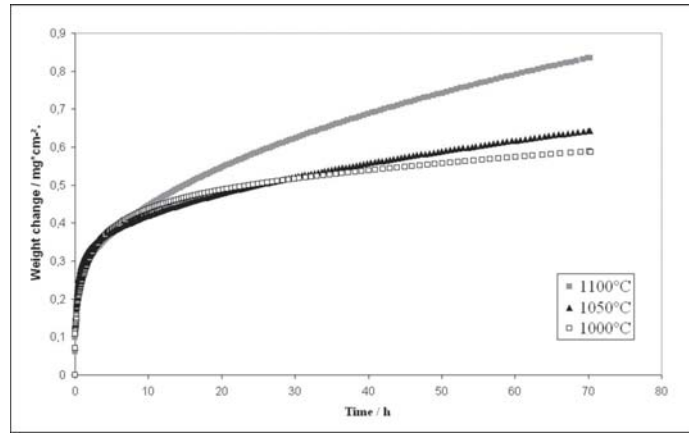


Fig 6.15 – Oxidation kinetics of NiCoCrAlY(hi-Al) at 1000°C, 1050°C and 1100°C.

The accelerated oxide growth measured on the specimen exposed in air at 1000°C during the first 1-5 hours compared to the growth rate measured on those exposed at higher temperatures could be correlated with the formation of metastable alumina, whose growth rate is known to be higher than that of the stable α - Al_2O_3 [Tolpygo-2].

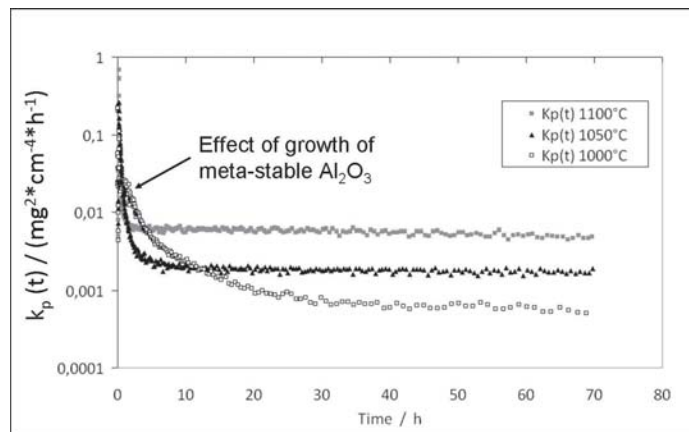


Fig 6.16 – Instantaneous $k_p(t)$ of NiCoCrAlY(hi-Al) at 1000°C, 1050°C and 1100°C.

In the SEM cross-sections after 72h of exposure at 1000°C (Fig. 6.17a), the whisker-like morphology of θ -Al₂O₃ was observed in the outer portion of the scale. Fluorescence spectroscopy data, however, indicated that the major part of the scale consisted of α -Al₂O₃, in agreement with the low $k_p(t)$ values in Fig. 6.16.

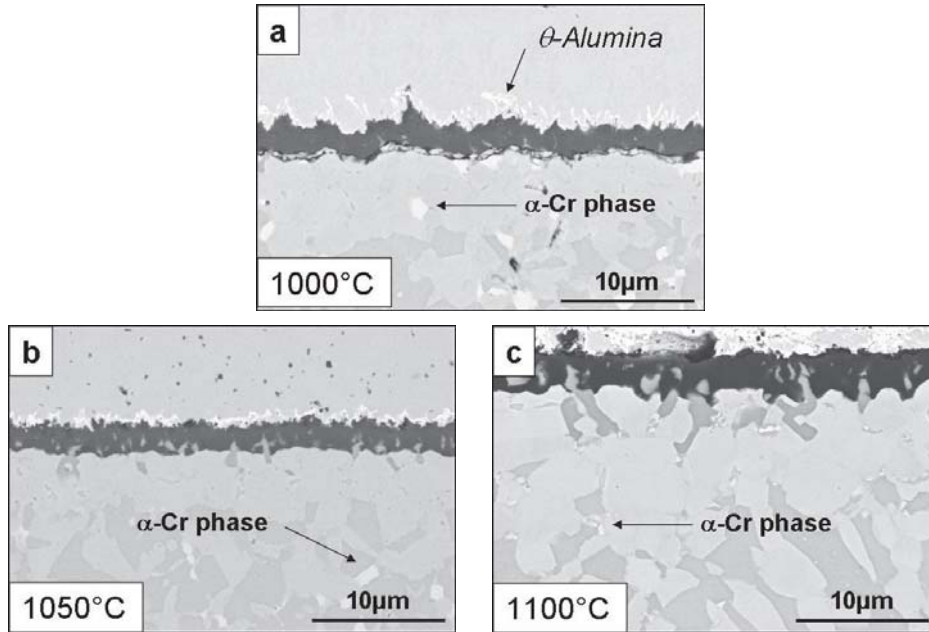


Fig 6.17 – TGO grown on free-standing NiCoCrAlY(hi-Al) specimens after 72h of isothermal oxidation in synthetic air at a) 1000°C, b) 1050°C and c) 1100°C.

The average TGO thickness of the specimen annealed at 1000°C was 2.2μm after 72h, while in the specimen annealed at 1100°C was 3.3μm. An interesting observation from this cross-section analysis was that the Y-incorporation in the TGO varied significantly in this temperature range. The tiny finger-like Y-aluminates observed in the oxide of the specimen exposed at 1000°C (Fig. 6.17a) strongly differ from the coarse Y-aluminates observed in the oxide of the sample exposed at 1100°C, where an enhanced Y-diffusion from the bulk took place (Fig. 6.17c). As mentioned on Fig. 6.9 this coating contains α -Cr as part of its microstructure

6.3.3.2 Temperature dependence of oxidation kinetics of the CoNiCrAlY-coating

A similar temperature dependence of oxidation kinetics and oxide morphology could be established for the CoNiCrAlY-coating. The weight change curves for this coating alloy are presented in Fig. 6.18. The growth of metastable alumina on the CoNiCrAlY-specimen annealed at 1000°C accelerated the oxidation kinetics during the initial 5 hours of exposure. As can be seen in Fig. 6.19, instantaneous $k_p(t)$ values for this lower temperature are superior than those measured on the specimens oxidized at 1050°C and 1100°C.

The TGO morphology of the annealed specimens is shown in Fig. 6.20, where it is appreciated how the Y-diffusion to the surface is promoted at higher temperatures. The presence of coarse Y-aluminates, generally found intruding in the alloy (Fig. 6.20c), might have altered not only the chemical composition of the oxide but also its growth rate due to the allowance for higher oxygen inward diffusion they establish [Kofstad-2]. With an average scale thickness of 3.8µm, this TGO formed in air at 1100°C nearly doubles that formed at 1000°C (average thickness 2.1µm).

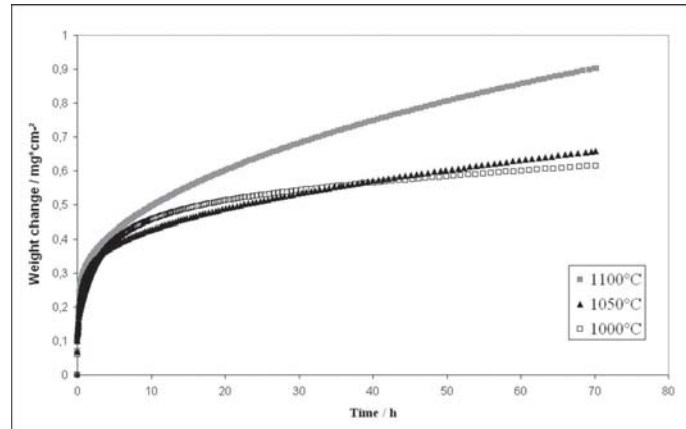


Fig 6.18 – Oxidation kinetics of CoNiCrAlY at 1000°C, 1050°C and 1100°C.

The observed differences in morphology between the scales formed at 1000°C (Fig. 6.20a) and at 1100°C (Fig. 6.20c) show that a temperature increase does not exclusively lead to accelerated oxidation kinetics in the MCrAlY-coatings but also involves the alteration of the oxide composition.

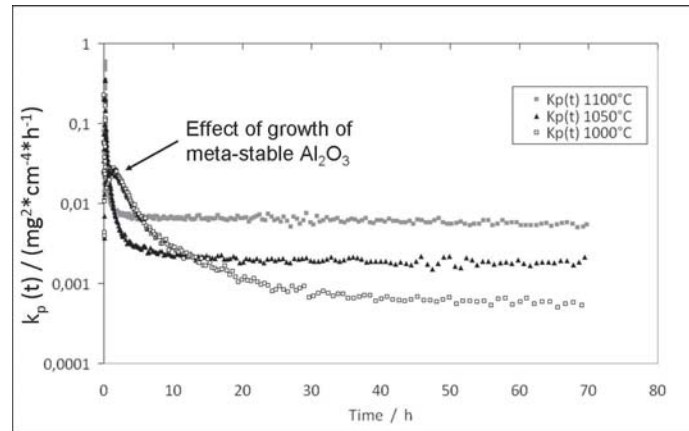


Fig 6.19 – Instantaneous $k_p(t)$ of CoNiCrAlY at 1000°C, 1050°C and 1100°C.

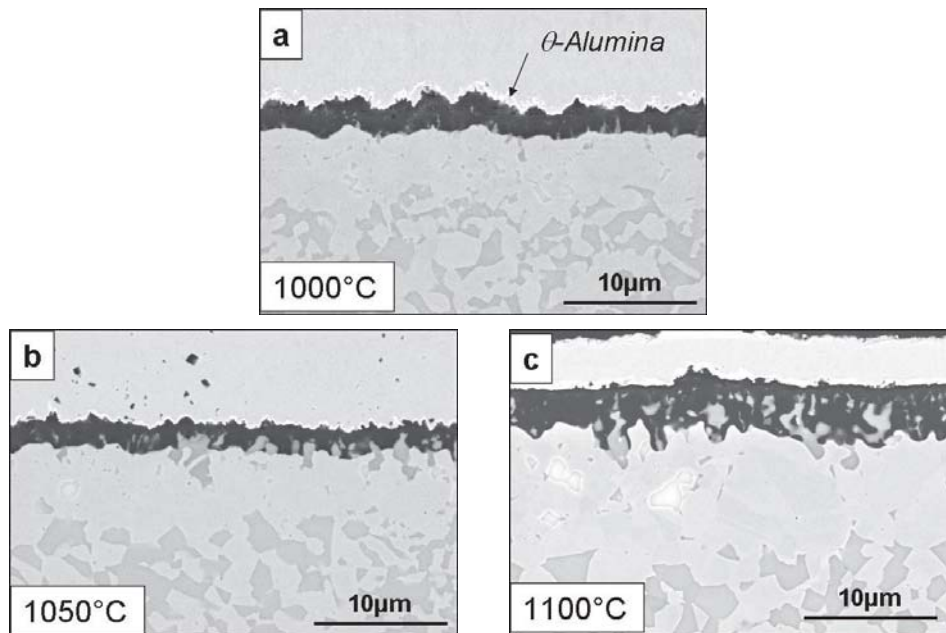


Fig 6.20 – TGO grown on free-standing CoNiCrAlY specimens after 72h of isothermal oxidation in synthetic air a) 1000°C, b) 1050°C and c) 1100°C.

For instance, the estimation of a critical oxide thickness to spallation (if existent) cannot be made by carrying out oxidation tests at different temperatures. Not only the thermal mismatch stress but also the nature and composition of the oxides obtained are not equal. An alternative method to predict such a parameter is proposed in chapter 10.

Since the TG-measurements on the free-standing NiCoCrAlY(lo-Al) exhibited a similar temperature dependence than the above presented coatings these results are omitted. They are instead shown in comparison in the next section.

6.3.3.3 Comparison of oxidation kinetics of MCrAlY-coatings

The weight change curves of the three free-standing coatings are presented together in Fig. 6.21 (for exposure at 1000°C) and in Fig. 6.22 (for exposure at 1100°C). Cross-section images of the respective specimens are shown in Figs. 6.23 and 6.24.

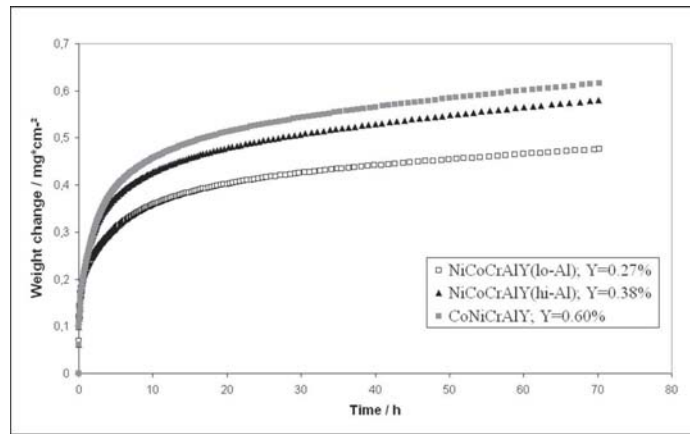


Fig 6.21 – Oxidation kinetics of MCrAlYs at 1000°C (Y contents shown in wt.-%).

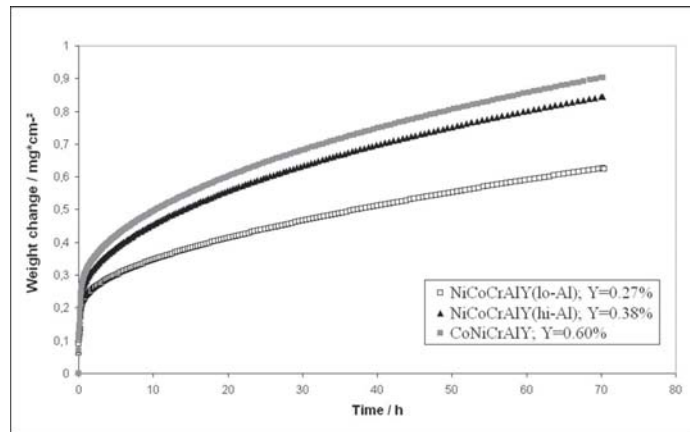


Fig 6.22 – Oxidation kinetics of MCrAlYs at 1100°C (Y contents shown in wt.-%).

When annealed under the same conditions at both 1000°C and 1100°C, the slowest scale growth was registered for the NiCoCrAlY(lo-Al) coating alloy, followed by the NiCoCrAlY(hi-Al), and the fastest scale growth was measured on the CoNiCrAlY.

An interesting observation in the plots in Figs. 6.21 and 6.22 is that the scale growth seem to depend on the Y-concentration in the materials.

Regarding the TGO thickness, clearly thinner scales formed on the NiCoCrAlY(lo-Al) after annealing at both the temperatures shown in Figs. 6.23 and 6.24, in agreement with the tendencies observed in the weight gain curves.

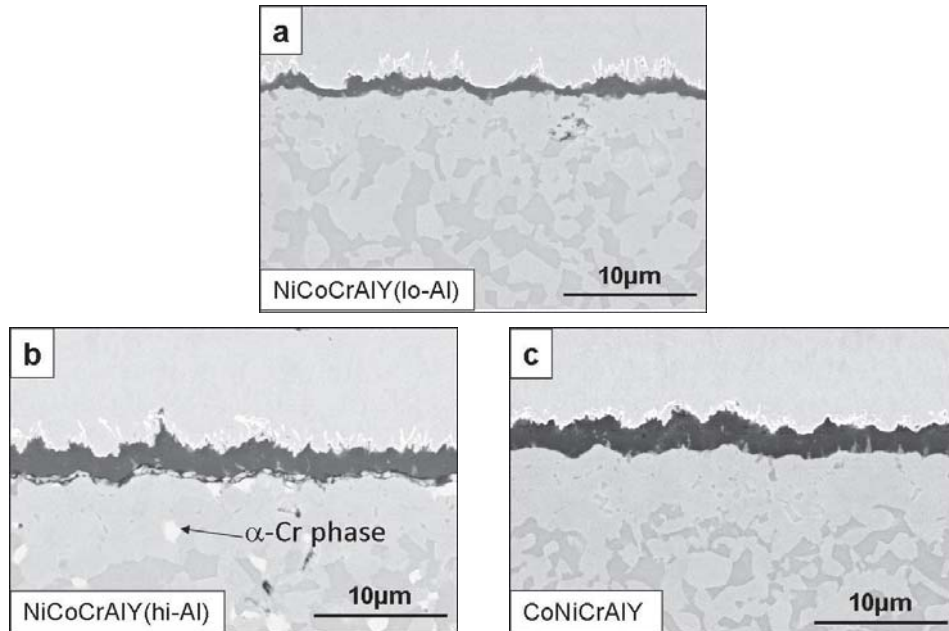


Fig 6.23 – TGO grown on free-standing a) NiCoCrAlY(lo-Al), b) NiCoCrAlY(hi-Al) and c) CoNiCrAlY after 72h of isothermal oxidation in synthetic air at 1000°C.

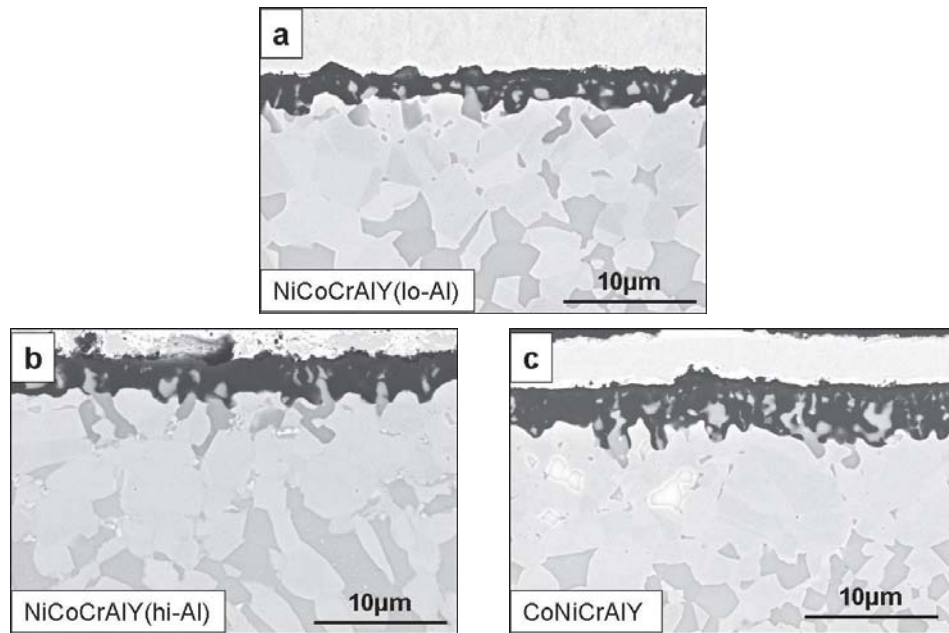


Fig 6.24 – TGO grown on free-standing a) NiCoCrAlY(lo-Al), b) NiCoCrAlY(hi-Al) and c) CoNiCrAlY after 72h of isothermal oxidation in synthetic air at 1100°C.

6.3.4 Oxidation kinetics and scale adherence on MCrAlY-coatings during cyclic exposure

In order to assess the oxide scale adherence, long-term cyclic exposures (2h high temperature/ 15min cooling) up to 1300h were conducted on 2mm thick free-standing samples in laboratory air at 1100°C. Prior to the cyclic oxidation, the specimen surface was ground with 1200 grit and subsequently heat treated (2h at 1100° + 24h at 845°) in vacuum. During the test, specimen weighing took place after every 18h at high temperature. Cross section analysis was carried out upon completion of the experiments

The evolution of the specimen mass gain in the course of the test is plotted as function of time in Fig. 6.25. The curves show during the first 200h of exposure that the oxide growth is slightly faster in the CoNiCrAlY coating than in the Ni-base coatings, in agreement with the thermogravimetric measurements of the previous sections. An early mass loss, associated with oxide spallation, was registered in the NiCoCrAlY(lo-Al) specimen already after 150h; this tendency prevailed becoming more pronounced as the test continued. In the plot it can be observed that after 500h this sample had lost so much oxide that the relative mass change turned negative. Due to the pronounced spallation the cyclic exposure of this coating alloy was prematurely stopped after 918h.

Steadily increasing mass was registered on the other coatings for longer times; the turning-point on the curves was determined after 780h for the NiCoCrAlY(hi-Al) specimen and after 980h for the CoNiCrAlY. From this data is derived that the strongest oxide/metal adhesion is present in the Co-base coating despite its faster oxide growth and thus, thicker oxide scale.

Cross section images of the specimens upon test completion are presented in Fig. 6.26. As expected, only rests of the TGO could be found in the NiCoCrAlY(lo-Al) specimen after 918h testing (Fig. 6.26a). The few remnant oxide pegs, evidence that the delamination occurred predominantly along the oxide/metal interface. In spite of being macroscopically intact, the TGO grown on the NiCoCrAlY(hi-Al) specimen during the 1300h testing exhibits in cross section a series of short cracks generally running parallel to the oxide/metal interface, which actually seem to have coalesced into a long continuous crack in the area shown by the SEM micrograph (Fig. 6.26b). The scale reached an average thickness of 12 μ m after the cyclic exposure.

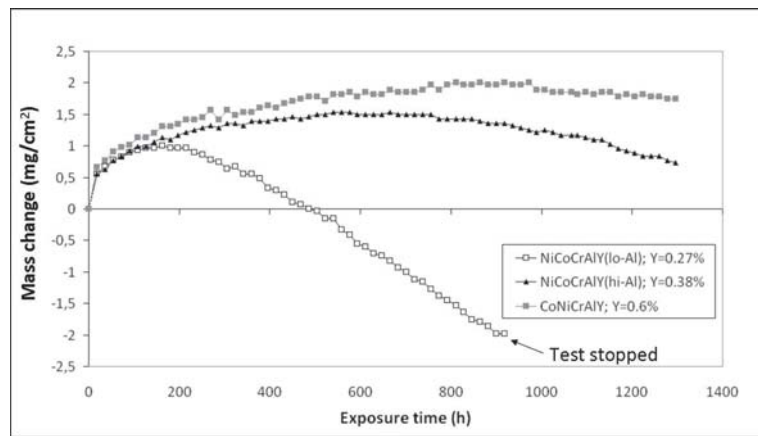


Fig 6.25 – Mass change of 2mm thick free-standing MCrAlY specimens during 1300h of cyclic exposure in air at 1100°C.

The CoNiCrAlY specimen presented an adherent oxide in all the analyzed areas (Fig. 6.26c), despite the presence of numerous coarse Y-aluminates which locally accelerated the oxide growth to thicknesses over 20 μ m. The average oxide thickness was 13 μ m. In addition, a large presence of Y-oxides, located 20-40 μ m beneath the oxide/metal interface was also observed in this coating alloy, contrasting with the Ni-base coatings.

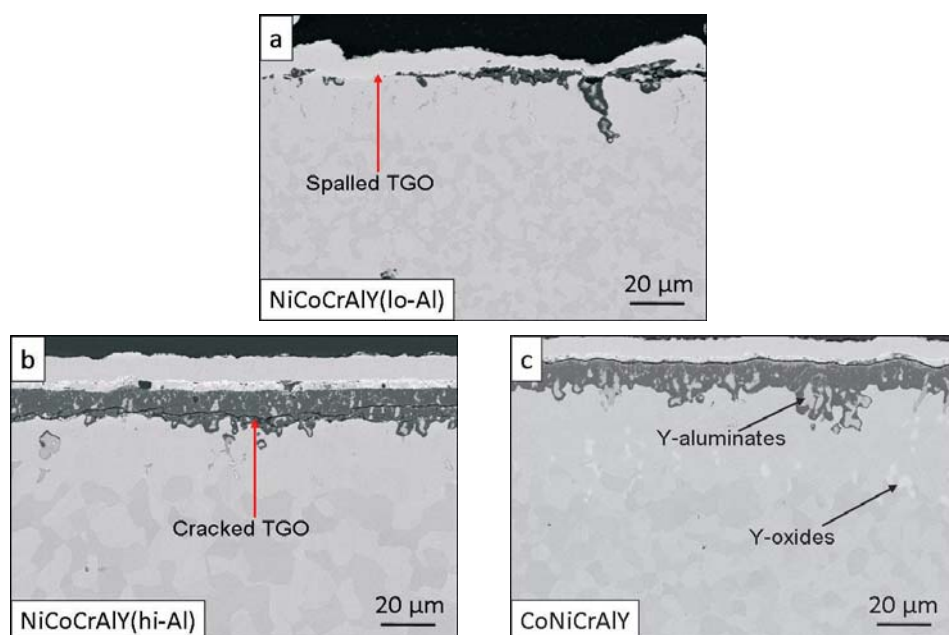


Fig 6.26 – BSE- images of 2mm thick free-standing a) NiCoCrAlY(lo-Al), b) NiCoCrAlY(hi-Al) and c) CoNiCrAlY specimens after 1300h (NiCoCrAlY(lo-Al) after 918h) of cyclic exposure in air at 1100°C.

The mass change plot of Fig. 6.25 showed that the coating alloy with the highest Y-content (CoNiCrAlY) exhibited a better scale adherence under the cyclic conditions than the two Ni-base coatings with lower Y-content. Indeed, the shortest time to oxide spallation was registered for the NiCoCrAlY(lo-Al), which is the coating with the lowest Y-contents.

Besides the Y-content, another possible reason for a worse scale adherence on the Ni-base coatings could be the differences in the coating microstructure or phase transformations in the materials. It is evident from Fig. 6.17 that the NiCoCrAlY(hi-Al) coating contains after high-temperature exposure light-phase precipitates identified as α -Cr, which could not be observed in the Co-base coating.

6.4 Summary and final comments

The CoNiCrAlY coating exhibited a better scale adherence in all three studied specimen types, both under discontinuous and cyclic oxidation conditions in spite of a reproducibly faster oxide growth compared to the Ni-base coatings. Aiming to determine the possible causes of this finding and considering the variations in microstructure observed in

the specimens, it was proposed to investigate the microstructure of the studied MCrAlYs. These results follow in the next chapter.

Additionally, the results of this chapter indicate that other material-independent parameters seemed to influence the scale composition and morphology on the studied coatings in particular by altering the amount and distribution of Y/Al mixed-oxides. These parameters were identified as surface roughness, specimen thickness and processing. Studies on free-standing coatings with controlled variations of these parameters are thus necessary.

Furthermore, regarding the specimen thickness it was observed that the Y-content is an important factor on the oxidation behavior and TGO adherence. Hence, the question arose whether the results on 2mm thick free-standing MCrAlY specimens can be directly transferred to 0.15mm thick coatings (typical for TBC systems), which evidently possess a smaller amount of Y available, despite having the same concentration. This point is clarified in chapter 8 by repeating the same experiment on thinned free-standing specimens.

Regarding the specimen processing, it is necessary to find out if the different treatment sequence used in the preparation of the free-standing specimens for: 1) the TG measurements in synthetic air (surfaces ground after the heat treatment) and 2) the discontinuous and cyclic exposures in laboratory air (surfaces ground before the heat treatment) have a significant influence on the oxidation behavior of the coatings.

7. Temperature dependence of phase relationships in different MCrAlY-coatings

7.1 General remarks

It was concluded in chapter 6 that the CoNiCrAlY-coating exhibits a better scale adherence than the two Ni-base coatings studied despite faster oxide growth (Figs. 6.21, 6.22, 6.25). Such a conclusion contradicts the classical understanding that a fast-growing scale would tend to spall before a slow-growing scale [Barrett, Tolpygo-1]. It was introduced that the observed microstructural differences in the coatings might have an influence on scale growth kinetics and adherence. This chapter is thus dedicated to study the microstructure of the three coating alloys in question and its possible influence on the oxide growth, morphology and adherence. A broad temperature range covering both typical service temperatures in turbines and laboratory testing temperatures was selected.

For this study 2mm thick free-standings coatings were isothermally annealed in laboratory air at four different temperatures. The exposure times were increased with decreasing temperatures in order to achieve equilibrium microstructures in all the test samples, i.e. at 1100°C for 25h, at 1000°C for 75h, at 900°C for 150h and at 800°C for 300h. This exposure conditions were derived from the experiences with Ni-base superalloys, which typically reach equilibrium after 24h at 845°C [Heinicke]. The specimens were subsequently quenched in water to preserve their actual high temperature microstructures. Cross-section analysis was carried out in areas far away from the sample's surface to exclude the effects of element depletion caused by oxidation.

Parallel to the heat treatments, thermodynamic calculations of phase equilibria and quantification of the chemical composition of the predicted phases under the experimental conditions were carried out for the MCrAlY-materials with the software package ThermoCalc®.

Additionally, the physical coefficient of thermal expansion (CTE) was measured on the studied coatings in the temperature range 500 to 1100°C according to the procedure described in [Muñoz-2] in order to determine more precisely possible phase transformations and their associated volume changes.

7.2 Modeling of phase equilibria in MCrAlY-coatings

The ThermoCalc predictions were done using a new extended database (TTNi7[®]) and compared with the experimental results, whereby it was found previously by Achar et al. [Achar] that this software has a limitation for calculations in alloys with cobalt concentrations higher than 16 at.-%, as it is the case for the CoNiCrAlY-coating in this study. Furthermore, the used software database did not include thermodynamic data for Y-containing compounds, which therefore could not be taken into account.

7.2.1 Modelling of phase equilibria in NiCoCrAlY(lo-Al)

According to the calculations, four different phases are found in the NiCoCrAlY(lo-Al) coating in the studied temperature range (Fig. 7.1). An important feature in the calculations is the gradual phase transformation γ' to γ predicted to occur between 700 and 820°C. The presence of the σ -(Cr,Co) phase is predicted for this coating composition presumably due to its Re-content and its high Co-concentration. The latter phase is observed to be stabilized in a wide temperature range (until approx. 950°C). Above 1000°C the microstructure in this coating alloy is predicted to be composed of γ and β , γ being dominant with increasing temperatures.

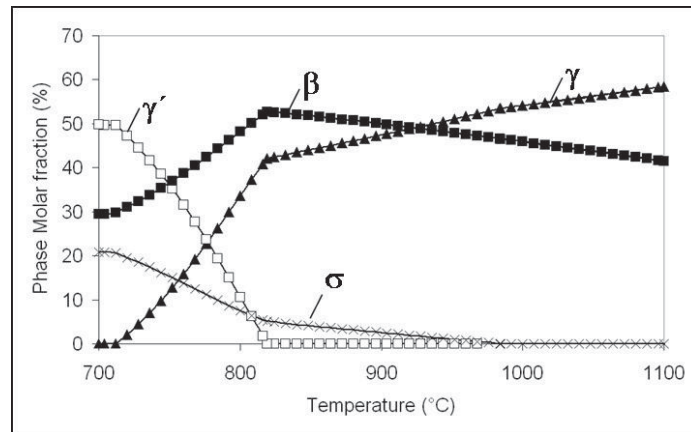


Fig 7.1 – Molar fractions of phases in the temperature range 700-1100°C calculated by ThermoCalc for the NiCoCrAlY(lo-Al) coating.

7.2.2 Modelling of phase equilibria in NiCoCrAlY(hi-Al)

The phase transformation γ' to γ is also predicted in the NiCoCrAlY(hi-Al), though in this coating it is expected to occur abruptly at 880°C instead of gradually as in the other Ni-base coating.

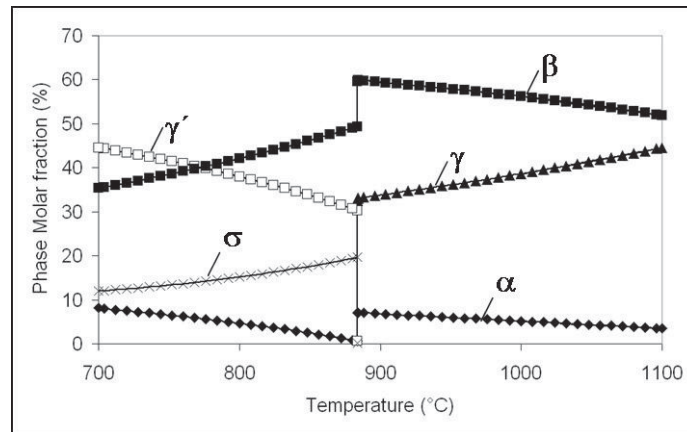


Fig 7.2 – Molar fractions of phases in the temperature range 700-1100°C calculated by ThermoCalc for the NiCoCrAlY(hi-Al) coating.

As seen in Fig. 7.2, the complete microstructure seems to be affected by this transformation; one of these changes (if temperature is increased above 880°C) is the abrupt increase in the amount of β -NiAl, due to the lower solubility of Al in the newly formed γ -Ni phase. A second feature is the instability of the σ -(Cr,Co) phase above 880°C. The chromium released due to the dissociation of this phase, leads to an increase of the α -Cr phase. Contrary to the σ -(Cr,Co), the α -Cr phase remains stable even at 1100°C promoted in part due to the presence of rhenium as previously reported by other authors [Achar,Täck] and the higher Cr-concentration in this coating. This is also in agreement with the experimental observations in this work (Figs. 6.5, 6.9 and 6.23).

7.2.3 Modelling of phase equilibria in CoNiCrAlY

When modeling the microstructure of the CoNiCrAlY-coating, the presence of three phases is predicted in the studied temperature range, as shown in Fig. 7.3. At 1100°C this coating is composed exclusively of γ and β , the volume fractions of these phases are comparable to those of the NiCoCrAlY-coatings. However, at lower temperatures the γ -Ni

phase is predicted to be stable, and the γ' -Ni₃Al phase absent, in the Co-base coating. Furthermore, the σ -(Cr,Co) phase is stable in a broader temperature range in this material than in the Ni-base ones, (compare with Figs. 7.1 and 7.2). This is also promoted by the high concentration of Co (above 25 wt.-%).

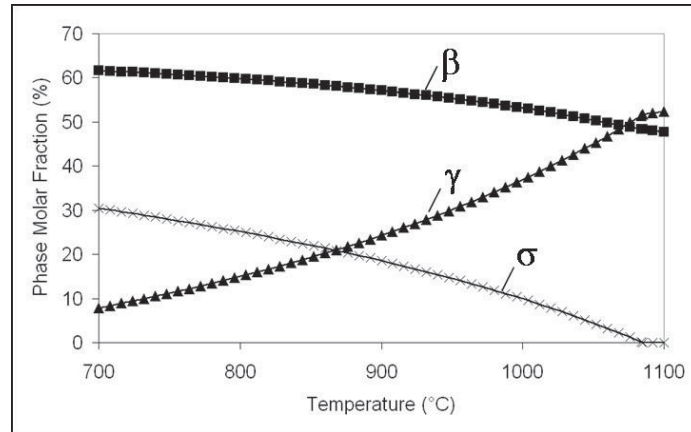


Fig 7.3 – Molar fractions of phases in the temperature range 700-1100°C calculated by ThermoCalc for the CoNiCrAlY-coating.

7.3 Microstructure of annealed MCrAlYs in the temperature range 800-1100°C

7.3.1 Microstructure at 1100°C

The phases present in the 2mm thick specimens after annealing were identified by EDX and XRD in areas far away from the oxide/metal interface to avoid the effects of oxidation. Fig. 7.4 shows the cross section of MCrAlY-coatings after 25h of annealing at 1100°C. The microstructure of the NiCoCrAlY(lo-Al) is composed solely of the γ - and β -phases (Fig. 7.4a), whereas in the NiCoCrAlY(hi-Al), an alloy richer in Cr, isolated precipitates of α -Cr with dimensions of up to 2 μ m diameter are part of the microstructure (Fig. 7.4b) in agreement with the ThermoCalc predictions. The CoNiCrAlY specimen exhibits besides the predominant phases γ and β , particles corresponding to Ni-Y intermetallic phases (Fig. 7.4c), which are not predicted by ThermoCalc due to the fact that the used thermodynamic database does not contain data on yttrium containing compounds.

The absence of the α -Cr phase in the NiCoCrAlY(lo-Al) and in the CoNiCrAlY-coating can be explained by two factors: first, the high concentration of Co which increases

the solubility of chromium in the γ -phase and second, the absence of rhenium in the Co-base coating and its lower concentration in the NiCoCrAlY(lo-Al). Re is known to stabilize the α -Cr phase [Singheiser-1].

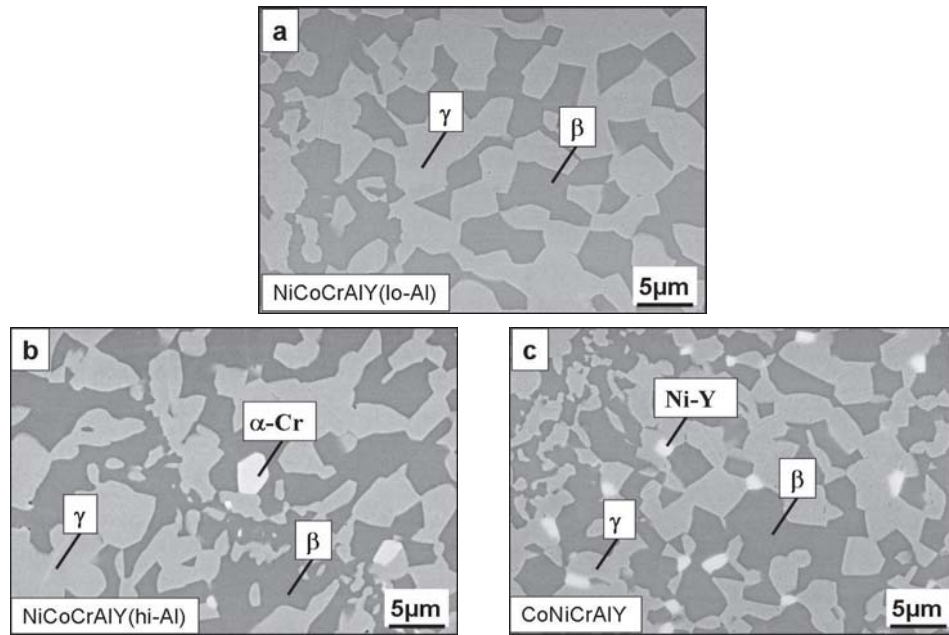


Fig 7.4 – SEM cross sections of specimens after 25h isothermal air exposure at 1100°C and subsequent water quenching. Ni-Y refers to intermetallic phases
a) NiCoCrAlY(lo-Al); b) NiCoCrAlY(hi-Al); c) CoNiCrAlY.

The observation of a Ni(Co)Y intermetallic phase in the CoNiCrAlY, and not in the Ni-base coatings, might be an indication that the Ni(Co)Y compounds are stabilized by cobalt. This assumption is supported by the binary phase diagrams Co-Y and Ni-Y, which show that at high temperatures Co_{17}Y_2 possesses a substantial homogeneity range and is stable at lower Y-concentrations compared to Ni_{17}Y_2 . This finding is considered of importance for the oxidation behavior of this material. If yttrium is bound in the intermetallic phases at this temperature, its flux to the surface is expected to be slower compared to the studied Ni-base coatings. In the latter materials Y is in solid solution in the γ -phase, hence, it is expected to be transported to the coating surface at faster rates. Chapters 8 and 9 treat some effects a different mobility/ diffusion rate of Y to the surface can have on the TGO morphology and adherence.

7.3.2 Microstructure at 1000°C

When exposed in air at 1000°C for 75h, the two-phase microstructure of the NiCoCrAlY(lo-Al) shows no difference to that observed after exposure at 1100°C (Fig. 7.5a), in accordance with the ThermoCalc calculations (Fig. 7.1). On the contrary, the NiCoCrAlY(hi-Al) exhibits a larger volume fraction of α -Cr precipitates than when exposed in air at 1100°C (Fig. 7.5b). Moreover, at this temperature, this phase apparently also precipitates in form of tiny, spherical particles which are smaller than 0.5 μ m inside large β -phase precipitates. Additionally, at 1000°C, Ni-Y intermetallic phases are also found in the microstructure of the Ni-base coating. Apparently, the Y-solubility limit in γ - (and β -phase) was exceeded at this temperature, different to 1100°C. The fact that the limit was not exceeded in the NiCoCrAlY(lo-Al) is logic considering that this coating has the lowest Y-concentration of the three bond coats in question.

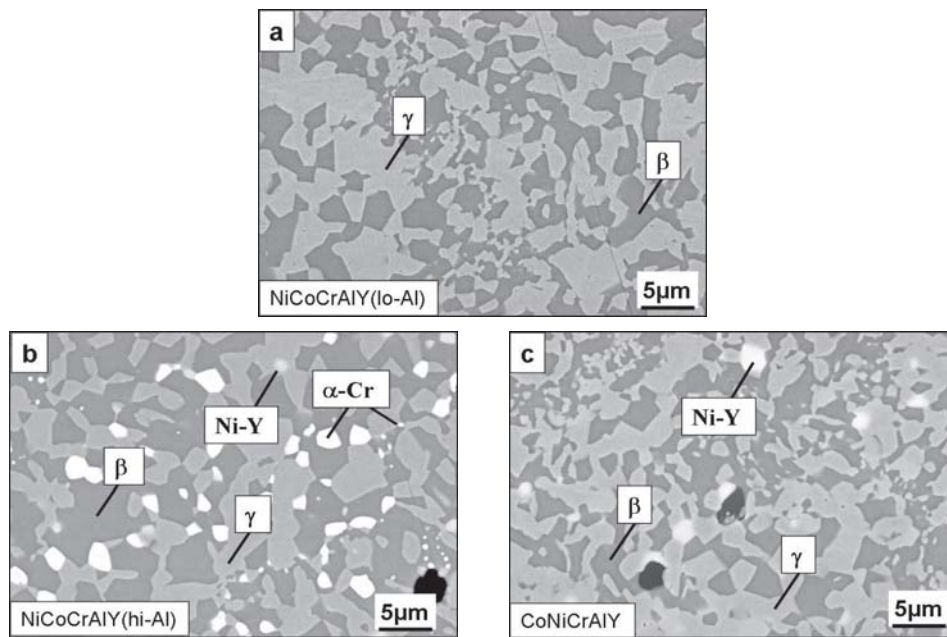


Fig 7.5 – SEM cross sections of specimens after 75h isothermal air exposure at 1000°C and subsequent water quenching. Ni-Y refers to intermetallic phases
a) NiCoCrAlY(lo-Al); b) NiCoCrAlY(hi-Al); c) CoNiCrAlY.

The microstructure of the CoNiCrAlY-coating obtained experimentally at 1000°C (Fig. 7.5c) does not differ noticeably from that obtained at 1100°C: it is composed of γ , β and Ni-Y intermetallic phases. Contrary to the modeling calculations, no evidence of the σ -

(Cr,Co) phase was found in the EDX and XRD spectra. One explanation for this might be that σ is a slow-forming phase [Muñoz-1], and the 75h of exposure might have not been a sufficient time for its well-defined formation. Furthermore, in contrast to the NiCoCrAlY(hi-Al) coating, due to the absence of an element with a high atomic number (Re) in CoNiCrAlY, the σ -(Cr,Co) phase in backscattered electron images has a grey contrast similar to that of γ , making its detection difficult.

7.3.3 Microstructure at 900°C

After annealing at 900°C, Ni-Y intermetallic phases were also observed in the NiCoCrAlY(lo-Al) (Fig. 7.6a); at this temperature, Y seems to be at least partially bound in all three coatings. In the NiCoCrAlY(hi-Al), numerous tiny α -Cr precipitates are found inside the β -phase particles. This suggests that the solubility of Cr in the dominant phases γ and β significantly decreases with decreasing temperature. In addition, few σ -particles also belong to the microstructure of this coating at 900°C (Fig. 7.6b). In contrast, ThermoCalc predicts a complete dissolution of the σ -phase above 880°C. This discrepancy might be related to the slow kinetics of σ -phase formation as pointed out above.

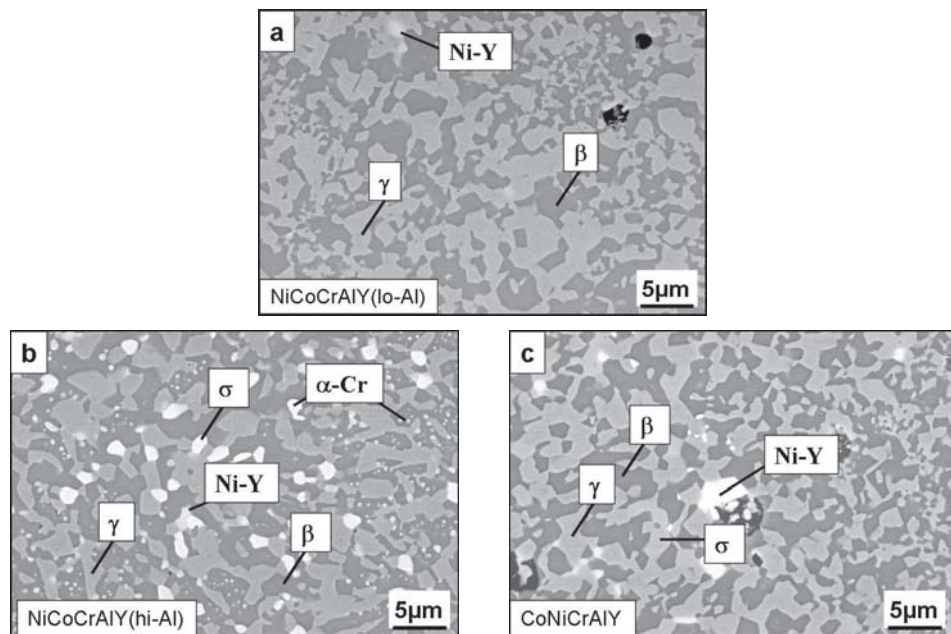


Fig 7.6 – SEM cross sections of specimens after 150h isothermal air exposure at 900°C and subsequent water quenching. Ni-Y refers to intermetallic phases
a) NiCoCrAlY(lo-Al); b) NiCoCrAlY(hi-Al); c) CoNiCrAlY.

Although at first sight the microstructure of the CoNiCrAlY-coating does not exhibit substantial differences with that observed for this coating at higher temperatures (a γ -Ni matrix, β -grains and finely distributed Ni-Y precipitates), XRD spectra from the specimen (Fig. 7.7) and various EDX measurements in the matrix revealed the coexistence of γ with the σ -(Cr,Co) phase as also predicted thermodynamically (Fig. 7.3). As discussed above, in the absence of Re, the differentiation between γ and σ -phases in the SEM-images is extremely difficult because of similar average atomic number for both phases.

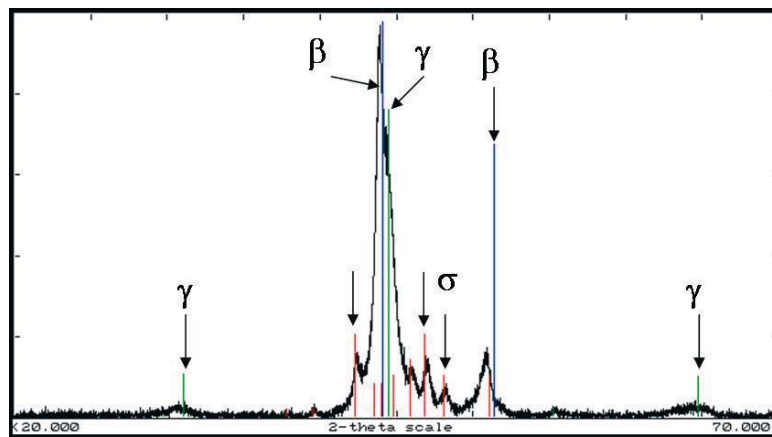


Fig 7.7 – XRD spectrum of CoNiCrAlY after 150h isothermal air exposure at 900°C and subsequent water quenching.

7.3.4 Microstructure at 800°C

The microstructures obtained after annealing at 800°C strongly deviate from those observed at 1100°C. Both Ni-base coatings contain γ' -Ni₃Al; in the high-Al modification this phase actually replaces γ -Ni as matrix. In contrast, in the CoNiCrAlY-coating, Co stabilizes the γ -phase by increasing its Al-solubility [Achar,Czech-2,Täck].

σ -phase particles can be observed after annealing at 800°C in the NiCoCrAlY(lo-Al). Large volume fractions of Cr-rich phases (σ and α) are found in the NiCoCrAlY(hi-Al) promoted by its relatively high Re- and Cr-contents (Fig. 7.8b). The β -particles contain very small α -Cr precipitates, as also observed by other authors [Baufeld]. The α -Cr was detected in the XRD spectra and the tiny precipitates were identified with WDX-mappings in TEM (Fig. 7.9). The existence of α -Cr can be correlated with a very low solubility of chromium in

the β -phase at 800°C. Such a microstructure is expected to considerably affect the mechanical properties of the coating material; in this case, the large amount of the brittle Cr-Re-rich phases and the absence of the γ -Ni phase can reduce the ductility of the MCrAlY-coating, and thus deteriorate the performance of the system, as also indicated in [Rae,Täck].

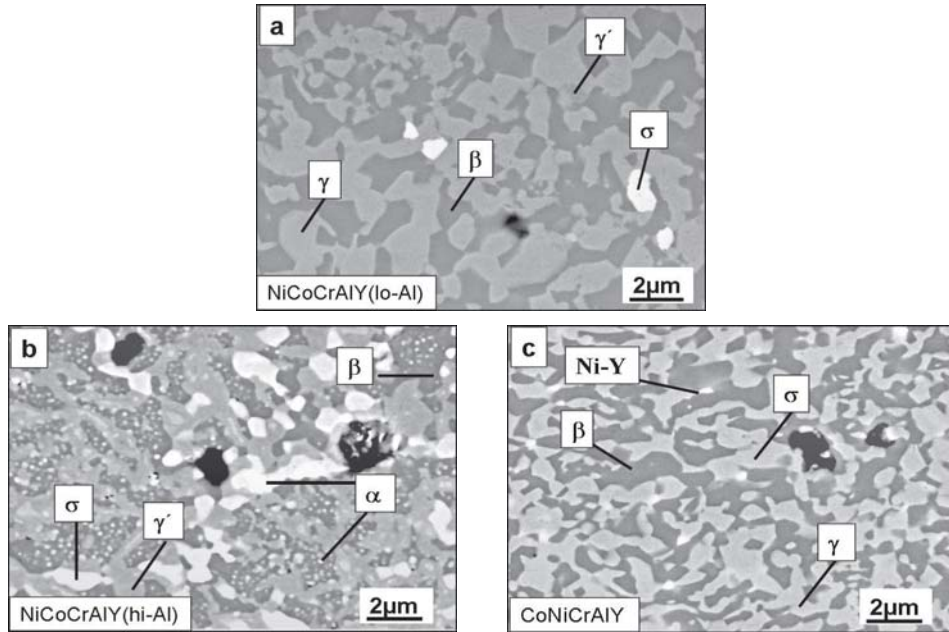


Fig 7.8 – SEM cross sections of specimens after 300h isothermal air exposure at 800°C and subsequent water quenching. Ni-Y refers to intermetallic phases
a) NiCoCrAlY(lo-Al); b) NiCoCrAlY(hi-Al); c) CoNiCrAlY.

The microstructure of the CoNiCrAlY-coating at 800°C resembles that observed at 900°C, with the difference that at the lower temperature the volume fraction of the Cr-rich σ -phase increased at the expense of the γ -phase.

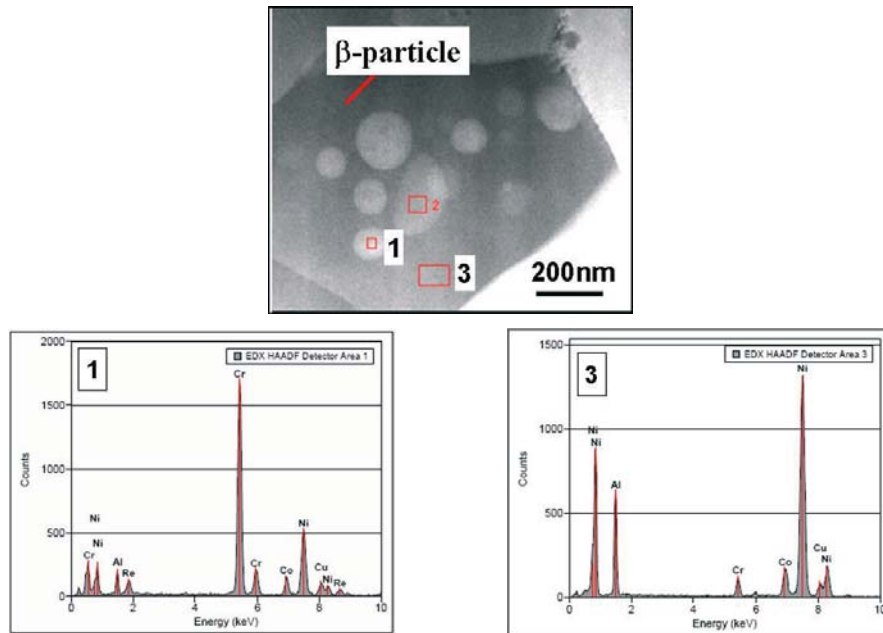


Fig 7.9 – TEM measurements on a β -particle in the NiCoCrAlY (hi-Al) after 300h isothermal air exposure at 800°C. Area 1 identified as α -Cr; area 3 identified as β -NiAl.

7.4 Physical CTE measurements on free-standing MCrAlYs

The coefficients of thermal expansion (CTE) were in argon from room temperature to 1100°C as explained in chapter 5. The results of this test in the temperature range 500-1000°C shown in Fig. 7.10 permitted detecting phase transformations in the Ni-base coatings by the appearance of peaks in the CTE values. For the NiCoCrAlY(lo-Al) this peak was registered in the temperature range 720-820°C, being in good agreement with the thermodynamic predictions of a phase transformation γ' to γ (Fig. 7.1) and the corresponding experimental observations (Figs. 7.6 and 7.8). A sharper peak in the CTE values with a maximum at 830°C was obtained for the NiCoCrAlY(hi-Al), correlated with the phase transformation γ' to γ predicted by the thermodynamic calculations although there is a discrepancy in the temperature at which this should occur (around 880°C in Fig. 7.2). The microstructures observed experimentally are in concordance with this result; this coating exhibited a γ matrix when annealed at temperatures above 900°C (Fig. 7.6) and a γ' matrix when annealed at 800°C (Fig. 7.8). The fact that the peak for this material appears sharper than that of the NiCoCrAlY(lo-Al) might be related to the fact that the phase transformation it undergoes is

abrupt according to the thermodynamic calculations (Fig. 7.2) whereas in the latter it is expected to occur gradually with changing temperature (Fig. 7.1).

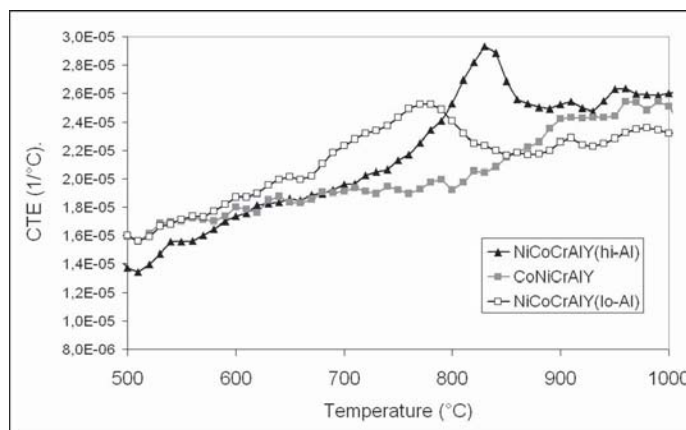


Fig 7.10 – Physical CTE as a function of temperature for the studied coatings.

The physical CTE values in the studied temperature range for the CoNiCrAlY do not show any abrupt change that could be associated with a phase transformation, in agreement with ThermoCalc predictions. Previous experiments [Muñoz-2] showed that a “peak” as found in the CTE-curve for the NiCoCrAlY-coatings (Fig. 7.10), is suppressed by increasing the coating Co-content.

7.5 Accuracy of thermodynamic calculations

7.5.1 Accuracy of phase composition calculations

Summarizing it can be said that the accuracy of the ThermoCalc calculations in the temperature range 800-1100°C was good in comparison with the EDX-measurements on the test specimens. To avoid a lengthy presentation of all the analyzed data, a selected condition for one of the coatings, the NiCoCrAlY(hi-Al) exposed in air at 800°C, is shown in Table 7.1. Despite the complex microstructure with heterogeneous, small phase precipitates found (Fig. 7.8b), a good agreement between the experimental and the calculated values is observed. Unfortunately for the Y-containing compounds no comparison was possible due to their absence in the software database.

Phase		Al	Cr	Co	Ni	Re
σ	Experimental	1,0	61,0	23,2	13,7	1,3
	ThermoCalc	0,2	65,9	23,0	9,4	1,5
γ'	Experimental	20,8	10,9	8,6	59,8	0
	ThermoCalc	20,6	8,5	8,3	62,6	0
β	Experimental	33,6	6,6	6,9	52,9	0
	ThermoCalc	31,8	7,9	8,5	51,8	0
α	Experimental	0	92,5	3,5	0	3,8
	ThermoCalc	0	89,8	4,2	0,8	5,2

Table 7.1 – Comparison of thermodynamic calculations with EDX measurements on test specimen NiCoCrAlY(hi-Al) after 300h annealing at 800°C. All values reported in wt.-%.

7.5.2 Accuracy of volume fraction calculations

The ThermoCalc software package not only calculates the molar fraction of every phase but also its volume fraction. In order to quantify this on the test specimens, the gray scale intensities of the SEM micrographs were separated using the image processing software analySIS[®]; an example is shown in fig 7.11. The phases exhibiting very similar grey intensities in the SEM images, e.g. the bright phases α -Cr, σ -(Cr,Co) and Ni-Y intermetallics, were combined into a single gray field and a sum of their phase volumes was determined.

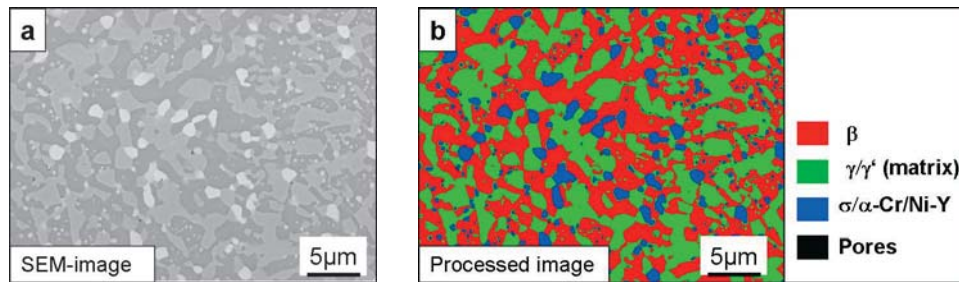


Fig 7.11 – Image processing for volume fraction quantification using analySIS[®].
Example of test specimen NiCoCrAlY(hi-Al) after 150h of annealing at 900°C
a) SEM-image; b) Phase colored map produced by the software.

In order to obtain a rough estimate of the software accuracy, the phase area fraction was simplified to be equal to the phase volume fraction and compared with the thermodynamic calculations. This quantification for the NiCoCrAlY(hi-Al) is presented in Fig. 7.12. A good agreement was observed for the bright phases in the SEM images (α -Cr, σ -

(Cr,Co) and Ni-Y intermetallics). In this comparison, the Ni-Y intermetallics, not predicted by the software, were simply assumed to be included in the sum ($\alpha + \sigma$). A good agreement was, however, not the case for the dominant phases γ and β , for which the calculated values seem to deviate from the microstructural analysis data presented in section 7.2 especially at 900°C, near the phase transformation temperature.

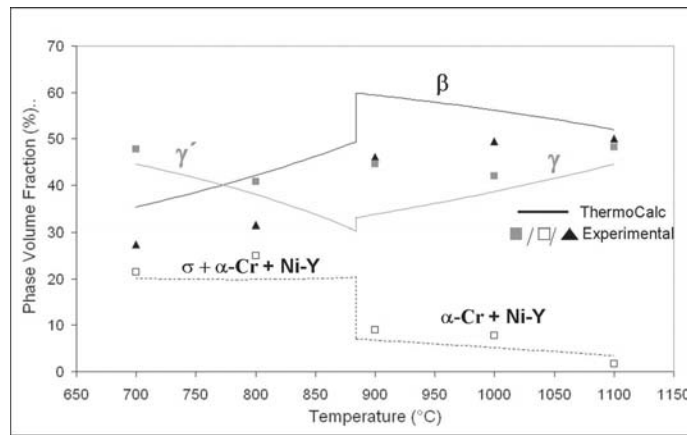


Fig 7.12 – Comparison of phase volume fraction calculated by ThermoCalc with that estimated on test specimens for NiCoCrAlY(hi-Al), as a function of temperature.

A similar deviation to that in the hi-Al modification was observed in the NiCoCrAlY(lo-Al) material between the measured and calculated values beneath the transformation temperature (Fig. 7.13). The amount of bright phases (σ -(Cr,Co) and Ni-Y intermetallics) was less than in the above presented coating alloy, therefore a good statistical agreement was harder to achieve. The tendency of σ and Ni-Y volume fractions to decrease with increasing temperature can nevertheless be recognized.

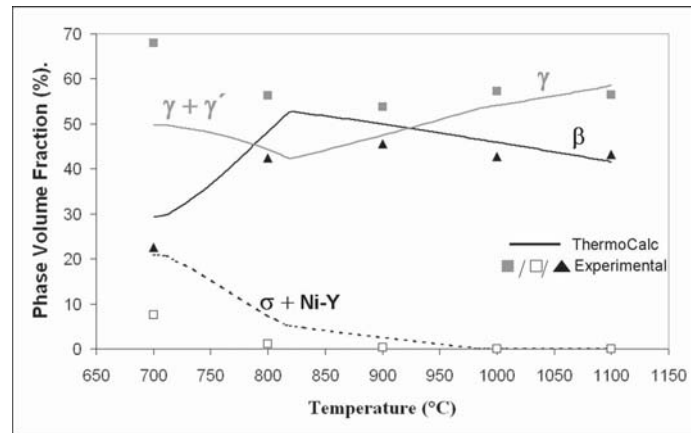


Fig 7.13 – Comparison of phase volume fraction calculated by ThermoCalc with that estimated on test specimens for NiCoCrAlY(10-Al).

The difficulty to distinguish the σ -phase from the γ -phase in the SEM images in the CoNiCrAlY-coating (as discussed in section 7.2) caused a large deviation of the volume fraction values from those calculated for these phases. For this reason, the presentation of this result is omitted.

7.6 Correlation of experimental findings with observations in a gas turbine blade after service

The microstructure analysis of the bond coat alloys in the previous sections showed that, within the temperature intervals of 100°C studied, especially in the NiCoCrAlY(hi-Al) coating major noticeable changes took place.

With the help of image processing such temperature-dependant changes can be better appreciated (see Fig. 7.14). With increasing temperature, the total amount of α , σ and Ni-Y particles is drastically reduced, besides the amount of tiny α -Cr particles within β decreases. Additionally, large grain sizes, together with a decreased amount of porosity are observed as temperature augments. The latter effect can be understood in terms of Arrhenius temperature dependence of diffusion controlled processes, i.e. the grain growth and sintering rates are accelerated at higher temperatures. A similar temperature-dependence analysis was reported in [Ellison].

The variations in MCrAlY-microstructures observed in Fig. 7.14, quantified by image analysis software, can be used to estimate the temperature in the bond coat during service in a gas turbine, which is generally difficult to assess. Moreover, it can be verified which areas along a blade profile are subjected to the highest thermal loads in operation. According to design values, the hotter areas for the BC in a blade with film/convective cooling are located in the trailing edge while the cooler ones are found behind the leading edge [Boyce], as presented in Fig. 7.15.

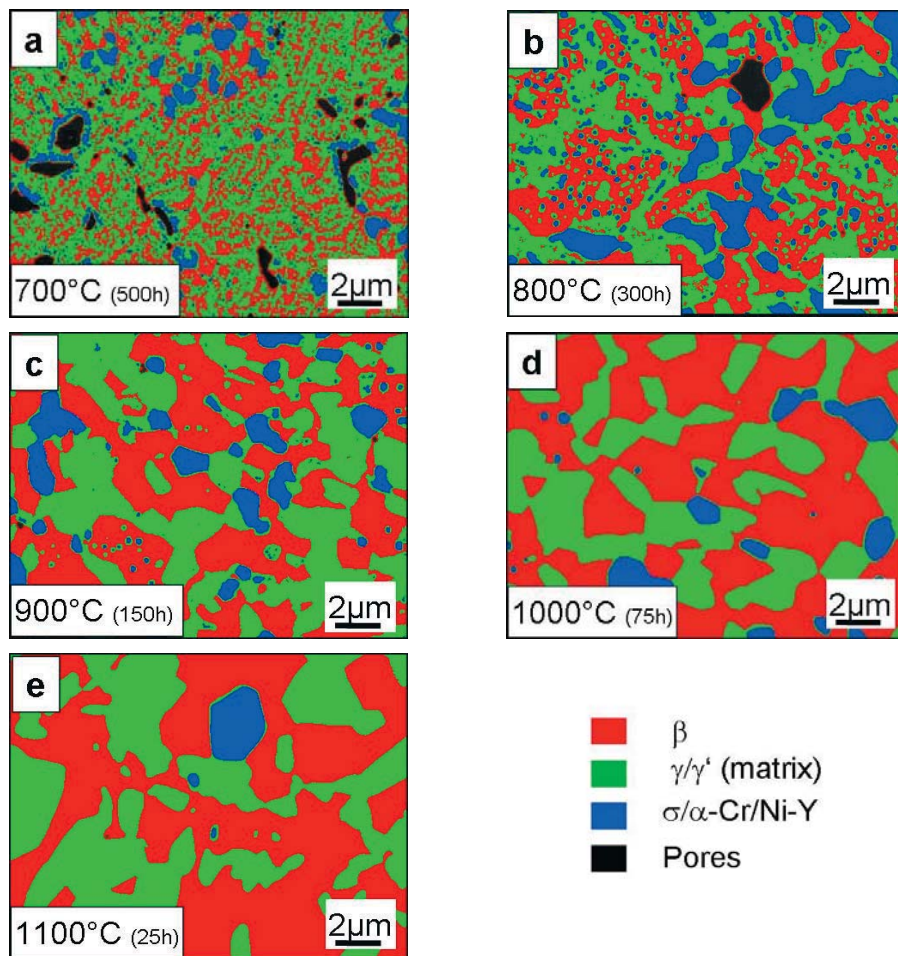


Fig 7.14 – Microstructure variation with temperature on NiCoCrAlY(hi-Al) test specimens.
a) 700°C; b) 800°C; c) 900°C; d) 1000°C; a) 1100°C.

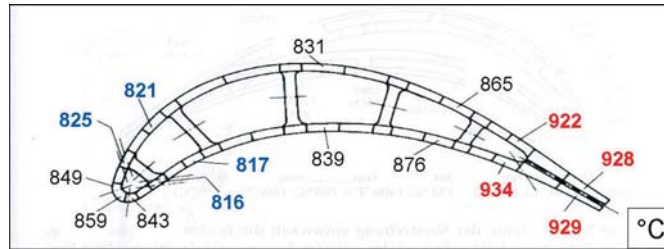
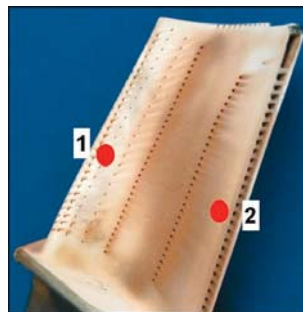


Fig 7.15 – Temperature at the bond coat. Example of estimated design values for a film/convective cooled blade [Boyce].

The BC microstructure of a gas turbine blade was investigated after approx. 16000h (equiv.: averaged operation time excluding shutdowns) of service in a power plant and compared with the experimental findings. The areas examined were chosen in the middle of the approximately 200 μ m thick bond coat, in order to minimize the effects of oxidation and/or interdiffusion with the blade's superalloy on the coating phase composition. Prior to this analysis, it was verified with EDX that the actual chemical composition of the coating corresponded to its nominal one. It is thus possible to compare it with the analyzed MCrAlY specimens.



Leading edge

Trailing edge

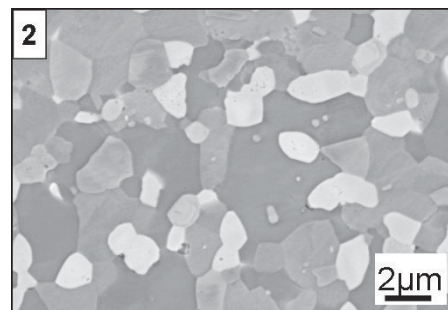
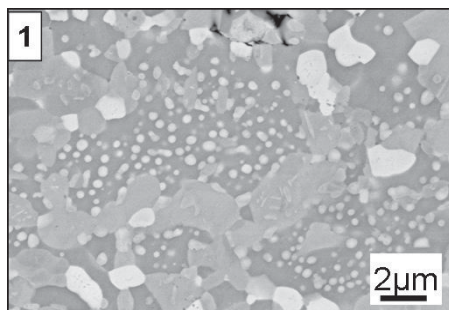


Fig 7.16 – SEM cross-section images of the BC microstructure in the leading edge (1) and in the trailing edge (2) of a gas turbine blade after 16000h (equiv.) of operation.

The commercial NiCoCrAlY(hi-Al) bond coat in the blade exhibits some microstructural differences depending on the analyzed location (fig 7.16). The area shown in fig 7.16 corresponding to the leading edge exhibits numerous tiny α -Cr particles inside the β -phase whereas in the area corresponding to the trailing edge these Cr-Re-rich phases are almost exclusively formed as larger particles. The processed SEM-image from the investigated area of the leading edge (Fig. 7.17a) is presented in Fig. 7.17b.

Turbine blade (leading edge)

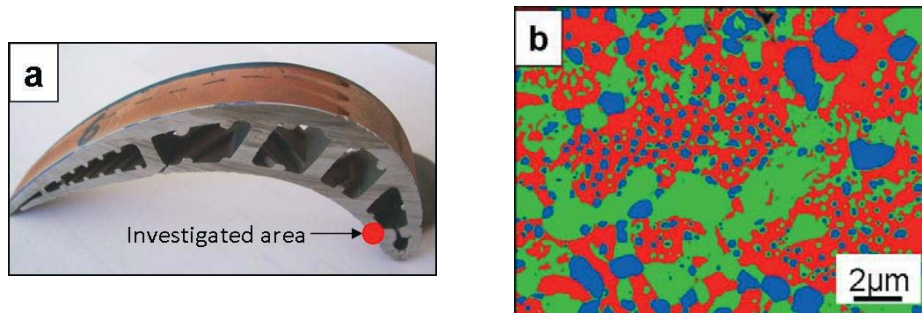
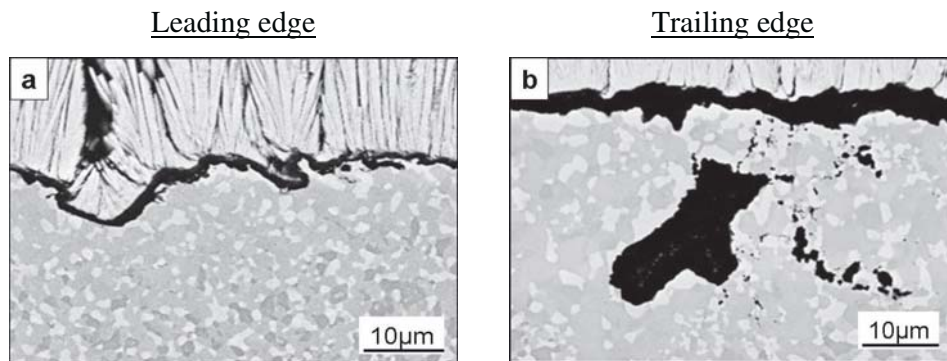


Fig 7.17 – Investigated area on the leading edge of the turbine blade after 16000h (equiv.) of operation (a) and BC microstructure of the NiCoCrAlY(hi-Al) coating in this location (b).

An optical comparison of the BC microstructure observed in the leading edge of the turbine blade with that found in the free-standing specimens after isothermal annealing (Fig. 7.14) suggests that the temperature of the coating in this area of the blade was close to 800°C during operation. Measurements of the TGO thickness on the cross-sectioned blade are in agreement with this temperature estimation, since it did not exceed 2µm after the long time operation (Fig. 7.18). On the contrary, the average oxide thickness in the selected areas of the trailing edge was over 3µm. This area was presumably exposed to a less intensive air cooling.

A comparison of the BC phase distribution observed in the trailing edge of the blade (Fig. 7.19) with the annealed test specimens of Fig. 7.14 indicates that the coating in this area of the blade might be exposed to a temperature of around 900°C during service. Although the coatings compared were subjected to different cooling rates, i.e. the specimens were quenched whereas the blade experienced a slower cooling; it is known that σ is a slow-forming phase [Muñoz-1] hence, it is not believed to be a product of the lower cooling rate in the blade but of the actual temperature during the hours of exposure.



7.18 – SEM cross-section images of the TGO in the leading edge (a) and in the trailing edge (b) of a gas turbine blade after 16000h (equiv.) of operation.

The orders of magnitude of these values are in agreement with temperature estimates carried out for a Co-base bond coat in a different turbine blade after service using another methodology in [Dahl]. The authors estimated a metal temperature during operation of 796 (± 11) °C at the “coldest” location along the profile, and a temperature of 956 (± 2) °C at the “hottest” location.

Turbine blade (trailing edge)

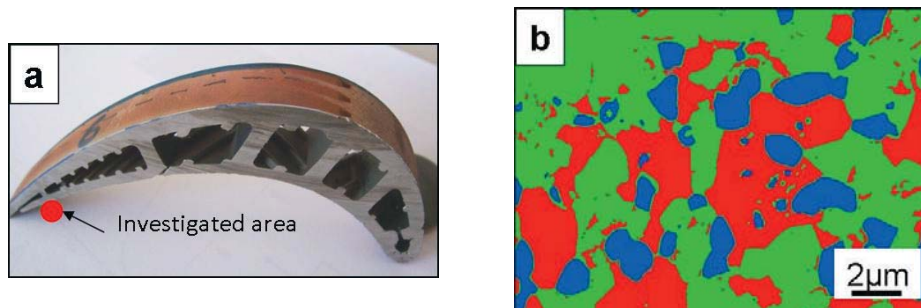


Fig 7.19 – Investigated area on the trailing edge of the turbine blade after 16000h (equiv.) of operation (a) and BC microstructure of the NiCoCrAlY(hi-Al) coating in this location (b).

7.7 Summary for temperature dependence of coatings’ phase compositions

The thermodynamic calculations of phase stability carried out with ThermoCalc[®] proved to be in good agreement with the experimental findings.

The microstructural investigation has provided a tool for estimating the real operation temperatures the coating alloys are exposed at in practical applications. The results showed

that they are clearly lower than the temperatures at which usually the laboratory oxidation tests are conducted, i.e. above $T = 1000^{\circ}\text{C}$ [Lechner].

The conducted microstructural studies showed that the Ni-base coatings undergo phase transformations γ' to γ at temperatures between $700\text{-}900^{\circ}\text{C}$ while the CoNiCrAlY coating has phase stability in the wide temperature range investigated ($700\text{-}1100^{\circ}\text{C}$). It was proved that such phase transformations considerably increase the CTE of the coating alloys, which might have an effect on the scale adherence if these temperatures are reached or exceeded in operation (in the latter case the development of higher TGO stresses is expected upon cooling). Furthermore, the large formation γ' and brittle Cr-Re-rich phases such as $\alpha\text{-Cr}$ is expected to reduce the creep relaxation capability [Gleeson-1] especially in the NiCoCrAlY(hi-Al). These facts could tentatively explain why a lower residual oxide stress and more prompt oxide scale spallation was observed from the Ni-base coatings compared to the Co-base despite lower oxide growth rates on the former materials.

The CTE changes associated with the phase transformations cannot, however, explain differences in the scale resistance to spallation between the two Ni-base coatings. The NiCoCrAlY(lo-Al) coating, with a smaller CTE "kink", showed earlier and more extensive scale spallation in cyclic oxidation tests than NiCoCrAlY(hi-Al) (see Fig. 6.25). Therefore, there should be an additional effect responsible for the worse scale adherence on NiCoCrAlY(lo-Al), probably related to the scale microstructure and morphology, which will be studied in detail in the following chapters.

8. Geometrical effects on the oxide growth and morphology in MCrAlY-coatings

8.1 General Remarks

During the investigation in chapter 6 some geometrical variations in the bond coat originated during its production were observed. Especially the coating thickness and surface roughness seemed to vary in the test specimens. The variations in roughness go beyond the fact that an APS-TBC system has a rough bond coat surface while an EB-PVD system has a smoothened, nearly-flat coating surface. As shown in Fig. 8.1, VPS-deposited coatings can exhibit different degrees of roughness; the specimen surface in micrograph 8.1a has a lower amplitude-to-wavelength ratio than that in fig 8.1b.

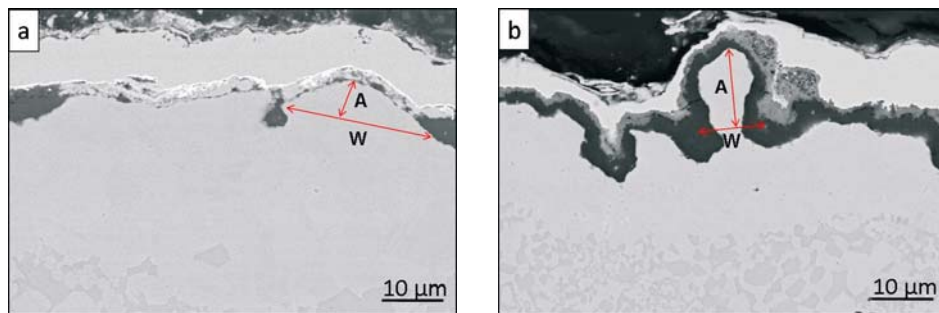


Fig 8.1 – SEM/BSE images of VPS CoNiCrAlY coatings after 16h of exposure in air at 1100°C exhibiting differences in roughness: a) low amplitude-to wavelength ratio; b) high amplitude-to wavelength ratio.

By comparing the thickness of different coatings produced with VPS, significant variations, arising from the deposition parameters, are found as illustrated in fig 8.2. The SEM images show two different batches of overlay coatings, one with an approx. 160μm thick coating, and another with an approx. 260μm thick BC. This variation in thickness was not only observed in test specimens but also in analyzed turbine blades.

In addition to these observations, it was annotated in chapter 6 that the scale uniformity and adherence on rough surfaces differed to those on flat surfaces, and that the scales grown on thick specimens exhibited a different morphology than those grown on thin specimens. This chapter is dedicated to understand why variations in these two geometrical parameters can influence the oxidation behavior of nominally equal MCrAlY coatings.

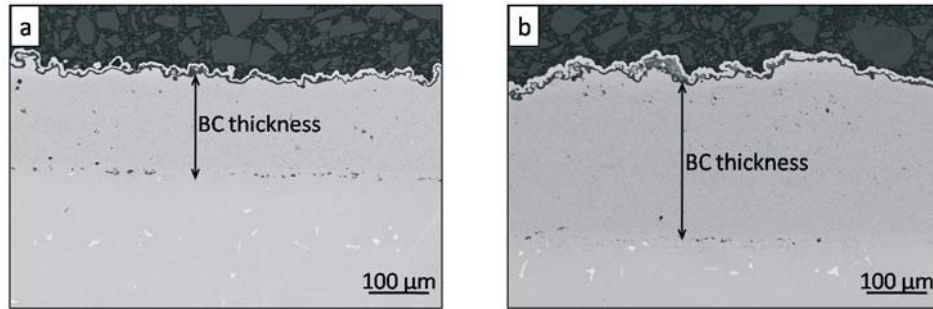


Fig 8.2 – SEM/BSE images of VPS-deposited overlay coatings after 16h of exposure in air at 1100°C exhibiting differences in thickness: a) NiCoCrAlY(hi-Al) with 160μm thick BC; b) CoNiCrAlY with 260μm thick BC.

8.2 Effect of coating roughness

It was reported by some authors that the surface roughness of the bond coat affected the scale adherence during cyclic oxidation. This effect is generally attributed to the generation of out-of-plane tensile stresses in convex surface areas [Yanar-1,Yanar-3,EvansA-3]; however, the effect of roughness on the oxide scale morphology and microstructure has not been extensively studied. In this investigation, free-standing and overlay coatings preserving its original roughness after VPS- and HVOF-deposition were subjected to discontinuous oxidation experiments.

8.2.1 TGO growth and morphology on rough surfaces

Fig. 8.3 shows cross-section images of free-standing NiCoCrAlY(hi-Al) in the heat treated state prior to oxidation, and after chosen exposure times in air at 1100°C. After vacuum (10^{-5} mbar) heat treatment (2h at 1100°C + 24h at 845°C), no continuous alumina scale had formed on the rough surface. Only small Al_2O_3 islands were observed (Fig. 8.3a). A subsequent exposure in air at 1100°C originated the formation of a TGO inhomogeneous in thickness and in chemical composition. With increasing exposure times, coarse Y-Aluminates formed being concentrated in the concave surface areas (also named “valleys” in this work) while the oxide in the convex surface areas (also named “peaks” in this work) was composed of “purer” alumina. The TGO growth in the valleys was observed to be more accelerated than in the peaks, which is in accordance with the fact that the Y-rich oxide compounds offer a faster diffusion path to oxygen than a dense pure Al_2O_3 layer [Kofstad-2,Ryan]. The SEM images also show that the β -depletion is stronger in the peaks than in valleys, which can be explained by a higher surface-to-volume ratio in the former. Finally, several cracks in the

oxide scale are observed in the specimen exposed for 406h; as mentioned before, tensile stresses tend to develop in the peaks leading to a more pronounced spallation in these areas.

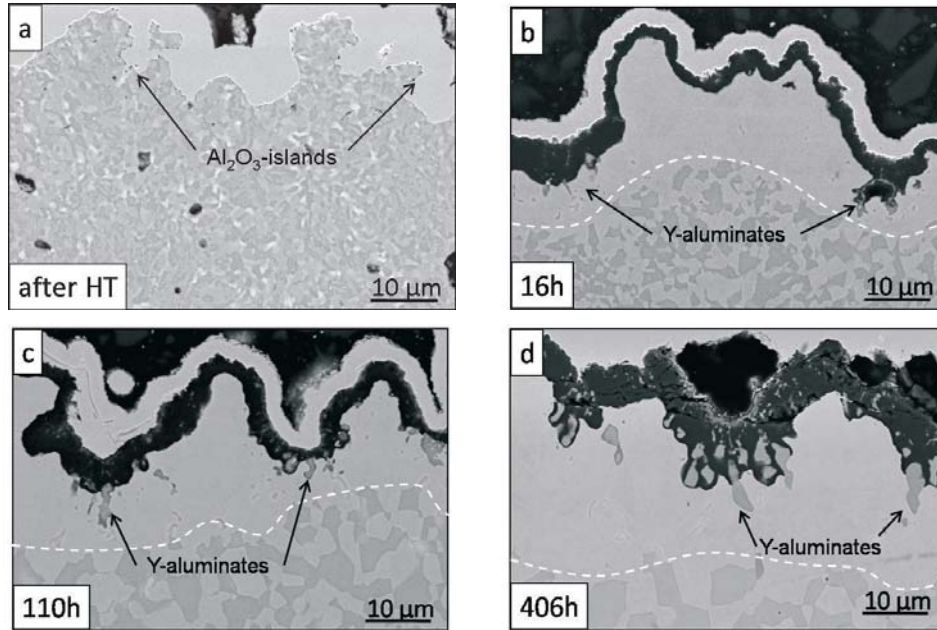


Fig 8.3 – SEM/BSE images of 2mm thick free-standing NiCoCrAlY(hi-Al) after a) heat treatment and b) 16h; c) 110h; d) 406h of discontinuous exposure in air at 1100°C. Dotted line delimitates the β-depletion zone.

Similar non-homogeneities were observed in the oxide grown on free-standing CoNiCrAlY specimens, i.e. thicker scale with more Y-rich oxide compounds in the valleys and thinner scales with less Y-aluminates in the peaks. A well distinguishable spinel top layer is part of the TGO in this Co-rich coating, as was also observed in the experiments presented in chapter 6. In Figs. 8.4b and 8.4d Y-aluminates are indicated in the micrographs, while Y-oxides are pointed out in Fig. 8.4c. In reality both types of compounds are generally found in the specimens; usually Y-aluminates form in the area of high O-activity and Y-oxides beneath this area as explained in section 6.3.2. A similar characterization of these compounds on a rough surface is presented in section 8.1.3.

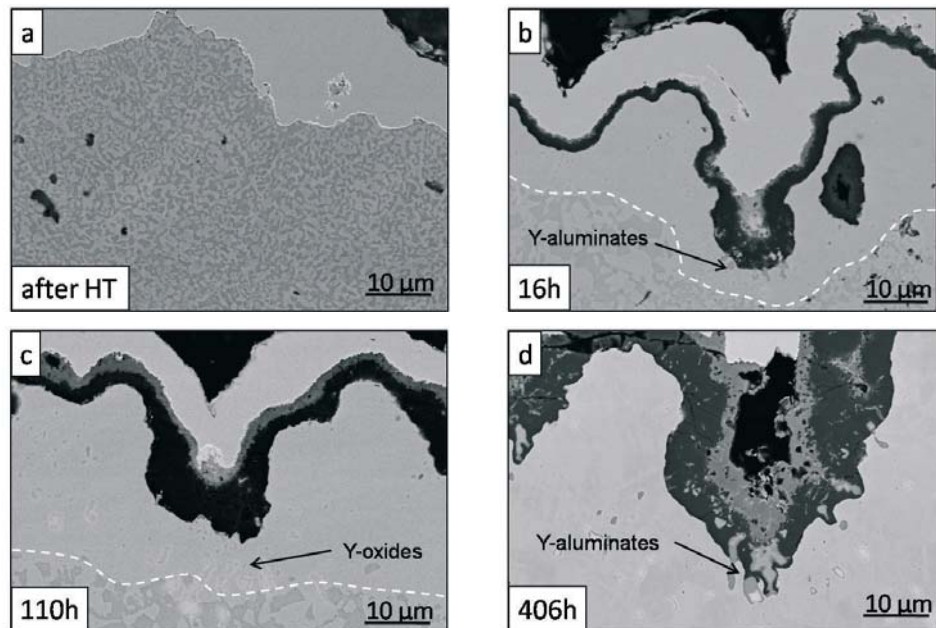


Fig 8.4 – SEM/BSE images of 2mm thick free-standing CoNiCrAlY after a) heat treatment and b) 16h; c) 110h; d) 406h of discontinuous exposure in air at 1100°C. Dotted line delimitates the β -depletion zone.

Fig. 8.5 shows cross section images of free-standing NiCoCrAlY(10-Al) specimens after identical heat treatment and oxidation conditions as the materials shown above. Despite some possible effect of the chemical composition, the described effect of roughness on the TGO morphology is also seen in the 2mm thick samples of this coating material. The mechanistic explanation for this effect, especially noticeable in Fig. 8.5d, is given in section 8.2.4.

A useful tool to unequivocally identify and locate these Y-rich compounds is cathodoluminescence (CL) imaging in SEM. An example of a free-standing CoNiCrAlY specimen after 25h isothermal exposure in air is presented in Fig. 8.6, where a clearly inhomogeneous TGO formed on its rough surface exhibiting spinel nodules in the peaks and Y-rich compounds in the valleys.

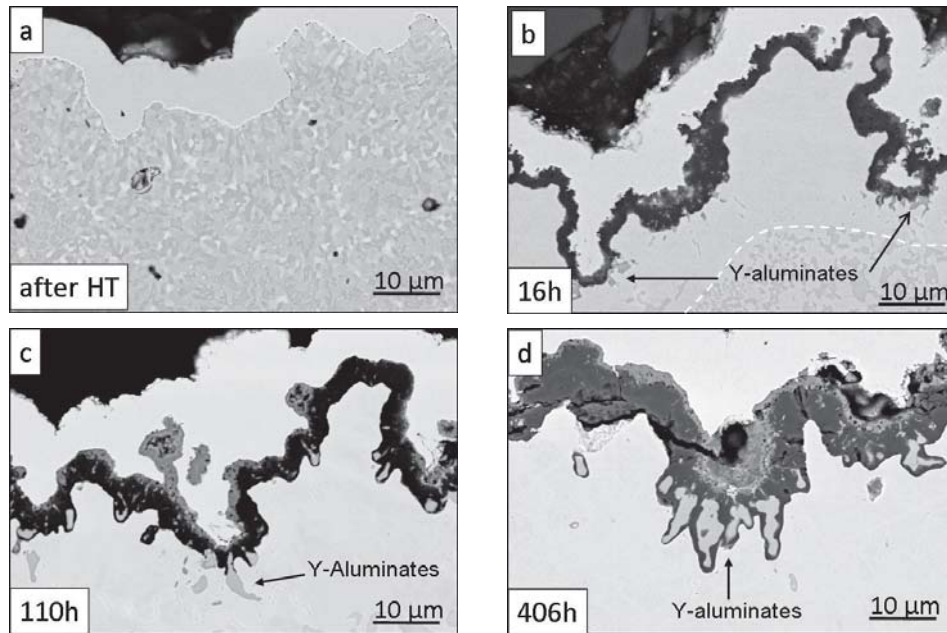


Fig 8.5 – SEM/BSE images of 2mm thick free-standing NiCoCrAlY(10-Al) after a) heat treatment and b) 16h; c) 110h; d) 406h of discontinuous exposure in air at 1100°C. Dotted line delimitates the β -depletion zone.

The surface roughness not only may cause an unequal distribution of spinels but also promotes their more extensive formation due to a more rapid depletion of yttrium and aluminum, which are the elements that form the most stable oxides in a MCrAlY (see mechanism in section 8.2.4). This effect is more pronounced in the Co-rich coating as observed even in macroscopic scale in Fig. 8.7a; the SEM micrographs show a well distinguished spinel top layer on the rough surface (Fig. 8.7c) and a hardly noticeable mixed oxide formation on the flattened opposite side of the same specimen (Fig. 8.7d).

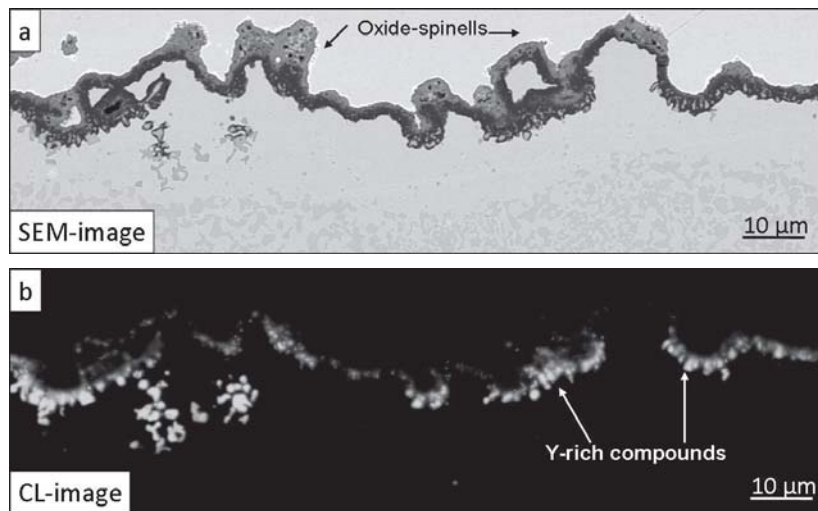


Fig 8.6 – 2mm thick free-standing NiCoCrAlY(hi-Al) after 25h isothermal exposure in air at 1100°C; a) BSE-image; b) CL-image.

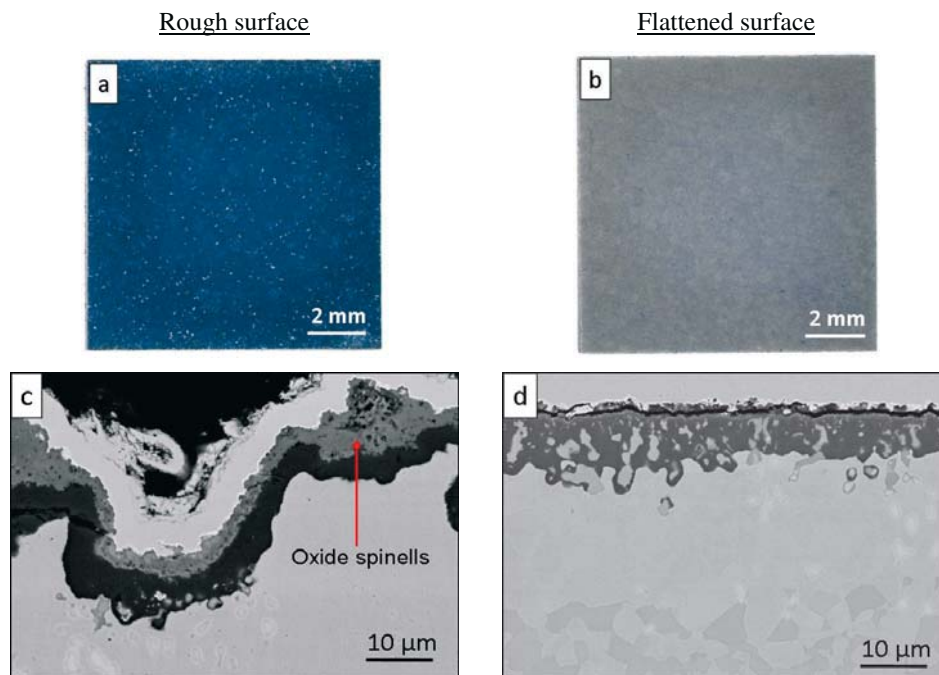


Fig 8.7 – 2mm thick free-standing CoNiCrAlY specimen after 406h of discontinuous exposure in air at 1100°C. Macroscopic images: a) rough surface, b) flattened surface; SEM cross-section images: c) rough surface, d) flattened surface

8.2.2 Temperature dependence of the effect of roughness

Complementary experiments using 2mm thick free-standing CoNiCrAlY specimens confirmed that roughness also causes a non-uniform TGO upon exposure in air at lower temperatures (900°C and 1000°C). This effect is however less pronounced than at 1100°C presumably due to the lower diffusion rates of yttrium at these temperatures, as can be seen in Fig. 8.8.

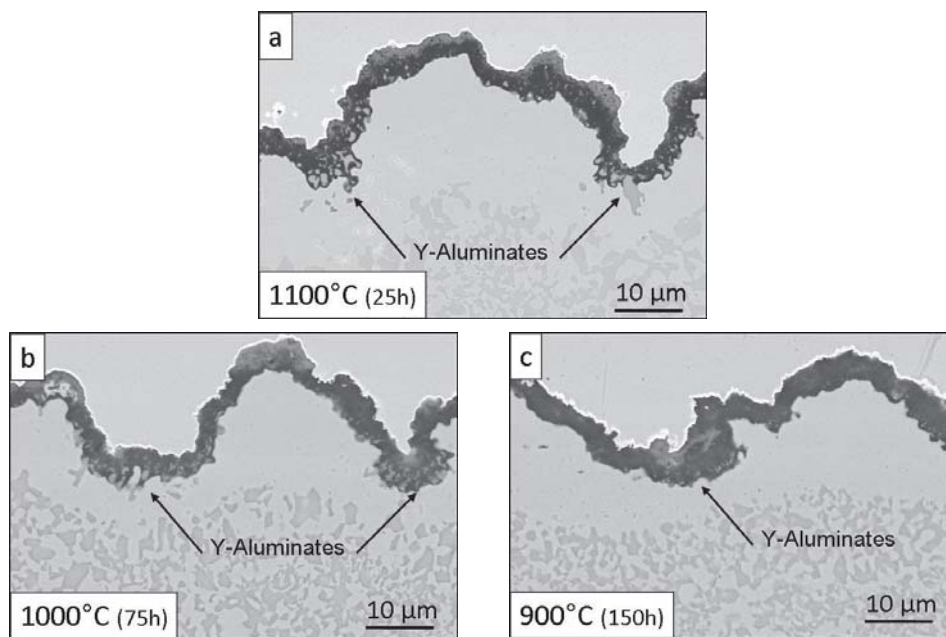


Fig 8.8 – Temperature dependence of the effect of roughness: 2mm thick free-standing CoNiCrAlY specimens after isothermal exposure in air at a) 1100°C, b) 1000°C, c) 900°C.

8.2.3 Characterization of Y-rich compounds

With the help of EDX-mappings, Y-rich compounds concentrated in the concave surface areas (valleys) could be differentiated. The Y-oxides usually found as internal oxidation in the alloy could be distinguished from the Y-aluminates that generally form when these oxides are incorporated in the TGO or in the area of high O-activity, as a result of their reaction with Al (Fig. 8.9). In a SEM micrograph with good contrast, the grey particles located at the oxide/metal interface can be easily differentiated from the bright particles located deeper in the metal. By analyzing the maps of the single elements, the latter particles having higher concentrations of Y and no Al can be correlated with Y-oxides (Y_2O_3) whereas

the former, having lower concentrations of Y but presence of Al, can be correlated with Y-aluminates (YAlO_3 and $\text{YAl}_5\text{O}_{12}$). The two different types of Y-aluminates that form in MCrAlYs upon exposure at high temperatures were characterized in section 6.3.2 in oxidized flat surfaces. It was shown that the meta-stable phase YAP tends to transform into YAG. However, if the Al-activity is low, e.g. if the particle is enclosed in the oxide, this transformation reaction is slowed down.

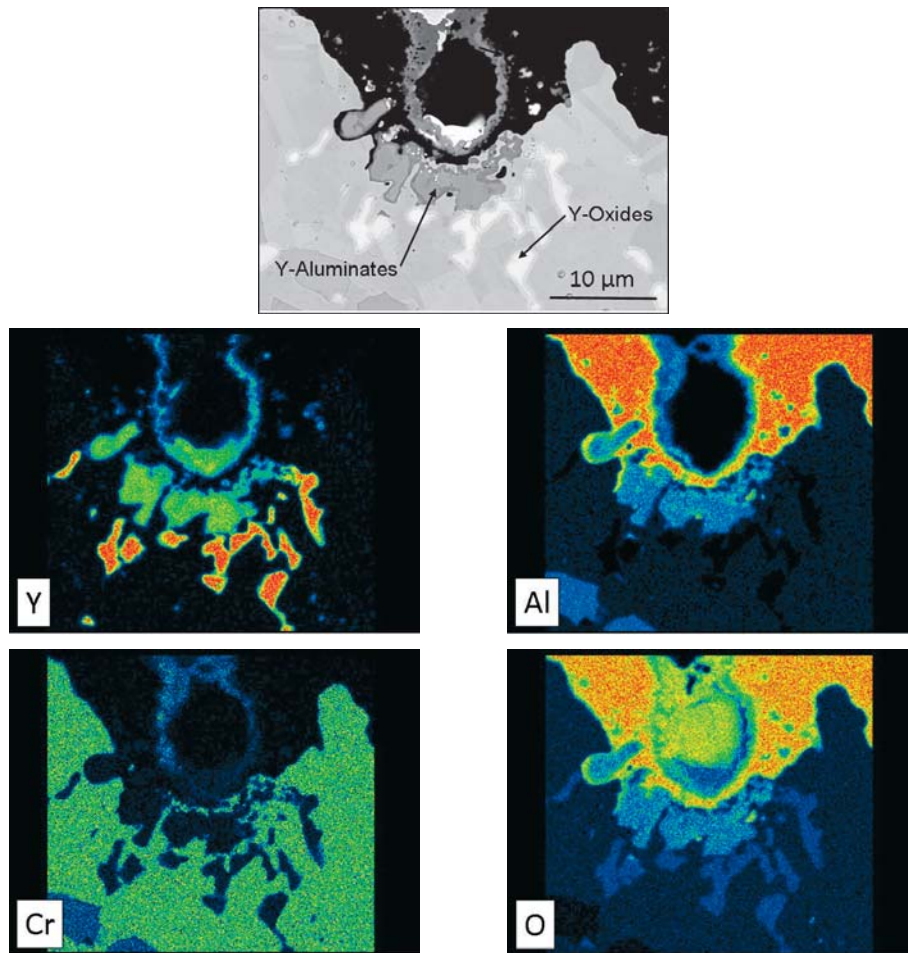


Fig 8.9 – EDX-maps showing Y, Al, Cr and O concentrations on a valley of a free-standing CoNiCrAlY coating with rough surface after 110h discontinuous exposure in air at 1100°C.

8.2.4 Mechanistic explanation of the effect of roughness

The non-uniform distribution of Y-oxides in a rough surface after high temperature exposure can be better appreciated in an optical metallographic image (Fig. 8.10a). The opposite side of the same 2mm thick specimen shown in Fig. 8.10a was ground before heat treatment and oxidation; this flat surface exhibits in contrast a uniform distribution of Y-oxides (Fig. 8.10b).

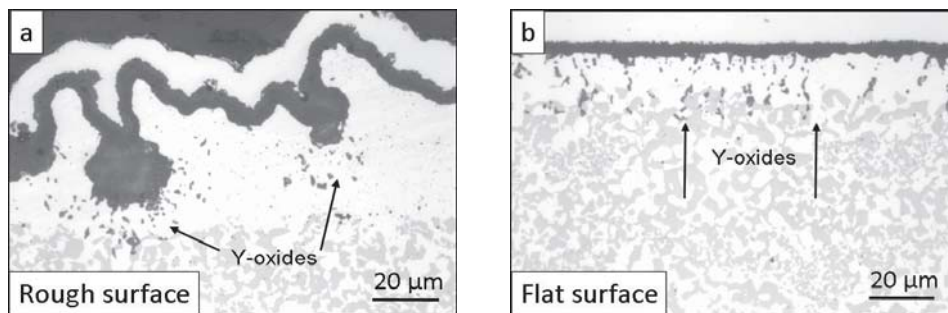


Fig 8.10 – Distribution of Y-oxides in a) rough surface and b) flat surface of a 2mm thick free-standing CoNiCrAlY after 110h discontinuous exposure in air at 1100°C.

This geometrical effect can be explained as follows: during vacuum heat-treatment and initial stages of oxidation, yttria rapidly builds up in the surface since it is the most stable oxide that can form in the MCrAlY-alloy (Fig. 8.11a). These Y-rich oxides consume part of the Al from the surface during its transformation to Y-aluminates, causing a local depletion of both yttrium and aluminum especially in the convex areas of the coating, where consequently non-protective spinels will form. However, with further exposure a protective alumina layer is established underneath these mixed oxides (Fig. 8.11b). At later stages of exposure, yttrium diffuses from the bulk of the coating predominantly to the concave areas, whereupon the diffusion path is shorter and the aluminum activity is higher than in the convex areas, enabling the growth of yttrium-rich precipitates (pegs). Having these areas a high O-activity, the reaction of Y-oxides with Al is promoted resulting in formation of Y-aluminates. More extensive incorporation of yttrium-aluminates in the oxide scale in the concave areas enhances oxygen inward diffusion through the scale, having as a result, a locally faster oxide growth (Fig. 8.11c) [Czyrska,Kofstad-2]. The local variations of the oxide composition and morphology on rough MCrAlY-surfaces indicate that definition of a critical TGO thickness in such systems is not possible. In addition, the stress in the oxide, which has been shown to be

the driving force for failure, has a different distribution on the rough surfaces compared to flat surfaces; in the latter the out-of-plane stress component prevails [HeM,Mumm,Tolpygo-3].

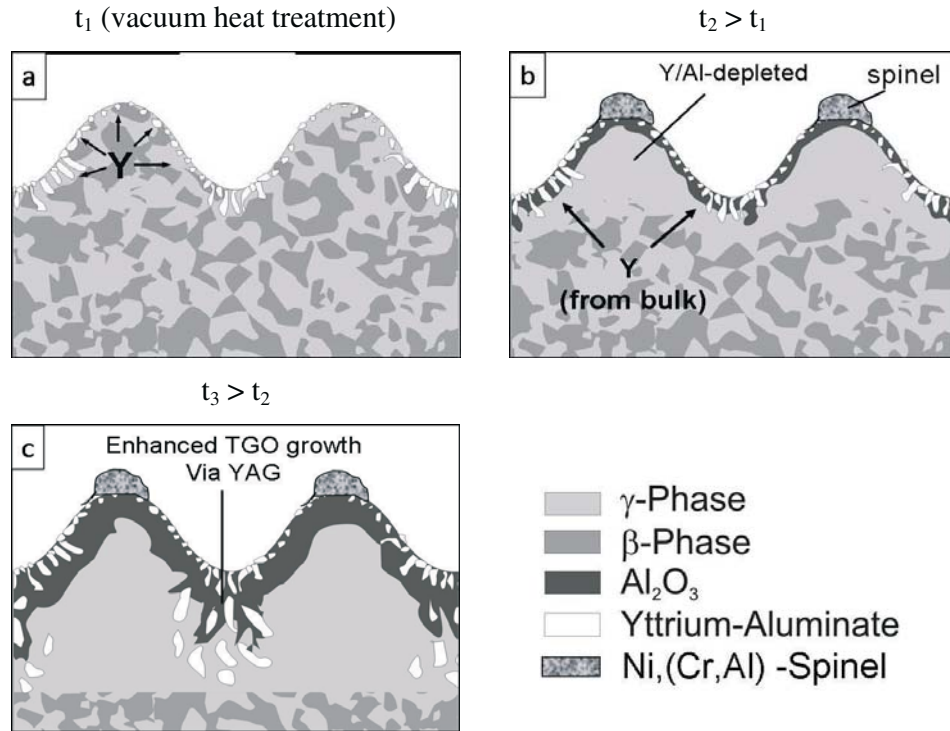


Fig 8.11 – Schematic illustration of the effect of roughness on the formation of a non-uniform TGO [Gil].

8.2.5 Limitations of the effect of roughness

As pointed out in the previous section, the effect of surface geometry is based on a non-uniform depletion of yttrium along rough surfaces. However, the fact that the amount of Y-rich oxide pegs is considerably higher in the valleys than in the peaks presupposes that this element, on the one hand is available in the necessary amounts in the coating and on the other hand, that it is mobile.

The first requirement was proven by using free-standing specimens with reduced thickness to 0.3mm of the same NiCoCrAlY(1o-Al) batch, and comparing it to the 2mm thick ones presented in Fig. 8.5. These free-standing specimens were intentionally thinned to

reduce their Y-reservoir. The material grinding was carried out only on one side on the specimens in order to preserve their original rough surface on the opposite side.

Fig. 8.12 shows the oxide scales formed in the thinned samples after 110h and 406h of exposure in air at 1100°C. It can be observed that in the thinner samples the oxide scales seem more homogeneous in composition along the surface than in the thick samples (compare with Fig. 8.5). Formation of Y-rich oxide pegs did not occur in the 0.3mm thick coatings after being exposed under identical conditions as the thick specimens. This evidences that for this material, there is not enough Y in a 0.3mm thick layer to cause the observable effect of roughness described above. The influence of Y-reservoir is more thoroughly addressed in section 8.2.

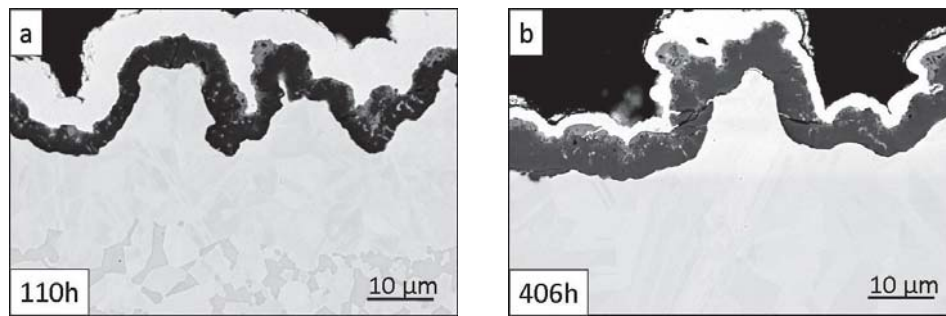


Fig 8.12 – Oxide grown on 0.3mm thick free-standing NiCoCrAlY(lo-Al) specimens after a) 110h and b) 406h of isothermal exposure in air at 1100°C.

The second requirement to induce the formation of non-uniform scales on rough surfaces stated that not only enough Y must be present in the coating but also the supply of this available yttrium to the surface must be enhanced. The outward diffusion of Y cannot take place when this element is somehow bound in the bulk.

The SEM micrographs in Fig. 8.13 illustrate this argument. The depicted cross sections show the oxide scales grown on HVOF-deposited (batch LZG; see chapter 5) 2mm thick free-standing NiCoCrAlY(lo-Al) specimens after exposure in air at 1100°C. These specimens were exposed under identical conditions to the VPS-deposited (batch LPM; see chapter 5) specimens shown in Fig. 8.5. The difference in TGO morphology between HVOF- and VPS-coatings is impressive, keeping in mind that both batches were composed of the same material. Thinner scales composed of almost exclusively Al_2O_3 formed on the HVOF specimens; the reasons for this difference are covered in detail in chapter 9. What is however

relevant to the present discussion, is that the bond coats deposited with HVOF exhibit very uniform scales along the surface, both in thickness and in composition. Non-uniformly distributed oxide-spinels and coarse Y-aluminates are absent in the TGO, different to the VPS-deposited coatings. The origin of this difference can be found in the oxygen content of the coating after deposition, which is according to chemical analysis, around 500 ppm (wt-%) in the plasma sprayed coating and around 2400 ppm (wt-%) in the HVOF-coating. An excess of oxygen in the MCrAlY is expected to partially bind after reaction the elements with the highest O-affinity, which are firstly yttrium and secondly aluminum. In the case of Y, a minor alloyed element (0.27 wt-% in this Ni-base coating), it is not surprising that most of it remains bound in the bulk in the form of oxides impeded to diffuse to the surface in the HVOF coating.

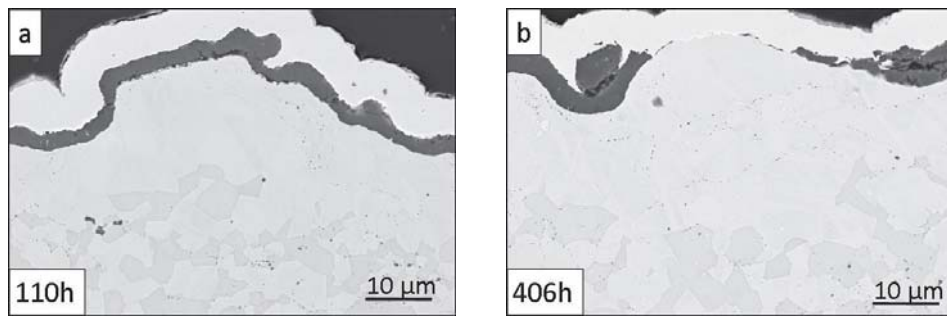


Fig 8.13 – Oxide grown on 2mm thick free-standing NiCoCrAlY(10-Al) specimens deposited with HVOF after a) 110h and b) 406h of isothermal exposure in air at 1100°C.

It is important to note that a partially spalled oxide observed in Fig. 8.13b cannot be considered as an indication of a worse scale adherence on the HVOF-coating compared to the VPS-coating. Statistic analysis across the samples surface led to the conclusion that this partial oxide spallation in the peaks is a common feature of rough surfaces in all free-standing coatings.

8.3 Effect of coating thickness

8.3.1 General remarks

It has been acknowledged in recent works that the specimen thickness can affect the oxidation behavior of an alloy. For FeCrAl-based commercial alloys it was reported that the propensity to scale damage during cyclic oxidation in air 1200°C, is increased with increasing specimen thickness (from 0.5 to 2mm) [Naumenko-1]. In similar tests on CMSX-4 specimens, different oxide growth and scale-spallation rates were found on 100µm thick samples than in 500µm thick ones [Orosz].

Indications of the influence this geometrical parameter can have on the oxidation behavior of MCrAlY-coatings were observed in the previous section after comparing the oxides formed on rough surfaces of 0.3mm and 2mm thick specimens of the same batch after exposure in air at 1100°C (Figs. 8.5 and 8.12). However, after the cognitions gained in the previous section on the effect of roughness, the present study focuses on the oxide formed on flat surfaces during cyclic and discontinuous high temperature exposure in order to avoid the formation of locally inhomogeneous scales. For this purpose, free-standing specimens were flattened and thinned by grinding to 1200 grit surface finish prior to the vacuum heat treatment.

By establishing the coating thickness as a variable, the idea of this investigation is to concentrate on the influence of the yttrium reservoir, which is defined as the effective amount of yttrium available for the incorporation in the TGO. More precisely, the yttrium reservoir is determined by the yttrium concentration and the volume to surface ratio of the coating. The latter can be understood as a first approximation as the coating thickness.

8.3.2 Effect of coating thickness during discontinuous oxidation

Vacuum annealed free-standing MCrAlY specimens of original thickness (2mm) and thinned specimens (0.15 and 0.7 mm) were oxidized at 1100°C for a total exposure time of 120 hours. The measured mass change values obtained for the CoNiCrAlY specimens are shown in Fig. 8.14.

A clear proportionality between the mass gain rate and the specimen thickness was found. For the 0.15mm thick specimen the mass change registered after 120h of exposure was close to 0.65 mg/cm². For the 2mm thick sample the mass change was around 1 mg/cm². The metallographic cross sections after the 120h exposure demonstrate that the extent of Y/Al-oxide precipitates and the thickness of the oxide scale depend on the initial specimen thickness (Fig. 8.15), the scale being thinner for the thinner specimens, in agreement with the plot in Fig. 8.14. Another clear correlation could be established between the specimen thickness and the depth of internal oxidation of yttrium, which was found to be around 30µm in the thickest specimen, 20µm in the 0.7mm thick specimen and inexistent in the thinnest specimen.

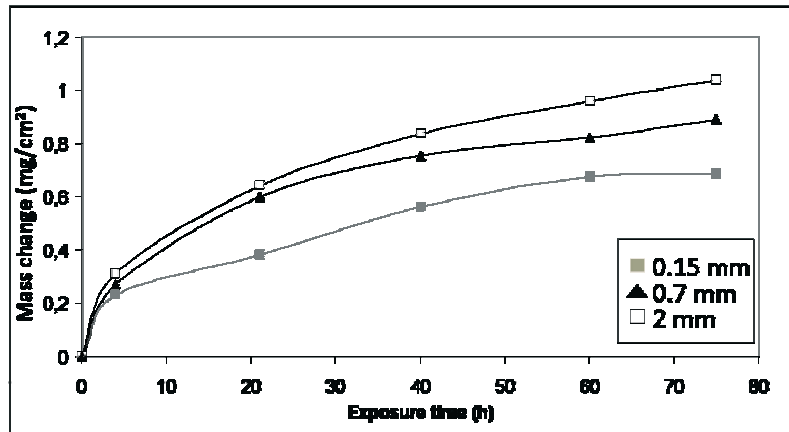


Fig 8.14 – Measured mass change of 0.15, 0.7 and 2mm thick free-standing CoNiCrAlY specimens during 76h of isothermal exposure in air at 1100°C.

These results strongly indicate that during long term oxidation at 1100°C the incorporation of yttrium into the scale and thus also the growth rate of the alumina scale are limited by the yttrium reservoir in the specimen. The oxide formed on the 0.15mm thick free-standing coating has a similar thickness, composition and morphology as that on the 0.15 - 0.2 mm thick bond coat beneath a TBC which was presented in chapter 6 (compare Figs. 8.15a and 6.4d). This strongly indicates that the differences in oxidation rates between the TBC specimen and the free-standing coatings (Fig. 8.15) are mainly related to differences in the yttrium reservoir in the coating, and an effect of Al-depletion can definitely be excluded.

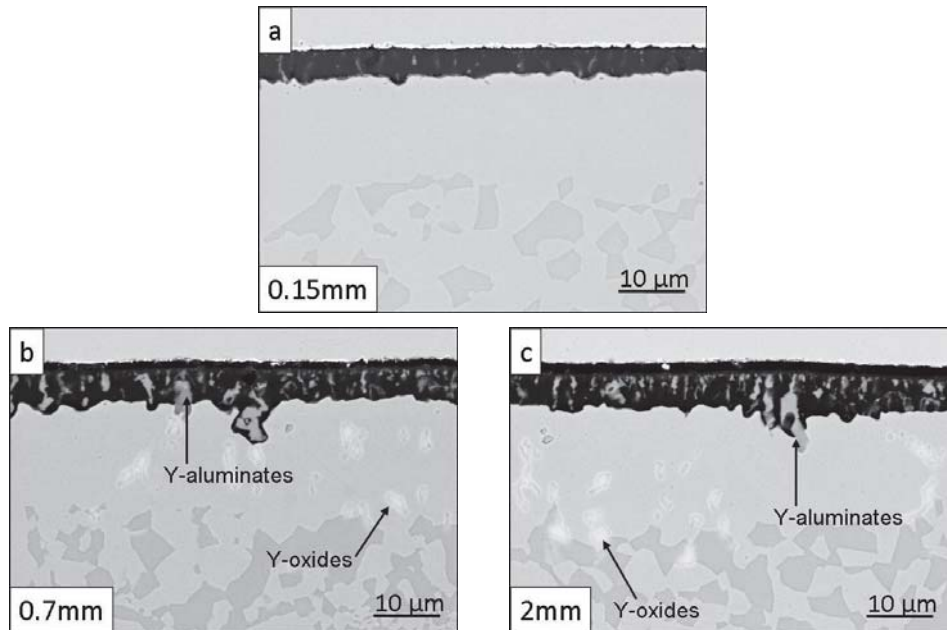


Fig 8.15 – SEM cross sections of a) 0.15, b) 0.7 and c) 2mm thick free-standing CoNiCrAlY specimens after 120h discontinuous exposure in air at 1100°C.

Aiming to prove if the effect of the Y-reservoir extends to lower temperatures, free-standing coatings were oxidized in air at 1000°C for up to 1220h. The mass gains of the NiCoCrAlY(lo-Al) specimens during exposure in air shows a higher oxide growth rate with increasing specimen thickness (Fig. 8.16) similar to the observations at 1100°C.

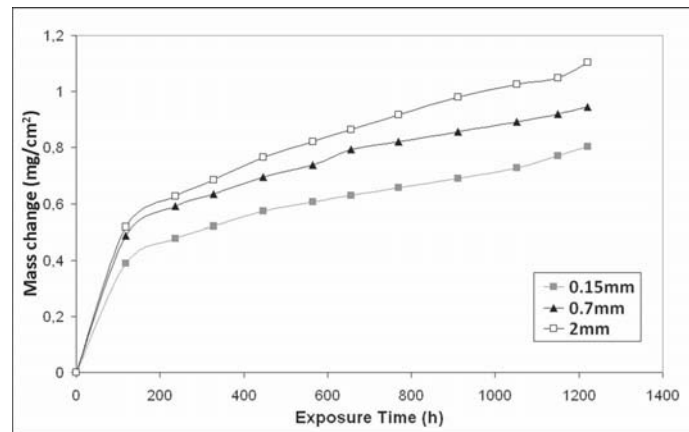


Fig 8.16 – Measured mass change of 0.15, 0.7 and 2mm thick free-standing NiCoCrAlY(lo-Al) specimens during 1220h of isothermal exposure in air at 1000°C.

SEM cross sections of the free-standing NiCoCrAlY(hi-Al) coatings of different thickness after the 1220h exposure are presented in Fig. 8.17. The results are, however, similar for the other two materials. As it was found after the tests at 1100°C (Fig. 8.15), thicker scales, richer in coarse Y-aluminates formed in the 0.7 and 2mm thick specimens. The average TGO thickness of the latter reached 5.2μm and 5.4μm respectively, whereas in the 0.15mm thick specimen it reached only 4μm. The depth of Y-internal oxidation exhibits a direct dependence with the sample thickness as well.

In the optical micrographs of Fig. 8.18, it is easy to see that Y-oxides are only present as tiny precipitates in the vicinity of the oxide/metal scale in the 0.15mm thick specimen (Fig. 8.18a), whereas these compounds form as deep as 20-30μm in the alloy in the 2mm thick specimen (Fig. 8.18c). In Fig 8.18b is observed that the Y-reservoir in the 0.7mm thick sample was enough to form large amounts of Y-rich pegs in the scale but not enough to form the same extent of Y-internal oxidation.

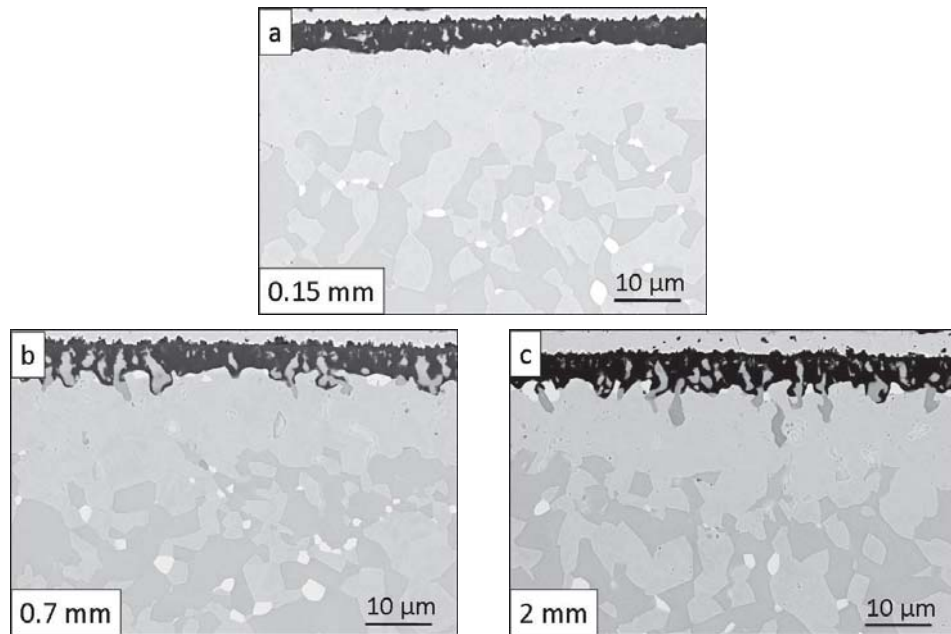


Fig 8.17 – SEM images of a) 0.15, b) 0.7 and c) 2mm thick free-standing NiCoCrAlY(hi-Al) specimens after 1220h of discontinuous exposure in air at 1000°C.

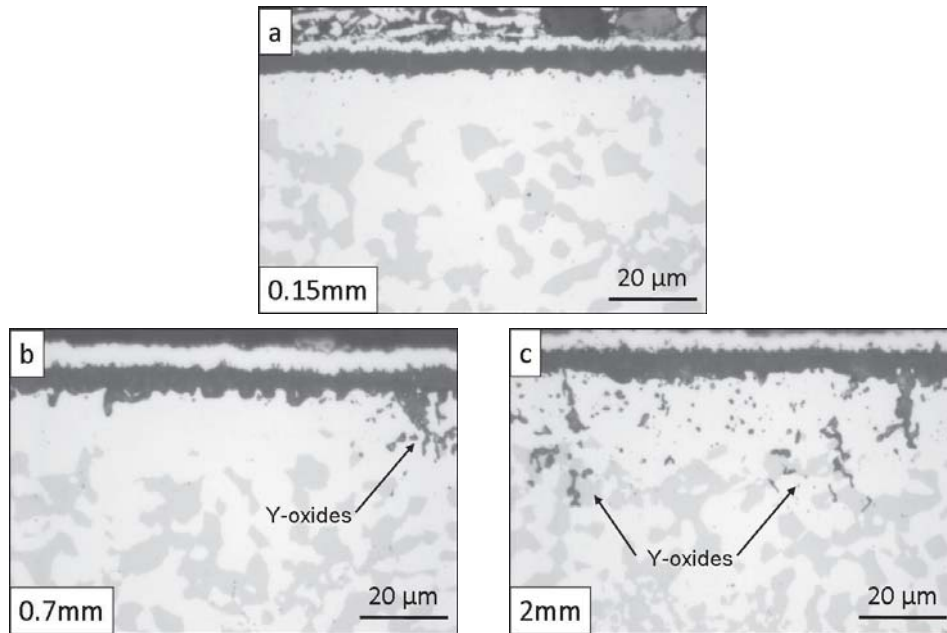


Fig 8.18 – Optical micrographs of a) 0.15, b) 0.7 and c) 2mm thick free-standing NiCoCrAlY(hi-Al) specimens after 1220h of discontinuous exposure in air at 1000°C.

8.3.3 Effect of coating thickness during cyclic oxidation

The discontinuous tests revealed the influence of the Y-reservoir on the TGO growth rate and morphology; however no indications of its influence on the scale adherence were obtained for the selected exposure conditions. For this reason, cyclic oxidation tests (2h heating, 15min cooling) in air at 1100°C up to 1300h were carried out in order to monitor specifically the scale resistance to spallation. Since the extent of the described effect in the 0.7mm thick specimens did not substantially differ from that in the 2mm thick specimens (see section 8.3.2), the former were omitted from the cyclic experiments. Specimen weighing and consequent mass change calculations took place after every 18h at high temperature during testing as had been introduced in section 6.3.4

After the cyclic exposure of the 0.15mm thick free-standing coatings, the three tested bond coats showed qualitatively similar material-dependent tendencies as the 2mm thick specimens (compare Figs. 6.25 and 8.19). These were a period of scale growth (mass change increase) followed by mass change decrease. The initiation of scale spallation was observed earlier on the NiCoCrAlY(lo-Al) and later on the NiCoCrAlY(hi-Al). For the 0.15mm thick

CoNiCrAlY specimen there was no clear evidence of scale spallation. The cyclic testing of the NiCoCrAlY(lo-Al) specimen was stopped after 918h due to pronounced spallation. In Fig. 8.20 are plotted together the mass change curves of specimens of the same material with different thickness.

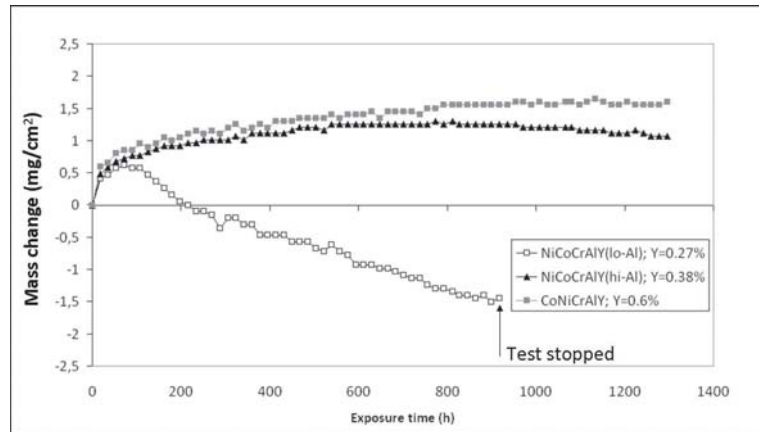


Fig 8.19 – Mass change of 0.15mm thick free-standing MCrAlY specimens during 1300h of cyclic exposure in air at 1100°C.

Comparing the mass change data of Fig. 8.20 it can be said that in spite of significant material-dependent differences in oxidation kinetics (see section 6.3), the effect of Y-reservoir was observed in all bond coats. The TGO growth on the 2mm thick specimens was 20-40% faster compared to that on their thinner counterparts. The reason for this effect is a more pronounced enrichment of coarse Y-aluminates in the thicker samples, which act as short-circuit paths for oxygen transport through the scale, as indicated by SEM cross section images in Fig. 8.21 (note that the TGO on NiCoCrAlY(lo-Al) specimens had spalled before completion of the test and therefore could not be analyzed in cross section). On the 0.15mm thick CoNiCrAlY specimen the average TGO thickness reached 8 μ m (Fig. 8.21a) while on the 2mm thick this value exceeded 14 μ m; pegs formed locally up to approximately 20 μ m (Fig. 8.21b). In the case of NiCoCrAlY(hi-Al), the scale on the thinned specimen reached an average of 7 μ m in thickness (Fig. 8.21c) while that formed on the 2mm thick specimen reached 12 μ m (Fig. 8.21d).

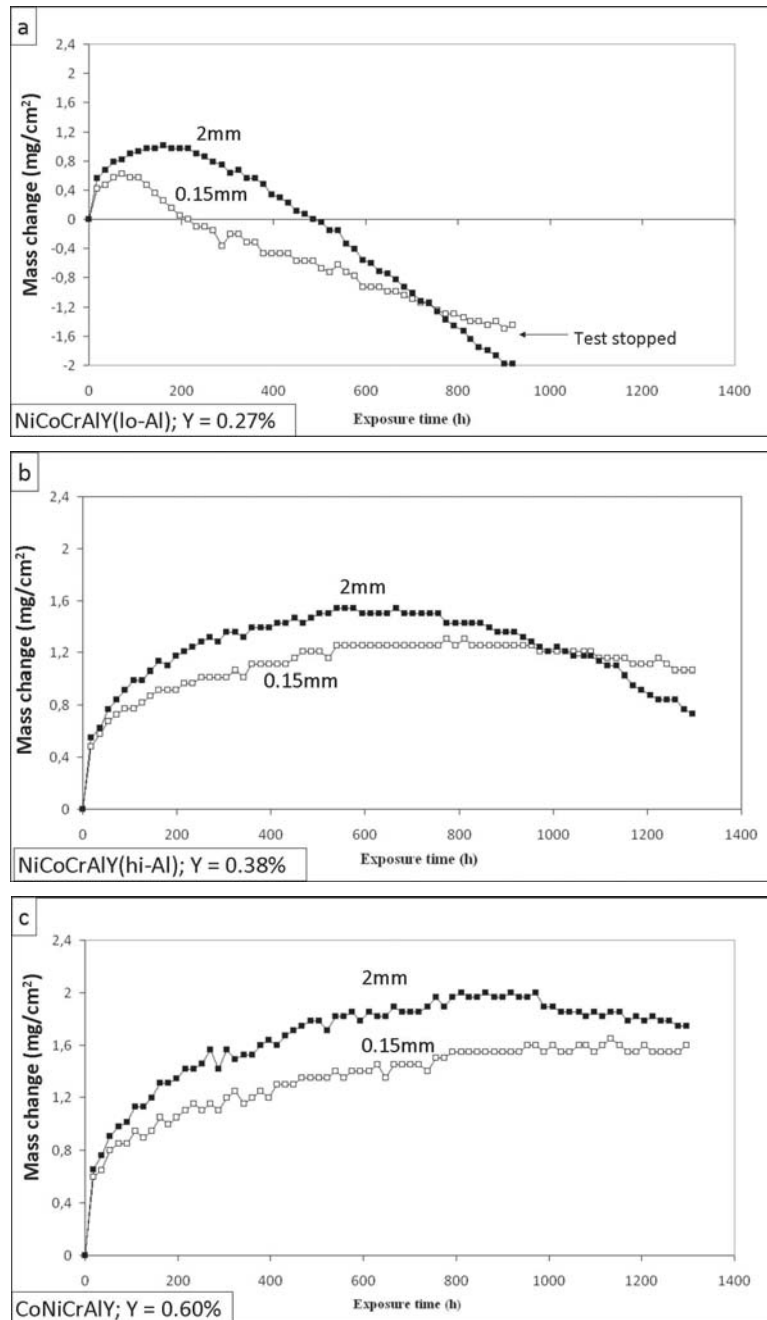
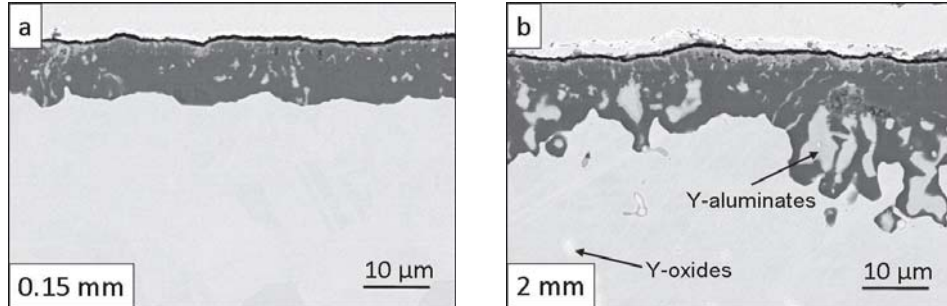


Fig 8.20 – Mass change of 0.15 and 2mm thick free-standing a) NiCoCrAlY (lo-Al), b) NiCoCrAlY (hi-Al), c) CoNiCrAlY specimens during 1300h of cyclic exposure in air at 1100°C.

CoNiCrAlY



NiCoCrAlY(hi-Al)

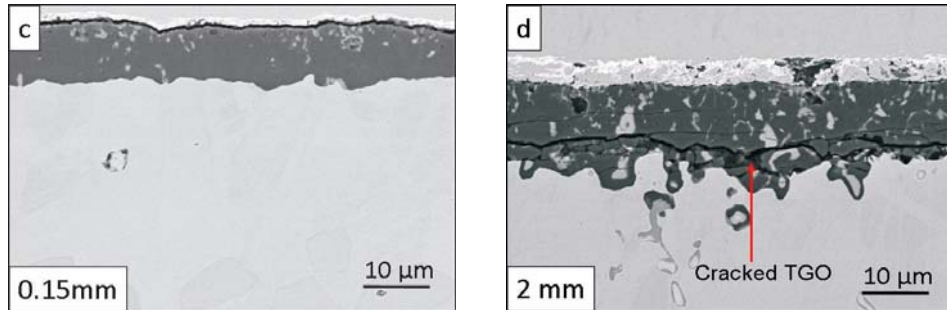


Fig 8.21 – SEM images of thick free-standing CoNiCrAlY specimens a) 0.15mm thick, b) 2mm thick and NiCoCrAlY (hi-Al) specimens c) 0.15mm thick, d) 2mm thick after 1300h of cyclic exposure in air at 1100°C.

One interesting aspect regarding the scale adherence is that in the coatings with higher concentrations of yttrium (0.38 wt.-% for the NiCoCrAlY(hi-Al) and 0.60 wt.-% for the CoNiCrAlY) a measurable mass loss in the thin specimens is seen to start later than in the thick specimens. More precisely, in the CoNiCrAlY coating, the effect is observed after approximately 1000h of exposure on the thick specimens whereas in the thin specimens this was not observed after the total exposure of 1300h (Fig. 8.20c). In the NiCoCrAlY(hi-Al), noticeable mass loss was seen to begin after 600h of cyclic exposure in the 2mm thick specimen and only after 800h in the 0.15mm thick one (Fig. 8.20b).

For the NiCoCrAlY(lo-Al), however, the measurable mass loss is seen to start later in the 2mm thick specimens than in the thinned specimens. It was observed to occur after 180h in the 2mm thick specimens, and already after 90h on the 0.15mm thick specimen (Fig. 8.20a).

The mass change data of Fig. 8.20 for NiCoCrAlY(hi-Al) and CoNiCrAlY is in agreement with macroscopic pictures of the specimens after the cyclic exposure, which show clear signs of oxide spallation in the 2mm thick specimens while the thinned samples of both coatings exhibit an intact scale (Fig. 8.22). One explanation for this effect is the possibility of oxide stress relaxation through metal creep in the thin specimens as suggested by [EvansH-3] and as also illustrated in a SEM-image with a lower magnification (Fig. 8.23a). This relaxation is much more restrained in the massive 2mm thick specimens, so that the thermal stresses are expected to be higher in the oxide in this case. Another reason can be that due to the high growth rate on thick samples a critical scale thickness for spallation is reached earlier than in thin samples.

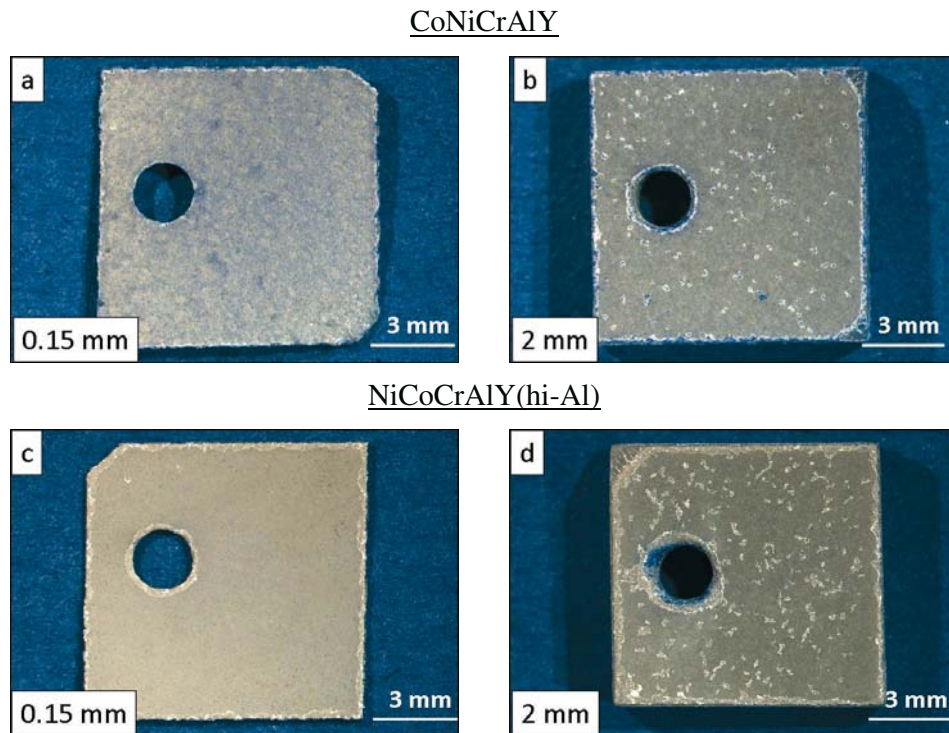


Fig 8.22 – Macroscopic pictures of free-standing CoNiCrAlY specimens a) 0.15mm thick, b) 2mm thick and NiCoCrAlY (hi-Al) specimens c) 0.15mm thick, d) 2mm thick after 1300h of cyclic exposure in air at 1100°C.

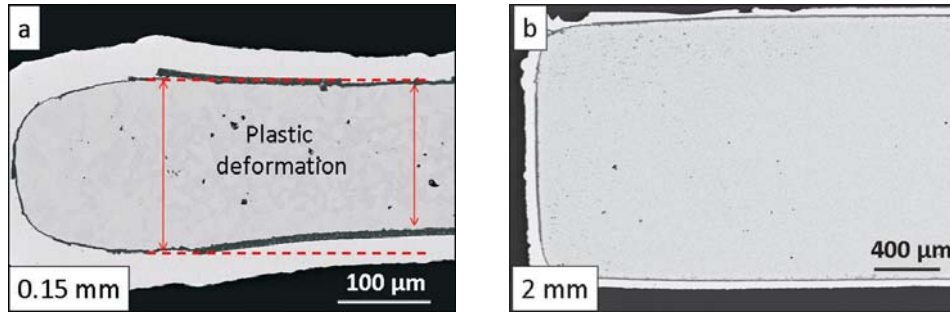


Fig 8.23 – Creep deformation observed in thin specimen leading to stress relaxation. Example of free-standing NiCoCrAlY(hi-Al) specimens a) 0.15mm thick, b) 2mm thick after 1300h of cyclic exposure in air at 1100°C.

8.3.4 Discussion on the effect of Y-reservoir on the TGO growth rate and adherence

Assessing the experimental observations of this section it can be said that the growth rate, morphology and adherence of the TGO can be affected by the yttrium reservoir in the MCrAlY coating. It is known from a large number of studies [Allam,Mennicke,Pint-2,Prescott] that the presence of yttrium in the coating is crucial for the TGO adherence. A new finding of the present work is, however, that the availability of Y for scale doping is determined not only by the Y-content but also by the coating thickness. It can be therefore expected that an exhaustion of the yttrium reservoir will lead to TGO spallation.

Experiments conducted in this work indicate that an increase of Y-reservoir (either through a higher Y-concentration (Figs. 6.25 and 8.19) or a higher coating thickness (Fig. 8.20a)) improved the scale adherence under the test conditions. This can explain the longer time to scale spallation in the 2 mm thick NiCoCrAlY (lo-Al) compared to the 0.15 mm thin specimen. However, an excess of this element reservoir in the coating might become adverse for the protective oxidation. A high yttrium reservoir leads to a high growth rate of the TGO [Nijdam-3] which should lead to earlier spallation by reaching faster the critical scale thickness, as it is apparently the case for the 2 mm thick NiCoCrAlY (hi-Al) and CoNiCrAlY in the present work. In addition, the coarse Y/Al-oxide precipitates that abundantly form in the TGO in the presence of large Y-reservoirs might be crack initiation sites [Naumenko-1] as has been observed in various test specimens (Fig. 8.24). This is understood by considering two factors. Firstly, the transformation reaction $\text{Al}_2\text{O}_3 + \text{YAP} (\text{Y}_2\text{O}_3) \rightarrow \text{YAG}$ is associated with a volume increase of 11% [Hay]. This can result in a higher oxide growth stress upon incorporation of the internal Y_2O_3 and/or YAP precipitates in the inwardly growing Al_2O_3 scale.

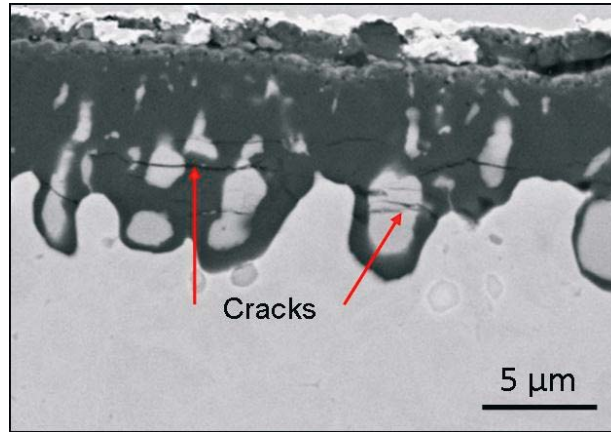


Fig 8.24 – Cracks in TGO preferentially across or in the immediate vicinity of coarse Y/Al-oxide pegs. 2mm thick CoNiCrAlY specimen after 406h of isothermal oxidation in air at 1100°C.

Secondly, once the garnet phase is established, the resulting TGO will be composed of two different compounds (alumina and coarse Y/Al-oxides) with different properties (CTE: $8.9 \times 10^{-6}/\text{K}$ for polycrystalline YAG and $6 \times 10^{-6}/\text{K}$ for Al_2O_3 , as reported by [Khattak]). This can cause an additional thermal mismatch inside the scale that could result in crack formation upon cooling. In contrast, a compact “purer” alumina scale will not offer such areas of concentration of stresses and has thus, a higher tolerance to the exerted compression [EvansA-2].

8.4 Summary on the geometrical effects

The oxidation studies on rough surfaces showed that this geometry can induce the formation of non-homogeneous scales and a non-uniform distribution of internal oxide precipitates. The resulting oxide can be substantially different to that grown on a flat surface of the same coating alloy.

Regarding the results presented on the effect of coating thickness, it is derived that for a given Ni(Co)CrAlY system, an optimum yttrium reservoir exists to obtain a compromise between the beneficial effect on oxide adherence without promoting a vast formation of Y/Al-compounds and hence extensively enhancing the growth rate of the oxide scale. A schematic representation of this compromise is depicted in Fig. 8.25.

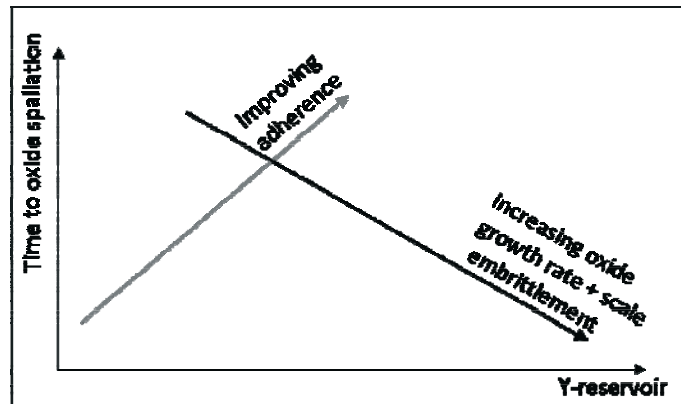


Fig 8.25 – Schematic representation of the positive and negative effects of the Y-reservoir.

Based on these considerations, 2mm thick specimens of CoNiCrAlY and NiCoCrAlY(hi-Al) seem to have large Y-reservoirs above an optimum value. In contrast, 0.15mm thick coatings of the same materials seem to be closer to the optimum Y-reservoir.

For the NiCoCrAlY(lo-Al), 2mm thick specimens have an Y-reservoir closer to the optimum level than 0.15mm thick samples. Considering a low Y-content (0.27 wt.-%) and an oxygen content of 440 wt.-ppm (Table 5.2) most of the Y present in this material is expected to be tied up in oxide compounds. The result is an extremely small Y-reservoir in the 0.15 mm thin specimen, leading to a very early time to scale spallation.

An essential finding of the present investigation is that the optimum yttrium doping of the oxide scale is determined by the thickness-dependant yttrium reservoir in the coating, rather than the Y-concentration only. An important implication of this finding for the practice is that the yttrium content for obtaining optimum TGO growth rate and adherence in a 100 μm thick BC layer will differ from that in a 200 μm BC.

Finally, the free-standing specimens thinned to 0.15mm have similar Y-reservoirs to the TBC specimens studied in chapter 6.1. However, one major difference exists in the sequence of processing steps between the free-standing coatings and the bond coats in the TBC samples. In the test samples the surface flattening was carried out before the vacuum heat treatment. In contrast, the composite bond coat + superalloy in the studied TBC specimens was subjected first to heat treatment and then to surface smoothing prior to EB-PVD TBC deposition. The implications of this processing difference on the MCrAlY oxidation behavior are investigated in chapter 9.

9. Effect of pre-treatment and processing on the oxidation behavior of MCrAlY-coatings

9.1 General remarks

The first part of this work determined important differences in the oxidation behavior and phase distribution depending on the chemical composition of the bond coat. Furthermore, the preceding chapter showed that the oxidation behavior of a MCrAlY-coating with fixed chemical composition can be also influenced by geometrical parameters such as surface roughness and coating thickness. Based on these findings, in the following investigation the bond coat chemical composition and the geometrical parameters mentioned above are kept constant by using specimens of the same material and with identical dimensions and surface roughness. The focus in this chapter is given to the influence of coating processing parameters. The parameters selected are the processing sequence for the production of smooth surfaces, the heat treatment conditions and the amount of oxygen impurities introduced during coating deposition.

The bond coat surface smoothening prior to EB-PVD TBC deposition can be carried out either before or after the heat treatment. Different manufacturers follow different processing sequences. Whether this can noticeably influence the oxidation behavior and scale adherence was investigated in the present work by high temperature exposure of free-standing coatings with flattened surfaces (1200 grit) produced in two different ways:

- Surface flattening (approx. 100µm of material removal) and subsequent vacuum heat treatment, further denoted in this work as Heat Treated (HT)
- Vacuum heat treatment and subsequent surface flattening, further denoted in this work as Heat Treated and Ground (HT+G). This procedure implied an approximate material removal of 100µm in depth after the heat treatment.

The second part of the study treats how the oxidation resistance of the bond coat is affected by the heat treatment conditions, which are established in practice to optimize the mechanical properties of the substrate. The use of a different superalloy as substrate can therefore imply the adoption of different heat treatment conditions. The standard two-stage vacuum heat treatment applied for the IN738LC was alternatively replaced by single-stage treatments in vacuum, both at high and low temperatures, and by an annealing in air at 900°C.

Ultimately, this chapter treats the influence on the oxidation behavior of impurities introduced during MCrAlY coating. The only impurity dealt with in particular is oxygen (see chemical analysis table 5.2). For this purpose a new batch of free-standing NiCoCrAlY(10-Al) was produced by HVOF, thus, with a higher oxygen content.

9.2 Effect of surface processing sequence (Heat treated vs. heat treated and ground)

As previously introduced, the objective of this chapter is to assess the effects of processing avoiding the influence of other parameters treated until now. Free-standing MCrAlY-coatings with different thickness and chemical composition were therefore treated separately. The specimens subjected to direct comparisons had thus the same Y-reservoir. Additionally, all the specimens dealt with had the same surface finish of 1200 grit.

The only parameter varied in this section for direct comparisons was the processing sequence. The consequence of this different processing sequence is that one type of specimens (HT) preserve the modifications of the surface induced during vacuum heat treatment (2h at 1120°C + 24h at 845°C) and in the second type of specimens (HT+G) these modifications were eliminated by removing 100µm of the surface after the heat treatment. The following section proves this statement. Please note that the total final thickness of the HT+G specimens was equal to the HT ones, since the surface removal was applied to both, only the sequence varied. Both types of specimens were subsequently exposed in air at 1100°C in order to investigate if the different processing sequence has an influence on the oxidation behavior of the coatings.

9.2.1 Modifications of the surface chemical composition by vacuum heat treatment

The technical vacuum used for the heat treatment is in the order of 10^{-5} mbar. Under these conditions, residual oxygen was shown by several authors to react at the coating surface [Braue, Gil, Naumenko-2], whereby Y could oxidize. With higher Y-contents and better vacuum quality this oxidation can even produce a continuous layer of Y_2O_3 at the surface [Naumenko-2].

The detection of yttrium oxide precipitates formed during the two-stage heat treatment was performed using cathodoluminescence (CL) imaging (Fig. 9.1). It is appreciated in the

CL-images that Y, having a high O-affinity, diffuses to the surface and oxidizes during this vacuum annealing. A continuous Al_2O_3 scale did not form under these vacuum conditions as shown by the SEM/BSE-images. Regarding the distribution of the yttria precipitates, it is observed that most of them are concentrated in the top 2-3 μm .

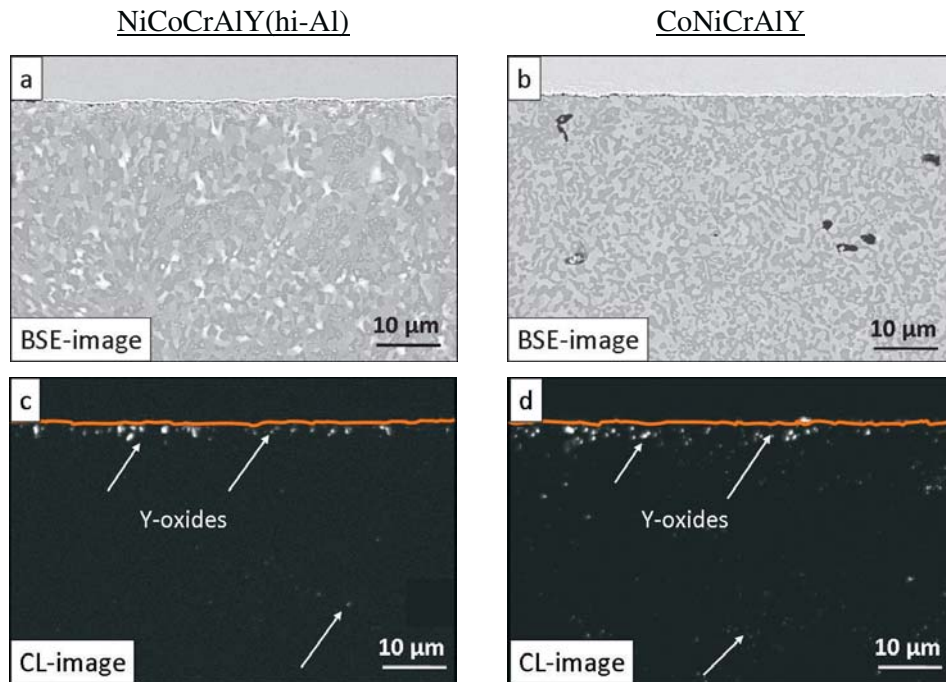


Fig 9.1 – Y oxidation at the surface vicinity in 2mm thick free-standing NiCoCrAlY (hi-Al) specimens a) SEM/BSE-image, c) CL-image and CoNiCrAlY specimens b) SEM/BSE-image, d) CL-image after vacuum heat treatment. Solid line indicates the specimen surface

The SEM-observations were confirmed by SNMS depth profiles as illustrated in Fig. 9.2. A strong Y-enrichment is measured in the first tenths of a micrometer at the specimen surface. This enrichment might have formed during initial stages of oxidation by surface segregation of Y and its reaction with oxygen. The second peak in Y-concentration formed due to internal oxidation of Y, which also occurred during the second stage of heat treatment (24h at 845°C). The enrichment of Y at the surface of the NiCoCrAlY(hi-Al) seems to be superior to that in the CoNiCrAlY-coating in spite of a lower Y-content in the former material (0.38 wt.-% vs. 0.60 wt.-% respectively). The lower mobility of Y in the latter material can be explained by the higher stability of the (Ni,Co)Y intermetallic phases (chapter 7) and a higher O-content after deposition (table 5.2). A lower diffusivity of Y in a Co-base material than in a Ni-base material might also explain this observation.

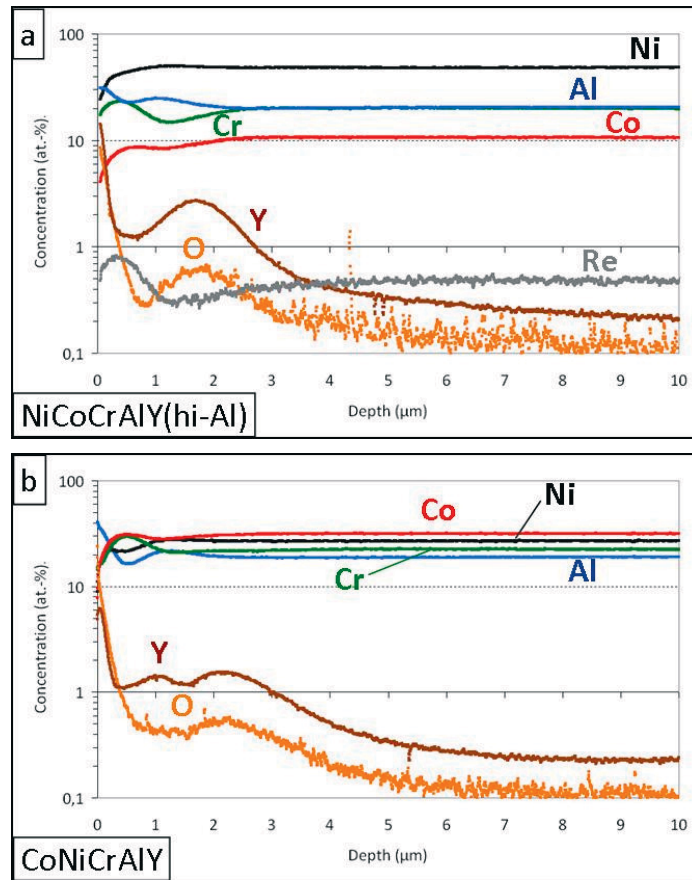


Fig 9.2 –SNMS concentration profiles showing the zone affected by the vacuum heat treatment (2h at 1120°C + 24h at 845°C) at the surface of 2mm thick a) NiCoCrAlY(hi-Al) and b) CoNiCrAlY specimens (values in at.-%).

Furthermore, a detailed analysis of the SNMS-profiles in Fig. 9.2 shows that aluminum is also enriched at the surface similar to yttrium (see section 6.3.2). Comparison of the Y, Al and O profiles indicates that the Al-enrichment is related to the formation of Y/Al-mixed oxide (YAP) precipitates as also confirmed by EDX-analysis. As a consequence of YAP-formation local Al-depletion in the sub-surface (ca. 0.5 μm depth) coating regions occurs, while Cr exhibits peaks of concentration to compensate this effect.

The strong enrichment of yttrium at the surface has as a logical consequence the formation of a depletion zone beneath the surface. By plotting the actual concentration and comparing it to the original concentration before the vacuum annealing (obtained from chemical analysis, table 5.1) it is appreciated that in the case of CoNiCrAlY, the enrichment zone corresponds to the first 5 μm of depth and the depletion zone beneath reaches until

approximately 35 μm deep (Fig. 9.3). Hence, removing circa 100 μm of material from the MCrAlY will exclude the effects observed, meaning that the Y-concentration of a HT+G specimen will be very similar to that of the bulk coating.

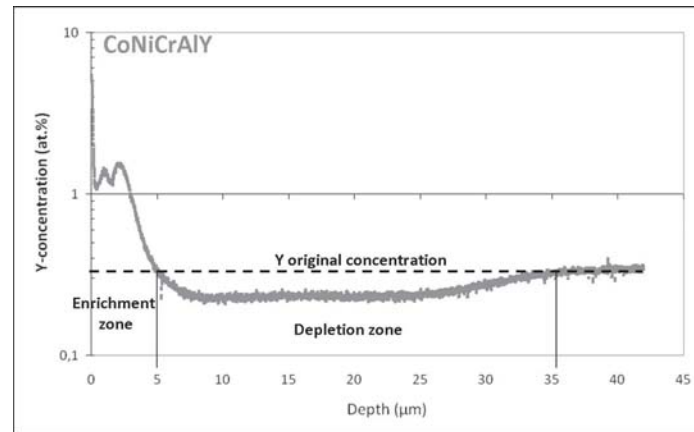


Fig 9.3 – Y enrichment (values in at.-%) and depletion zones in the surface vicinity seen in a SNMS concentration profile of a 2mm thick free-standing CoNiCrAlY specimen after vacuum heat treatment (2h at 1120°C + 24h at 845°C).

The SNMS depth profiles show that the chemical composition of the surface of MCrAlY-coatings is indeed modified during the heat treatment applied. The area of influence reaches 3-5 μm depth for the major alloying elements and 30-40 μm for Y. Hence, the removal of the top 100 μm in a thick 2mm free-standing specimen after the heat treatment (HT + G) is expected to result in a surface with an unaltered chemical composition.

9.2.2 Discontinuous exposure of MCrAlYs with different initial surface condition

9.2.2.1 Discontinuous exposure of NiCoCrAlY(hi-Al) with different initial surface condition

After exposing identical specimens of the same material with different surface conditions in air at 1100°C, noticeable differences are determined already after short times. Fig 9.4 shows SEM-images of the NiCoCrAlY(hi-Al) specimens after 16h of high temperature exposure in air. Essentially different scales formed on HT and HT+G specimens. In the former the average scale thickness of 3.5 μm is larger than that of the latter (2.5 μm in average). More surprising are the different scale morphologies obtained. On the specimen oxidized in heat treated state a thin layer of Y-rich oxides and spinels are observed on the

outermost part of the scale. On the HT+G specimen these oxide phases seem to be absent in this region of the TGO. The bulk of the oxide on the HT specimen is mainly composed of Al_2O_3 , as seen especially in the EDX mapping for Al (Fig. 9.4), whereas that of the HT+G specimen contains additionally coarse Y/Al-oxides. Y-oxide precipitates are found deeper in the area below the oxide/metal interface in the HT specimen than in the HT+G.

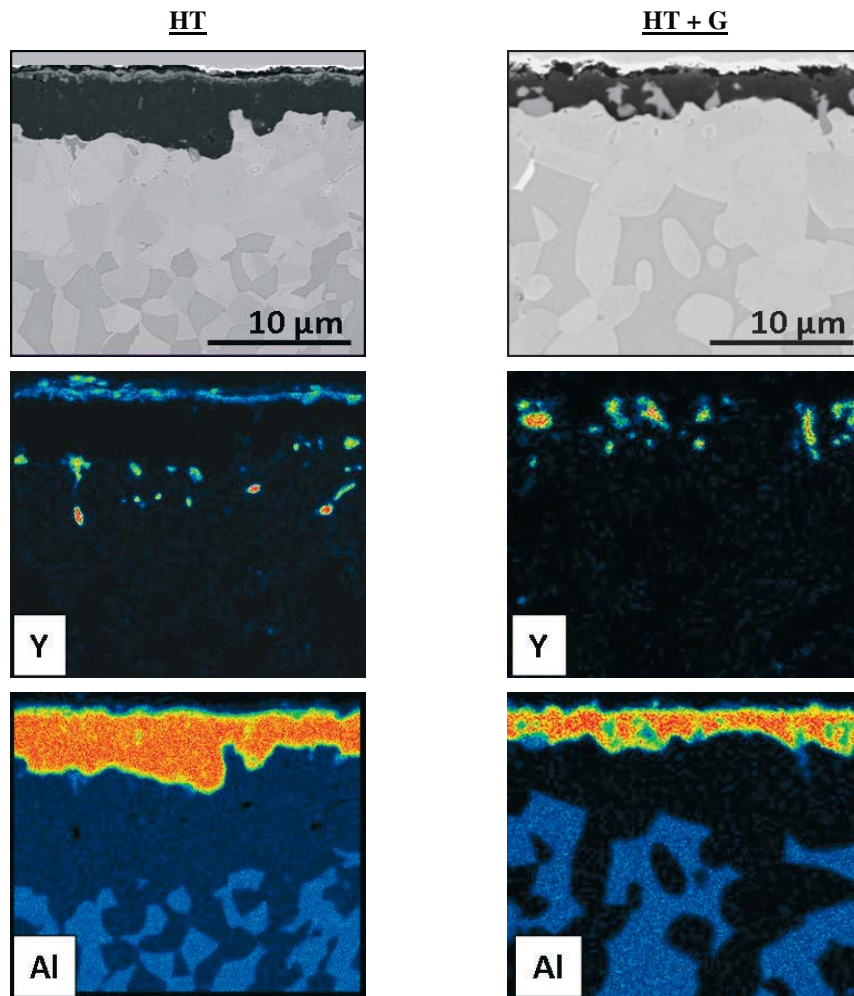


Fig 9.4 –SEM images and EDX mappings of Y and Al of 2mm thick free-standing NiCoCrAlY(hi-Al) specimens HT (left), and HT+G (right), after 16h of discontinuous oxidation in air at 1100°C.

SNMS element profiles (Fig. 9.5) of the specimens shown in Fig. 9.4 corroborate the findings of the SEM/EDX cross section analysis (please note that the Re-profiles were omitted to avoid overwhelming the plots). On the external portion of the scale (0 - 1μm depth)

a strong Y enrichment took place in the HT specimen (Fig. 9.5a). An enrichment of Cr in this area indicates the formation of Cr-rich spinels, in agreement with the SEM- observations. In contrast, the outer portion of the TGO in the HT+G specimen is seen to be Al-oxide (Fig. 9.5b). The most external part of this scale (0 - 0.1 μ m depth) has, with Y-concentrations of 0.15 - 0.25 at.-%, no significant enrichment of this reactive element.

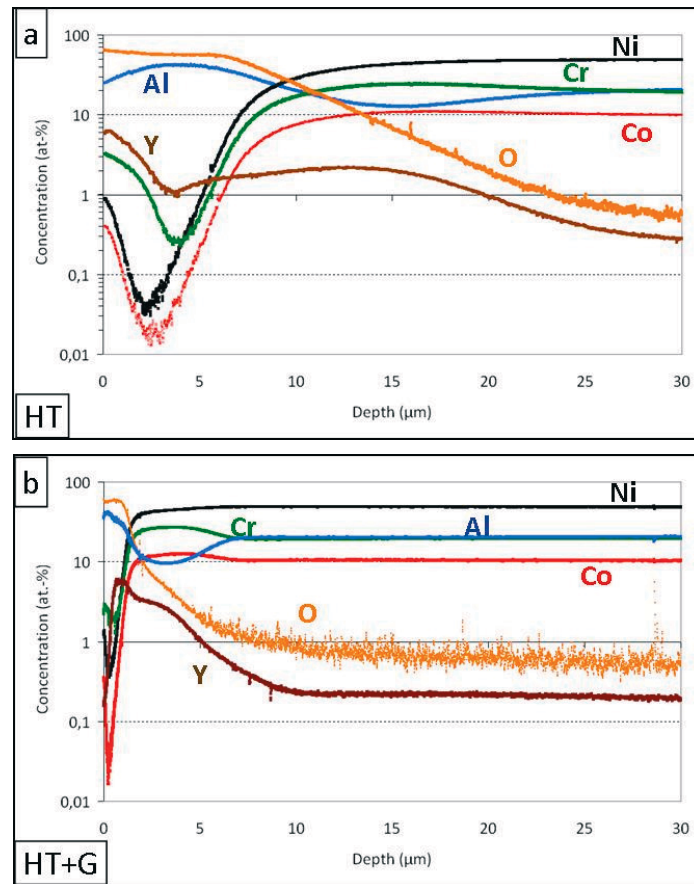


Fig 9.5 –SNMS concentration profiles of 2mm thick free-standing NiCoCrAlY(hi-Al) specimens with different initial surface condition a) HT and b) HT+G after 16h of discontinuous exposure in air at 1100°C.

As mentioned above, the Y-concentration reaches a maximum in the HT specimen at the gas/oxide interface, whereas in the HT+G specimen the maximum is registered at a depth between 0.5 - 2 μ m, corresponding to the location of coarse Y-aluminates in the middle and in the lower half of the scale seen in Fig. 9.4. Furthermore, the pronounced Y-internal oxidation reaches depths of 25 - 30 μ m in the HT specimen and of only 15 μ m in the HT+G one, in agreement with the EDX mappings of Fig. 9.4.

The different composition in the outer scale apparently promoted a faster oxide growth during early stages of oxidation in the HT specimen. The faster scale growth can be explained by the presence of Y-rich oxides at the surface, which provide short-circuit paths for oxygen diffusion. It has been shown that the oxygen diffusion coefficient in Y_2O_3 ($2.2 \times 10^{-11} \text{ cm}^2/\text{s}$) is considerably higher than that in Al_2O_3 , where it amounts to $1 \times 10^{-17} \text{ cm}^2/\text{s}$ (data measured at 700°C) [Ryan]. In addition, the spinels also present in the outer scale are porous mixed oxides that also offer short-circuit paths for faster O-transport than the compact alumina in the outer scale of the HT+G specimen. As a consequence of the faster TGO growth, a more extensive Al-depletion zone forms in the HT specimen as observed on the plots of Fig. 9.4.

After a longer exposure of 406h, the scale on the HT specimen is with an average thickness of $8\mu\text{m}$ still slightly thicker than that of on the HT+G specimen, which accounted for $7\mu\text{m}$. In the HT specimen the Y-aluminate phases formed predominantly in the middle and in the lower half of the TGO (Fig. 9.6a). In contrast, in the HT+G specimen they are also found in immediate proximity to the outer boundary (Fig. 9.6b). This is in qualitative agreement with the preceding observations, which showed that in the HT+G specimen, Y/Al-oxides formed even during the early stages of oxidation (Fig. 9.4). After 406h, this difference in the Y-distribution between HT and HT+G specimens is however observed only in the outermost part of the scale. The reason for this is a large Y-reservoir in these 2mm thick coatings. Therefore, enough yttrium could diffuse from the bulk after the longer exposure independent of its initial distribution at the surface. Results of similar tests conducted on thin specimens follow in section 9.2.3.

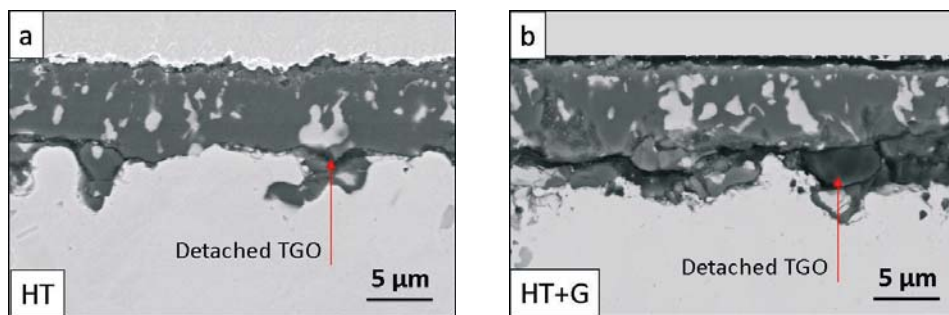


Fig 9.6 –SEM images of 2mm thick free-standing NiCoCrAlY(hi-Al) specimens with different initial surface condition: a) HT, c) HT+G after 406h of discontinuous oxidation in air at 1100°C .

9.2.2.2 Discontinuous exposure of CoNiCrAlY with different initial surface conditions

After high-temperature exposure of free-standing CoNiCrAlY-specimens, similar differences were found between the samples with different initial surface conditions. As discussed above for NiCoCrAlY(hi-Al) thicker oxide scales formed on the HT specimens, with a high concentration of Y-oxides and (Cr,Co)-spinel in its outer region and of alumina in the bulk oxide. In contrast, thinner scales formed on the HT+G specimens with an Al₂O₃-rich outer scale and large presence of Y-aluminates in the oxide bulk (Fig. 9.7). In this bond coat material however, internal oxidation of yttrium in an area 5-10µm beneath the

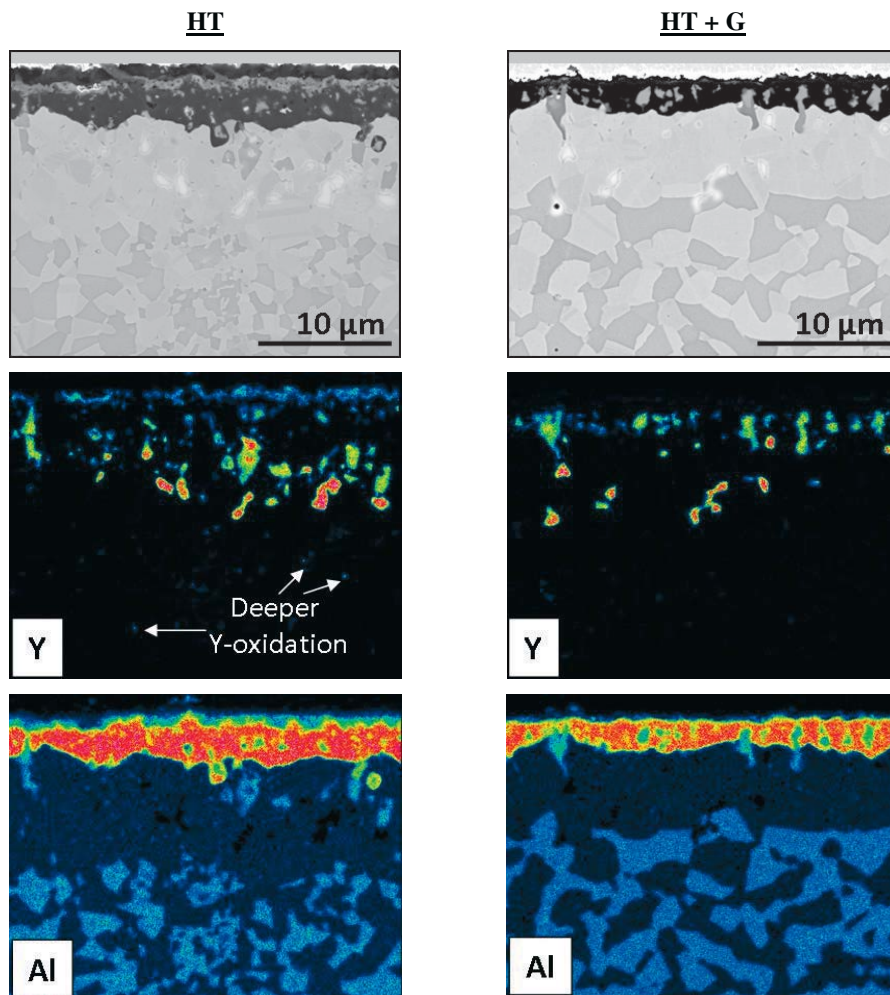


Fig 9.7 –SEM images and EDX mappings of Y and Al of 2mm thick free-standing CoNiCrAlY specimens HT (left), and HT+G (right), after 16h of discontinuous oxidation in air at 1100°C.

oxide/metal interface is observed in both HT and HT+G specimens. This difference with the Ni-base coating can be understood by considering a higher Y-content (reservoir) in the Co-base material together with a slower mobility of Y as mentioned in section 9.2.1.

SNMS-depth profiles confirm the findings of the SEM/EDX analysis (Fig. 9.8). The elevated concentration of Al over a wider depth in the HT specimen observed in Fig. 9.8a is not only due to a thicker TGO but also due to a more extensive formation of internal Y-aluminates in the β -depletion zone as found in the microscopy analysis. As mentioned above, a faster inward diffusion of oxygen might have been favored by the presence of Y-oxides at the surface of this specimen.

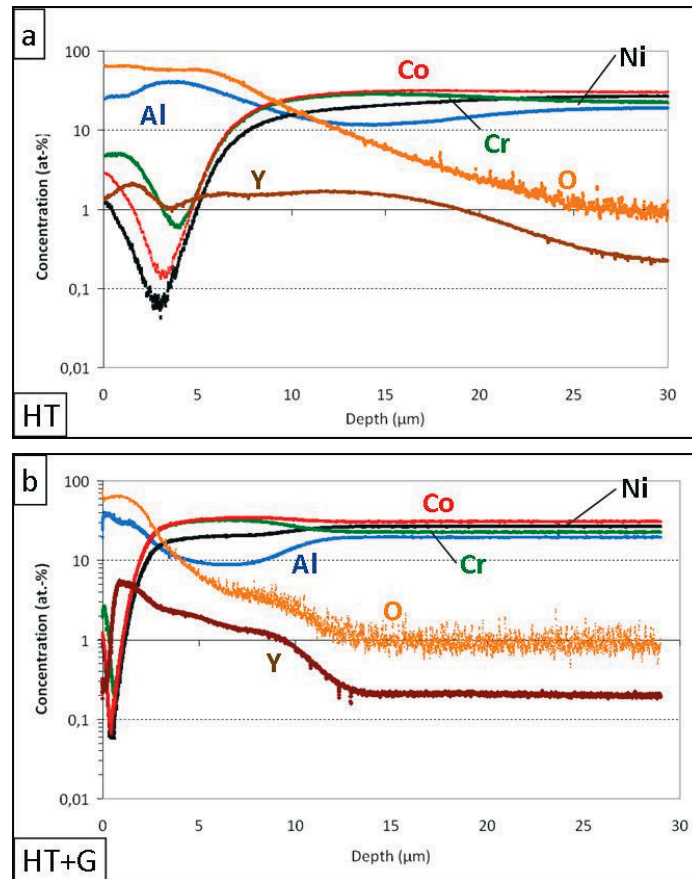


Fig 9.8 – SNMS concentration profiles of 2mm thick free-standing CoNiCrAlY specimens with different initial surface condition a) HT and b) HT+G after 16h of discontinuous exposure in air at 1100°C.

During 406h of discontinuous exposure in air at 1100°C, the scales on the HT specimen thickened slightly faster than those on the HT+G specimen, with final average thickness values of 8µm and 7µm respectively (Fig. 9.9). The different distribution of Y-aluminates inside the TGO, associated with a different initial surface condition, was more evident for this coating alloy. With the help of image processing, the areas of the TGO composed of Al_2O_3 and Y-aluminates were distinguished and quantified (Figs. 9.9c and 9.9d). With this data the volume fraction of the Y-aluminates in the scale was calculated, with 35% being higher in the HT specimen than in the HT+G one, where it was 21%.

As commented in the previous section, coarse Y-aluminates are more concentrated in the middle and lower half of the scale in the case of HT specimen, whereas a series of finer Y-aluminates are found concentrated less than a micrometer below the outer scale boundary in the HT+G specimen. A large Y-reservoir favors however the formation of coarse precipitates in the lower half of the scale also in the latter specimen type upon longer exposures.

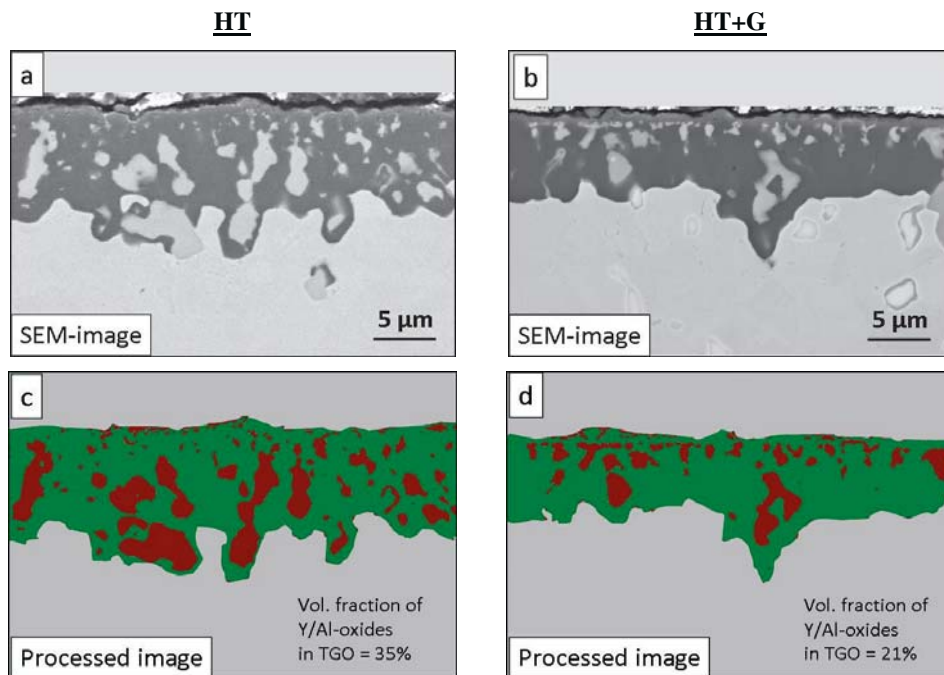


Fig 9.9 –SEM (a,b)- and processed images (c,d) of 2mm thick free-standing CoNiCrAlY specimens HT (left), and HT+G (right), after 406h of discontinuous oxidation in air at 1100°C.

9.2.2.3 Discontinuous exposure of NiCoCrAlY(lo-Al) with different initial surface condition

The SEM-images depicted in Fig. 9.10 show differences in the scales grown on free-standing specimens of NiCoCrAlY(lo-Al) coating with a variation of the initial surface condition after high-temperature air exposure. The TGO on the HT specimen grew to an average thickness of 3 μ m after 16h and of 5 μ m after 406h, while the scale on the HT+G thickened up to 2 μ m and 4 μ m after the same duration. The outermost part of the oxide is mainly composed of Y- and Cr-rich oxides in the HT specimen and of alumina in the HT+G specimen. The formation of coarse Y-aluminate pegs in the scale occurred earlier in the HT+G specimen (see Figs. 9.10a and 9.10b). In contrast, in the HT specimen the Y-aluminates in the outer part of the scale are much finer and consequently the scale growth is initially faster. Coarser Y-aluminate precipitates are only found predominantly in the middle and in the lower half of the TGO, as observed above for the other bond coat materials.

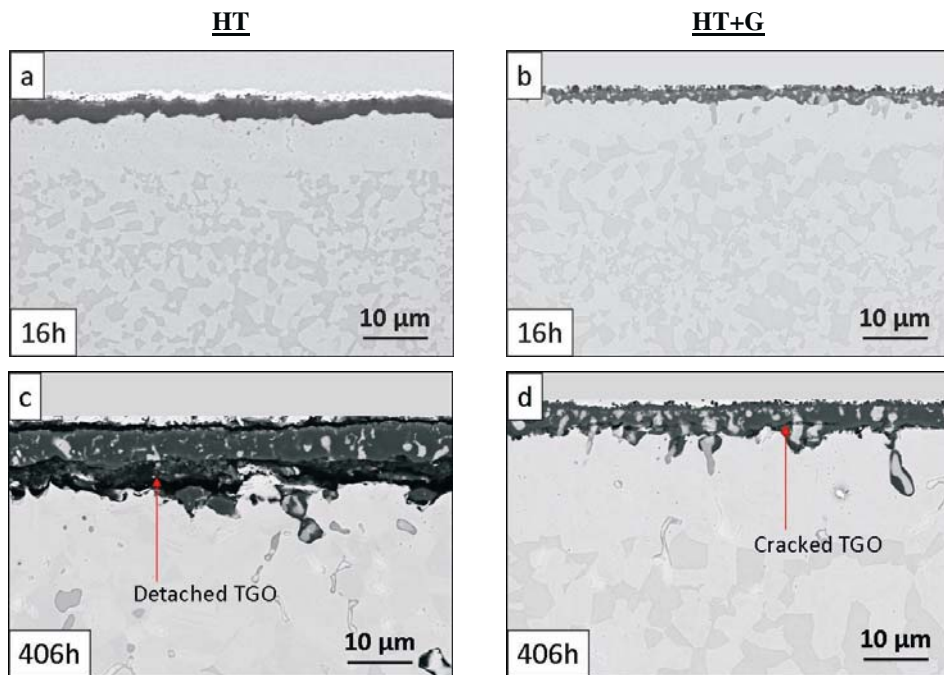


Fig 9.10 –SEM images of 2mm thick free-standing NiCoCrAlY(lo-Al) specimens with different initial surface condition: HT after a) 16h, c) 406h and HT+G after b) 16h, d) 406h of discontinuous oxidation in air at 1100°C.

The β -depletion zone reached deeper in the specimen with initial HT surface condition, approximately 30 μ m beneath the oxide/metal interface and only 15 μ m beneath this interface in the specimen ground after heat treatment. More Al was consumed in the former specimen not only due to the faster scale thickening but also to the formation of Y-aluminates in this β -depleted region. After 406h of exposure, the loss of scale adhesion seemed to be stronger in the HT specimen, although the scale on the HT+G specimen exhibited numerous cracks.

9.2.3 Cyclic exposure of MCrAlYs with different initial surface condition (HT vs. HT+G)

9.2.3.1 Cyclic exposure of 2mm thick MCrAlYs with different initial surface condition

A quantification of the influence of the initial surface condition on the oxide growth rate and adherence was carried out by exposing HT and HT+G free-standing specimens under cyclic conditions. The mass changes on 2mm thick specimens during 1300h of exposure in air at 1100°C are shown in fig 9.11. It can be noted that (before mass loss occurs) in all three coating materials the removal of the surface regions altered by the heat treatment (HT+G initial surface condition) led to a slower oxide growth rate. In the case of NiCoCrAlY(hi-Al) and CoNiCrAlY the mass gain on the HT specimens were around 25% higher than on the HT+G specimens.

Cross section micrographs of free-standing Co-base coatings after the long-term exposure confirmed that thicker scales and oxide spinels formed on the HT specimen (Fig. 9.12a). Additionally in this specimen, the Y-aluminates incorporated in the TGO were found to be coarser than in the HT+G specimen. The scales formed on all Ni-base coatings spalled during the cyclic exposure or upon test completion and could not be therefore analyzed in cross-section. In the case of the NiCoCrAlY(lo-Al) the experiment had to be stopped due to pronounced spallation after 918h.

An interesting observation is that the upper scale boundary of the HT sample roughened during the cyclic exposure (Fig. 9.12a), whereas in the HT+G it remained flat (Fig. 9.12b). The reason why the oxide surface roughens in these specimens is still unclear; however the volume increase associated with the transformation $\text{Al}_2\text{O}_3 + \text{YAP (Y}_2\text{O}_3) \rightarrow$

YAG can be an explanation [Hay]. Due to the enrichment of Y at the outer scale of the HT specimens (Figs. 9.5 and 9.8) this reaction is likely to take place.

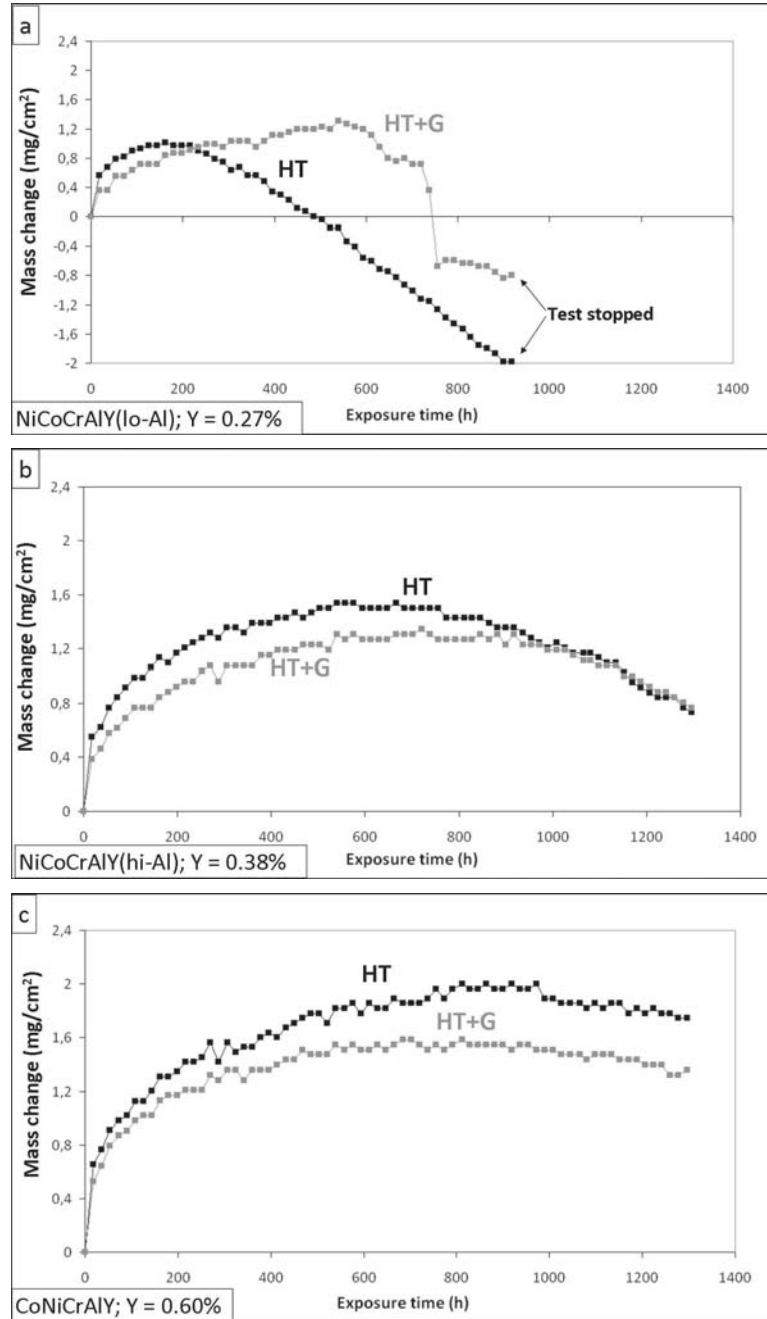


Fig 9.11 – Mass change of 2mm thick free-standing a) NiCoCrAlY (lo-Al), b) NiCoCrAlY (hi-Al), c) Co-NiCrAlY specimens with different initial surface condition during 1300h of cyclic exposure in air at 1100°C.

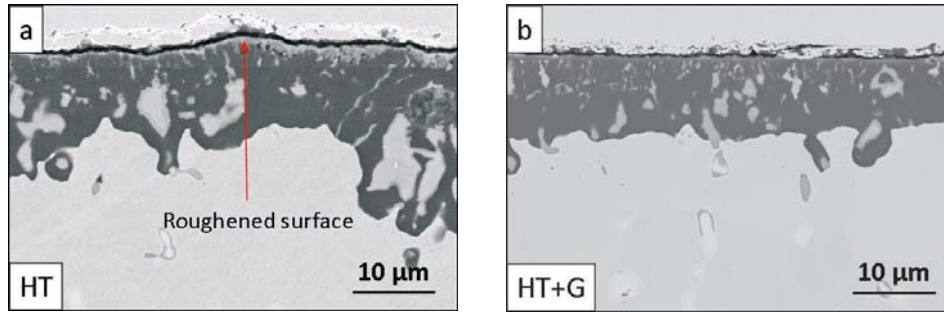


Fig 9.12 – SEM images of 2mm thick free-standing CoNiCrAlY coatings with different initial surface condition: a) HT and b) HT+G after 1300h of cyclic exposure in air at 1100°C.

The scale adherence was seen to be considerably improved in the NiCoCrAlY(10-Al) with HT+G initial surface condition, where the beginning of mass loss was registered to occur after approximately 550h instead of 220h as registered for the HT specimen (Fig. 9.11a). Since pronounced scale spallation occurred earlier for this coating, a new set of specimens was oxidized for 100h in order to appreciate the morphologic differences of the oxide scales formed. As pointed out in the previous section, in the HT specimens thicker scales formed with presence of Cr/Co-rich spinels in the surface and deeper oxidation of yttrium (Fig. 9.13a) than in the HT+G samples where Y/Al-aluminates richly incorporated in the TGO beneath a thin, alumina-rich zone (Fig. 9.13b). It is also observed for these specimens that the outer surface of the HT sample tends to roughen while that of the HT+G remains flat.

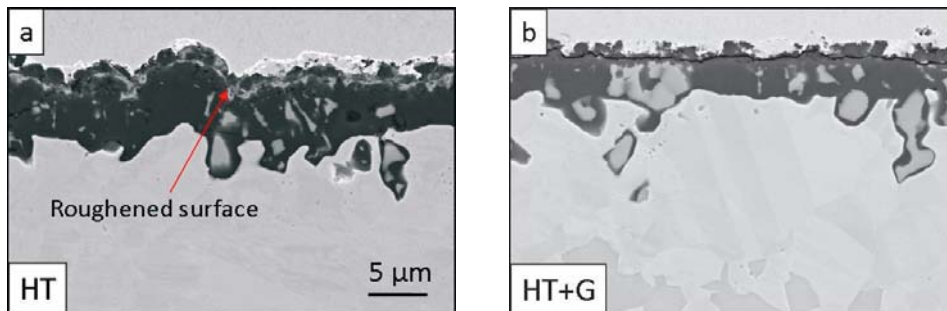


Fig 9.13 – SEM images of 2mm thick free-standing NiCoCrAlY(10-Al) specimens with different initial surface condition: a) HT and b) HT+G after 100h of cyclic exposure in air at 1100°C.

9.2.3.2 Cyclic exposure of 0.15mm thick MCrAlYs with different initial surface condition

After having determined that the Y-reservoir can strongly influence the oxidation behavior of a MCrAlY coating (section 8.3), it was decided to study the effect of the initial surface condition also in 0.15mm thick specimens by exposing them to identical cyclic conditions as described above. The respective mass change plots are presented in Fig. 9.14. As reported for the 2mm thick specimens, the scale growth rate proved to be reduced for the 0.15mm thick specimens, ground after the heat treatment (HT+G).

For the thinned specimens however, this reduction was lower: for the HT specimen of the NiCoCrAlY(hi-Al) coating the mass gain was registered to be approximately 12% higher (Fig. 9.14b), and for the CoNiCrAlY approx. 14% higher (Fig. 9.14c) than in the corresponding HT+G specimens (these values were around 25% in the thick specimens). This finding leads to the conclusion that the magnitude of the effect of the initial surface condition is dependent on the yttrium reservoir.

The effect on the scale adherence is more noticeable in the NiCoCrAlY(lo-Al) coating alloy. While in the HT specimen mass loss is already registered after 90h, no mass loss was detected during the 918h of exposure in the HT+G specimen. SEM cross section images of specimens of this material cyclically oxidized for 100h show a roughened oxide with barely no Y/Al-precipitates in the HT specimen (Fig. 9.15a), whereas a flat TGO with presence of such precipitates in its upper half is seen in the HT+G specimen (Fig. 9.15b).

The specimens with good scale adherence after 1300h cyclic exposure were analyzed in cross section and are presented in Fig. 9.16. As it was concluded in the previous chapter, the existence of a lower Y-reservoir in thinned specimens hinders the formation of coarse Y-Aluminates in the oxide and in its immediate vicinity. The finer precipitates that actually form in these thin specimens are differently distributed, i.e. they tend to form in the proximity of the surface in the HT+G specimens beneath a “purer” alumina scale (see Figs. 9.16b and 9.16d), while they tend to form deeper in the HT specimens (see Figs. 9.16a and 9.16c).

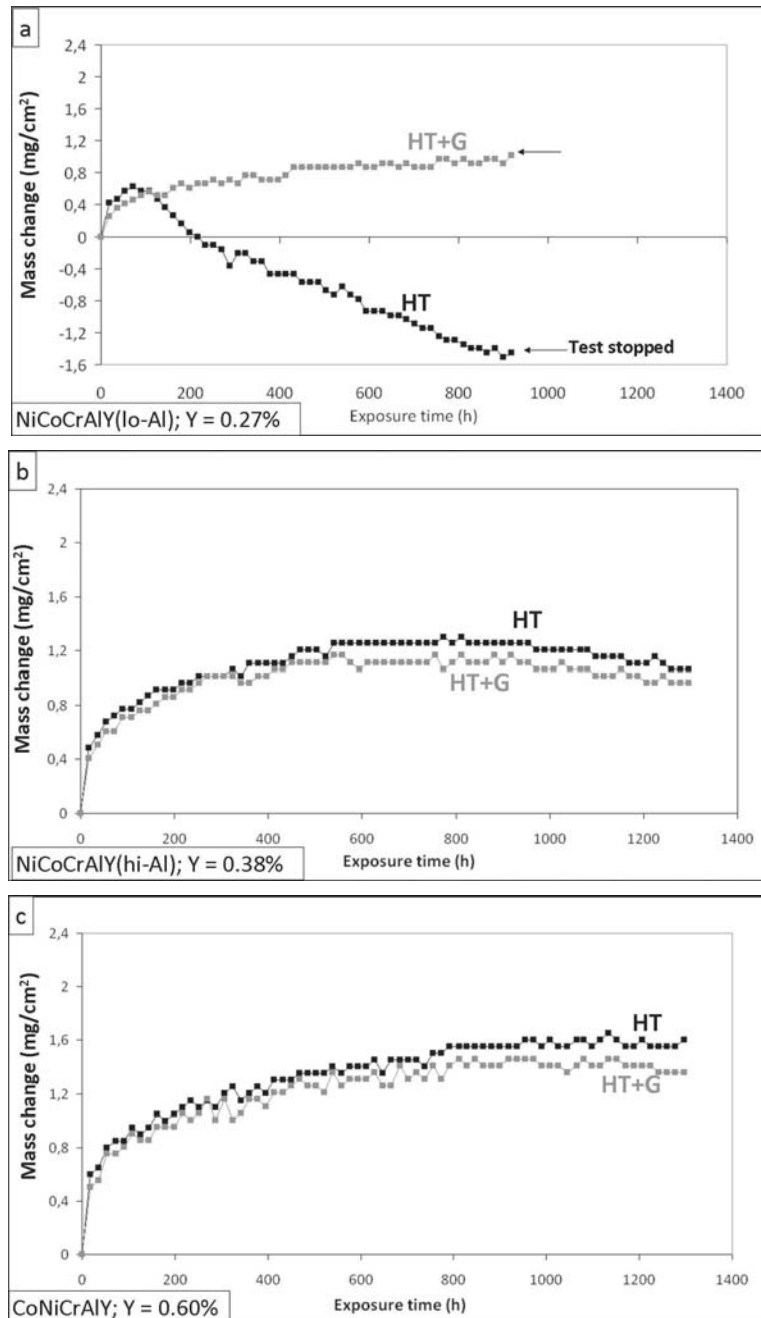


Fig 9.14 – Mass change of 0.15mm thick free-standing a) NiCoCrAlY (lo-Al), b) NiCoCrAlY (hi-Al), c) Co-NiCrAlY specimens with different initial surface condition during 1300h of cyclic exposure in air at 1100°C.

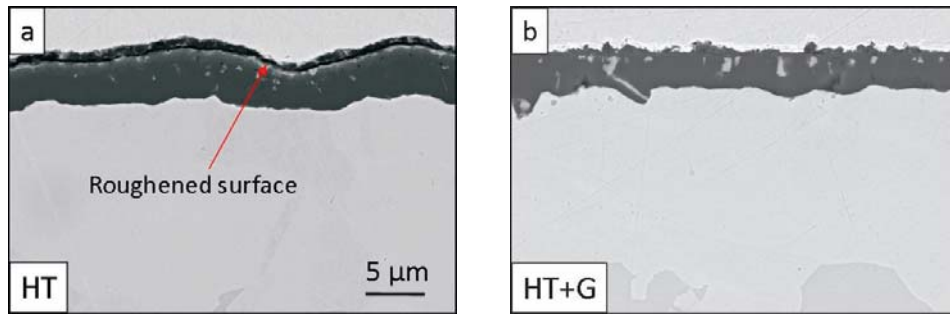


Fig 9.15 – SEM images of 0.15mm thick free-standing NiCoCrAlY(lo-Al) specimens with different initial surface condition: a) HT and b) HT+G after 100h of cyclic exposure in air at 1100°C.

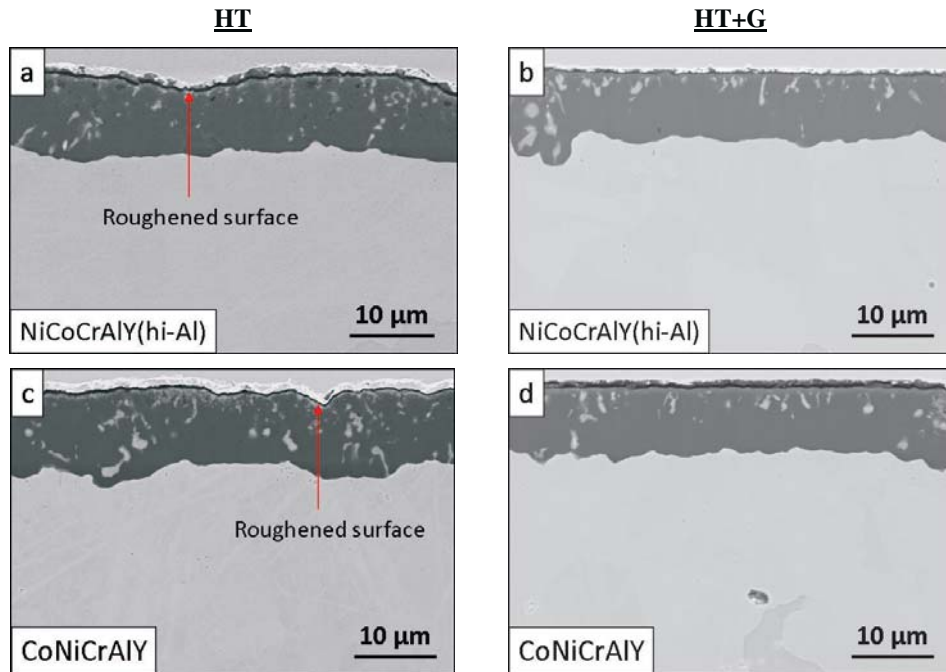


Fig 9.16 – SEM images of 0.15mm thick free-standing coatings: NiCoCrAlY(hi-Al) a) HT and b) HT+G; CoNiCrAlY c) HT and d) HT+G after 1300h of cyclic exposure in air at 1100°C

As it was remarked for the thick CoNiCrAlY specimens, the surface composition had been modified by the vacuum heat treatment (HT). In this case, transformation of Y-rich oxide compounds associated with the volume change, can lead to a surface roughening upon air oxidation. This effect was observed in all three coating materials. In contrast, when the Y-rich oxides formed at the surface during heat-treatment had been removed prior to oxidation (HT+G), the outermost part of the scale, which is rich in aluminum oxide, remained flat

during the high temperature air oxidation. This effect was observed although both types of specimens were subjected to the same surface finishing (1200 grit) before oxidation testing.

The surface roughening in HT specimens caused sample deformation that could be observed even on macroscopic scale in thin specimens (see Figs. 9.17a and 9.17c). Additionally, by comparing Figs. 9.17a and 9.17b it can be seen that the TGO had spalled in a large area of the surface of the HT specimen while no signs of spallation can be determined at this scale for the HT+G specimen.

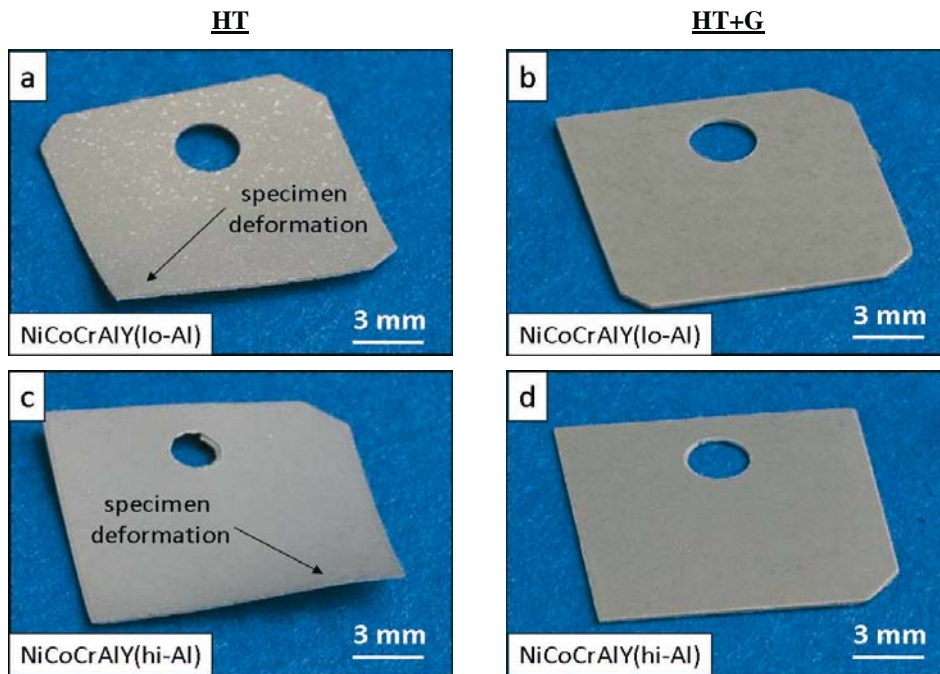


Fig 9.17 – Macroscopic pictures of 0.15mm thick free-standing coatings: NiCoCrAlY(lo-Al) a) HT and b) HT+G; NiCoCrAlY(hi-Al) c) HT and d) HT+G after 100h of cyclic exposure in air at 1100°C

9.2.4 Mechanism of the effect of the initial surface condition on the MCrAlY oxidation

It was shown in the preceding sections that the initial surface condition has a reproducible effect on the oxidation behavior of the MCrAlY coatings studied. In order to explain this effect it is necessary to consider the surface chemical composition and microstructure that result from the vacuum heat treatment.

In section 9.2.1 it was proved that driven by residual oxygen partial pressure under the technical vacuum conditions, yttrium diffuses to the surface and oxidizes (Fig. 9.1), as shown in a schematic at t_0 in Fig. 9.18. The SNMS profiles for Y, Al and O in Fig. 9.4 indicate that Y-rich oxide compounds formed during the heat treatment are Y-aluminates. This is reasonable considering the high Al-activity in the coating. The formation of Y-aluminates leave a depleted area underneath, which reaches according to the SNMS profiles until 30 - 40 μm deep for Y and 0.5- 1 μm deep for Al.

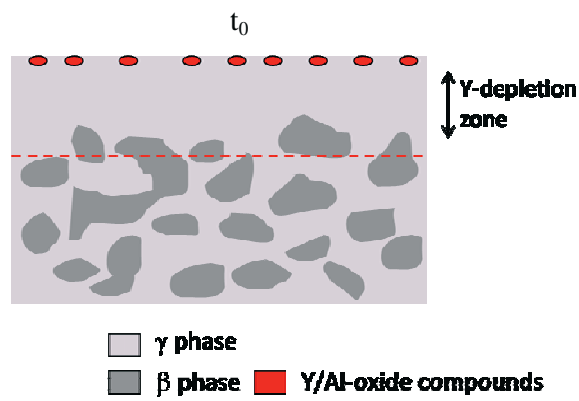


Fig 9.18 – Schematic representation of the surface alteration during vacuum heat treatment.
Dotted line indicates the area removed after heat treatment on a HT+G specimen.

The dotted line in Fig. 9.18 indicate the area removed after heat treatment on a HT+G specimen, which includes the above mentioned depletion areas of Y and Al. Hence, inherently different surface conditions are established on HT and HT+G specimens prior to oxidation (t_1 in Fig. 9.19). In the former, Y and Al have been oxidized in the sub-surface region and thus depleted in the metallic matrix. Consequently, elements with lower O-affinity (Cr and Co) oxidize in the initial stages of high temperature exposure, forming non-protective spinels (t_2 in Fig. 9.19).

In contrast, in the HT+G specimens the original coating chemical composition prevails after having removed the zone affected by the heat treatment (t_1 in Fig. 9.19). In this case the transient oxidation stage of Cr and Co is suppressed and the elements with the highest oxygen affinity are oxidized (Y and Al). However, under the high oxygen partial pressure of atmospheric air, due to fast kinetics Y is rapidly depleted, therefore rather pure Al_2O_3 forms (t_2 in Fig. 9.19). After a closed alumina scale had formed the oxygen flux is greatly reduced. Y can, therefore, diffuse from the bulk to form Y/Al-compounds (t_3 in Fig. 9.20).

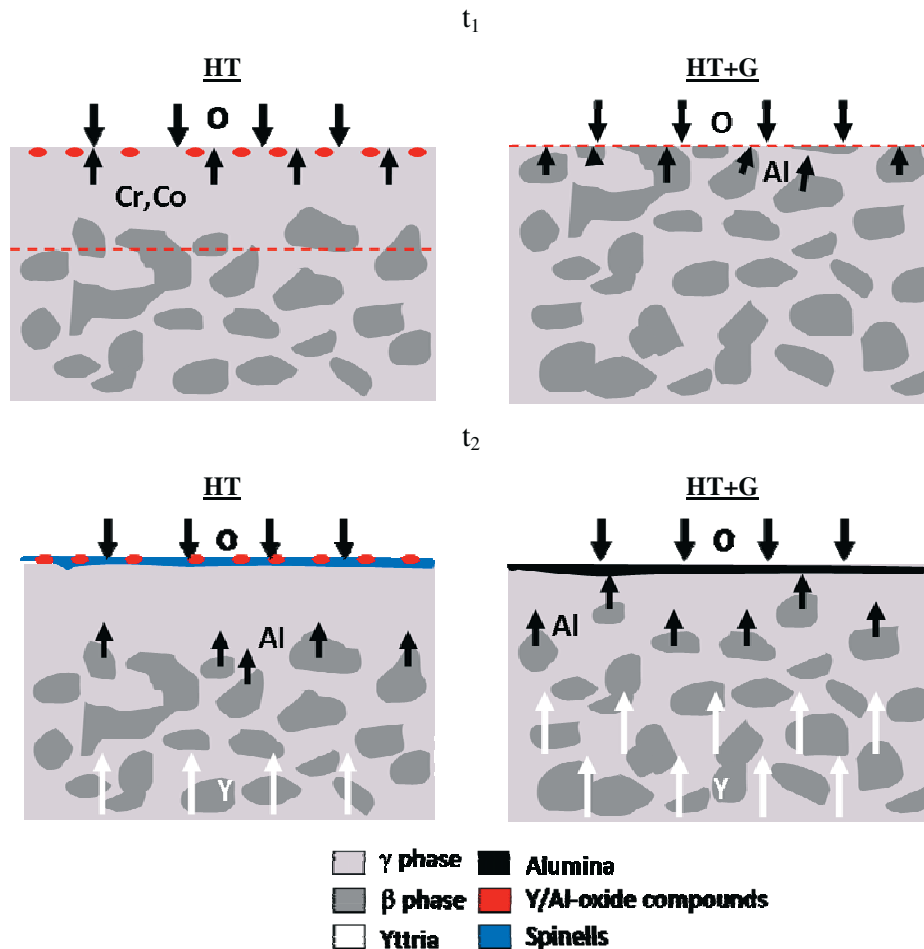


Fig 9.19 – Schematic representation of the surface oxidation during early stages of high temperature exposure in specimens with different initial surface condition. Dotted lines delimitate the area removed after heat treatment on a HT+G specimen.

In the case of the HT specimen, where a local depletion of Y prevails, its diffusion from the bulk takes longer so that predominantly alumina forms below the outer layer of spinel and Y/Al-oxides formed on the top (t_3 in Fig. 9.20). The latter microstructure allows initially fast inward diffusion of oxygen in the coating resulting in a faster oxide growth rate. Eventually, the protective alumina scale develops.

If the yttrium reservoir is large enough (e.g. in 2mm thick specimens), the diffusion of this element will continue, enabling the formation of coarse Y/Al-oxides deeper in the inward growing TGO and later on, of internal yttria precipitates in the metal. However, They will be differently distributed in HT and HT+G specimens (t_4 in Fig. 9.20).

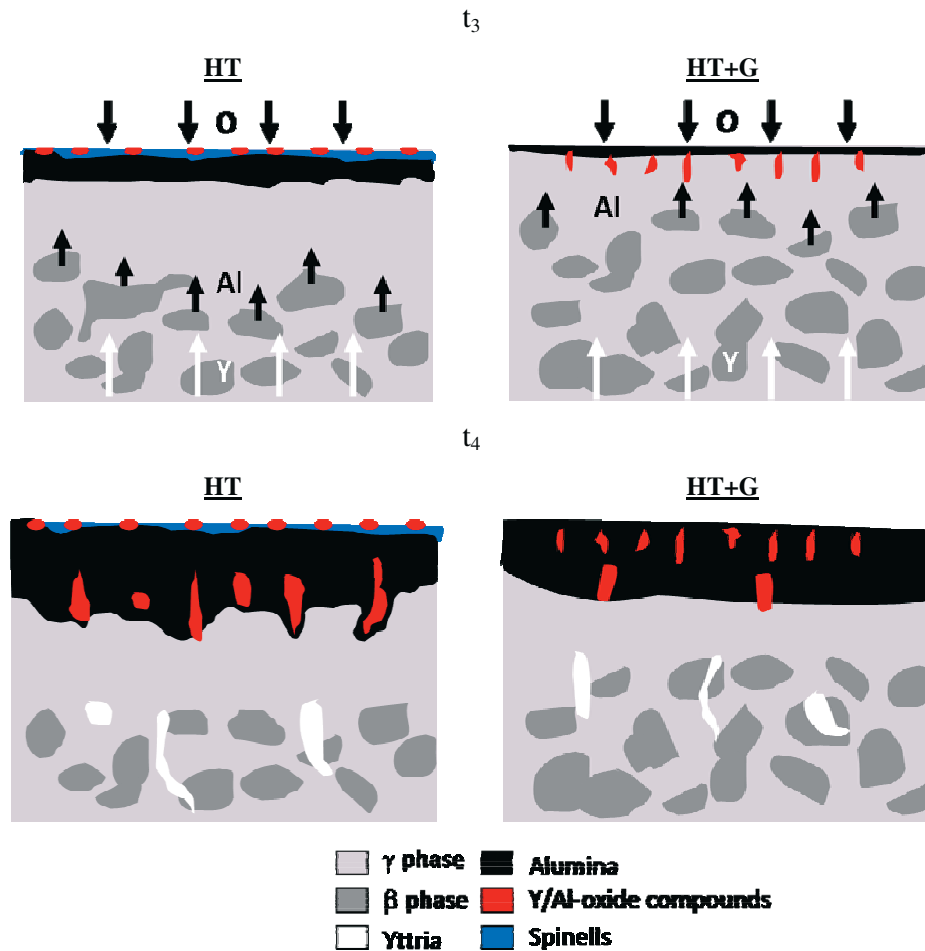


Fig 9.20 – Schematic representation of the surface oxidation during advanced stages of high temperature exposure in thick specimens with different initial surface condition.

The reason why the TGO adherence was better in HT+G NiCoCrAlY(10-Al) specimens than in HT ones is probably related to the small Y-reservoir in this bond coat. Apparently, critical Y-depletion from the bond coat occurred during heat treatment in 0.15mm thick specimens of this material. As a consequence, the scale adherence is lost after relatively short times during cyclic oxidation. In addition, the scale morphologies developed on the heat-treated surfaces are fast growing and prone to rumpling. This can be related to high growth stresses arising in the scales due to spinel formation and/or transformation of Y_2O_3 (YAP) into YAG [Hay]. The latter assumption can also explain the macroscopic deformation of the thin specimens oxidized in the heat-treated condition without subsequent grinding (HT).

Contrary to HT, in HT+G specimens the Y-reservoir is retained prior to oxidation. A flat alumina scale develops and Y is incorporated as pegs (Fig. 9.15). This scale morphology and the availability of Y in the bulk during oxidation result in improved scale adherence in HT+G, compared to HT.

Different to NiCoCrAlY(lo-Al), no major effect of the pre-treatment procedure on the scale adherence was found under the selected test parameters with the specimens of NiCoCrAlY(hi-Al) and CoNiCrAlY. This can be due to their higher Y-contents (reservoirs). The specimens indicate that no critical Y-depletion occurred during heat-treatment in the two latter coatings. In the latter case, the high Y-reservoir levels out the pre-treatment effects on the scale morphology and resistance to spallation during subsequent oxidation.

9.3 Effect of heat treatment conditions

9.3.1 General remarks

After realizing that the changes of the bond coat surface composition induced by the vacuum heat treatment can significantly influence its oxidation behavior, a set of new experiments was planned. In these experiments the heat treatment conditions were deliberately varied and their effect the oxidation behavior studied. For this purpose, free-standing MCrAlY-coatings (both 0.3mm and 2mm thick) were annealed prior to high-temperature oxidation according to the following procedures:

- 24h in air at 900°C
- 2h in vacuum (10^{-5} mbar) at 1100°C
- 24h in vacuum (10^{-5} mbar) at 900°C

After the annealing the specimens were cooled down by direct exposure to room temperature. The oxidation experiments with the heat treated samples were performed under similar conditions as the previous sections in order to have a direct comparison with the standard heat treatment (2h at 1120°C + 24h at 845°C).

9.3.2 Alteration of the surface chemical composition by alternative heat treatments

The alteration of the surface chemical composition caused by the single-stage treatments was studied by SNMS element concentration profiles (Fig. 9.21). In order to be brief, only the results of NiCoCrAlY(hi-Al) annealed in vacuum at 1100°C and pre-oxidized at 900°C are presented in this part. The most noticeable feature when comparing both plots is that during air exposure at 900°C an alumina layer is formed on the surface while during the 2h vacuum annealing at 1100°C, mainly Y oxidizes in near-surface regions. As explained in the previous section, in the latter case, the enrichment of Y at the surface will cause the formation of Y/Al-oxides in these regions. These Y and Al distributions are different from those in the coating annealed for 24h in air. In the latter case the alumina scale formation suppresses the Y-enrichment at the surface.

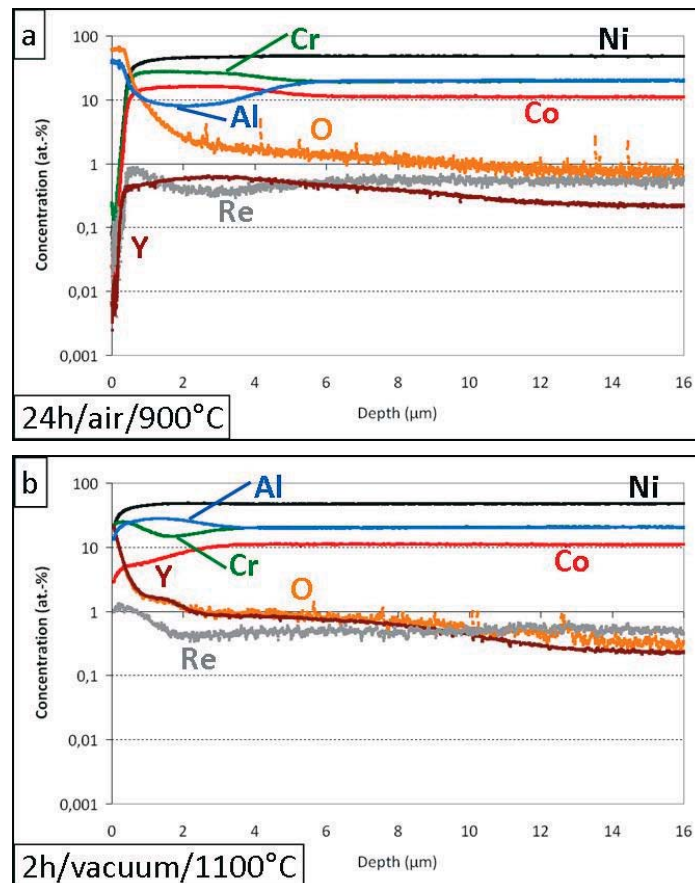


Fig 9.21 – SNMS concentration profiles of 2mm thick free-standing NiCoCrAlY(hi-Al) specimens after different heat treatment conditions a) 24h/ air/ 900°C and b) 2h/ vacuum/ 1100°C.

Fig. 9.22 shows SEM-images of the annealed specimens. The results are in agreement with the SNMS profiles. An approximately 1 μm thick Al_2O_3 scale formed on the specimen annealed in air (Fig. 9.22a), while no visible Al oxidation took place on the specimens annealed in vacuum (Figs. 9.22b and 9.22c). The coating microstructures are also different in agreement with the temperature dependence of the coating phase composition, as discussed in chapter 7. The bright, tiny α -Cr particles inside the β phase were shown to precipitate at temperatures below 1000°C in this MCrAlY. This difference in microstructure however does not have a decisive influence in this investigation since all the specimens are subsequently exposed in air at 1100°C. Hence, the microstructure typical for this temperature will prevail.

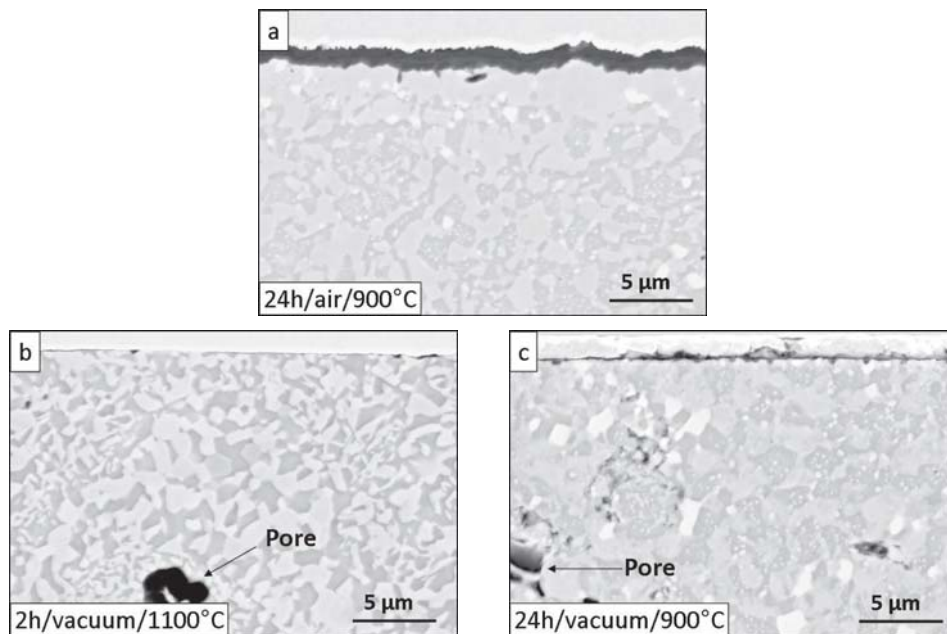


Fig 9.22 – SEM images of 2mm thick free-standing NiCoCrAlY(hi-Al) specimens after different heat treatment conditions: a) 24h/ air/ 900°C, b) 2h/ vacuum/ 1100°C and c) 24h/ vacuum/ 900°C.

9.3.3 Discontinuous exposure of MCrAlYs subjected to alternative heat treatments

The specimens with alternative heat treatments were subsequently exposed in air at 1100°C up to 406h. Concentration depth profiles were obtained by SNMS after 16h of exposure, as presented in Fig. 9.23. It is noticed after this short exposure that the TGO on the pre-oxidized specimen is still thicker than in the specimens annealed in vacuum. By comparing the latter, the smaller area of Al-depletion suggests that the scale has grown slower on the specimen annealed at 900°C than on that annealed at 1100°C.

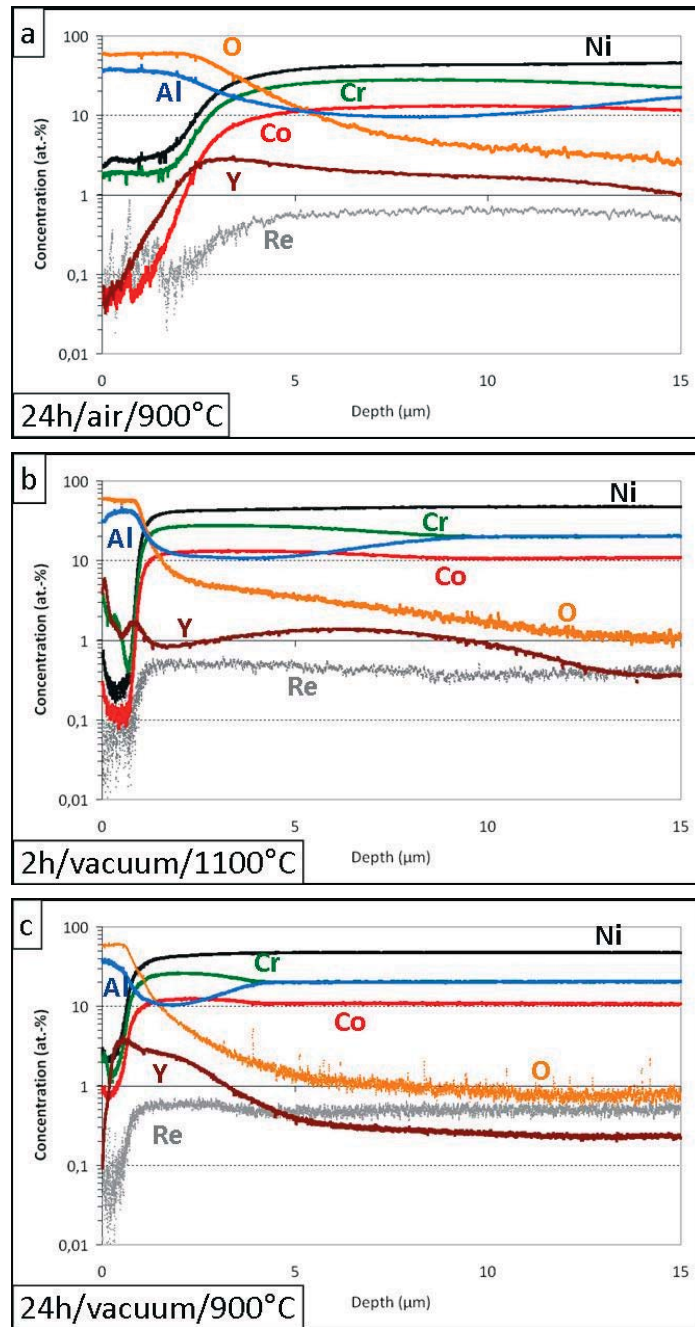


Fig 9.23 – SNMS concentration profiles of 2mm thick free-standing NiCoCrAlY(hi-Al) with different heat treatment conditions: a) 24h/ air/ 900°C, b) 2h/ vacuum/ 1100°C and c) 24h/ vacuum/ 900°C after 16h of isothermal exposure in air at 1100°C.

An interesting observation is that the concentration of aluminum reaches a maximum at the surface in the specimens annealed at 900°C, both in air and in vacuum, indicating the

formation of almost exclusively Al_2O_3 , while the concentration of this element presents a maximum at depths between 0.5-1.5 μm in the specimen annealed at 1100°C. In the latter case an enrichment of Cr and Y is found at the surface (see Fig. 9.23).

These profiles also indicate different depths of maximum concentration of internal oxidation of Y depending on the pre-treatment. In the case of vacuum heat treatment at 1100°C, the strong Y-enrichment at the surface (0 - 1 μm) is due to internal oxidation during annealing (Fig. 9.21). A wider “peak” around 3-10 μm below the surface formed as a result of internal oxidation of Y during subsequent exposure in air. On the specimens heat-treated at 900°C no Y-enrichment is observed at the very surface after oxidation. This is due to the fact that the Y-diffusion is slower at lower temperatures. Therefore, during heat treatment in vacuum at 900°C, Y is internally oxidized without reaching the surface (Fig. 9.23c). A similar situation occurs in the specimen during air annealing at 900°C (Fig. 9.23a).

SEM cross section images of 0.3mm thick specimens after 110h of exposure are presented in Fig. 9.24. It is noted that the average TGO thickness of the specimen annealed in vacuum at 900°C reached 3.9 μm (Fig. 9.24c), and so did not considerably differ from that of the specimen pre-oxidized at 900°C in air, which reached 3.7 μm (Fig. 9.24a). The specimens annealed in vacuum for 2h at 1100°C showed in contrast formation of pegs intruding into the coating up to 10 μm in depth. In the places without pegs the scale thickness was, however, similar to the 900°C-treated samples.

This observation in Fig. 9.24 indicate that the heat treatments done on the NiCoCrAlY(hi-Al) specimens influenced the morphology of the scales grown during air oxidation, as was anticipated by the SNMS plot of Fig. 9.23.

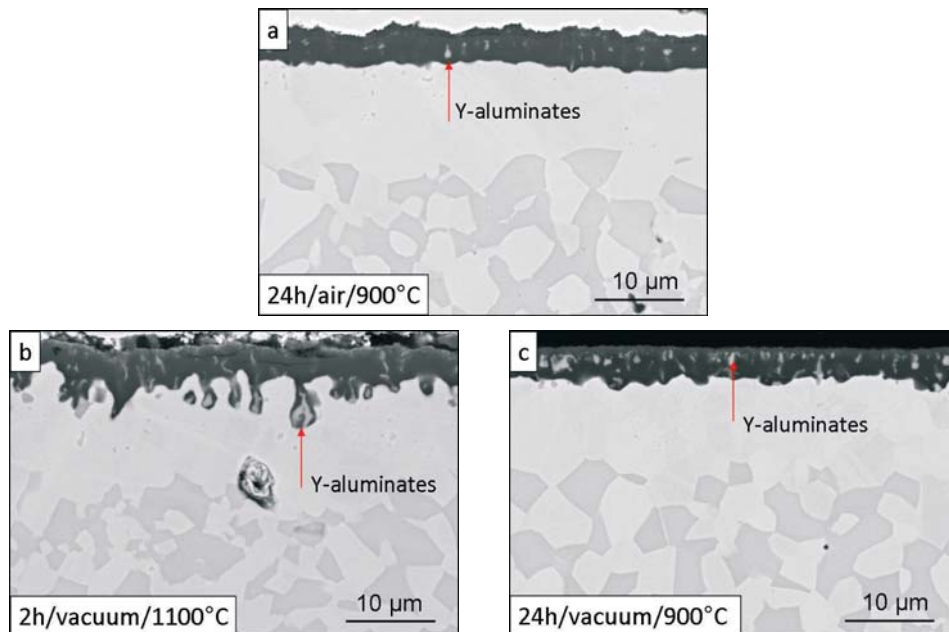


Fig 9.24 – SEM images of 0.3mm thick free-standing NiCoCrAlY(hi-Al) coatings with different heat treatment conditions: a) 24h/ air/ 900°C, b) 2h/ vacuum/ 1100°C and c) 24h/ vacuum/ 900°C after 110h of discontinuous exposure in air at 1100°C.

Fig. 9.25 shows that this effect was reproducible also in thinned free-standing CoNiCrAlY coatings. Most of the coarse Y-aluminates formed in the specimens annealed in vacuum at 1100°C are concentrated in an area 5-10μm below the oxide surface, while they were found 1-7μm deep beneath this surface in the specimens pre-treated at 900°C. For this coating material, a clearer evidence of (Cr,Co)-rich spinel formation was found in the sample annealed at the higher temperature.

After exposing thinned NiCoCrAlY(lo-Al) specimens under the same conditions differences in Y-distribution are difficult to observe due to the lower Y-reservoir in this coating (Fig. 9.26). However, another interesting finding was obtained, the scale of the specimens annealed in vacuum at 1100°C roughened during high temperature exposure (Fig. 9.26b), while it remained flat on the specimens pretreated at 900°C (Figs. 9.26a and 9.26c). This mechanical deformation was observed in section 9.2 in specimens with initial surface condition affected by heat treatment (HT specimens). If this zone affected by heat treatment was removed, the deformation was hindered (HT+G specimens).

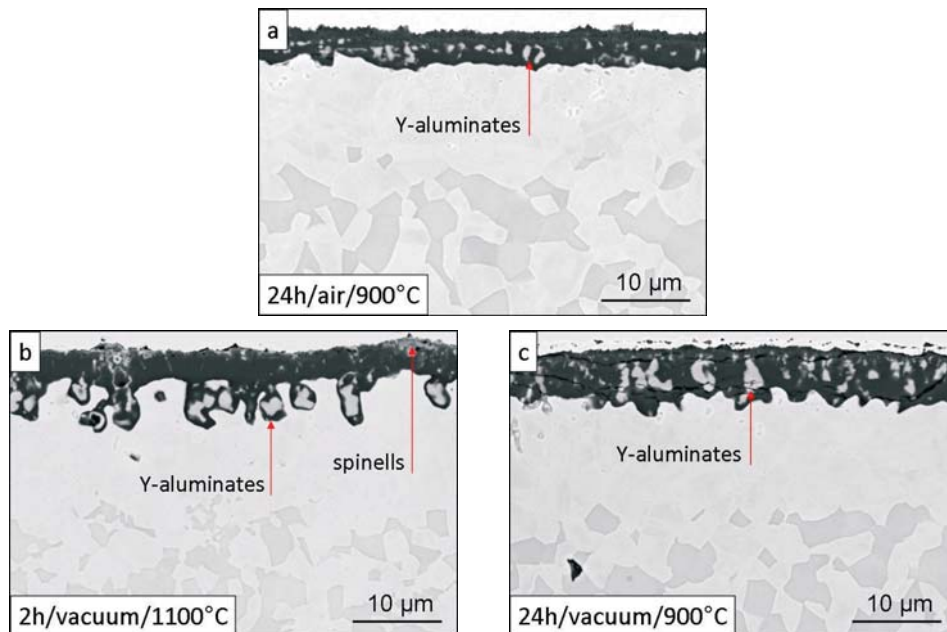


Fig 9.25 – SEM images of 0.3mm thick free-standing CoNiCrAlY coatings with different heat treatment conditions: a) 24h/ air/ 900°C, b) 2h/ vacuum/ 1100°C and c) 24h/ vacuum/ 900°C after 110h of discontinuous exposure in air at 1100°C.

The present analysis gives an additional proof that the enrichment of Y at the surface during the first stage of vacuum annealing (2h at 1120°C), and the volume changes associated with YAG formation during oxidation might be responsible for the surface roughening. If vacuum annealing is performed at lower T (24h at 900°C), the slowly diffusing yttrium is not enriched the surface. The scale roughening was also observed on 2mm thick specimens of NiCoCrAlY(lo-Al) pre-treated in vacuum at 1100°C, in spite of being more massive samples as appreciated in Fig. 9.27.

This investigation proves that the oxidation behavior of a MCrAlY-coating can be affected by the heat treatment parameters. There is an important practical implication of this observation. Since the MCrAlY coating heat treatment is optimized for the superalloy substrate, the same coating could exhibit different oxidation behavior on different base materials.

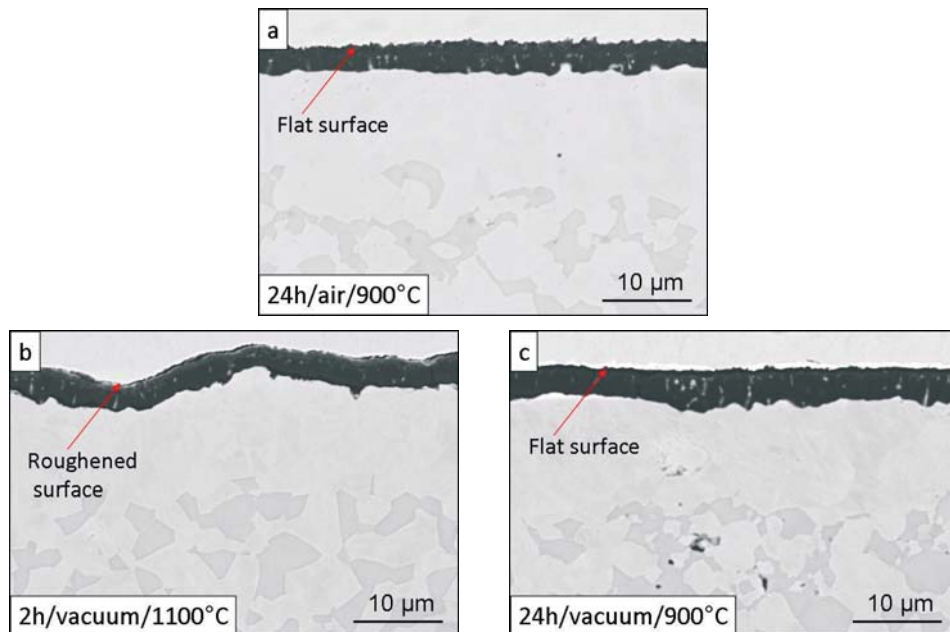


Fig 9.26 – SEM images of 0.3mm thick free-standing NiCrAlY(10-Al) coatings with different heat treatment conditions: a) 24h/ air/ 900°C, b) 2h/ vacuum/ 1100°C and c) 24h/ vacuum/ 900°C after 110h of discontinuous exposure in air at 1100°C.

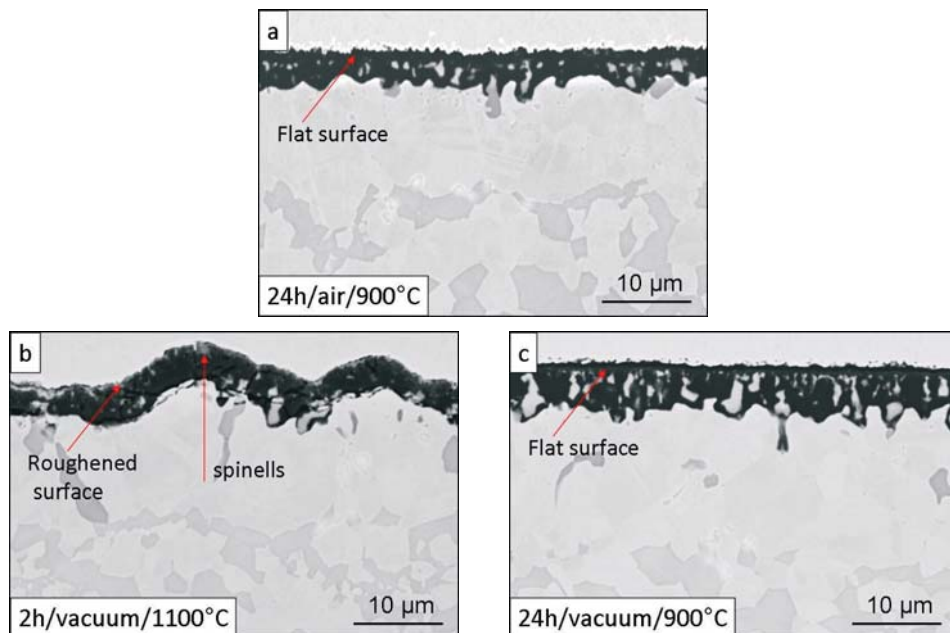


Fig 9.27 – SEM images of 2mm thick free-standing NiCrAlY(10-Al) coatings with different heat treatment conditions: a) 24h/ air/ 900°C, b) 2h/ vacuum/ 1100°C and c) 24h/ vacuum/ 900°C after 110h of discontinuous exposure in air at 1100°C.

Finally, it should be noted that similar to the observations made in the previous section, for coatings with large Y-reservoirs after long oxidation times the effect of heat treatment procedure on the scale growth and adherence is leveled out.

9.4 Effect of oxygen impurities on the oxidation behavior of VPS MCrAlY-coatings

9.4.1 General remarks

It is well known that the O-impurities can affect the Y-incorporation into the alumina scales on MCrAlY-coatings [Gudmundsson, Naumenko-2]. In the present work it was decided to study whether local variations in the O-content in the coating could take place. For this purpose, chemical analysis was carried out on pieces from different locations of the original VPS-deposited plate. Contrary to as normally proceeded, specimens were cut out not only from the central area of the plate but also from the edge or areas near-by the edge of the plate (Fig. 9.28). The chemical analysis showed that non-negligible differences in oxygen and carbon content exist especially between areas of the center of the plate and areas at the edge of the plate (table 9.1). The O-content in areas from the center of the plate was around 450 wt.-ppm whereas in areas from the edge of the plate was around 700 wt.-ppm.

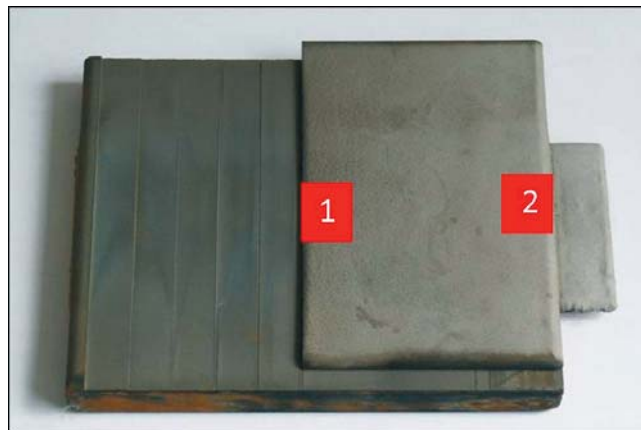


Fig 9.28 – VPS-deposited NiCoCrAlY(10-Al) plate showing areas with different oxygen contents

Area	C (ppm)	O (ppm)
1	8	458
2	41	728

Table 9.1 – C and O contents (wt.-%) after chemical analysis on areas 1 and 2 shown in Fig. 9.30 of the NiCoCrAlY(10-Al) plate produced by VPS.

After this finding it was decided to specifically study the oxidation behavior of specimens from different locations of the plate upon oxidation in air at 1100°C. Furthermore, in order to expand the range of MCrAlY oxygen content, an additional NiCoCrAlY(lo-Al) was produced by HVOF and tested. The respective chemical analysis of the newly produced plate confirmed that the O-content is with 2400 ppm significantly higher than in VPS-produced coatings. For this batch, no significant differences in O-content were found across the 120 x 100 mm plate. Apart from the difference in oxygen content, the chemical composition of the HVOF plate did not exhibit any substantial difference with that of the VPS, as shown in Table 5.1. Neither the microstructure nor porosity in the HVOF specimens deviated noticeably from the VPS specimens.

For the specimen preparation all other parameters apart from O-content were kept constant: only one coating material was investigated, the NiCoCrAlY(lo-Al), from which only 2mm thick free-standing specimens with flattened surfaces (1200 grit) were used. The flattening was conducted prior to the heat treatment, i.e. the specimens had initial HT surface condition (see section 9.2), and the vacuum annealing applied was the standard two-stage treatment (2h at 1120°C + 24h at 845°C). The only -known- variable in the specimens tested in this part is their oxygen content in the as-sprayed state, the VPS specimens from the center of the plate contained approximately 450 ppm of oxygen, those from the edge around 700 ppm and the HVOF specimens approx. 2400 ppm (wt.-ppm).

9.4.2 Isothermal oxidation of free-standing MCrAlYs with varying O-content

After exposing specimens of NiCoCrAlY(lo-Al) isothermally in air at 1100°C and single cooling to room temperature, differences in the oxide adherence are found even at macroscopic scale (Fig. 9.29). While the HVOF specimen exhibits a fully adherent TGO, partial spallation occurred in the VPS specimens, seemingly more pronounced in the specimen with the lowest O-content.

SEM cross section images after an exposure of 110h at 1100°C show significant differences in the scales formed in the different specimens. In the HVOF-deposited sample a flat, adherent TGO formed with average thickness of 2µm and composed almost exclusively of Al₂O₃ (Fig. 9.30a). The bulk of the metal exhibits abundant tiny oxide precipitates of Al and Y, as typical for the coatings deposited with this technique.

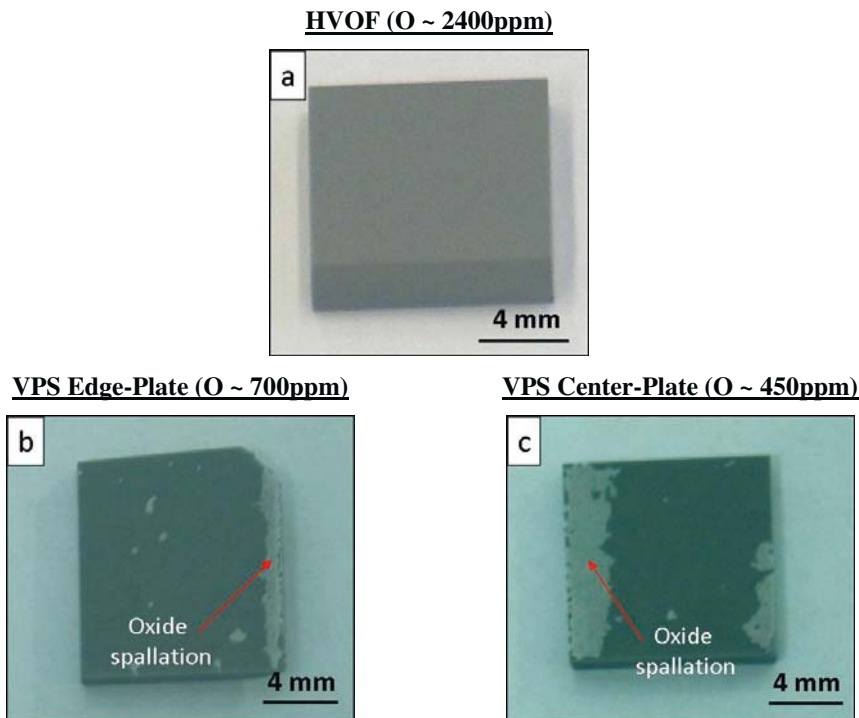


Fig 9.29 – Macroscopic images of 2mm thick free-standing NiCoCrAlY(lo-Al) coatings with different oxygen content: a) 2400 ppm, b) 700 ppm and c) 450 ppm after 406h of isothermal exposure in air at 1100°C.

In the VPS specimen cut out from the edge, with an approximate O-content of 700 ppm, Y was largely incorporated in the oxide scale leading to a high density of Y-aluminates both in the oxide, in pegs and beneath the oxide/metal interface. Cracks were found in the TGO running parallel to this interface. The oxidation of the VPS specimen removed from the center of the plate was harsher after the 110h air exposure. In this case not only was Y vastly incorporated in the oxide, but also TGO and coating surface roughening occurred. In addition, this scale contained a larger number of cracks. Apart from the Y-aluminates formed in the immediate vicinity of the interface, coarse Y-oxide precipitates formed as deep as 30-40µm below the oxide.

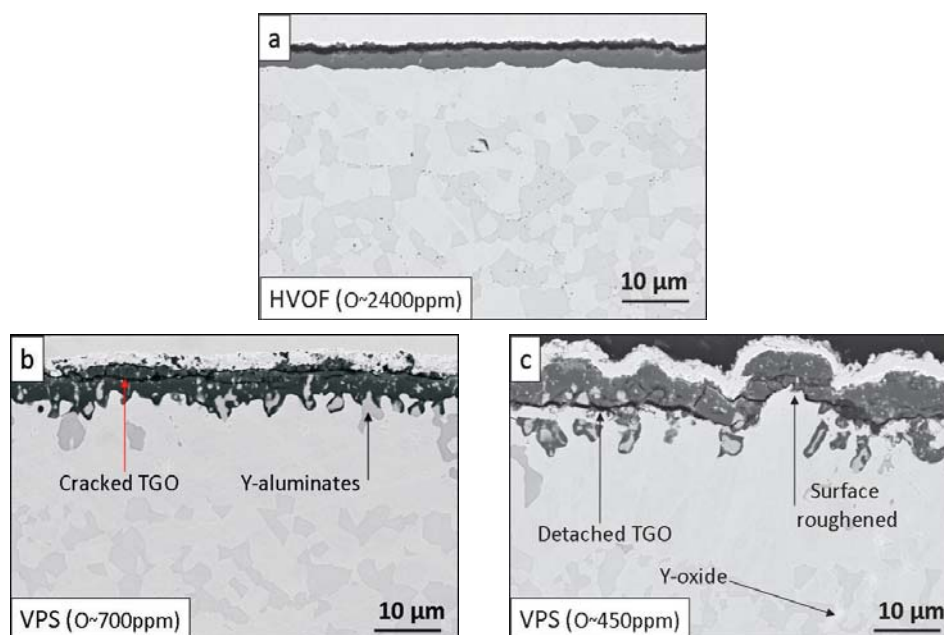


Fig 9.30 – SEM images of 2mm thick free-standing NiCoCrAlY(lo-Al) coatings with different oxygen content: a) 2400 ppm, b) 700 ppm and c) 450 ppm after 110h of isothermal exposure in air at 1100°C.

After observing these differences in oxide growth and morphology it is important to recall that the specimen were exposed simultaneously in the furnace, have the same nominal chemical composition, and were identically pretreated. A larger O-content in the bond coat can bind the “excess” of yttrium and hence, reduce the detrimental effects described in section 8.3.4 (uncontrolled incorporation in the scale and accelerated oxide growth). The roughened surface on the specimen (Fig. 9.30c) with a lower initial O-content (450 ppm) resembles those exposed without grinding after the heat treatment (HT) observed in section 9.2. It was then explained that a strong enrichment of Y in the outermost part of the surface during vacuum annealing (and the associated volume change with transformation to Y/Al-compounds) induced additional growth stresses in the scale that could deform this zone or even the whole specimen if it is not too massive. With the present finding it is shown that this effect is attenuated or even avoided if part of the yttrium is bound in the bulk of the metal, for example by oxygen (Figs. 9.30a and 9.30b).

Oxidizing other specimens for longer times (406h) permitted observing the consequences of Y-binding for the scale adherence (Fig. 9.31). The HVOF specimen (Fig. 9.31a) exhibits an adherent TGO that only slightly thickened (average thickness of 3µm) with respect to that analyzed after 110h of exposure. In contrast, the scales grown on the VPS

specimen, with less O-content, exhibit thicknesses two times greater than that on the HVOF and actually detached during metallographic preparation, what can be considered as an indication of a weakened adhesion (Figs. 9.31b and 9.31c).

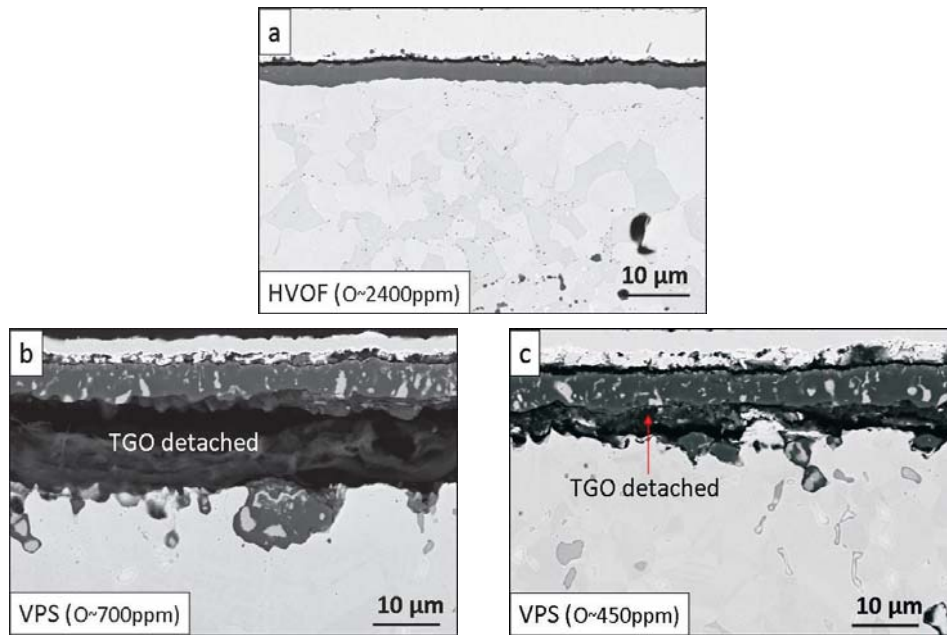


Fig 9.31 – SEM images of 2mm thick free-standing NiCoCrAlY(10-Al) coatings with different oxygen content: a) 2400 ppm, b) 700 ppm and c) 450 ppm after 406h of isothermal exposure in air at 1100°C.

The presence of internal oxide precipitates was better recognized with optical micrographs as shown in Fig. 9.32. The HVOF specimen possesses numerous tiny precipitates mainly of Al-oxide, but also in minor proportion of Y-oxide, uniformly distributed across the coating bulk. These oxides formed during coating manufacturing and heat treatment.

The internal oxidation in the VPS specimens has a different morphology, characterized by coarser precipitates mainly of yttria concentrated in the vicinity of the oxide/metal interface. These oxides formed during air exposure as a result of Y and O flux in opposite directions. In the O-richer specimen cut out from the edge of the plate, such precipitates are found concentrated on the top 20µm beneath the interface oxide/metal (Fig. 9.32b). In the O-poorer specimen removed from the center of the plate these oxides reach as deep as 60µm below that interface (Fig. 9.32c). The depth of the coarse yttria precipitates is plotted for all three specimens in Fig. 9.33. Please note that this diagram refers only to the internal oxidation

of Y occurred during air exposure; the oxidation occurred during the MCrAlY deposition, seen as fine precipitates homogenously distributed across the bulk in the HVOF specimen is not considered.

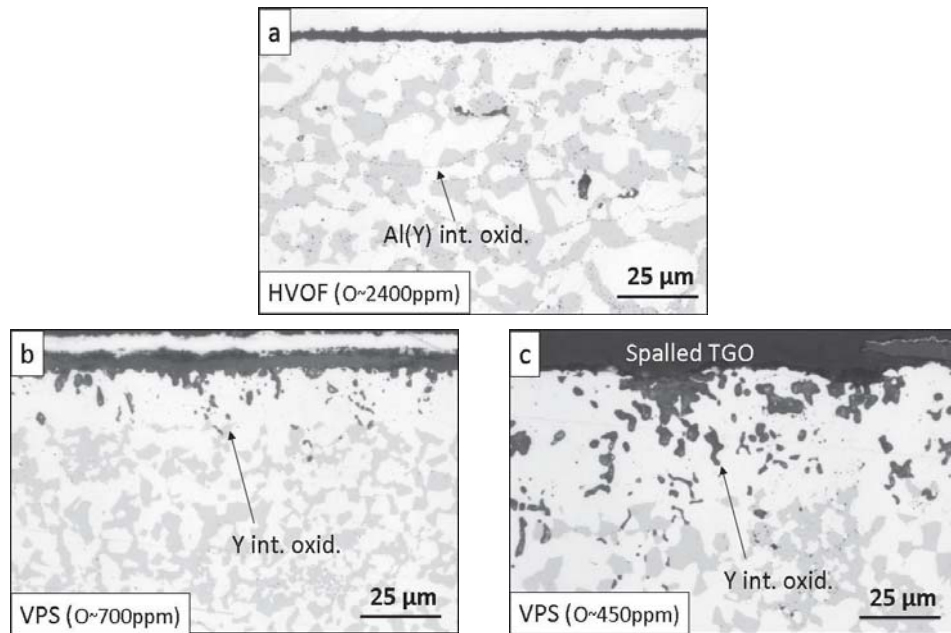


Fig 9.32 – Optical microscopic images of 2mm thick free-standing NiCoCrAlY(Al) coatings with different oxygen content: a) 2400 ppm, b) 700 ppm and c) 450 ppm after 406h of isothermal exposure in air at 1100°C.

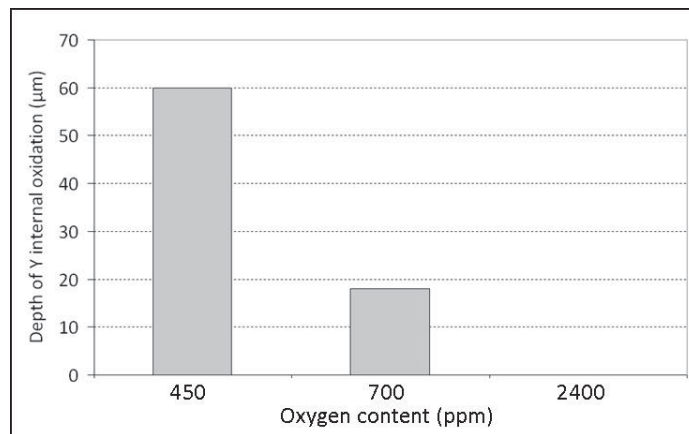


Fig 9.33– Depth of coarse yttria precipitates (formed during air exposure) in 2mm thick free-standing NiCoCrAlY(Al) coatings with different oxygen content after 406h of isothermal exposure in air at 1100°C.

Another interesting aspect is that despite the partial binding of Al during spraying in the HVOF sample, in the form of tiny Al(Y)-oxide precipitates, the depletion of the Al-rich β -

phase is minimal compared to the depleted zones in the VPS samples. The extent of this depletion is 4 times higher in the VPS specimen with lower O-content than in the HVOF one as illustrated in Fig. 9.34.

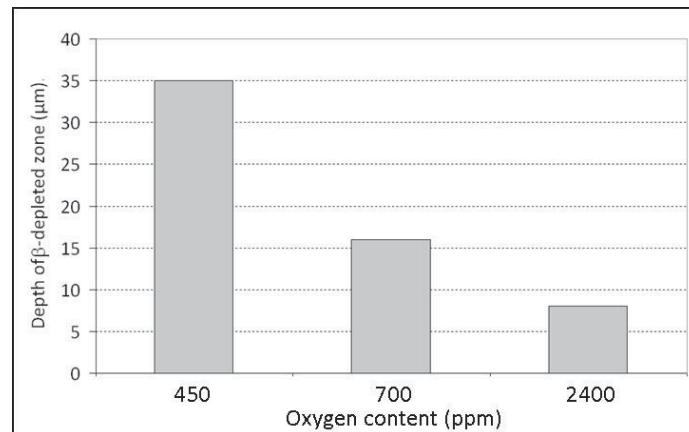


Fig 9.34 – Depth of β -depleted zone in 2mm thick free-standing NiCoCrAlY(lo-Al) coatings with different oxygen content after 406h of isothermal exposure in air at 1100°C.

9.4.3 Estimation of amount of Y bound in MCrAlYs with varying O-content

In order to have an estimate on how much yttrium remains available for incorporation into the scale, i.e. in solid solution or in the form of Ni_xY_z intermetallic phases, in the different specimens according to the O-content, a simple atomic weight ratio of yttria (Y_2O_3) is calculated:

$$\frac{Y}{O} = \frac{178}{48} = 3.7$$

Using this data it was estimated how much Y in the coating is tied up into oxides by the oxygen impurities during spraying:

Specimen	Y-content (wt-%)	O-cont (wt.-ppm)	Est. Y bound (wt-%)	Y-Reservoir present as oxide
VPS (center)	0.27	450	0.17	63%
VPS (edge)	0.27	700	0.26	96%
HVOF	0.22	2400	0.89	100%

Table 9.2 – Estimated amount of Y that could be bound by the oxygen impurities in the NiCoCrAlY(lo-Al) specimens investigated.

Since the concentration of yttrium in this coating alloy is 0.27 (wt.-%), it is observed from the estimates that in a specimen removed from the center of the VPS-plate, approx. 63% of the Y-reservoir is bound. The remaining 37% of the reservoir should be available for incorporation into the scale. This explains why an excess of Y diffusing to the surface upon high temperature exposure is observed in the specimens from this area.

In those specimens cut out from the edge of the same plate, according to this estimation 96% of the Y-reservoir is bound. However in reality, minor local variations of the O-content in this area are expected to determine whether Y is fully bound as internal oxides or part of it is actually available for incorporation into the scale during air exposure at high temperature (as was the case for the specimens shown in Figs. 9.32b and 9.33b). In any case, the amount of yttrium available for incorporation in the scale, and thus to influence the oxidation, is lower in these specimens, compared to those from the central area.

In the investigated HVOF MCrAlY coatings, there is so much oxygen that theoretically up to 0.89% could have been bound internally to form yttria. Since the actual concentration of Y only amounts to 0.22%, it is according to the thermodynamic oxide stability wholly bound and the remaining oxygen will react with the element with Al. This explains why in the HVOF specimens, tiny precipitates of Al(Y)-oxide were found all across the coating bulk and why no Y/Al-pegs formed in the scale or in the scale/metal interface in this material.

These experiments show how sensitive the oxidation behavior of a MCrAlY can be to slight variations on the amount of oxygen impurities resulting from the bond coat deposition. In this case, the study was carried out on specimens removed from MCrAlYs deposited over a 120 x 100 mm steel plate. However, similar variations in the amount of oxygen impurities could be expected for turbine blades, which have larger and more complex surfaces with areas of high concavity and convexity.

This study shows that the Y-reservoir depends on the form in which Y is present in the coating. Oxygen impurities introduced by processing reduce the amount of “free” Y by tying it up into oxides. This effect cannot be considered as negative only. The 2mm thick specimens presented in this section, with larger Y-reservoirs, reaffirm that oxygen impurities can reduce to some extent the negative effects of yttrium “overdoping” (described in section 8.3.4):

accelerated oxide growth rate, faster tendency to scale adherence loss and generation of stresses that can deform the surface.

In the 2mm thick HVOF specimens the “excess” of yttrium is bound and hence, hindered to diffuse to the surface during high temperature exposure. Consequently a thin, slow-growing alumina scale has formed. Whether this scale has sufficient resistance to spallation during long-term cyclic exposure should be verified in additional future work.

9.5 Summary on the effects of pre-treatment

This investigation demonstrated that the oxidation behavior, and consequently the oxide adherence, of MCrAlY-coatings can be strongly influenced by processing parameters, even if the chemical composition and the known geometrical parameters (coating thickness and surface roughness) are kept constant.

The alteration of the surface initial condition during heat treatment (HT) can significantly influence the oxidation behavior compared to the case where these superficial effects are removed (HT+G). In the first case, an Y-enrichment at the surface, promotes the formation of Y/Al-compounds and spinels in the early oxidation stages. In the second case, mainly alumina can form initially. It was observed that the concentration of Y at the surface of a MCrAlY with initial as-heat-treated condition can even cause mechanical deformation due to transformation into Y-aluminate phases. These findings are relevant considering the processing sequence followed between bond coat surface smoothening and component heat treatment during production of EB-PVD systems. In the presence of a large Y-reservoir, the further incorporation of Y into the scale upon high temperature exposure can level out the modifications of chemical composition at the surface introduced by HT.

The second part of the investigation proved that a variation of the heat treatment parameters (temperature, time, atmosphere) can cause important differences in TGO growth rate and morphology. It was shown that during the first stage of heat treatment (2h in vacuum at 1100°C) the diffusion of Y to the surface is enabled and the formation of alumina suppressed. Heat treatments at 900°C, both in air and in vacuum, permitted the formation of an alumina layer in the initial oxidation stages and consequently Y/Al-rich compounds

formed beneath this layer. The risk of surface deformation in this case was reduced or even eliminated.

Ultimately, it was shown that even if all the parameters known until now to influence the oxidation behavior are kept constant (geometric and processing-dependent), variations of oxygen impurities introduced during spraying of MCrAlY coatings can also lead to considerable changes in the oxide growth rate, morphology and adherence. These differences originated from the binding of Y by O into oxides. In the presence of an excessive Y-reservoir, this effect can be positive, since the overdoping on an alumina scale can be prevented. Significant variations of oxygen content can be even found within the same batch, or transferred to practical applications, within the same component. This investigation concentrated in the NiCoCrAlY(10-Al), since in the other MCrAlYs only a partial tying up of Y is achieved due to higher Y-concentrations, the effects are thus not so pronounced.

10. Effect of the TGO growth rate on the lifetime of TBC systems

10.1 General Remarks

It is well established in the literature that the thermally grown oxide often represents the starting point for failure which ends up with the topcoat delamination in a TBC system [Gell-1, Pint-1, Yanar-4]. A controlled and predictable oxidation of the MCrAlY coating, which also involves the knowledge of the TGO characteristics at failure, is therefore desired in such a coating system for design and modeling purposes of turbine blades. Several authors [Kim, Tolpygo-4] suggested that a critical oxide scale thickness to TBC failure (which is proportional to a critical thickness for onset of oxide spallation) can be defined for TBC's produced by electron-beam physical vapor deposition (EB-PVD). Different values of the scale thickness to failure were reported by Yanar and Meier for different EB-PVD TBC systems [Yanar-1]. Moreover, indications were found [Yanar-2, Nijdam-1] that for the same system, the critical oxide scale thickness might depend on the pre-treatment procedures of the MCrAlY bond coat prior to the TBC-deposition.

If the assumption of the critical TGO thickness for TBC failure is correct, then a variation of the TGO growth rate should result in a variation of the time to TBC failure. However, throughout this work, when different oxide growth rates have been encountered for the same material, they have been associated with inherently different oxide scales, i.e. scales with different morphologies, chemical composition and in some cases, mechanical properties. The parameters varied to induce different oxide growth rates in the MCrAlY material are:

- Exposure temperature,
- Coating thickness (yttrium-reservoir),
- Surface roughness,
- Processing sequence,
- Heat treatment parameters and
- Amount of oxygen impurities.

Even after a separate variation of any of these parameters different TGO growth rates were obtained but the scales formed were inherently different in morphology and

composition. Hence, the use of this information for the estimation of a critical oxide thickness would be misleading.

In order to find out whether a change in the scale growth rate in MCrAlY bond coats quantitatively affects the TBC-lifetime, one should in an ideal case be able to change only the scale growth rate without changing other parameters, such as scale morphology and adherence. In the current chapter an attempt has been made to find out an alternative experimental parameter that enables this estimation.

For this purpose, a variation of the oxygen partial pressure of the atmosphere was used to influence the scale growth rate based on the indications found in previous studies with FeCrAl-base, alumina forming alloys [Kolb] and on observations from other authors [Nijdam-4]. According to these contributions the alumina scale growth rate can be influenced by a change in oxygen partial pressure (p_{O_2}) in the atmosphere. The main reason for the latter effect was shown to be the change in the chemical potential gradient across the scale rather than modification of the alumina defect structure and associated changes to different coefficients. Hence, the oxidation rate was predicted to decrease with decreasing p_{O_2} ; a good agreement was observed between the calculated rates and thermogravimetric measurements.

10.2 Lifetime of EB-PVD-coated specimens in air and Ar- 4% H₂ - 2% H₂O environments at 1100°C

In the present study cylindrical TBC specimens containing the NiCoCrAlY(10-Al) as bond coat (batch KHZ, section 5.2) were cyclically exposed at 1100°C in two different atmospheres, a high p_{O_2} atmosphere (air; $p_{O_2} = 0.2$ bar) and a low p_{O_2} atmosphere (Ar-4%H₂-2%H₂O; $p_{O_2} = 10^{-14}$ bar). In this case, the cycles were set with 4h at high temperature and 1h cooling. The relatively long cooling dwells were necessary in order to guarantee that the specimens reach a near-room temperature (below 80°C), since the gas-recipient system had a relatively large thermal mass. Therefore, the heating/cooling rates were lower in these experiments than in the cyclic tests presented in chapters 6, 8 and 9.

A variation of the TGO growth rate was achieved; after 100h, the oxide scale grown on the specimen exposed in air was 3.1µm thick (in average) while that formed on the specimen exposed in Ar-4%H₂-2%H₂O was 2.2 µm thick and after 300h the TGOs thickened

to 4.7 μm and 3.2, respectively (Fig. 10.1), these differences were better appreciated when plotted together (Fig. 10.2). Note that although the oxide detached from the bond coat during cross-section preparation in all cases, the TBC had not exhibited any macroscopic sign of damage after test completion at 100h and 300h.

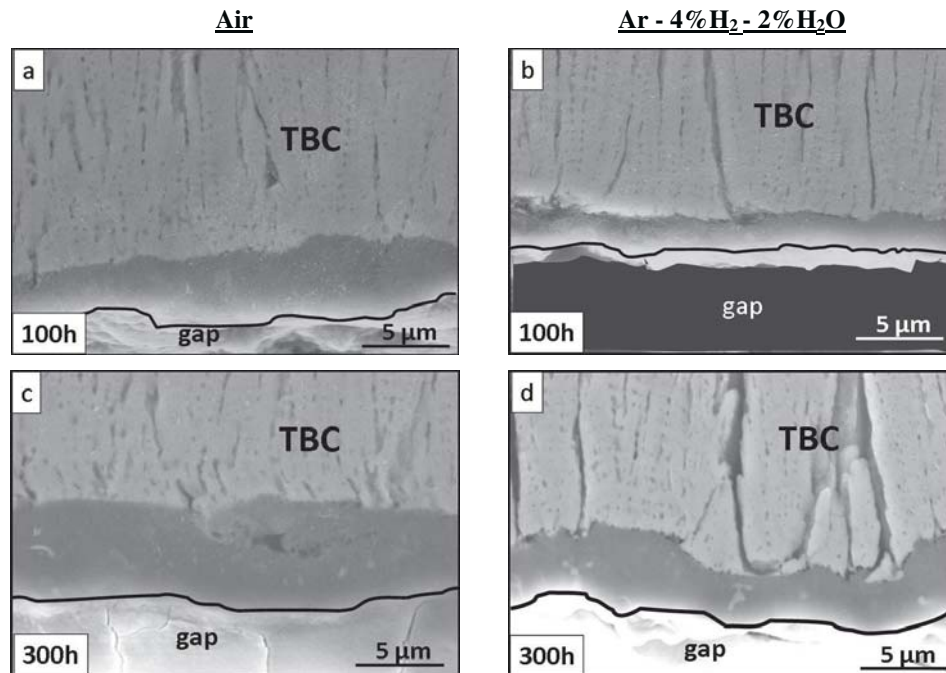


Fig 10.1 – SEM images of oxide grown in EB-PVD TBC specimens with NiCoCrAlY(10-Al) bond coat after cyclic exposure in air for: a) 100h; c) 300h and in Ar-4% H_2 -2% H_2O for: b) 100h; d) 300h at 1100°C. Solid line delimitates the detached TGOs

An exceptional improvement in scale adherence was obtained for this coating material when the surface was ground after the vacuum heat treatment (section 9.2.3), as it was proceeded for the production of the EB-PVD coated specimens. However, the surface of the free-standing coatings described in section 9 were flattened by 1200 grit grinding, after which approximately 100 μm of material were removed, whereas the bond coat surface smoothening prior to EB-PVD deposition was carried out by cut wire peening, which generally involves a less extensive material removal (and thus, of the surface affected by the heat treatment) as reported by [Naumenko-2]. Consequently, only a smaller improvement is expected for the adherence in these TBC specimens, and the scale detachment upon metallographic preparation is therefore not surprising.

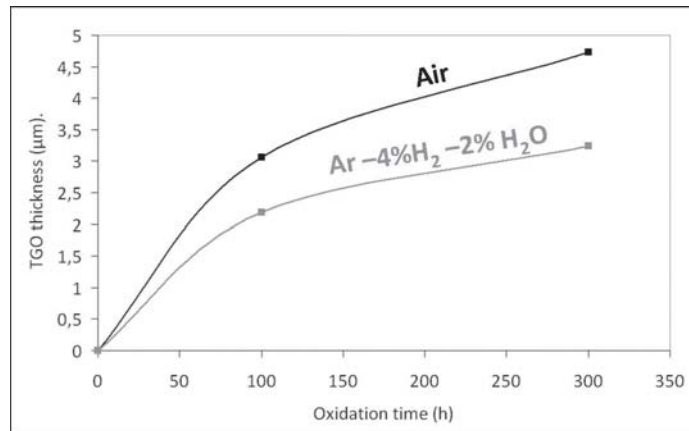


Fig 10.2 – Thickness evolution in TBC specimens with NiCoCrAlY(10-Al) bond coat after cyclic exposure in air Ar-4% H_2 -2% H_2O at 1100°C.

The extent of β -depletion after the exposure correlates with the differences of TGO growth rate; it is namely more accelerated in the specimens exposed in air than in those exposed in Ar-4% H_2 -2% H_2O . After 100h, nearly 50% of this Al-rich phase had been consumed in the specimen exposed in air (Fig. 10.3a) and around 25% in the specimen exposed in Ar-4% H_2 -2% H_2O (Fig. 10.3b). After 300h, the depletion was complete in the bond coat of the specimen exposed in air (Fig. 10.3c), whereas in that of the specimen exposed in the low pO_2 atmosphere reached approximately 65% (Fig. 10.3d).

An important observation is the fact that the oxide scales in Fig. 10.1, with different TGO growth rates, are almost identical with respect to microstructure and morphology, different to the results listed in section 10.1, where a different oxide growth rate was always associated with a variation of the scale composition and morphology, in some cases even of the internal stresses generated.

Subsequently, new identical specimens were exposed in the two atmospheres until TBC failure; the lifetime of the ceramic coating was 560h when exposed in air and 1060h when exposed in Ar-4% H_2 -2% H_2O . The TGO thickness at failure could not be measured since the oxide completely spalled off together with the ceramic coating, as it is frequently found for EB-PVD TBC coatings. Therefore, the available TGO thickness data after 100h and 300h in both atmospheres (Fig. 10.2) was extrapolated to estimate the TGO thickness at failure assuming a power law time dependence for the thickening rate [Echsler-1]. As can be seen in Fig. 10.4, the estimated TGO thickness at TBC failure is ca. 6 μm for both

atmospheres, which is apparently the critical TGO thickness for the studied EB-PVD TBC system under the used temperature cycling conditions.

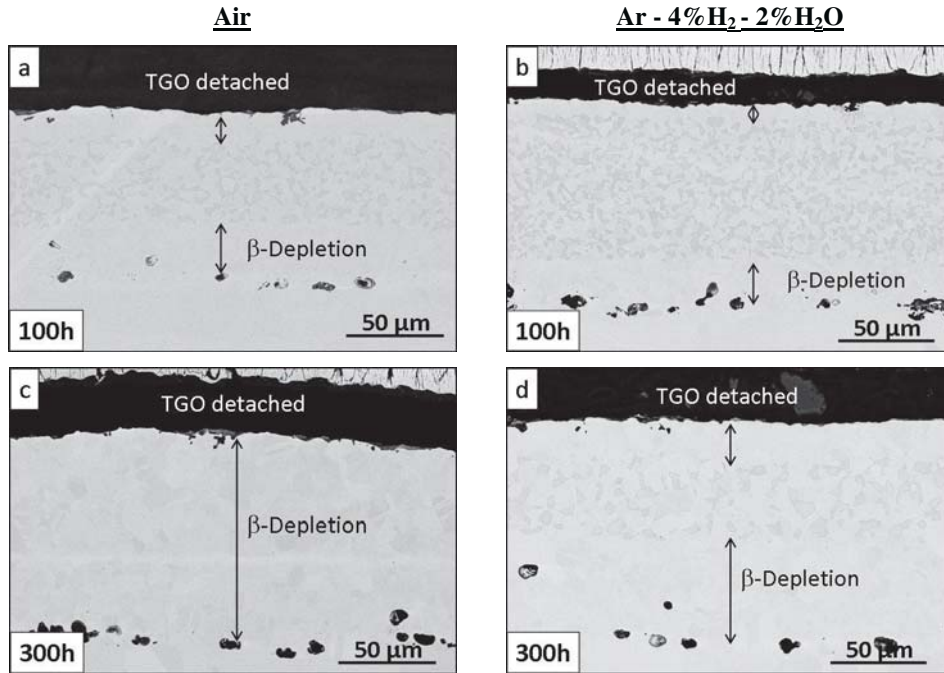


Fig 10.3 – Bond coat overview showing β -depletion in EB-PVD TBC specimens with NiCoCrAlY(10-Al) bond coat after cyclic exposure in air for: a) 100h; c) 300h and in Ar-4% H_2 -2% H_2O for: b) 100h; d) 300h at 1100°C.

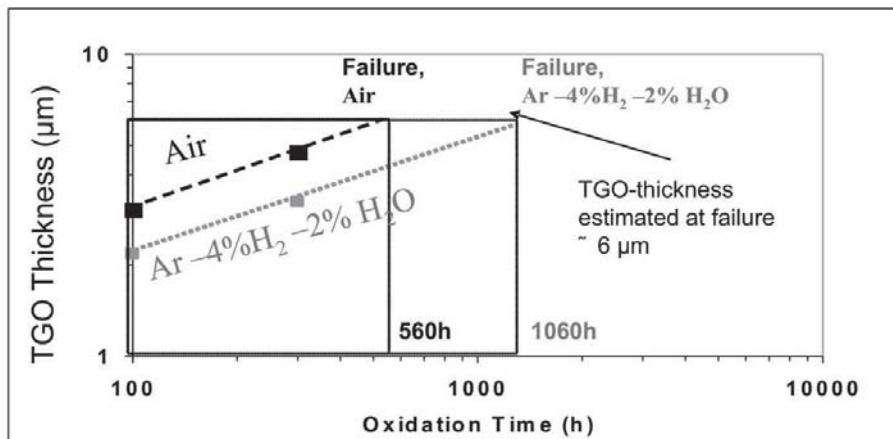


Fig 10.4 – Double logarithmic plot of TGO thickness as function of time for TBC specimens with NiCoCrAlY(10-Al) bond coat after cyclic exposure in air and in Ar-4% H_2 -2% H_2O at 1100°C, with estimation of thickness values at failure time

10.3 Lifetime of APS-coated specimens in Air + 2% H₂O and Ar- 4% H₂ - 2% H₂O environments at 1100°C

A similar investigation in atmospheres with different oxygen partial pressures was conducted with APS specimens. In this case, the high pO₂ atmosphere selected was humid air (Air + 2% H₂O; pO₂ = 10^{-0.7} bar) and the low pO₂ atmosphere was Ar- 4% H₂ - 2% H₂O (pO₂ = 10⁻¹⁴ bar) as in the previous investigation. The cylindrical specimens had the same geometry and were composed of the same materials as those described in the previous section, i.e. IN738/ NiCoCrAlY(lo-Al)/ YSZ, with the difference that no smoothening treatment was applied and the ceramic topcoat was deposited with APS.

The TBC lifetime of the APS-coated specimens showed as in the previous case a strong dependence on the atmosphere. It was, with 2052h, considerably longer for the specimen exposed in the low pO₂ atmosphere than for that exposed in the high pO₂ atmosphere, which exhibited failure after 648h (Fig. 10.5).

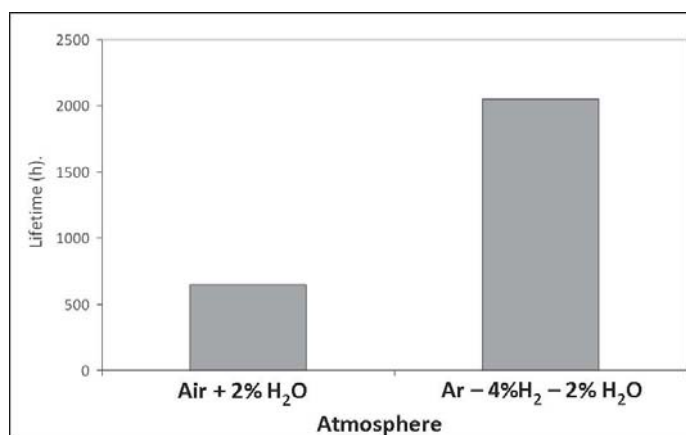


Fig 10.5 – Lifetime of TBC specimens with NiCoCrAlY(lo-Al) bond coat after cyclic exposure in humid air and in Ar-4%H₂-2%H₂O at 1100°C,

Cross section images of specimens exposed cyclically (cycles: 4h at high temperature, 1h cooling) in both atmospheres at 1100°C for shorter times (100h and 300h) are presented in Fig. 10.6. After these exposure times the TGO growth rate was indeed higher for the specimens exposed in humid air, e. g. after 100h it exceeds, with an average of 5μm (Fig. 10.6a), that grown in the specimen exposed in the Argon atmosphere which thickened to an average of 3.1μm (Fig. 10.6b). However, it is observed that the scale thickness on these rough

surfaces is harder to estimate due to strong variations between peaks and valleys. These variations were explained to be caused by a non-homogeneous Y-enrichment in the scale (section 8.2).

Beyond the non-uniform scales formed in all specimens, generally characterized by an enrichment of Y-aluminates in the valleys and of spinels in the peaks, it is appreciated that the composition of the scales grown in the different atmospheres deviate significantly. Spinel formation is much more pronounced on the samples exposed in humid air than those exposed in Ar- 4% H₂ - 2% H₂O. After 300h the top layer of the TGO is fully covered by these Cr-rich mixed oxides along the surface (Fig. 10.6c). Another factor that contributed to the extensive spinel formation was a local Al-depletion at the bond coat surface observed after APS-deposition (Fig. 10.7).

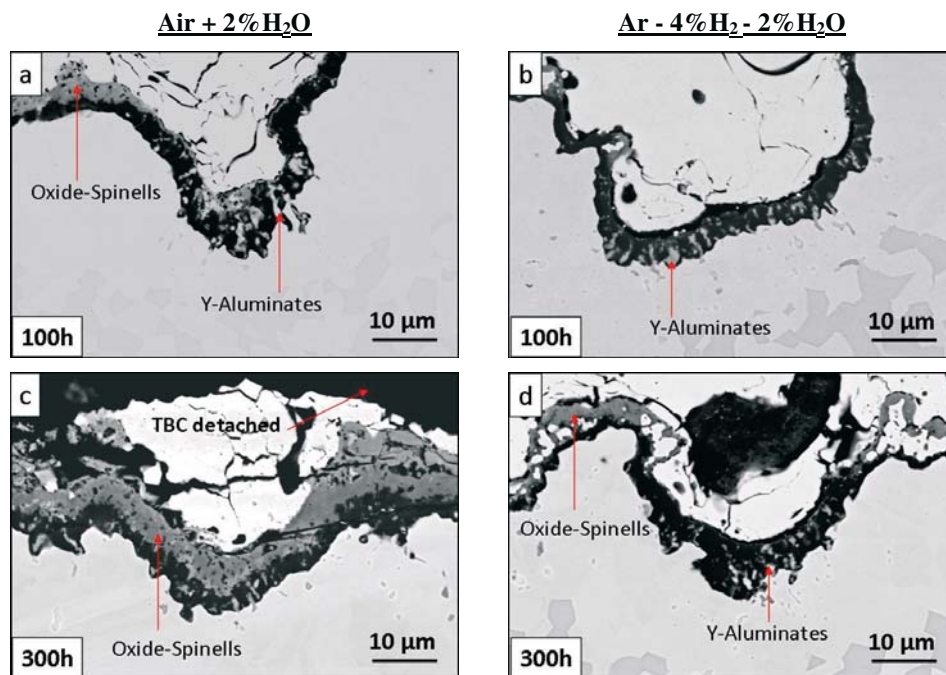


Fig 10.6 – SEM images of oxide grown in APS-TBC specimens with NiCoCrAlY(10-Al) bond coat after cyclic exposure in humid air for: a) 100h; c) 300h and in Ar-4%H₂-2%H₂O for: b) 100h; d) 300h at 1100°C.

In the peaks of the rough surfaces, Y and Al are depleted during vacuum heat treatment or initial oxidation stages at a much faster rate compared to the valleys. Consequently spinel formation occurs in the peaks and Y-Al mixed oxides pegs in the valleys (see section 8.2). Consequently, having obtained scales with different composition after

exposure in these atmospheres, no estimation of a critical oxide thickness to failure can be done for these APS-TBC systems.

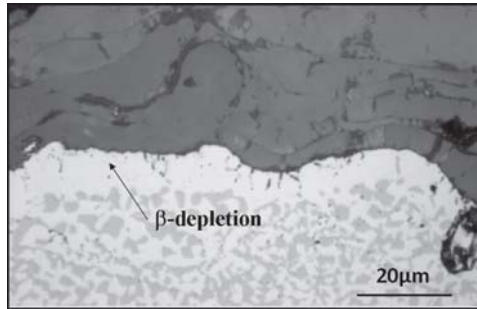


Fig 10.7 – Optical microscopic image showing beta-phase depletion in APS-TBC specimens with NiCoCrAlY(10-Al) bond coat in the as-received state

The TBC lifetime of the APS specimen exposed in Ar- 4% H_2 - 2% H_2O was considerably longer than that of the EB-PVD specimen exposed in the same atmosphere. This can be understood, among other reasons, by the possibility of stress relaxation through oxide cracking before definite TBC spallation takes place. Evidence of this effect was found by observing numerous cracks in the TGO, parallel to the oxide/metal interface, during the cross-section analysis of the failed APS-TBC specimen (Fig. 10.8).

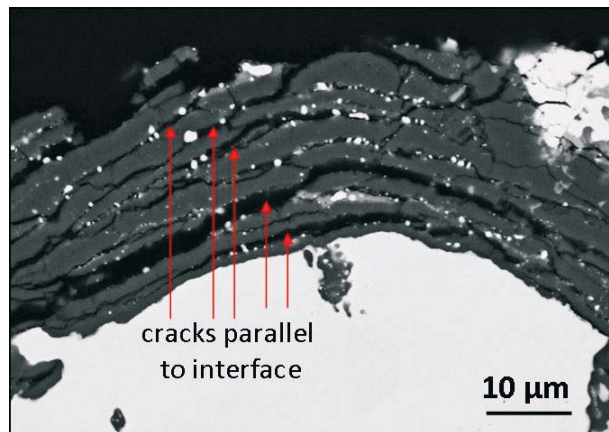


Fig 10.8 – Multiple cracks in TGO of APS-TBC specimen with NiCoCrAlY(10-Al) bond coat after 2052h of cyclic exposure in Ar-4% H_2 -2% H_2O at 1100°C.

Tang et al. reported that this phenomenon occurs mainly on the convex surface areas (peaks) where the tensile stresses originated by the thermal mismatch between bond coat and oxide reach a maximum [Tang]. If the TBC does not spall, the crack generated generally at

the oxide/metal interface is stopped (see t_1 in Fig. 10.9). Further exposure at high temperature will cause new oxide to grow beneath the crack (since the alumina scale is inward growing) (t_2 in Fig. 10.9) leading to the accumulation of cracks parallel to the oxide/metal interface (t_3 in Fig. 10.9). Despite this occurrence, APS-TBC spallation typically takes place either in the TBC, at the interface TBC/TGO or through the TGO.

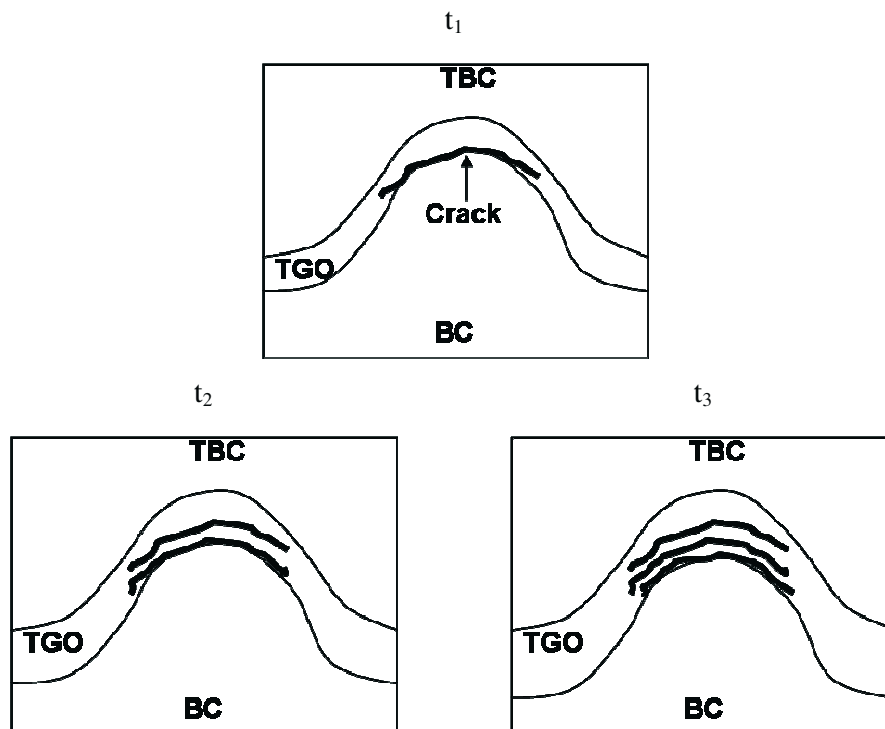


Fig 10.9 – Schematic of development of multiple cracks in TGO in a APS-TBC specimen.

10.4 Summary and final comments

Throughout this work it has been shown that the composition, morphology and, therefore, the growth rate of the oxide scales on MCrAlY-coatings can be significantly affected by variations of numerous parameters:

- Exposure temperature,
- Coating thickness (yttrium-reservoir),
- Surface roughness,
- Processing sequence,
- Heat treatment parameters and
- Amount of oxygen impurities.

In particular, these factors were found to have an effect on the amount and distribution of the internal yttrium-rich oxides in the coating surface and sub-surface regions, which in turn decisively influenced the oxidation behavior and produced inherently different scales.

On the contrary, the exposure of EB-PVD TBC specimens in atmospheres with considerably different oxygen partial pressures enabled the formation of oxide scales at different growth rates which were identical in morphology and composition. The outcome of the latter experiment indicated that a critical TGO thickness to topcoat failure exists for a given EB-PVD TBC system with a MCrAlY-coating, provided that the above listed parameters are kept constant.

Such estimation was not possible for an APS-TBC system with similar bond coat, since inhomogeneous scales formed on the rough BC surfaces. This was seen to be originated by the alterations of the coating chemical composition during vacuum heat treatment. Additionally, the damage mechanism in APS-TBC systems is entirely different

11. Summary and Conclusions

The first part of this investigation showed that the studied CoNiCrAlY bond coat exhibited a better alumina scale adherence than the two Ni-base coatings studied despite reproducible faster oxidation kinetics. The effect was observed in all three studied specimen types (TBC specimens, overlay coatings and free-standing coatings) both under discontinuous and cyclic oxidation conditions.

One reason for these observations was found to be a better phase stability over a wide temperature range (800-1100°C) in the CoNiCrAlY, whereas the Ni-base coatings undergo phase transformations $\gamma \rightarrow \gamma'$ upon cooling at temperatures between 700-900°C. It was proved that such phase transformations associated with volume changes considerably increase the CTE of the coating alloys leading to the development of higher thermal stresses in the scale upon cooling. Furthermore, it was shown that the high cobalt concentration in CoNiCrAlY increases the solubility of Cr in the matrix phase γ -Ni, hindering the formation of brittle Cr-rich phases such as α -Cr. These phases, likely to form in both Ni-base coatings along with γ' , can reduce the creep relaxation capability of the coating and in general be detrimental with respect to mechanical properties, e.g. fatigue. Ni(Y) intermetallic phases exhibited a higher stability in the CoNiCrAlY coating than in the Ni-base ones at temperatures above 1000°C. This could result in a slower diffusion of Y to the surface in the Co-base coating during high temperature exposure.

The experimental temperature dependence of MCrAlY microstructure provided a tool for estimating the real temperatures in the bond coats of a gas turbine during service. The results showed that they are clearly lower (800°C-900°C) than the temperatures at which usually the accelerated laboratory tests are conducted, i.e. above $T = 1000^\circ\text{C}$. Hence, considering the differences in the coating phase composition observed in this work between 1000°C and 800°C, care should be taken when extrapolating the laboratory results to real applications.

Another reason for the better resistance to scale spallation of the CoNiCrAlY coating can be its higher Y-content and higher stability of Ni(Co)Y-intermetallic phases compared to the Ni-base coatings. Therefore, the Y-reservoir might be consumed at a slower rate in the former coating material.

Beyond the chemical composition of a MCrAlY-coating, there are geometrical parameters that influence its oxidation behavior:

- The oxidation studies on rough surfaces showed that this geometry can induce the formation of non-homogeneous scales and a non-uniform distribution of internal oxidation, provided that the yttrium content is large enough and it is not tied up in stable compounds during manufacturing. The differences are originated by a non-uniform depletion of the elements with high O-affinity (Y and Al). A more rapid Y and Al depletion in the convex areas of the coating promotes local formation of (Cr,Co)-rich oxide spinels. The Y supplied from the bulk to the coating surface preferentially forms Y/Al-oxide pegs in the concave areas since they possess a higher Al-activity and establish shorter diffusion paths. As a result, the scales formed on rough surfaces have a different chemical composition and morphology in convex and concave regions.
- The bond coat thickness proved to influence the oxidation behavior, by establishing the Y-reservoir of the coating. For a given MCrAlY system, an optimum yttrium reservoir exists to obtain a compromise between the beneficial effect on oxide adherence without promoting a vast formation of Y/Al-compounds, which enhance the growth rate of the oxide scale and at the same time, may impose additional thermal and growth stresses. In order to define this optimum yttrium reservoir it is absolutely necessary to take into account the actual coating thickness and not only its Y-concentration.

For a given chemical composition, coating processing parameters can also have a strong influence on the oxidation behavior of a MCrAlY during high temperature exposure:

- The exact sequence of heat treatment and surface smoothening steps in MCrAlY-BC preparation for EB-PVD TBC deposition may affect the oxide growth rate, morphology and adherence. If the surface smoothening is done prior to heat treatment (HT), during the first step of vacuum annealing at 1100°C, yttrium will tend to oxidize at the surface and form Y-aluminates, consuming also Al in the near-surface regions. The local depletion of Y and Al promotes the formation of spinels at the surface upon air exposure. Especially in thin coatings with a small Y-content, i.e. those with a small Y-reservoir, the Y-depletion results in deterioration of the scale adherence. A volume increase associated with spinel formation and transformation of yttria (and YAP) to YAG leads to high growth stresses

that could eventually cause mechanical deformation of the coating surface. The protective alumina scale will only form beneath this layer of Y-aluminates and spinels.

On the contrary, if the surface smoothening is done after the heat treatment (HT+G), the Y-enrichment at the surface is eliminated and thus the formation of a purer alumina layer during early oxidation stages is observed. This layer offers a better barrier for oxygen inward diffusion and results in lower oxide growth rates, and additionally reduces or eliminates the risk of surface mechanical deformation. Since Y in this case is not depleted in the sub-scale region, it is expected to be incorporated in the TGO as Y/Al-mixed oxide pegs beneath the alumina scale formed in early stages. The effect of heat treatment is, however, leveled out to a large extent in coatings with a high Y-reservoir. These findings are relevant for optimizing the production steps of EB-PVD TBC systems.

- The TGO growth rate and morphology can also be affected by the heat treatment parameters. The mechanism behind this effect is the modification of Y-distribution in the coating. Annealing at lower temperatures, e.g. at 900°C, at high and low oxygen partial pressures prevents Y-enrichment at the surface, which occurs during annealing in vacuum at 1100°C. The scale that forms is instead composed of an external, almost pure, alumina layer and Y/Al-rich compounds beneath, comparable to the morphology obtained with the HT+G initial surface condition. Similarly, the risk of scale/surface deformation in this case was reduced or even eliminated.
- The amount of oxygen impurities in a MCrAlY coating can strongly influence the mobility and content of “free” Y, and thus, to which extent this element can act at the surface during oxidation. This is especially true for MCrAlYs with a low Y-content, like the studied NiCoCrAlY(10-Al). A high oxygen content in the coating introduced during vacuum spraying binds yttrium as internal oxides and hinders partially or totally its diffusion to the surface, reducing its effects on the MCrAlY oxidation. In contrast, in the presence of low oxygen contents, most of the Y in the bond coat will be in solid solution “free” to diffuse to the surface. In other words the impurity content has an effect on the Y-reservoir. In order to observe these differences, only minor variations of the O-content are required, which can even exist within the same batch or within the same component.

The exposure of EB-PVD TBC specimens in atmospheres with considerably different oxygen partial pressures enabled the growth of oxide scales at different rates which were identical in morphology and composition. This permitted the correlation of the scale growth rates with lifetimes obtained in different atmospheres and suggested that a critical TGO thickness for topcoat failure exists for a given EB-PVD TBC system with a MCrAlY bond coat, provided that the above listed parameters are kept constant. The latter condition is important since those parameters were found to have an effect on the amount and distribution of the internal yttrium-rich oxides in the coating surface and sub-surface regions, which in turn decisively influenced the oxidation behavior and produced inherently different scales.

The estimation of a critical TGO thickness on the rough MCrAlY surfaces of APS-TBC systems was not possible due to the fact that non-uniform oxide scales form, with local variations in chemical composition and morphology. These differences originate from a non-homogeneous depletion of O-affine elements (Y and Al) during vacuum heat treatment and early oxidation stages along the rough surfaces as explained above.

As a general closure comment it can be stated that the oxidation behavior of a MCrAlY coating at high temperatures proved throughout this work to be very sensitive to slight variations in not only concentration but also in reservoir, mobility and distribution of yttrium. Moreover, it was evidenced that these variations can occur within the same material batch and can be technically very difficult to control. It is therefore believed that the full potential of the commercial MCrAlY bond coats, i.e. reliable operation of TBC-coated components at bond coat temperatures of 1000°C, cannot be exploited in a large scale production in the way the coatings are manufactured nowadays. Methods that assure a better reproducibility and predictability of the oxidation behavior of these coating materials at elevated temperatures are necessary.

12. References

- [**Abell**] J. Abell, I. Harris, B. Cockayne, B. Lent, An investigation of phase stability in the Y_2O_3 – Al_2O_3 system, *Journal of materials science*, 9 (1974) pp. 527-537
- [**Achar**] D.R.G. Achar, R. Muñoz-Arroyo, L. Singheiser and W.J. Quadakkers, Modelling of phase equilibria in MCrAlY coating systems, *Surface and coatings technology*, 187 (2004) pp. 272-283
- [**Allam**] I.M. Allam, D.P. Whittle, J. Stringer, The oxidation behavior of CoCrAl systems containing active element additions, *Oxidation of metals*, 12 (1978) pp. 35-66
- [**Anton**] R. Anton, W.J. Quadakkers, Untersuchungen zu den Versagensmechanismen von Wärmedämmschicht-Systemen im Temperaturbereich von 900°C bis 1050°C bei zyklischer Temperaturbelastung (PhD Thesis), Report JUEL-4056, Forschungszentrum Jülich GmbH, (2003)
- [**Barrett**] C. Barrett, C. Lowell, Comparison of isothermal and cyclic oxidation behavior of twenty-five commercial sheet alloys at 1150°C, *Oxidation of metals*, 9 (1975) pp. 307-355
- [**Baufeld**] B. Baufeld, M. Schmücker, Microstructural evolution of a NiCoCrAlY coating on an IN100 substrate, *Surface and coatings technology*, 199 (2005) pp. 49-56
- [**Beele**] W. Beele, N. Czech, W.J. Quadakkers, W. Stamm, Long-term oxidation tests on a Re-containing MCrAlY coating, *Surface and coatings technology*, 94-95 (1997) pp. 41-45
- [**Bennett**] M. Bennett, High Temperature Corrosion Characterization by the Combined Use of Surface Microsurgery and Surface Analysis, *Surface and interface analysis*, 22 (1994) pp. 421-430
- [**Boyce**] M. Boyce. Gas turbine engineering handbook. Springer-Verlag, Berlin (1999)
- [**Braue**] W. Braue, K. Fritscher, U. Schulz, C. Leyens, R. Wirth, Nucleation and growth of oxide constituents on NiCoCrAlY bond coats during the different stages of EB-PVD TBC deposition and upon thermal loading, *Materials science forum*, 461-464 (2004) pp. 899-906
- [**Clarke-1**] D.R. Clarke, C.G. Levi, Materials design for the next generation thermal barrier coatings, *Annual reviews of materials research*, 33 (2003) pp. 383-417
- [**Clarke-2**] D.R. Clarke, Stress generation during high-temperature oxidation of metallic alloys, *Current opinion in solid state and materials science*, 6 (2002) pp. 237-244
- [**Czech-1**] N. Czech, F. Schmitz, W. Stamm, Improvement of MCrAlY coatings by addition of rhenium, *Surface and coatings technology*, 68 (1994) pp. 17-21
- [**Czech-2**] N. Czech, F. Schmitz, W. Stamm, Microstructural analysis of the role of rhenium in advanced MCrAlY coatings, 76 (1995) pp. 28-33

- [**Czyrska**] A. Czyrska-Filemonowicz, R. Versaci, D. Clemens, W.J. Quadakkers, in: S.B. Newcomb, M.J. Bennett (Eds.), *Microscopy of oxidation 2*, the institute of materials, London (1993) p. 288.
- [**Dahl**] K. Dahl, J. Hald, Estimation of metal temperature of MCrAlY coated IN738 components based on interdiffusion behaviour, *Energy materials*, 1 (2006) pp. 106-115
- [**DeMasi**] J.T. DeMasi-Marcin, D.K. Gupta, Protective coatings in gas turbine engines, *Surface and coatings technology*, 68-69 (1994) pp. 1-9
- [**Donachie**] M. Donachie, S. Donachie, *Superalloys – a technical guide*, ASM international technical books committee, 2nd Edition, Materials Park, USA (2002)
- [**Douglass**] D.L. Douglass, A critique of internal oxidation in alloys during the post-Wagner era, *Oxidation of metals*, 44 (1995) pp. 81-111
- [**D'Silva**] A. D'Silva, V. Fassel, X-ray excited luminescence of the rare earths, in *Handbook on the physics and chemistry of rare earths vol. 3*, by K. Gschneidner and L.R. Eyring, North Holland Publishing Company, New York (1979) p. 441
- [**Echsler-1**] H. Echsler, D. Renusch, M. Schütze, Bond coat oxidation and its significance for life expectancy of thermal barrier coating systems, *Materials science and technology*, 20 (2004) pp. 307-318.
- [**Echsler-2**] H. Echsler, *Oxidationsverhalten und mechanische Eigenschaften von Wärmedämmschichten und deren Einfluss auf eine Lebensdauer vorhersage*, (PhD Thesis), RWTH Aachen (2003)
- [**Ellison**] K. Ellison, J. Daleo, K. Hussain, , *Proceedings of the 10th international symposium on superalloys* (ed. K. Green), Warrendale, USA (2004) pp. 759-768
- [**EvansA-1**] A. G. Evans, J. W. Hutchinson, Y. Wei, Interface adhesion: effects of plasticity and segregation, *Acta materialia*, 47 (1999) pp. 4093-4113
- [**EvansA-2**] A. G. Evans, D.R. Mumm, J.W. Hutchinson, G.H. Meier, F.S. Pettit, Mechanics controlling the durability of thermal barrier coatings, *Progress in materials science* 46 (2001) pp. 505-553
- [**EvansA-3**] A.G. Evans, G.B. Crumley, R.E. Demaray, *Oxidation of metals* 20 (1983) pp. 193
- [**EvansH-1**] H.E. Evans, A. Strawbridge, R.A. Carolan, C.B. Ponton, Creep effects on the spallation of an alumina layer from a NiCoCrAlY coating, *Materials science and engineering A225* (1997) pp. 1-8
- [**EvansH-2**] H.E. Evans, M.P. Taylor, Diffusion cells and chemical failure of MCrAlY bond coats in thermal-barrier coating systems, *Oxidation of metals*, 55 (2001) pp.17-34

- [EvansH-3]** H.E. Evans, Stress effects in high temperature oxidation of metals, *International materials reviews*, 40 (1995) pp. 1-40
- [Fox]** P. Fox, G.J. Tatlock, Effect of tantalum additions on oxidation of overlay coated superalloys, *Materials science and technology*, 5 (1989) pp. 816
- [Gell-1]** M. Gell, E. Jordan, K. Vaidyanathan, K. McCarron, B. Barber, Y.H. Sohn, V. Tolpygo, Bond strength, bond stress and spallation mechanics of thermal barrier coatings, 120 (1999) pp. 53-60
- [Gell-2]** M. Gell, S. Sridharan, M. Wen, E. Jordan, Photoluminescence piezospectroscopy: a multi-purpose quality control and NDI technique for thermal barrier coatings, *International journal of applied ceramic technology* 1 (2004) pp. 316-329
- [Gil]** A. Gil, V. Shemet, R. Vassen, M. Subanovic, J. Toscano, D. Naumenko, L. Singheiser, W.J. Quadackers, Effect of surface condition on the oxidation behaviour of MCrAlY coatings, *Surface and coatings technology*, 201 (2006) pp. 3824-3828
- [Gleeson-1]** B. Gleeson, Thermal barrier coatings for aeroengines applications, *Journal of propulsion and power*, 22 (2006) pp. 375-383
- [Gleeson-2]** B. Gleeson, W. Wang, S. Hayashi, D. Sordellet, Effects of platinum on the interdiffusion and oxidation behavior of Ni-Al-based alloys, *Materials science forum*, 461-464 (2004) pp. 213-222
- [Goward]** G. Goward, Progress in coatings for gas turbines, *Surface and coatings technology*, 108-109 (1998) pp. 73-79
- [Grabke]** H. J. Grabke, Thermogravimetry, in *Guidelines on methods and testing in high temperature corrosion research*, Ed. H. Grabke and D. Meadowcroft, The institute of materials, London (1995) pp. 52-61
- [Gudmundsson]** B. Gudmundsson, B. Jacobsson, Yttrium oxides in vacuum-plasma –sprayed CoNiCrAlY coatings, *Thin solid films*, 173 (1989) pp. 99-107
- [Hay]** R. Hay, Kinetics and deformation during the reaction of yttrium-aluminum perovskites and alumina to yttrium-aluminum garnet, *Journal of the american ceramic society*, 77 (1994) pp. 1473–85
- [HeJ]** J. He, D. Clarke, Determination of the piezospectroscopic coefficients for chromium-doped sapphire, *Journal of the American ceramic society*, 78 (1995) pp. 1347-1353
- [HeM]** M.Y. He, A. G. Evans, J.W. Hutchinson, Effects of morphology on the decohesion of compressed thin films, *Materials science and engineering*, 245 (1998) pp. 168-181

- [Heinicke]** B. Heinicke, Schädigung von Wärmedämmschichtsystemen mit unterschiedlichen Haftvermittlerschichten unter zyklischer Beanspruchung (PhD Thesis). Technische Universität Darmstadt, Shaker Verlag (2004)
- [Huntz]** A. Huntz, The role of active elements in the oxidation behaviour of high temperature alloys. Elsevier, London (1989), p 81
- [IEA]** World Energy Outlook 2004. International Energy Agency, Paris, (2004)
- [Khattak]** C.P. Khattak, F.F. Wang, Perovskites and garnets, in Handbook on the physics and chemistry of rare earths vol. 3, by K. Gschneidner and L.R. Eyring, North Holland Publishing Company, New York (1979) p. 597
- [Kim]** G.M. Kim, N.M. Yanar, E.N. Hewitt, F.S. Pettit, G.H. Meier, The effect of the type of thermal exposure on the durability of thermal barrier coatings, Scripta Materialia, 46 (2002) pp. 489-495
- [Kofstad-1]** P. Kofstad, High temperature corrosion, Elsevier applied science publishers ltd, Barking, UK (1988)
- [Kofstad-2]** P. Kofstad, Nonstoichiometry, diffusion, and electrical conductivity in binary metal oxides, Wiley, New York (1972)
- [Kolb]** A. Kolb-Telieps, D. Naumenko, W.J. Quadackers, G. Strehl, R. Newton, High Temperature Corrosion of FeCrAlY / Aluchrom YHf in environments relevant to exhaust gas systems, in Materials Aspects in Automotive Catalytic Converters, WILEY-VCH Verlag GmbH, Weinheim, Germany (2001)
- [Lechner]** C. Lechner, J. Seume. Stationäre Gasturbinen. Springer-Verlag, Berlin (2003)
- [Leckie]** R.M. Leckie, S. Krämer, M. Rühle, C.G. Levi, Thermochemical compatibility between alumina and $\text{ZrO}_2\text{-GdO}_{3/2}$ thermal barrier coatings, Acta materialia, 53 (2005) pp. 3281–3292
- [Levi]** C.G. Levi, E. Sommer, S.G. Terry, A. Catanoiu, M. Rühle, Alumina grown during deposition of thermal barrier coatings on NiCrAlY, Journal of the american ceramic society, 86 (2003) pp. 676–85
- [Li-1]** M.H. Li, X.F. Sun, J.G. Li, Z.Y. Zhang, T. Jin, H.R. Guan, Z.Q. Hu, Oxidation behavior of a single-crystal Ni-base superalloy in air-I: at 800 and 900°C, Oxidation of metals, 59 (2003) pp. 591-605
- [Li-2]** M.H. Li, X.F. Sun, T. Jin, H.R. Guan, Z.Q. Hu, Oxidation behavior of a single-crystal Ni-base superalloy in air II: at 1000, 1100 and 1150°C, Oxidation of metals, 60 (2003) pp. 195-210

- [**Majerus**] P. Majerus, Neue Verfahren zur Analyse des Verformungs- und Schädigungsverhaltens von MCrAlY-Schichten im Wärmedämmschichtsystem (PhD Thesis). Forschungszentrum Jülich GmbH, (2003)
- [**Meier**] G.H. Meier, N. Birks, Introduction to the high-temperature oxidation of metals, Arnold, London (1983)
- [**Mennicke**] C. Mennicke, M.-Y. He, D. R. Clarke, J. S. Smith, Acta Materialia, 48 (2000) pp. 2941
- [**Monceau**] D. Monceau, F. Crabos, A. Melié, B. Pieraggi, Effects of bond coat preoxidation and surface finish on isothermal and cyclic oxidation, high temperature corrosion and thermal shock resistance of TBC systems, Materials science forum, 369-372 (2001) pp. 607-614
- [**Mumm**] D.R Mumm, A.G. Evans, Mechanisms controlling the performance and durability of thermal barrier coatings, Key engineering materials, 197 (2001) pp. 199-230
- [**Muñoz-1**] R. Muñoz, J. Pérez, W.J. Quadakkers, Influence of the MCrAlY alloys microstructure on the resistance against oxidation at elevated temperature (PhD Thesis), Univ. Complutense de Madrid, (2002)
- [**Muñoz-2**] R. Muñoz, D.Clemens, F. Tietz, R. Anton, W.J. Quadakkers, L. Singheiser, Influence on composition and phase distribution on the oxidation behaviour of NiCoCrAlY alloys, Materials science forum, 369-372 (2001) pp. 165-172
- [**Naumenko-1**] D. Naumenko, J. Quadakkers, Effects of metallurgical chemistry and service conditions on the oxidation limited life time of FeCrAl-based components (PhD Thesis), Report JUEL-3948, ISSN 0944-2952, Forschungszentrum Jülich GmbH, (2002)
- [**Naumenko-2**] D. Naumenko, M. Subanovic, E. Wessel, L. Niewolak, L. Singheiser, M. Kamruddin, J. Quadakkers, Effect of manufacturing parameters on the oxidation resistance of MCrAlY-coatings and bondcoats in power-generation gas-turbines, in Proceedings of the 2007 Parsons conference, by A. Strang, W. Banks, G. McColvin, J. Oakey, R. Vanstone, ISBN 1-86125-168-8, IOM communications Ltd., London (2007) pp. 193-204
- [**Naumenko-3**] D. Naumenko, B. Gleeson, E. wessel, L. Singheiser, J. Quadakkers, Correlation between the microstructure, growth mechanism and growth kinetics of alumina scales on a FeCrAlY-alloy, Metallurgical and materials transactions 38A (2007) pp. 2974-2983
- [**Nesbitt**] J. Nesbitt, B. Nagaraj, J. Williams, Effect of Hf additions to Pt aluminide bond coats on EB-PVD TBC life, Elevated temperature coatings: science and technology IV, edited by J.M. Hampikian, N.B. Dahotre, J. Morral, TMS, Warrendale, PA, USA (2001) p. 79

- [Nicholls-1]** J. R. Nicholls, N. J. Simms, W.Y. Chan, H.E. Evans, Smart overlay coatings – concept and practice, *Surface and coatings technology*, 149 (2002) pp. 236-244
- [Nicholls-2]** J. R. Nicholls, Designing oxidation-resistant coatings, *Journal of metals*, 52 (2000) pp. 28-35
- [Nicholls-3]** J. R. Nicholls, K.J. Lawson, A. Johnstone, D.S. Rickerby, Low thermal conductivity EB-PVD thermal barrier coatings, *Materials science forum*, 369-372 (2001) pp. 595-606
- [Nijdam-1]** T.J. Nijdam, L.P.H. Jeurgens, J.H. Chen, W.G. Sloof, On the microstructure of the initial oxide grown by controlled annealing and oxidation on a NiCoCrAlY bond coating, *Oxidation of metals*, 64 (2005) pp. 355-377
- [Nijdam-2]** T.J. Nijdam, Promoting exclusive α -Al₂O₃ growth upon high temperature oxidation of NiCoCrAlY alloys (PhD Thesis), ISBN 90-90199-10-1, Technische Universiteit Delft, (2005)
- [Nijdam-3]** T.J. Nijdam, W.G. Sloof, Effect of reactive element oxide inclusions on the growth kinetics of protective oxide scales, *Acta materialia*, 55 (2007) pp. 5980–5987
- [Nijdam-4]** T.J. Nijdam, L.P.H. Jeurgens, W.G. Sloof, Promoting exclusive α -Al₂O₃ growth upon high-temperature oxidation of NiCrAl alloys: experiment versus model predictions, *Acta materialia*, 53 (2005) pp. 1643-1653.
- [Orosz]** R. Orosz, U. Krupp, H. Christ, D. Monceau, The influence of specimen thickness on the high temperature corrosion behavior of CMSX-4 during thermal-cycling exposure, *Oxidation of metals*, 68 (2007) pp. 165-176
- [Padture]** N. Padture, M. Gell, E. Jordan, Thermal barrier coatings for gas-turbine engine applications, *Science*, 296 (2002) pp. 280-284
- [Peters]** M. Peters, C. Leyens, U. Schulz, W. Kaysser, EB-PVD thermal barrier coatings for aeroengines and gas turbines, *Advanced engineering materials*, 3 (2001) pp. 193-204
- [Phillips]** M.A. Phillips, B. Gleeson, Beneficial effects of rhenium additions on the cyclic-oxidation resistance of β -NiAl + α -Cr alloys
- [Pint-1]** B.A. Pint, I.G. Wright, W.Y. Lee, Y. Zhang, K. Prüßner, K.B. Alexander, Substrate and bond coat compositions: factors affecting alumina scale adhesion, *Materials science and engineering*, A245 (1998) pp. 201–211
- [Pint-2]** B.A. Pint, Experimental observations in support of the dynamic-segregation theory to explain the reactive-element effect, *Oxidation of metals*, 45 (1996) pp. 1-37
- [Prescott]** R. Prescott and M.J. Graham, The formation of aluminum oxide scales on high-temperature alloys, *Oxidation of metals*, 38 (1992) pp. 233-254

- [Quadakkers-1]** W.J. Quadakkers, V. Shemet, D. Sebold, R. Anton, E. Wessel L. Singheiser, Oxidation characteristics of a platinized MCrAlY bond coat for TBC systems during cyclic oxidation at 1000°C, *Surface and coatings technology*, 199 (2005) pp. 77-82
- [Quadakkers-2]** W.J. Quadakkers, A.K. Tyagi, D. Clemens, R. Anton, L. Singheiser, The significance of bond coat oxidation for the life of TBC coatings, *Elevated temperature coatings: science and technology III*, edited by J.M. Hampikian and N.B. Dahotre, TMS, Warrendale, PA, USA (1999) p. 119
- [Quadakkers-3]** W.J. Quadakkers, L. Singheiser, Practical aspects of the RE effect, *Materials science forum*, 369-372 (2001) pp. 77-92
- [Quadakkers-4]** W.J. Quadakkers, H. Viehhaus, The application of surface analysis techniques in high temperature corrosion research, *Proceedings of EFC-Workshop “Methods and testing in high temperature corrosion” 1994*, The institute of materials, (1995)
- [Quadakkers-5]** W. J. Quadakkers, H. Holzbrecher, K. G. Briefs, H. Beske, Differences in growth mechanisms of oxide scales formed on ODS and conventional wrought alloys, *Oxidation of metals*, 32 (1989) pp. 67-88
- [Rae]** C.M.F. Rae and R.C. Reed, Primary creep in single crystal superalloys: Origins, mechanisms and effects, *Acta Materialia*, 55 (2007) pp. 1067-1081
- [Raffaitin]** A. Raffaitin, F. Crabos, E. Andrieu, D. Monceau, Advanced burner-rig test for oxidation–corrosion resistance evaluation of MCrAlY/superalloys systems, *Surface and coatings technology* 201 (2006) pp. 3829–3835
- [Rahmel]** A. Rahmel, V. Kolarik, Metallography, electron microprobe and X-ray structure analysis, *Proceedings of EFC-Workshop “Methods and testing in high temperature corrosion” 1994*, The institute of materials, (1995)
- [Roth]** R. Roth, *Phase diagrams for ceramists vol. XI*, The American ceramic society, Westerville, USA (1995)
- [Ryan]** N.E. Ryan, High-temperature corrosion protection, in *Handbook on the physics and chemistry of rare earths vol. 21*, by K. Gschneidner and L.R. Eyring, North Holland Publishing Company, New York (1979) p. 123
- [Sariouglu]** S. Sariouglu, J.R. Blachere, F.S. Pettit, G.H. Meier, J.L. Smialek, C. Mennicke, The effects of reactive elements additions, sulfur removal, and specimen thickness on the oxidation behaviour of alumina-forming Ni- and Fe-based alloys, *Materials science forum*, 251-254 (1997) pp. 405-412

- [**Schulz**] U. Schulz, M. Menzebacha, C. Leyens, Y.Q. Yang, Influence of substrate material on oxidation behavior and cyclic lifetime of EB-PVD TBC systems, *Surface and coatings technology*, 146 –147 (2001) pp. 117–123
- [**Seal**] S. Seal, S.C. Kuiry, L.A. Bracho, Studies on the surface chemistry of oxide films formed on IN-738LC Superalloy at elevated temperatures in dry air, *Oxidation of Metals*, 56 (2001) pp. 583-603
- [**Selcuk**] A. Selcuk, A. Atkinson, Analysis of the Cr^{3+} luminescence spectra from thermally grown oxide in thermal barrier coatings, *Materials Science and Engineering A335* (2002) pp. 147-156
- [**Sergo**] V. Sergo, D.R. Clarke, Observation of subcritical spall propagation of a thermal barrier coating, *Journal of the american ceramic society*, 81 (1998) pp. 3237–42
- [**Singheiser-1**] L. Singheiser. Investigations on reduction of high temperature corrosion of metallic materials by technical alloying measures and coatings, Univ. Erlangen-Nürnberg, 1991
- [**Singheiser-2**] L. Singheiser, R. Steinbrech, W.J. Quadakkers, D. Clemens, B. Siebert, Thermal barrier coatings for gas turbine applications – failure mechanisms and life prediction, *Materials for advanced power engineering 1998 – Proceedings of the 6th Liège conference II*, J. Lecomte-Beckers, F. Schubert. P.J. Ennis, Schriften des Forschungszentrum Jülich (1998)
- [**Smeggil**] J.G. Smeggil, A.W. Funkenbusch, N.S. Bornstein, the effects of laser surface processing on the thermally grown oxide scale formed on a Ni-Cr-Al-Y composition, *Thin solid films*, 119 (1984) pp. 327-335
- [**Smialek**] J. Smialek, Maintaining adhesion of protective Al_2O_3 scales, *Journal of metals*, 52 (2000) pp. 22-25
- [**Sohn**] Y.H. Sohn, K. Vaidyanathan, M. Ronski, E.H. Jordan, M. Gell, Thermal cycling of EB-PVD/MCrAlY thermal barrier coatings: II. Evolution of photo-stimulated luminescence, *Surface and coatings technology* 146-147 (2001) pp. 102–109
- [**Stecura**] S. Stecura, Effects of yttrium, aluminum and chromium concentrations in bond coatings on the performance of zirconia-yttria thermal barriers, *Thin solid films*, 73 (1980) pp. 481-489
- [**Stott**] F.H. Stott, The oxidation of alumina-forming alloys, *Materials science forum*, 251 (1997) pp. 19-32
- [**Täck**] U. Täck, The influence of cobalt and rhenium on the behaviour of MCrAlY coatings (PhD thesis), Tech. Univ. Freiberg, 2004, p.25, p.151, p. 169

- [**Tang**] F. Tang, J. Schoenung, Local accumulation of thermally grown oxide in plasma sprayed thermal barrier coatings with rough top-coat/bond-coat interfaces, *Scripta materialia*, 52 (2005) pp. 905–909
- [**Taylor-1**] T.A. Taylor, D.F. Bettridge, Development of alloyed and dispersion-strengthened MCrAlY coatings, *Surface and coatings technology*, 86-87 (1996) pp. 9-14
- [**Taylor-2**] T.A. Taylor, J.K. Knapp, Dispersion-strengthened modified MCrAlY coatings produced by reactive deposition, *Surface and coatings technology*, 76-77 (1995) pp. 34-40
- [**Tolpygo-1**] V.K. Tolpygo, D.R. Clarke, Morphological evolution of thermal barrier coatings induced by cyclic oxidation, *Surface and coatings technology*, 163 (2003) pp. 81-86
- [**Tolpygo-2**] V.K. Tolpygo, D.R. Clarke, Microstructural study of the theta-alpha transformation in alumina scales formed on nickel-aluminides, *Materials at high temperatures*, 17 (2000) pp. 59-70
- [**Tolpygo-3**] V.K. Tolpygo, D.R. Clarke, Wrinkling of α -alumina films grown by oxidation II. Oxide separation and failure, *Acta materialia*, 46 (1998) pp. 5167-5174
- [**Tolpygo-4**] V.K. Tolpygo, D.R. Clarke, K.S. Murphy, Oxidation-induced failure of EB-PVD thermal barrier coatings, *Surface and coatings technology*, 146 (2001) 124-131
- [**Vassen**] R. Vassen, X. Cao, F. Tietz, D. Basu, D. Stöver, Zirconates as new materials for thermal barrier coatings, *Journal of the american ceramic society*, 83 (2000) pp. 2023–2028
- [**VGB**] Zahlen und Fakten zur Stromerzeugung 2005. Verein der Grosskesselbetreiber, Essen, (2005) www.vgb.org
- [**Watanabe**] M. Watanabe, T. Xu, C.G. Levi, A.S. Gandhi, A.G. Evans, Shear band formation in columnar thermal barrier oxides, *Acta materialia*, 53 (2005) pp. 3765–3773
- [**Wellman**] R.G. Wellman, J.R. Nicholls, A mechanism for the erosion of EB-PVD TBCs, *Materials science forum*, 369-372 (2001) pp. 531-538
- [**Yanar-1**] N.M. Yanar, G. Kim, S. Hamano, F.S. Pettit, G.H. Meier, Microstructural characterization of the failures of thermal barrier coatings on Ni-base superalloys, *Materials at high temperatures*, 20 (2003) pp. 495-506
- [**Yanar-2**] N.M. Yanar, F.S. Pettit, G.H. Meier, Effects of bond coat processing on the durability of thermal barrier coatings, *Materials science forum*, 426-432 (2003) pp. 2453-2458
- [**Yanar-3**] N. M. Yanar, F. S. Pettit, G. H. Meier, Failure characteristics during cyclic oxidation of YSZ thermal barrier coatings deposited via EB-PVD on platinum aluminide and on NiCoCrAlY bond coats with processing modifications for improved performances, *Metallurgical and materials transactions A*, 37 (2006) pp. 1563-1580

- [Yanar-4]** N.M. Yanar, M.J. Stiger, M. Maris-Sida, F.S. Pettit, G.H. Meier, The effects of high temperature exposure on the durability of thermal barrier coatings, *Key engineering materials*, 197 (2001) pp. 145-164
- [Zhao]** L. Zhao, M. Parco, E. Lugscheider, High velocity oxy-fuel thermal spraying of a NiCoCrAlY alloy, *Surface and coatings technology*, 179 (2004) pp. 272–278
- [Zhu]** H.X. Zhu, N.A. Fleck, A.C.F. Cocks, A.G. Evans, Numerical simulations of crack formation from pegs in thermal barrier systems with NiCoCrAlY bond coats, *Materials science and engineering A*, 404 (2005) pp. 26–32

Acknowledgements

Special thanks to Dmytro Naumenko and W. Joe Quadackers, for their vision, guidance, analysis, and all the time they dedicated to improve this work.

To Aleksander Gil, for greatly contributing with the production and analysis of the results contained in this work.

To Prof. Lorenz Singheiser, for enabling the conception of this work and supporting it.

To Prof. Gerry Meier (Univ. of Pittsburgh), for offering valuable discussions to part of the results obtained.

To the colleagues of IEF-2, H. Cosler, A. Kick, E. Wessel, A. Everwand, L. Niewolak, V. Gutzeit, and P. Lersch, for helping with some of the experiments and contributing with the different analysis techniques employed during the various investigations.

To Werner Stamm (SIEMENS AG), for providing the materials to carry out this work.

To Robert Vaßen and Karl-Heinz Rauwald (IEF-1) for manufacturing the specimens necessary for this study.

To all the colleagues of the high temperature corrosion group, Joanna, Pawel, Javier, Marko, Marek, Leszek, Thomas, Vladimir, Peng, Mark, Emmanuel, Dmytro, Aleksander and Joe, for all their help and for making this time joyful.

To my family and friends for being always beside me during this time.

Dear God, none of this would have been possible without your help

1. **Einsatz von multispektralen Satellitenbilddaten in der Wasserhaushalts- und Stoffstrommodellierung – dargestellt am Beispiel des Rureinzugsgebietes**
von C. Montzka (2008), XX, 238 Seiten
ISBN: 978-3-89336-508-1
2. **Ozone Production in the Atmosphere Simulation Chamber SAPHIR**
by C. A. Richter (2008), XIV, 147 pages
ISBN: 978-3-89336-513-5
3. **Entwicklung neuer Schutz- und Kontaktierungsschichten für Hochtemperatur-Brennstoffzellen**
von T. Kiefer (2008), 138 Seiten
ISBN: 978-3-89336-514-2
4. **Optimierung der Reflektivität keramischer Wärmedämmschichten aus Yttrium-teilstabilisiertem Zirkoniumdioxid für den Einsatz auf metallischen Komponenten in Gasturbinen**
von A. Stuke (2008), X, 201 Seiten
ISBN: 978-3-89336-515-9
5. **Lichtstreuende Oberflächen, Schichten und Schichtsysteme zur Verbesserung der Lichteinkopplung in Silizium-Dünnschichtsolarzellen**
von M. Berginski (2008), XV, 171 Seiten
ISBN: 978-3-89336-516-6
6. **Politiksznarien für den Klimaschutz IV – Szenarien bis 2030**
hrsg.von P. Markewitz, F. Chr. Matthes (2008), 376 Seiten
ISBN 978-3-89336-518-0
7. **Untersuchungen zum Verschmutzungsverhalten rheinischer Braunkohlen in Kohledampferzeugern**
von A. Schlüter (2008), 164 Seiten
ISBN 978-3-89336-524-1
8. **Inorganic Microporous Membranes for Gas Separation in Fossil Fuel Power Plants**
by G. van der Donk (2008), VI, 120 pages
ISBN: 978-3-89336-525-8
9. **Sinterung von Zirkoniumdioxid-Elektrolyten im Mehrlagenverbund der oxidkeramischen Brennstoffzelle (SOFC)**
von R. Mücke (2008), VI, 165 Seiten
ISBN: 978-3-89336-529-6
10. **Safety Considerations on Liquid Hydrogen**
by K. Verfondern (2008), VIII, 167 pages
ISBN: 978-3-89336-530-2

11. **Kerosinreformierung für Luftfahrtanwendungen**
von R. C. Samsun (2008), VII, 218 Seiten
ISBN: 978-3-89336-531-9
12. **Der 4. Deutsche Wasserstoff Congress 2008 – Tagungsband**
hrsg. von D. Stolten, B. Emonts, Th. Grube (2008), 269 Seiten
ISBN: 978-3-89336-533-3
13. **Organic matter in Late Devonian sediments as an indicator for environmental changes**
by M. Kloppisch (2008), XII, 188 pages
ISBN: 978-3-89336-534-0
14. **Entschwefelung von Mitteldestillaten für die Anwendung in mobilen Brennstoffzellen-Systemen**
von J. Latz (2008), XII, 215 Seiten
ISBN: 978-3-89336-535-7
15. **RED-IMPACT**
Impact of Partitioning, Transmutation and Waste Reduction Technologies on the Final Nuclear Waste Disposal
SYNTHESIS REPORT
ed. by W. von Lensa, R. Nabbi, M. Rossbach (2008), 178 pages
ISBN 978-3-89336-538-8
16. **Ferritic Steel Interconnectors and their Interactions with Ni Base Anodes in Solid Oxide Fuel Cells (SOFC)**
by J. H. Froitzheim (2008), 169 pages
ISBN: 978-3-89336-540-1
17. **Integrated Modelling of Nutrients in Selected River Basins of Turkey**
Results of a bilateral German-Turkish Research Project
project coord. M. Karpuzcu, F. Wendland (2008), XVI, 183 pages
ISBN: 978-3-89336-541-8
18. **Isotopengeochemische Studien zur klimatischen Ausprägung der Jüngerer Dryas in terrestrischen Archiven Eurasiens**
von J. Parplies (2008), XI, 155 Seiten, Anh.
ISBN: 978-3-89336-542-5
19. **Untersuchungen zur Klimavariabilität auf dem Tibetischen Plateau - Ein Beitrag auf der Basis stabiler Kohlenstoff- und Sauerstoffisotope in Jahringen von Bäumen waldgrenznaher Standorte**
von J. Griessinger (2008), XIII, 172 Seiten
ISBN: 978-3-89336-544-9

20. **Neutron-Irradiation + Helium Hardening & Embrittlement Modeling of 9%Cr-Steels in an Engineering Perspective (HELENA)**
by R. Chaouadi (2008), VIII, 139 pages
ISBN: 978-3-89336-545-6
21. **Messung und Bewertung von Verkehrsemissionen**
von D. Klemp, B. Mittermaier (2009), ca. 230 Seiten, erscheint in Kürze
ISBN: 978-3-89336-546-3
22. **Verbundvorhaben APAWAGS (AOEV und Wassergenerierung) – Teilprojekt: Brennstoffreformierung – Schlussbericht**
von R. Peters, R. C. Samsun, J. Pasel, Z. Porš, D. Stolten (2008), VI, 106 Seiten
ISBN: 978-3-89336-547-0
23. **FREEVAL**
Evaluation of a Fire Radiative Power Product derived from Meteosat 8/9 and Identification of Operational User Needs
Final Report
project coord. M. Schultz, M. Wooster (2008), 139 pages
ISBN: 978-3-89336-549-4
24. **Untersuchungen zum Alkaliverhalten unter Oxycoal-Bedingungen**
von C. Weber (2008), VII, 143, XII Seiten
ISBN: 978-3-89336-551-7
25. **Grundlegende Untersuchungen zur Freisetzung von Spurstoffen, Heißgaschemie, Korrosionsbeständigkeit keramischer Werkstoffe und Alkalirückhaltung in der Druckkohlenstaubfeuerung**
von M. Müller (2008), 207 Seiten
ISBN: 978-3-89336-552-4
26. **Analytik von ozoninduzierten phenolischen Sekundärmetaboliten in *Nicotiana tabacum* L. cv Bel W3 mittels LC-MS**
von I. Koch (2008), III, V, 153 Seiten
ISBN 978-3-89336-553-1
27. **IEF-3 Report 2009. Grundlagenforschung für die Anwendung**
(2009), ca. 180 Seiten
ISBN: 978-3-89336-554-8
28. **Influence of Composition and Processing on the Oxidation Behavior of MCrAlY-Coatings for TBC Applications**
by J. Toscano (2009), 168 pages
ISBN: 978-3-89336-556-2

1. **Einsatz von multispektralen Satellitenbilddaten in der Wasserhaushalts- und Stoffstrommodellierung – dargestellt am Beispiel des Rureinzugsgebietes**
von C. Montzka (2008), XX, 238 Seiten
ISBN: 978-3-89336-508-1
2. **Ozone Production in the Atmosphere Simulation Chamber SAPHIR**
by C. A. Richter (2008), XIV, 147 pages
ISBN: 978-3-89336-513-5
3. **Entwicklung neuer Schutz- und Kontaktierungsschichten für Hochtemperatur-Brennstoffzellen**
von T. Kiefer (2008), 138 Seiten
ISBN: 978-3-89336-514-2
4. **Optimierung der Reflektivität keramischer Wärmedämmschichten aus Yttrium-teilstabilisiertem Zirkoniumdioxid für den Einsatz auf metallischen Komponenten in Gasturbinen**
von A. Stuke (2008), X, 201 Seiten
ISBN: 978-3-89336-515-9
5. **Lichtstreuende Oberflächen, Schichten und Schichtsysteme zur Verbesserung der Lichteinkopplung in Silizium-Dünnschichtsolarzellen**
von M. Berginski (2008), XV, 171 Seiten
ISBN: 978-3-89336-516-6
6. **Politiksznarien für den Klimaschutz IV – Szenarien bis 2030**
hrsg.von P. Markewitz, F. Chr. Matthes (2008), 376 Seiten
ISBN 978-3-89336-518-0
7. **Untersuchungen zum Verschmutzungsverhalten rheinischer Braunkohlen in Kohledampferzeugern**
von A. Schlüter (2008), 164 Seiten
ISBN 978-3-89336-524-1
8. **Inorganic Microporous Membranes for Gas Separation in Fossil Fuel Power Plants**
by G. van der Donk (2008), VI, 120 pages
ISBN: 978-3-89336-525-8
9. **Sinterung von Zirkoniumdioxid-Elektrolyten im Mehrlagenverbund der oxidkeramischen Brennstoffzelle (SOFC)**
von R. Mücke (2008), VI, 165 Seiten
ISBN: 978-3-89336-529-6
10. **Safety Considerations on Liquid Hydrogen**
by K. Verfondern (2008), VIII, 167 pages
ISBN: 978-3-89336-530-2

11. **Kerosinreformierung für Luftfahrtanwendungen**
von R. C. Samsun (2008), VII, 218 Seiten
ISBN: 978-3-89336-531-9
12. **Der 4. Deutsche Wasserstoff Congress 2008 – Tagungsband**
hrsg. von D. Stolten, B. Emonts, Th. Grube (2008), 269 Seiten
ISBN: 978-3-89336-533-3
13. **Organic matter in Late Devonian sediments as an indicator for environmental changes**
by M. Klopisch (2008), XII, 188 pages
ISBN: 978-3-89336-534-0
14. **Entschwefelung von Mitteldestillaten für die Anwendung in mobilen Brennstoffzellen-Systemen**
von J. Latz (2008), XII, 215 Seiten
ISBN: 978-3-89336-535-7
15. **RED-IMPACT
Impact of Partitioning, Transmutation and Waste Reduction Technologies on the Final Nuclear Waste Disposal
SYNTHESIS REPORT**
ed. by W. von Lensa, R. Nabbi, M. Rossbach (2008), 178 pages
ISBN 978-3-89336-538-8
16. **Ferritic Steel Interconnectors and their Interactions with Ni Base Anodes in Solid Oxide Fuel Cells (SOFC)**
by J. H. Froitzheim (2008), 169 pages
ISBN: 978-3-89336-540-1
17. **Integrated Modelling of Nutrients in Selected River Basins of Turkey**
Results of a bilateral German-Turkish Research Project
project coord. M. Karpuzcu, F. Wendland (2008), XVI, 183 pages
ISBN: 978-3-89336-541-8
18. **Isotopengeochemische Studien zur klimatischen Ausprägung der Jüngerer Dryas in terrestrischen Archiven Eurasiens**
von J. Parplies (2008), XI, 155 Seiten, Anh.
ISBN: 978-3-89336-542-5
19. **Untersuchungen zur Klimavariabilität auf dem Tibetischen Plateau - Ein Beitrag auf der Basis stabiler Kohlenstoff- und Sauerstoffisotope in Jahrringen von Bäumen waldgrenznaher Standorte**
von J. Griessinger (2008), XIII, 172 Seiten
ISBN: 978-3-89336-544-9

20. **Neutron-Irradiation + Helium Hardening & Embrittlement Modeling of 9%Cr-Steels in an Engineering Perspective (HELENA)**
by R. Chaouadi (2008), VIII, 139 pages
ISBN: 978-3-89336-545-6
21. **Messung und Bewertung von Verkehrsemissionen**
von D. Klemp, B. Mittermaier (2009), ca. 230 Seiten, erscheint in Kürze
ISBN: 978-3-89336-546-3
22. **Verbundvorhaben APAWAGS (AOEV und Wassergenerierung) – Teilprojekt: Brennstoffreformierung – Schlussbericht**
von R. Peters, R. C. Samsun, J. Pasel, Z. Porš, D. Stolten (2008), VI, 106 Seiten
ISBN: 978-3-89336-547-0
23. **FREEVAL**
Evaluation of a Fire Radiative Power Product derived from Meteosat 8/9 and Identification of Operational User Needs
Final Report
project coord. M. Schultz, M. Wooster (2008), 139 pages
ISBN: 978-3-89336-549-4
24. **Untersuchungen zum Alkaliverhalten unter Oxycoal-Bedingungen**
von C. Weber (2008), VII, 143, XII Seiten
ISBN: 978-3-89336-551-7
25. **Grundlegende Untersuchungen zur Freisetzung von Spurstoffen, Heißgaschemie, Korrosionsbeständigkeit keramischer Werkstoffe und Alkalirückhaltung in der Druckkohlenstaubfeuerung**
von M. Müller (2008), 207 Seiten
ISBN: 978-3-89336-552-4
26. **Analytik von ozoninduzierten phenolischen Sekundärmetaboliten in *Nicotiana tabacum* L. cv Bel W3 mittels LC-MS**
von I. Koch (2008), III, V, 153 Seiten
ISBN 978-3-89336-553-1
27. **IEF-3 Report 2009. Grundlagenforschung für die Anwendung**
(2009), ca. 180 Seiten
ISBN: 978-3-89336-554-8
28. **Influence of Composition and Processing on the Oxidation Behavior of MCrAlY-Coatings for TBC Applications**
by J. Toscano (2009), 168 pages
ISBN: 978-3-89336-556-2

Abstract

The adherence of the thermally grown oxide (TGO) to the bond coat is recognized to be crucial for the lifetime of thermal barrier coatings (TBC) in aircraft engine and gas turbine blades. This work studies the influence of the bond coat's chemical composition as well as geometrical and pre-treatment/processing parameters on the growth and adherence of this TGO.

The results demonstrate that all the latter can affect the oxidation behavior and TGO adherence on MCrAlY-bond coats, generally due to a variation of the yttrium reservoir, mobility and/or distribution in the coating. Finally, it was proven that if the parameters mentioned above are avoided, a critical TGO thickness to failure in EB-PVD TBC systems may exist.

Author

Juan Toscano studied mechanical engineering at the Universidad Simón Bolívar in Caracas, Venezuela. After completion of his master studies in energy systems at the FH Aachen, he joined the division of high temperature corrosion and protective coatings of the Institute for Energy Research (IEF-2) in the Forschungszentrum Jülich. He developed his PhD dissertation out of his work in the project "Methods for prediction and extension of the lifetime of gas turbine components with thermal barrier coatings". This dissertation was successfully evaluated at the Technical University of Aachen (RWTH) in June 2008.

Institute of Energy Research

IEF-2 Materials Microstructure and Characterization

The research topics of IEF-2 are focussed on the development and characterization of materials for efficient gas and steam power plants, for high temperature fuel cells and for future fusion reactor components subjected to high thermal loads. The scientific expertises of the institute cover microstructural investigations, surface analysis techniques and the physical, chemical, mechanical and corrosion behaviour of metallic high temperature materials and of ceramic materials used either as structural components or as elements of coating systems.